



Study and development of new materials for high temperature compact thermal storage applications

Imane Mahroug

► To cite this version:

Imane Mahroug. Study and development of new materials for high temperature compact thermal storage applications. Mechanics [physics]. Université de Bordeaux; CIC EnergiGUNE, 2021. English. NNT : 2021BORD0371 . tel-03652920

HAL Id: tel-03652920

<https://theses.hal.science/tel-03652920>

Submitted on 27 Apr 2022

HAL is a multi-disciplinary open access archive for the deposit and dissemination of scientific research documents, whether they are published or not. The documents may come from teaching and research institutions in France or abroad, or from public or private research centers.

L'archive ouverte pluridisciplinaire **HAL**, est destinée au dépôt et à la diffusion de documents scientifiques de niveau recherche, publiés ou non, émanant des établissements d'enseignement et de recherche français ou étrangers, des laboratoires publics ou privés.

CO-SUPERVISED THESIS PRESENTED
TO OBTAIN THE QUALIFICATION OF
DOCTOR OF
THE UNIVERSITY OF BORDEAUX
AND OF THE UNIVERSITY OF THE BASQUE
COUNTRY

DOCTORAL SCHOOL OF PHYSICS AND ENGINEERING (SPI)
DOCTORAL SCHOOL OF MASTER AND DOCTORAL (MDE)
SPECIALIZATION MECHANICS

By Imane MAHROUG

**STUDY AND DEVELOPMENT OF NEW MATERIALS FOR
HIGH TEMPERATURE COMPACT THERMAL STORAGE
APPLICATIONS**

Under the supervision of: Dr. Jean TOUTAIN
And: Dr. Stefania DOPPIU
Co-supervisor: Dr. Fouzia Achchaq

Viva on 13/12/2021

Members of the examination panel:

Mr. Jean-Christophe Batsale	Professor, University of Bordeaux	President
Mr. Frédéric KUZNIK	Professor, INSA Lyon	Recorder
Mr. Jean-Pierre BEDECARRATS	Professor, University of Pau	Recorder
Mrs. Ane Miren GARCIA	Associate Professor, UPV/EHU	Examiner
Mrs. Ana Lázaro	Associate professor, University of Zaragoza	Examiner

Titre: Étude et développement de nouveaux matériaux pour des applications de stockage thermique compact à haute température

Résumé

Les composés péritectiques ont été étudiés récemment en tant que matériaux prometteurs de stockage de l'énergie thermique à hautes températures. Dans une transformation péritectique, une phase liquide réagit avec au moins une phase solide, à une température bien définie, pour former une nouvelle phase solide. Les réactions péritectiques conduisant à la formation des composés péritectiques fournissent des densités énergétiques théoriques exceptionnelles. Les processus de charge et décharge du composé péritectique s'opèrent à température constante et pression atmosphérique à travers la réaction péritectique réversible, résultant en un simple système de stockage thermique offrant une densité énergétique plus élevée que celle des MCPs actuellement utilisés et comparable à celle des meilleures réactions gaz-solide en cours de développement.

Cette thèse vise à développer de nouveaux matériaux à base du composé péritectique $\text{Li}_4(\text{OH})_3\text{Br}$, à hautes performances en terme de densité énergétique, compacité, stabilité, et rentabilité, pour le stockage compact de l'énergie thermique dans des applications d'énergie solaire. Le choix du $\text{Li}_4(\text{OH})_3\text{Br}$ en tant que matériau de stockage thermique a été basé sur sa haute densité énergétique théorique (800 J/g à $\sim 300^\circ\text{C}$). La validation du choix de $\text{Li}_4(\text{OH})_3\text{Br}$ a été effectuée à travers une étude approfondie du système binaire LiOH-LiBr . Cette validation est motivée par les divergences importantes observées dans la littérature concernant les valeurs de température et d'enthalpie relatives à la réaction péritectique, ainsi que les composés stœchiométriques présents dans le diagramme de phase LiOH-LiBr . Les résultats ont permis d'établir un nouveau diagramme de phase qui s'adapte mieux aux résultats expérimentaux. De plus, une caractérisation complète des propriétés thermophysiques du $\text{Li}_4(\text{OH})_3\text{Br}$ a été effectuée. Les résultats ont permis d'élucider le mécanisme de formation du composé $\text{Li}_4(\text{OH})_3\text{Br}$. Il a été démontré que, pour se former, le composé stœchiométrique $\text{Li}_4(\text{OH})_3\text{Br}$ naît et se développe directement de la phase liquide sans avoir besoin de présence, ni de contact avec la phase pro-péritectique. L'effet des paramètres de synthèse sur les propriétés thermiques du $\text{Li}_4(\text{OH})_3\text{Br}$ a été étudié, permettant de développer et d'optimiser son processus d'élaboration. Globalement, les propriétés thermiques du $\text{Li}_4(\text{OH})_3\text{Br}$ sont appropriées à être utilisées dans des centrales solaires thermiques à Génération Directe de Vapeur (GDV) à haute pression (c.a. 100 bar). Ce matériau s'est

montré plus performant que le matériau de référence utilisé pour cette application (NaNO_3). En outre, des composites $\text{Li}_4(\text{OH})_3\text{Br}$ /Carbone ont été développés et étudiés dans le but d'améliorer les propriétés de stockage du sel. Une amélioration légère de la capacité de stockage a été obtenue pour les composites à faible teneur en carbone (1%). Par ailleurs, l'étude de la corrosion entre $\text{Li}_4(\text{OH})_3\text{Br}$ et les potentiels matériaux de structure du conteneur (Acier au carbone A516.Gr70, et l'acier inoxydable AISI 316) a été conduite dans différentes conditions expérimentales. L'acier inoxydable 316 semble être une option attrayante pour être utilisé comme matériau de réservoir pour $\text{Li}_4(\text{OH})_3\text{Br}$. En revanche, L'acier au carbone semble réagir avec le sel causant la dégradation de ce dernier. Enfin, des composites à forme stabilisée ont été développés et étudiés pour limiter le phénomène de corrosion des matériaux de réservoir par le sel, ce qui permettra la reconsidération de l'utilisation de l'acier au carbone comme matériau de structure de conteneur compte tenu de son faible coût comparé à l'acier inoxydable. Une méthodologie a été établie et suivie afin de sélectionner les meilleurs matériaux supports pour la stabilisation de forme du $\text{Li}_4(\text{OH})_3\text{Br}$. Elle consistait à, l'étude de la compatibilité chimique entre le sel et les matériaux supports, l'évaluation de la stabilité structurale des composites, l'analyse des propriétés thermodynamiques des composites, et l'étude de la stabilité cyclique. Le matériau céramique MgO a été sélectionnée comme le matériau support le plus approprié pour $\text{Li}_4(\text{OH})_3\text{Br}$. MgO assure la stabilité structurale du composite à une teneur de 50 % en poids. L'optimisation de la concentration de MgO essentielle pour une bonne stabilité structural du composite s'avérait nécessaire. À cette fin, différents céramiques MgO , présentant une mésoporosité et diverses propriétés texturales, structurales, et morphologiques, ont été synthétisés et testés comme matériaux supports pour le sel. L'objectif était de bénéficier de la mésoporosité au niveau des particules solides du MgO , grâce aux fortes forces capillaires qu'elle fournit, pour l'amélioration de la stabilité structurale du composite à une concentration de MgO plus faible. L'utilisation de particules poreuses de MgO a permis de réduire la part du matériau support dans le composite par 40%. De plus, l'homogénéité et la conductivité thermique des composites ont été améliorées.

Mots clés :

Composés péritectiques ; Stockage thermique ; Composite ; Haute température ; Sels inorganiques

Título: Estudio y desarrollo de nuevos materiales para aplicaciones de almacenamiento térmico compacto a alta temperatura.

Resumen

Los compuestos peritéticos han sido recientemente investigados como materiales prometedores para el almacenamiento de energía térmica a alta temperatura. El término peritético se refiere a una reacción en la que una fase líquida reacciona con al menos una fase sólida, a una temperatura definida, para formar una nueva fase sólida. Estas reacciones muestran densidades energéticas teóricas extraordinarias, son reversibles y tienen lugar a presión atmosférica y temperatura constante. Como resultado, se obtiene un sistema sencillo de almacenamiento isotérmico con una densidad energética potencialmente mucho mayor que la de los materiales de cambio de fase utilizados actualmente y comparable a la de las mejores reacciones gas-sólido en desarrollo.

Esta tesis tiene como objetivo desarrollar nuevos materiales basados en el compuesto estequiométrico peritético $\text{Li}_4(\text{OH})_3\text{Br}$ para el almacenamiento de energía térmica en aplicaciones de energía solar con altas prestaciones en términos de compacidad, estabilidad y rentabilidad. El $\text{Li}_4(\text{OH})_3\text{Br}$ fue el candidato seleccionado como material TES en base a la extraordinaria densidad energética teórica (800 J/g) que presenta alrededor de los 300 °C. Primeramente, se realizó una validación experimental del $\text{Li}_4(\text{OH})_3\text{Br}$ como material de almacenamiento térmico mediante una investigación exhaustiva del sistema binario LiOH-LiBr. La validación está motivada por las grandes discrepancias observadas en literatura para los valores de temperatura y entalpía de la reacción peritética, así como los de los compuestos estequiométricos presentes en el diagrama de fase LiOH-LiBr. Los resultados permitieron proponer un diagrama de fases modificado para el LiOH-LiBr que se adapta mejor a los resultados experimentales. Además, se llevó a cabo una caracterización exhaustiva de las propiedades termofísicas del $\text{Li}_4(\text{OH})_3\text{Br}$. Esto permitió dilucidar los mecanismos de formación del $\text{Li}_4(\text{OH})_3\text{Br}$. Se demostró que el $\text{Li}_4(\text{OH})_3\text{Br}$ no necesita ni la presencia ni el contacto con la fase pro-peritética para formarse. Nuclea y crece directamente a partir de la masa fundida por lo que se consigue una microestructura final de fase pura $\text{Li}_4(\text{OH})_3\text{Br}$. Se ha investigado también el efecto de las condiciones de síntesis sobre las propiedades de almacenamiento, lo que ha permitido proponer un proceso de síntesis de $\text{Li}_4(\text{OH})_3\text{Br}$ optimizado. En general, las propiedades de almacenamiento térmico del $\text{Li}_4(\text{OH})_3\text{Br}$

demostraron ser adecuadas para su aplicación en centrales termosolares de generación directa de vapor de alta presión (100 bar), mostrando mayores prestaciones que el material actualmente empleado para esta aplicación (NaNO_3). Además, se investigaron compuestos de $\text{Li}_4(\text{OH})_3\text{Br}$ /Carbono con el objetivo de mejorar las prestaciones de almacenamiento térmico del peritético. Se consiguió no sólo aumentar la conductividad térmica del material, sino que además se obtuvo una mejora de la capacidad de almacenamiento con un bajo dopaje de carbono. Por otro lado, se investigó la compatibilidad entre el $\text{Li}_4(\text{OH})_3\text{Br}$ y los posibles materiales del tanque de almacenamiento (acero al carbono A516.Gr70 y acero inoxidable AISI 316) en diversas condiciones de corrosión. El acero inoxidable 316 parece ser una opción adecuada para ser utilizado como material contenedor de $\text{Li}_4(\text{OH})_3\text{Br}$ en condiciones de atmósfera controlada. El acero al carbono, por el contrario, mostró reaccionar con la sal provocando su degradación. Por último, se desarrollaron compuestos de forma estabilizada a base de $\text{Li}_4(\text{OH})_3\text{Br}$ para mitigar las limitaciones de corrosión de los materiales contenedores por la sal. Se estableció una metodología para seleccionar los materiales de soporte adecuados para la estabilización de la forma del $\text{Li}_4(\text{OH})_3\text{Br}$, que incluía el estudio de la compatibilidad química entre la sal y los materiales de soporte, la evaluación del rendimiento antifugas, el análisis de las propiedades estructurales y termodinámicas del compuesto y el estudio de la estabilidad al ciclado. Se seleccionaron nanopartículas de polvo cerámico de MgO como el estabilizador de forma más conveniente para el $\text{Li}_4(\text{OH})_3\text{Br}$. Esta cerámica garantiza la estabilización de la forma con una carga de óxido del 50%. Para disminuir la carga en MgO del material final, se sintetizaron y probaron diferentes materiales mesoporosos de MgO que presentaban diversas propiedades texturales, estructurales y morfológicas como estabilizadores de forma. El objetivo era aprovechar la mesoporosidad de las partículas sólidas de MgO para mejorar la eficacia antifugas del composite a menor carga de óxido gracias a las fuertes fuerzas capilares que proporciona. La carga de MgO se redujo en un 40% al utilizar partículas de MgO porosas. Además, se mejoró la homogeneidad general y la conductividad térmica del composite.

Palabras clave:

Compuestos peritéticos; almacenamiento térmico; Compuestos; alta temperatura; sales inorgánicas.

Title: Development and study of new materials for high temperature compact thermal storage applications

Abstract

Peritectic compounds have been investigated recently as promising HT-TES materials. Peritectic refers to a reaction in which a liquid phase reacts with at least one solid phase, at a defined temperature, to form one new solid phase. These reactions show to afford outstanding theoretical energy densities. The charge/discharge processes of the peritectic compounds take place at constant temperature and atmospheric pressure through the reversible peritectic reaction. As a result, a simple thermal storage system is provided with, potentially, much higher energy density than that of currently used phase change materials and comparable to that of best gas-solid reactions under development.

This thesis aims at developing new materials based on the stoichiometric peritectic compound $\text{Li}_4(\text{OH})_3\text{Br}$ for thermal energy storage in solar power applications with high performances in terms of energy density, compactness, stability, and cost-effectiveness. $\text{Li}_4(\text{OH})_3\text{Br}$ was selected, as a candidate TES material, based on the outstanding theoretical energy density (800 J/g) it displays around 300 °C. In this study, an experimental validation of the choice of $\text{Li}_4(\text{OH})_3\text{Br}$, as thermal storage material, was carried out through an exhaustive investigation of the LiOH-LiBr system. This validation is driven by the large discrepancies observed in the literature related to the temperature and enthalpy values of the peritectic reaction, as well as the stoichiometric compounds present in LiOH-LiBr phase diagram. The results allowed to propose a modified phase diagram for LiOH-LiBr that better adapts to the experimental results. Additionally, a comprehensive characterization of the thermo-physical properties of $\text{Li}_4(\text{OH})_3\text{Br}$ was carried out. It allowed to elucidate the mechanisms of the formation of $\text{Li}_4(\text{OH})_3\text{Br}$. It was demonstrated that $\text{Li}_4(\text{OH})_3\text{Br}$ needs neither the presence nor contact with the pro-peritectic phase to form. It nucleates and grows directly from the melt so a pure phase $\text{Li}_4(\text{OH})_3\text{Br}$ final microstructure is achieved. The effect of the synthesis conditions on the storage properties has been investigated, allowing to develop and optimize a suitable synthesis process of $\text{Li}_4(\text{OH})_3\text{Br}$. Overall, thermal storage properties of $\text{Li}_4(\text{OH})_3\text{Br}$ showed to be suitable for application in high-pressure (c.a. 100 bar) Direct Steam Generation (DSG) solar thermal power plants, showing higher performances over the currently employed material for this application (NaNO_3). Moreover, $\text{Li}_4(\text{OH})_3\text{Br}$ /Carbon composites were

investigated with the aim of enhancing the thermal storage performances of the peritectic. Slight storage capacity enhancement was achieved at low carbon doping. Furthermore, the compatibility between $\text{Li}_4(\text{OH})_3\text{Br}$ and potential storage tank materials (Carbon Steel A516.Gr70 & Stainless Steel AISI 316) was investigated under various corrosion conditions. Stainless steel 316 seems to be a very attractive option to be used as a container material for $\text{Li}_4(\text{OH})_3\text{Br}$. Carbon steel, on the contrary, showed to react with the salt causing its degradation. Finally, $\text{Li}_4(\text{OH})_3\text{Br}$ based shape stabilized composites were developed to mitigate the corrosion limitations of container materials by the salt, which will allow reconsideration of the use of carbon steel as a container structure material given its low cost compared to the stainless steel. A methodology was established to select suitable supporting materials for shape stabilization of $\text{Li}_4(\text{OH})_3\text{Br}$. It included the study of chemical compatibility between the salt and the supporting materials, anti-leakage performance evaluation, structural and thermodynamic properties analysis of the composite and cycling stability study. The ceramic MgO nanopowder was selected as the most convenient shape stabilizer for $\text{Li}_4(\text{OH})_3\text{Br}$. This ceramic ensures the shape stabilization at 50 % oxide loading. The optimization of MgO loading was required to improve the overall storage capacity of the composite. For this purpose, different porous MgO materials with mesoporous pore size exhibiting various textural, structural and morphological properties were synthesized and tested as shape stabilizers. The objective was to benefit from the mesoporosity of solid MgO particles in improving the antileakage efficiency of the composite at lower oxide loading thanks to the strong capillary forces it provides. The MgO loading was decreased by 40 % while using porous MgO particles. Besides, the overall homogeneity and thermal conductivity of the composite was improved.

Keywords :

Peritectic compounds; Thermal storage; Composite; High temperature; inorganic salts

Research units

[I2M-TREFLE, ENSAM esplanade des arts et métiers, 33405 Talence Cedex]
[CICenergiGUNE 48 rue Albert Einstein parque technologique 01510 Vitoria Gasteiz]

Acknowledgment

I would like to convey my deepest appreciation to my supervisor Dr. Stefania Doppiu for her tremendous support, encouragement, and the knowledge I acquired from her throughout the period of my PhD I spent in CICenergiGUNE research centre. Her patient, continuous suggestions and motivations have inspired and helped me accomplish this work. My deepest recognition goes to Professor Elena Palomo del Barrio, the scientific director of the thermal storage group of CICenergiGUNE, for her innovative idea and constant guidance. It has been an honour to learn from both of them.

I would like to acknowledge my thesis director Dr. Jean Toutain for having given me the opportunity to work on this thesis. I'm also grateful to Dr. Fouzia Achchaq, Dr. Marie Duquesne, and Dr. Alexandre GODIN, for their enormous help and support during the period I spent in I2M-TREFL laboratory.

Many thanks to Polytechnique National Institute of Bordeaux (Bordeaux INP), and CIC energigUNE, for their financial support. I'm sincerely grateful to I2M-TREFLE laboratory and CIC energigUNE members with whom I shared beautiful moments.

I would like to thank Dr Jean-Luc Dauvergne, Dr. Angel Serrano, Dr. Yaroslav Grosu, Luis González-Fernández, and Dr. Eder Amayuelas Lopez, for their help and advice. I would also like to thank Yagmur Polat, Cristina Luengo, and Mikel Intxaurtieta for their enormous technical support and the wonderful time we spent together.

I would like to express my heartfelt gratitude to my father, Maamar Mahroug, my mother, Fatiha Becherif, and my brothers, Mohamed Amine, Hicham, and Rafik, for their unconditional love and endless support. Special gratitude goes to my dear friends Houda Kouidri Filali, Amina Merabet, and Sona Valiyaveetil, for their endless encouragement and support.

Table of contents

Abbreviations and Symbols	1
List of figures	3
List of table.....	7
General introduction.....	1
Chapter 1. State of the art in medium and high temperature thermal energy storage.....	16
1.1. Energetic and storage contexts overview	16
1.2. Thermal energy storage (TES)	19
1.2.1. Definition	19
1.2.2. Thermal energy storage applications.....	20
1.2.2.1. Concentrated solar power plants	20
1.2.2. Thermal energy storage technologies.....	22
1.2.3.1. Sensible heat storage (SHS)	23
1.2.3.2. Latent heat storage (LHS)	24
1.2.3.3. Thermochemical heat storage (TcHS).....	26
1.2.3.4. Peritectic heat storage (materials and technology).....	28
1.5. References	32
Chapter 2. Materials and characterization techniques.....	39
2.1. Materials.....	39
2.1.1. Materials and synthesis of LiOH-LiBr mixtures.....	39
2.1.2. Synthesis of peritectic compound $\text{Li}_4(\text{OH})_3\text{Br}$ – Reference protocol	40
2.1.3. Synthesis of peritectic compound $\text{Li}_4(\text{OH})_3\text{Br}$ –Modified reference protocol.....	40
2.1.4. Synthesis of $\text{Li}_4(\text{OH})_3\text{Br}$ /Carbon composites.....	41
2.1.5. Synthesis of $\text{Li}_4(\text{OH})_3\text{Br}$ based shape stabilized composites	41
2.1.5.1. Supporting materials for shape stabilization	41
2.1.5.2. Synthesis of MgO supporting material.....	43
2.1.5.3. Preparation of $\text{Li}_4(\text{OH})_3\text{Br}$ based shape stabilized composites.....	43
2.1.6. Corrosion test protocol	44
2.2. Characterization techniques	46
2.2.1. Morphological and structural characterization.....	46
2.2.1.1. X-ray powder diffraction (XRD).....	46
2.2.1.2. Scanning electron microscopy (SEM).....	47
2.2.1.3. Energy dispersive X-ray spectroscopy (EDS).....	49
2.2.1.4. Transmission electron microscopy (TEM).....	49
2.2.1.5. Brunauer-Emmett-Teller Analysis (BET)	50
2.2.1.7. Gas pycnometry.....	51

2.2.2. Thermophysical characterization	52
2.2.2.1. Differential scanning calorimetry (DSC)	52
2.2.2.2. Transient Plane Source (TPS) Hot Disk technique	53
2.3. References	53
Chapter 3. Study of the binary system LiOH-LiBr	56
3.1. Introduction	56
3.2. State of the art in LiOH/LiBr phase diagram	57
3.3. Experimental estimation of the phase diagram of the binary system LiOH-LiBr	60
3.3.1. Thermal Characterization of LiOH-LiBr mixtures	60
3.3.2. Structural characterization of LiOH-LiBr mixtures	65
3.3.2.1. X-ray diffraction analysis of LiOH-LiBr mixtures	65
3.3.2.2. In-situ XRD analysis for investigation of novel phase transition	66
3.3.3. Proposition of new phase diagram for LiOH-LiBr binary system	69
3.4. Conclusion.....	70
3.5. References	71
Chapter 4: Study of the peritectic compound $\text{Li}_4(\text{OH})_3\text{Br}$ as high temperature TES material in concentrating solar power applications	73
4.1. Introduction	73
4.2. Mechanism of formation of the peritectic compound $\text{Li}_4(\text{OH})_3\text{Br}$	73
4.3. Phase change behavior and thermophysical characterization of the peritectic compound $\text{Li}_4(\text{OH})_3\text{Br}$	75
4.4. The effect of the synthesis conditions on the storage properties of the peritectic compound $\text{Li}_4(\text{OH})_3\text{Br}$	78
4.4.1. Effect of synthesis cooling rate	78
4.4.2. Effect of synthesis atmosphere.....	80
4.5. Thermal cycling stability of the peritectic compound $\text{Li}_4(\text{OH})_3\text{Br}$	80
4.6. Specific heat capacity and thermal conductivity of the peritectic compound $\text{Li}_4(\text{OH})_3\text{Br}$	81
4.7. Structural characterization of the peritectic compound $\text{Li}_4(\text{OH})_3\text{Br}$	82
4.8. Assessment of $\text{Li}_4(\text{OH})_3\text{Br}$ as storage material in solar power applications.....	85
4.9. $\text{Li}_4(\text{OH})_3\text{Br}$ /Carbon composites	88
4.10. Conclusion.....	95
4.11. References	96
Chapter 5: Corrosion of container materials for CSP with $\text{Li}_4(\text{OH})_3\text{Br}$ peritectic salt	99
5.1. Introduction	99
5.2. Corrosion of Carbon Steel A516.Gr70 with $\text{Li}_4(\text{OH})_3\text{Br}$	100
5.2.1. Analysis of Carbon steel	100
5.2.1.1. X-ray diffraction analysis	100

5.2.1.2.	Cross-section analysis of the corrosion layer using SEM / EDS	103
5.2.1.3.	Surface analysis and morphology of the corrosion products formed on carbon steel	106
5.2.1.3.1.	Carbon Steel tested under Argon.....	106
5.2.1.3.2.	Carbon Steel tested under air.....	108
5.2.2.	Analysis of the peritectic salt $\text{Li}_4(\text{OH})_3\text{Br}$	108
5.2.2.1.	Thermal analysis	108
5.2.2.2.	Microstructural analysis.....	111
5.3.	Corrosion of Stainless steel AISI 316L with $\text{Li}_4(\text{OH})_3\text{Br}$	112
5.3.1.	Analysis of stainless steel 316.....	113
5.3.1.1.	X-ray diffraction analysis	113
5.3.1.2.	Cross-section analysis of the corrosion layer using SEM / EDS	115
5.3.1.3.	Surface analysis of SS 316 after corrosion	117
5.3.1.3.1.	SS 316 tested under Argon	117
5.3.1.3.2.	SS 316 tested under air	118
5.3.2.	Analysis of the peritectic salt $\text{Li}_4(\text{OH})_3\text{Br}$	119
5.3.2.1.	Thermal analysis	119
5.3.2.2.	Microstructural analysis.....	121
5.4.	Corrosion rate estimation	123
5.5.	Conclusion.....	124
Chapter 6:	$\text{Li}_4(\text{OH})_3\text{Br}$ based shape stabilized composites.....	127
6.1.	Introduction	127
6.2.	Selection of the most convenient supporting materials.....	129
6.2.1.	Screening methodology of the most convenient supporting material for shape stabilization of $\text{Li}_4(\text{OH})_3\text{Br}$	130
6.2.1.1.	Chemical compatibility of the supporting material with molten $\text{Li}_4(\text{OH})_3\text{Br}$	131
6.2.1.2.	Anti-leakage effectiveness and maximum salt loading.....	134
6.2.1.3.	Thermal and microstructural characterization and stability of $\text{Li}_4(\text{OH})_3\text{Br}$ based shape stabilized composites	137
6.3.	$\text{Li}_4(\text{OH})_3\text{Br}/\text{MgO}$ shape stabilized composites	141
6.3.1.	Characterization of as-prepared MgO samples	141
6.3.1.1.	Nano-crystalline MgO prepared by ball milling process (MgO-BM).....	141
6.3.1.2.	Particle size distribution of as-prepared MgO samples.....	144
6.3.1.3.	Porous structure of as-prepared MgO samples	148
6.3.1.4.	Microstructural analysis of the as-prepared MgO samples	152
6.3.2.	Characterization of $\text{Li}_4(\text{OH})_3\text{Br}/\text{MgO}$ composites	154
6.3.2.1.	Anti-leakage effectiveness and maximum salt loading.....	154
6.3.2.2.	Thermal characterization of $\text{Li}_4(\text{OH})_3\text{Br}/\text{MgO}$ composites	158

6.3.2.3. Cycling stability of $\text{Li}_4(\text{OH})_3\text{Br}$ /Porous-MgO composites	161
6.3.2.4 Microstructural analysis and thermal conductivity of PMgO based composite	162
6.4. Conclusion.....	166
6.5. References	167
General conclusions	173
Annex	177

Abbreviations and Symbols

Abbreviations

BET	Brunauer-Emmett-Teller
BSE	Back-scattered electrons
CS	Carbon Steel
CSP	Concentrated solar power
DSC	Differential scanning calorimetry
EDX	Energy-dispersive X-ray spectroscopy
GHGs	Green house gases
HTF	Heat transfer fluid
HT-TES	High temperature thermal energy storage
IUPAC	International Union of Pure and Applied Chemistry
LFR	Linear Frensel reflectors
LHS	Latent heat storage
MWCNTs	Multi-walled carbon nanotubes
nm	Nanometer
PCMs	Phase change materials
PDC	Parabolic dish collectors
PSD	Pore size distribution
PTC	Parabolic trough collectors
rGO	Reduced graphene oxide
SE	Secondary electrons
SEM	Scanning electron microscope
SHS	Sensible heat storage
STP	Solar power tower
SS	Stainless steel
SSA	Specific surface are
SS-composite	Shape stabilized composite
TEM	Transmission electron microscope
TES	Thermal energy storage
TFEC	Total final energy consumption

TPS	Transient Plane Source
x	mole fraction
XRD	X-ray diffraction

Symbols

ΔH	Enthalpy	J/g
C_p	Specific heat capacity	J/K.g
λ	Thermal conductivity	W/m.K
α	Thermal diffusivity	mm ² /s
T_{amb}	Ambient temperature	°C
T_m	Melting temperature	°C
ρ	Density	g/cm ³

List of figures

Figure 1.1. Trends and forecasts of global energy consumption. [2]	16
Figure 1.2. (a) Estimated renewable energy share of the total final energy consumption, 2018; (b) Estimated Renewable Energy Share of Global Electricity Production, End-2019 [4]	17
Figure 1.3. Shares of CSP plants integrating TES systems worldwide [5]	18
Figure 1.4. Thermal energy storage cycle [6].....	19
Figure 1.5. Energy storage and usage peaks during 24 hours [7].....	20
Figure 1.6. Operation principle of CSP a CSP plant [5]	21
Figure 1.7. Share of different types of CSP plants worldwide [5]	21
Figure 1.8. TES materials based on the different TES technologies, highlighting the category of the peritectic compounds through a combination of a melting/solidification and liquid/solid chemical reaction storage processes [16].....	22
Figure 1.9. Illustration of thermal energy storage technologies: (a) sensible heat storage; (b) latent heat storage; thermochemical heat storage.	22
Figure 1.10. Classification of latent heat storage materials.....	25
Figure 1.11. (a) Scheme of mechanism of formation of a stoichiometric peritectic compound on cooling; (b) phase diagram highlighting the peritectic composition. [87]	29
Figure 2.1. SEM images of the tested oxides: (a) MgO; (b) Fe ₂ O ₃ ; (c) CuO; (d) Al ₂ O ₃ ; (e) SiO ₂	43
Figure 2.2 Schematic represents the preparation process of shape stabilized composite.....	44
Figure 2.3. Schematic represents the corrosion test protocol.....	45
Figure 2.4. Temperature program applied for cycling corrosion test.....	45
Figure 2.5. Sample preparation for SEM+EDS cross-section analysis	46
Figure 2.6. Scheme of the core component of SEM microscope. [16].....	48
Figure 2.7. Scheme of the core component of TEM microscope. [16]	50
Figure 3.1. LiOH-LiBr phase diagram proposed by Sangster [1] based on the experimental data obtained by Scarpa [10] (black circles) and Hartwig et al. [12] (blue triangles).....	59
Figure 3.2. DSC thermograms upon heating (heating rate = 1 K/min) of LiOH-LiBr samples with different compositions from 0.19 to 0.84 molar fraction of LiOH.....	61
Figure 3.3. Zoom on DSC thermograms for LiOH-LiBr samples with composition within 0.19 and 0.67 molar fraction of LiOH.....	63
Figure 3.4. Measured enthalpies for transition T ₁ (blue line), eutectic + peritectoid reaction (orange line) and peritectic reaction (grey line).	64

Figure 3.5. LiOH-LiBr phase diagram proposed by Hartwig et al. [12] and experimental data obtained by DSC in this work (red symbols) and by Hartwig (blue symbols).	65
Figure 3.6. XRD results for some LiOH-LiBr selected compositions	66
Figure 3.7. XRD patterns after quenching a sample of composition 67 mol. % LiOH at 240 °C and 260 °C.....	67
Figure 3.8. In-situ XRD results of the sample 67mol. % LiOH after synthesis.	68
Figure 3.9. Sketch of possible LiOH-LiBr phase diagram according to the experimental analysis carried out, showing two peritectic compounds (2 – $\text{Li}_3(\text{OH})_2\text{Br}$ & 3 – $\text{Li}_4(\text{OH})_3\text{Br}$), one peritectoid (1 – $\text{Li}_2(\text{OH})\text{Br}$) and eutectic transition at 254 °C.	69
Figure 4.1. DSC thermograms of a sample of $\text{Li}_4(\text{OH})_3\text{Br}$: (a) heating stage; (b) cooling stage.	76
Figure 4.2. DSC thermograms (on cooling) with a cooling rate of 50 °C/min for LiOH-LiBr mixtures at $x = 0.75$ LiOH.	77
Figure 4.3. DSC thermograms (on cooling) with a cooling rate of 10 °C/min for LiOH-LiBr mixtures at $x = 0.75$ LiOH.	78
Figure 4.4. DSC thermograms (on heating, heating rate = 1 °C/min) for LiOH-LiBr mixtures at $x = 0.75$ LiOH prepared under argon atmosphere using different cooling rates during the synthesis stage.	79
Figure 4.5. DSC thermograms (on heating, heating rate = 1 °C/min) for LiOH-LiBr mixtures at $x = 0.75$ LiOH prepared under different atmospheres (argon and air).	80
Figure 4.6. Thermal cycling of $\text{Li}_4(\text{OH})_3\text{Br}$ under Argon and Air: (a) heating DSC curves (solid line represents test under Ar / dashed line represents test under Air); (b) evolution of the enthalpy ($T_2 + \text{Peritectic}$) upon cycling.....	81
Figure 4.7. Variation of the specific heat (C_p) with temperature obtained by DSC direct method.	82
Figure 4.8. X-ray diffraction spectrum obtained at room temperature for a sample (0.75 molar fraction of LiOH).....	84
Figure 4.9. TEM images of a sample (0.75 molar fraction of LiOH) prepared by the reference protocol described in section 2.1.	85
Figure 4.10. Effect of adding carbon nanoparticles on the cycling behavior of the storage material at $x = 0.75$ LiOH: (a) variation of the enthalpy of peritectic reaction over cycling; (b) Heating DSC thermograms after cycling.....	90
Figure 4.11. Carbon-based nanostructures: Graphene, Fullerene C_{60} , and MWCNT [26]	91
Figure 4.12. Multilayer graphene	93
Figure 4.13. TEM image of the tested rGO sheets	93
Figure 4.14. TEM images of MWCNT-based composite with 10 wt. % nanoparticle loading.	95
Figure 5.1. Images of CS samples before and after corrosion tests for different cycle numbers under different atmospheres.	100

Figure 5.2. XRD patterns of the surface of CS after corrosion tests at 350 °C for different cycle numbers: a) under Ar; b) under air; c) superposition of both patterns.	101
Figure 5.3. Cross-sectional analysis of the carbon steel tested under Ar after 150 corrosion cycle. a) SEM micrograph of the cross-section; b) enlargement of the region where the EDS is performed; c) EDS profile (Iron in orange line, Oxygen in green line, and Carbon in blue line).....	103
Figure 5.4. SEM-EDS cross-sectional analysis of the carbon steel samples tested under: Argon atmosphere (a) 300 cycles; (b) 600 cycles. Air atmosphere (c) 150 cycles; (d) 300 cycles; (e) 600 cycles.	105
Figure 5.6. SEM micrographs combined with EDS analysis of the surface of carbon steel samples tested under air: a) after 150 corrosion cycles; b) after 300 corrosion cycles; c) after 600 corrosion.	108
Figure 5.7. Heating DSC curves obtained on cooling at (1 K/min) of $\text{Li}_4(\text{OH})_3$ extracted after corrosion tests with Carbon steel for different cycle numbers: a) under Ar; b) under air; (solid line represents the corrosion sample; dash line represents the reference sample).....	110
Figure 5.8. SEM and EDX analyses of the salt $\text{Li}_4(\text{OH})_3\text{Br}$ after 600 corrosion cycles with the carbon steel: (a,b) under Ar; (c,d) under O_2 ; (a,c) the salt situated on the top of the corrosion crucible ; (b,d) the salt in contact with the metallic sample.....	112
Figure 5.9. Images of SS samples after corrosion tests for different cycle numbers under different atmospheres.....	113
Figure 5.10. XRD patterns of the surface of SS 316 after corrosion tests at 350 °C for different cycle numbers: a) under Ar; b) under air; c) superposition of both patterns.	114
Figure 5.11. Cross-sectional analysis of the SS 316 tested under Ar after 150 corrosion cycle. a) SEM micrograph of the cross-section; b) enlargement of the region where the EDS is performed; c) EDS profile (Iron in orange line, Oxygen in green line, Carbon in blue line, Chromium in red line, and Nickel in purple line).....	115
Figure 5.12. SEM-EDS cross-sectional analysis of the SS 316 samples tested under: Argon atmosphere (a) 300 cycles; (b) 600 cycles. Air atmosphere (c) 150 cycles; (d) 300 cycles; (e) 600 cycles.	117
Figure 5.13. SEM micrographs combined with EDS analysis of the surface of SS 316 samples tested under Ar: a) after 150 corrosion cycles; b) after 300 corrosion cycles; c) after 600 corrosion cycles.	118
Figure 5.14. SEM micrographs combined with EDS analysis of the surface of SS 316 samples tested under air: a) after 150 corrosion cycles; b) after 300 corrosion cycles; c) after 600 corrosion cycles.	118
Figure 5.15. Heating DSC curves obtained at (1 K/min) of $\text{Li}_4(\text{OH})_3\text{Br}$ extracted after corrosion tests with SS 316 for different cycle numbers: a) under Ar; b) under air; (solid line represents the corrosion sample; dash line represents the reference sample).....	120
Figure 5.16. SEM and EDX analyses of $\text{Li}_4(\text{OH})_3\text{Br}$ salt in the interface with SS 316 after 600 corrosion cycles, both under Ar and air.....	123
Figure 6.1. DSC curves of $\text{Li}_4(\text{OH})_3\text{Br}$ /oxide mixtures after compatibility tests recorded at 1°C/min: a- upon heating; b- upon cooling.	132
Figure 6.2. XRD results of $\text{Li}_4(\text{OH})_3\text{Br}$ /oxide mixtures after compatibility tests	134

Figure 6.3. SEM images of the ss-composite: (a) 50Li ₄ (OH) ₃ Br-50MgO; (b) 70Li ₄ (OH) ₃ Br-30Fe ₂ O ₃	138
Figure 6.4. DSC curves of Li ₄ (OH) ₃ Br-based shape stabilized composites: (a) Upon heating; (b) Upon cooling.....	139
Figure 6.5. Images of the composite of Li ₄ (OH) ₃ Br based shape stabilized composite before and after thermal cycling tests: (a) 50Li ₄ (OH) ₃ Br-50MgO; (b) 70Li ₄ (OH) ₃ Br-30Fe ₂ O ₃	140
Figure 6.6. DSC curves of Li ₄ (OH) ₃ Br-based shape stabilized composites after cycling stability tests: (a) 50Li ₄ (OH) ₃ Br-50MgO; (b) 70Li ₄ (OH) ₃ Br-30Fe ₂ O ₃	140
Figure 6.7. XRD patterns of milled MgO powders with milling time from 0 h to 64 h.....	141
Figure 6.8. Variation of crystalline size and lattice strain of milled MgO as a function of ball-milling time.....	142
Figure 6.9. 70Li ₄ (OH) ₃ Br/30MgO-BM ss-composites with milling time from 0 h up to 64 h after sintering showing salt leakage assessment.	144
Figure 6.10. Histogram and cumulative probabilities of particle size distribution, and Lognormal probability plot of particle size of (a) MgO-BM64h; (b)MgO-BMC; (c) Sifted peritectic salt powder; (d) MgO-BM32h; (e) SEM micrographs of as prepared PMgO after physical shaking process	146
Figure 6.11. (a) Different types of adsorption isotherms according to IUPAC classification;.....	148
(b) Different types of hysteresis patterns and the corresponding pore geometry [56]-[58]	148
Figure 6.12. a) N ₂ adsorption-desorption isotherms of as-prepared Porous MgO; b) Pore size distributions of as-prepared porous MgO.....	151
Figure 6.13. SEM images of (a-b-c-d) PMgO; (e-f) MgO-BMC; (g-h) MgO-BM64h	154
Figure 6.14. Schematic represents the microstructural evolution of Li ₄ (OH) ₃ Br/porous-MgO composite upon fabrication process and after cycling	154
Figure 6.15. Li ₄ (OH) ₃ Br/MgO ss-composites with different MgO samples after sintering.....	154
Figure 6.16. DSC curves of Li ₄ (OH) ₃ Br/Porous-MgO composites after thermal treatment recorded at 1°C/min: a- upon heating; b- upon cooling.	158
Figure 6.17. 70Li ₄ (OH) ₃ Br/30Porous-MgO composites with different MgO samples after 50 melting/solidification cycles.....	161
Figure 6.18. DSC thermograms (Normalized) on heating, heating rate = 1 °C/min of different Li ₄ (OH) ₃ Br/Porous-MgO composites before and after thermal cycling	161
Figure 6.19. Microstructural of 70Li ₄ (OH) ₃ Br/30PMgO composite (a) SEM micrographs prior thermal treatment; (b) EDS element mapping images prior thermal treatment; (c) SEM micrographs after thermal treatment; (d) EDS element mapping images after thermal treatment.....	164

List of table

Table 1.1. Salt based and mettalic alloys peritectic binary systems and their corresponding thermal storage properties (peritectic temperature (T_p); peritectic reaction enthalpy ΔH ; peritectic energy density (E_p); melting/transition temperature range ($\Delta T_{L \rightarrow p}$); and the energy density corresponding to the formation of both peritectic and pro-peritectic phases [87].....	30
Table 1.2. Comparison of different thermal storage technologies [88].....	30
Table 2.1. General information about the tested oxides.....	41
Table 2.2. Chemical composition of the studied steel samples.....	44
Table 3.1. Phase equilibria in LiOH-LiBr system according to currently available experimental data.....	58
Table 3.2. Phase transition temperatures of LiOH-LiBr mixtures obtained from DSC analysis.	62
Table 3.3. Enthalpies of phase transition of LiOH-LiBr mixtures obtained from DSC analysis.	63
Table 3.4. XRD quantitative analysis results – Experimental data have been obtained by fitting x-ray diffraction profiles by Rietveld method. Calculations have been performed using FactSage 7.3 based on the phase diagram proposed by Sangster [9].....	66
Table 4.1. Temperatures and enthalpies of phase transitions/reactions of LiOH-LiBr mixture at composition $x = 0.75$ on heating.	76
Table 4.2. Peritectic reaction teperatures and enthalpies corresponding to the samples prepared using different cooling rates during the synthesis stage.....	79
Table 4.3. Constant pressure specific heat values obtained by DSC direct method.....	82
Table 4.4. Thermal conductivity values of $Li_4(OH)_3Br$	82
Table 4.5. Phase change materials with melting point in the temperature range from 280 °C to 310 °C and enthalpy of melting above 150 J/g (data from Ref. [14]).	86
Table 4.6. Physical properties and price of $NaNO_3$ [12], [13], [16], and $Li_4(OH)_3Br$	88
Table 4.7. Peritectic temperature (T_p) and enthalpy (ΔH) of nanocomposites obtained by addition of carbon nanoparticles (C60: fullerene C60; MWCNT: multi-walled carbon nanotubes; rGO: reduced graphene oxide) to the salt.....	89
Table 5.1. Temperatures and enthalpies corresponding to the peritectic reaction of $Li_4(OH)_3Br$ after corrosion tests with CS under Argon and air compared to reference values.....	111
Table 5.2 Temperatures and enthalpies corresponding to the peritectic reaction of $Li_4(OH)_3Br$ after corrosion tests with SS 316 under Argon and air atmospheres compared to reference values	121
Table 5.3. Average corrosion attack thickness (μm) measured by SEM cross-sectional analysis and the corresponding corrosion rates related to CS A516.Gr70 tested under both air and argon atmosphere at 350 °C over various cycle numbers.....	123
Table 5.4. Industrial operability of A516 Gr70 according to the corrosion rate [19].....	124

Table 6.1. Temperatures and enthalpies corresponding to the peritectic reaction of different $\text{Li}_4(\text{OH})_3\text{Br}$ /oxide mixtures after compatibility tests.....	133
Table 6.2. $\text{Li}_4(\text{OH})_3\text{Br}$ -based ss-composites with different oxide loading after sintering showing salt leakage assessment.	135
Table 6.3. Temperatures and enthalpies corresponding to the peritectic reaction of different $\text{Li}_4(\text{OH})_3\text{Br}$ based ss-composites before and after thermal cycling.....	139
Table 6.4. The mean particle size and standard deviation of MgO samples	147
Table 6.5. BET surface areas and pore volume of different MgO samples determined from nitrogen adsorption-desorption isotherm.....	152
Table 6.6. Temperatures and enthalpies corresponding to the peritectic reaction of different $\text{Li}_4(\text{OH})_3\text{Br}$ /MgO composites after thermal treatment	160
Table 6.7. Temperatures and enthalpies corresponding to the peritectic reaction of different $\text{Li}_4(\text{OH})_3\text{Br}$ /Porous-MgO composites after thermal cycling. The reference enthalpy $\Delta H_{\text{Reference}} = \Delta H_{\text{Per.}}$ f, where f represents the mass fraction of salt within the composite.	162
Table 6.8. Thermal conductivity values of 70 $\text{Li}_4(\text{OH})_3\text{Br}$ /30PMgO.....	165

Resumen de tesis

El almacenamiento de energía térmica se basa en guardar la energía térmica en un medio de almacenamiento para utilizarla posteriormente como suministro de energía. Según el mecanismo de almacenamiento, el almacenamiento de energía térmica se ha explotado en tres tecnologías de almacenamiento diferentes: el almacenamiento de calor sensible (SHS) mediante materiales sólidos o líquidos, el almacenamiento de calor latente (LHS) con materiales de cambio de fase y el almacenamiento de calor termoquímico (TCM) con reacciones químicas reversibles. El SHS basado en sales fundidas es la tecnología que se aplica actualmente a nivel comercial. El éxito de las sales fundidas radica en que son relativamente baratas y son estables a altas temperaturas (hasta 560 °C), por lo que pueden soportar los ciclos Rankine convencionales de vapor. Sin embargo, ofrecen una baja densidad energética (30-70 kWh/m³) en comparación con los materiales LHS y TCS. En el caso de los LHS, las sales inorgánicas anhidras son los materiales de cambio de fase (PCM) más investigados. La densidad de energía volumétrica proporcionada por los LHS suele oscilar entre 80 kWh/m³ y 200 kWh/m³, lo que permite un sistema de almacenamiento más pequeño y potencialmente más barato en comparación con los SHS. El TCS proporciona una densidad de energía volumétrica teóricamente sobresaliente de 200-600 kWh/m³, cinco veces mayor que el LHS y diez veces mayor que el SHS. Sin embargo, el TCS se encuentra todavía en una fase muy temprana de desarrollo y presenta algunos inconvenientes que deben ser resueltos, como la baja cinética de reacción, la escasa capacidad de transferencia de calor y masa, la sinterización de los materiales, los complejos sistemas de almacenamiento y el consiguiente elevado coste.

Para las aplicaciones de alta temperatura, el desarrollo de los materiales y sistemas TES ha sido impulsado principalmente por la energía solar concentrada (CSP). La tecnología TES más implementada en la CSP es la de sales fundidas de doble tanque. Los sistemas TES pueden contribuir eficazmente a mejorar la capacidad de suministro de las centrales solares y a operar las centrales térmicas convencionales de manera más flexible. Conectados a una central eléctrica ya existente, o como sistema de almacenamiento autónomo, los TES también pueden contribuir a la gestión de la red, desplazando la carga o incluso sustituyendo a las centrales de potencia. Otra aplicación importante es la cogeneración, en la que los sistemas de

almacenamiento de energía térmica permiten desacoplar la producción y el uso de electricidad y calor para lograr una mayor eficiencia de conversión. Además, los TES también se utilizan para la recuperación de calor residual. El calor residual industrial se recupera y se almacena en un sistema TES y se utiliza posteriormente para reducir el suministro de energía primaria para el mismo proceso industrial o se transporta, si es necesario, a otros lugares. Entre otros, el cemento y el hormigón, la industria del papel, las fundiciones y las industrias metalúrgicas son los principales procesos industriales que aplican los sistemas TES para la recuperación del calor residual. El desarrollo de los sistemas de almacenamiento de energía térmica está condicionado por el desarrollo de nuevos materiales de almacenamiento térmico. De hecho, el diseño del tanque de almacenamiento y de los intercambiadores de calor depende de las propiedades termofísicas del material de almacenamiento (capacidad calorífica específica, densidad energética, conductividad térmica, cambio de volumen, rango de temperatura de funcionamiento, etc.). Por lo tanto, el desarrollo de nuevos materiales de alto rendimiento y rentables para el almacenamiento de energía térmica (TES) a alta temperatura se está convirtiendo en un campo de investigación muy activo. En este sentido, esta tesis presenta el estudio de las reacciones/transiciones peritéticas para el almacenamiento compacto de energía térmica a altas temperaturas. Se trata de una clase de reacciones novedosa y muy prometedora que puede utilizarse para aplicaciones de almacenamiento de energía térmica. Las reacciones peritéticas consisten en reacciones químicas que implican la reacción entre un sólido y un líquido formando un nuevo sólido. En cuanto a su aplicación, se comportarían como un sistema de almacenamiento térmico basado en el almacenamiento de calor latente, pero con una destacada densidad de energía efectiva teórica (200-400 kWh/m³ de reacción peritética, y 400-650 kWh/m³ de reacción peritética + fusión) muy superior a la de los materiales de cambio de fase utilizados actualmente y comparable a las mejores reacciones gas-sólido en desarrollo. Además, en lo que respecta a su aplicación, estos materiales funcionan a una temperatura casi constante a presión atmosférica, lo que da lugar a sistemas de almacenamiento de energía térmica sencillos y compactos con un coste de inversión atractivo. Por este motivo, estas reacciones se han estudiado en detalle con el objetivo de mejorar sus prestaciones y explotar al máximo su potencialidad.

Objetivos y alcance de la tesis

El objetivo principal de este trabajo de investigación es desarrollar nuevos materiales basados en reacciones peritéticas para el almacenamiento de energía térmica con altas prestaciones en

términos de densidad energética, compacidad, comportamiento reversible y bajo coste. El concepto de almacenamiento térmico peritético se basa en la liberación de energía durante la formación de compuestos químicos durante la reacción/transformación peritética. La energía térmica puede almacenarse mediante dos procesos consecutivos, un proceso de fusión-solidificación incongruente (formación de la fase peritética) y una reacción química líquido-sólido (formación peritética). El interés en estas reacciones viene dado tanto por sus densidades energéticas teóricas significativamente altas como, en cuanto a su aplicación, por la posibilidad de operar a temperatura casi constante a presión atmosférica dando lugar a sistemas de almacenamiento de energía térmica sencillos y compactos con un coste de inversión atractivo. En este trabajo se ha elegido el sistema de sales binarias de hidróxido de litio y bromuro de litio (LiOH-LiBr) debido a la alta densidad energética teórica que puede proporcionar su reacción/transición peritética (591 kWh/m^3) en comparación con otros sistemas de sales inorgánicas, así como su precio relativamente bajo en comparación con las aleaciones metálicas. El compuesto peritético $\text{Li}_4(\text{OH})_3\text{Br}$ se investigó a fondo para evaluar su utilidad potencial en aplicaciones de TES y optimizar sus prestaciones como material de TES de alta temperatura.

El presente trabajo de tesis se dividió en seis capítulos

El Capítulo 1 presenta el estado del arte del almacenamiento de energía térmica a media y alta temperatura, empezando por una visión general del contexto energético y de almacenamiento actual basado en las energías renovables, con especial atención al calor como fuente de energía primaria. Además, se describieron las diferentes tipologías de tecnologías de almacenamiento de energía térmica junto con el material utilizado en cada concepto de almacenamiento. Por otra parte, se dedicó un enfoque especial a los materiales y la tecnología de almacenamiento térmico peritético, destacando los avances realizados en este nuevo e innovador concepto de almacenamiento, las ventajas de estos materiales y la tecnología de almacenamiento en comparación con las otras tecnologías, así como los aspectos a mejorar.

El Capítulo 2 presenta los materiales utilizados en este estudio, así como los protocolos experimentales aplicados a:

- La síntesis de las mezclas LiOH-LiBr utilizadas para establecer el diagrama de fases del sistema binario LiOH-LiBr.

- La síntesis del compuesto peritético $\text{Li}_4(\text{OH})_3\text{Br}$. También se presenta la optimización del protocolo de síntesis del $\text{Li}_4(\text{OH})_3\text{Br}$ con el objetivo de simplificar el protocolo de referencia trabajando bajo atmósfera de aire en lugar de utilizar una atmósfera protectora de argón.
- El protocolo de síntesis de los compuestos $\text{Li}_4(\text{OH})_3\text{Br}$ /Carbono.
- La ruta sencilla de compresión en frío aplicada para la síntesis de composites de forma estabilizada de $\text{Li}_4(\text{OH})_3\text{Br}$
- El protocolo experimental seguido para sintetizar diferentes muestras de MgO utilizadas como materiales de soporte con diferentes propiedades estructurales, texturales y morfológicas.
- El protocolo de corrosión aplicado para estudiar la compatibilidad de los materiales del contenedor (Acero al Carbono A516.Gr70 y Acero Inoxidable AISI 316) con la sal peritética $\text{Li}_4(\text{OH})_3\text{Br}$ bajo diferentes condiciones operativas.
- Por último, se presentan las técnicas de caracterización de los materiales (morfológicas, estructurales y termofísicas), en particular, la descripción de los equipos utilizados, así como la descripción de las condiciones y parámetros de medición.

Capítulo 3.

En este capítulo se investigó a fondo el sistema de sales binarias LiOH-LiBr mediante Calorimetría Diferencial de Barrido (DSC) y análisis de rayos X. El objetivo era apoyar la consideración potencial del compuesto estequiométrico peritético $\text{Li}_4(\text{OH})_3\text{Br}$ como material compacto de TES y dilucidar las discrepancias significativas reportadas en la literatura con respecto a los valores de temperatura de los equilibrios de fase, las entalpías de reacción peritética (valores teóricos y experimentales), así como los compuestos estequiométricos presentes en el sistema. Se ha seguido un protocolo de análisis DSC específico que ha dado resultados fiables y ha permitido resolver el problema señalado en la bibliografía sobre la fuga de PCM durante el análisis DSC. A partir de nuestros resultados experimentales, se propuso un diagrama de fases LiOH-LiBr modificado que da una explicación satisfactoria a todas las observaciones realizadas. Incluye los compuestos estequiométricos $\text{Li}_2(\text{OH})\text{Br}$ (meseta peritectoide a $250\text{ }^\circ\text{C}$, $x \leq 0,666$), $\text{Li}_3(\text{OH})_2\text{Br}$ (estable entre $230\text{ }^\circ\text{C}$ y $280\text{ }^\circ\text{C}$, fundiendo peritectamente para $x \geq 0,5$) y $\text{Li}_4(\text{OH})_3\text{Br}$ (meseta peritectoide a $289\text{ }^\circ\text{C}$, $x \geq 0,5$). También muestra una transición eutéctica a $254\text{ }^\circ\text{C}$

aproximadamente, que se extiende por el rango de composición $x > 0$ a $x = 0,66-0,67$, con punto eutéctico en $x = 0,40$. Las discrepancias con los estudios anteriores se refieren también a las entalpías de transición. Cualquiera que sea la transición considerada; las entalpías medidas en este trabajo son mucho más bajas que las predichas por FactSage 7.3, donde se implementa el diagrama de fase LiOH-LiBr propuesto por Sangster en 2000. Dada la fiabilidad de nuestras medidas de DSC y teniendo en cuenta que las reacciones peritéticas y peritectoides identificadas se han completado (comprobadas por XRD), estas diferencias sólo pueden atribuirse a las probadas deficiencias del diagrama de fases de Sangster. Además, aunque es inferior al valor teórico, el valor de calor latente alcanzado por el $\text{Li}_4(\text{OH})_3\text{Br}$ es superior al de los materiales de la competencia considerados para aplicaciones de centrales eléctricas DSG de alta presión (100 bar). Finalmente, el $\text{Li}_4(\text{OH})_3\text{Br}$ fue aprobado como un material atractivo para aplicaciones compactas de TES a temperaturas cercanas a los 300 °C, siendo una alternativa potencial al NaNO_3 .

Capítulo 4 En este capítulo se han investigado a fondo las propiedades térmicas y estructurales del compuesto estequiométrico peritético $\text{Li}_4(\text{OH})_3\text{Br}$. Esto abarca la caracterización del $\text{Li}_4(\text{OH})_3\text{Br}$ como material de almacenamiento para aplicaciones cercanas a 300 °C mediante la medición de las temperaturas de transición (280-289 °C), las entalpías de reacción (247 J/g), los calores específicos (c.a. 1,68 J/g/K en sólido, 2,52 J/g/K en líquido) y la conductividad térmica (0,47 W/m/K a temperatura ambiente). Además, se ha observado un subenfriamiento moderado (6-9 °C) al ensayar muestras pequeñas (18 mg aproximadamente) a altas velocidades de enfriamiento (10-50 °C/min). Por lo tanto, no se espera que sea un problema en condiciones reales de uso, con grandes cantidades de producto y velocidades de enfriamiento mucho menores. También se ha investigado el efecto de las condiciones de síntesis sobre las propiedades de almacenamiento. Se concluye que ni la velocidad de enfriamiento aplicada durante la etapa de síntesis ni el tipo de atmósfera utilizada (aire ambiente y atmósfera protectora de argón) influyen en el rendimiento del material, lo que reduciría significativamente el coste de producción. Las pruebas de estabilidad de ciclos térmicos del $\text{Li}_4(\text{OH})_3\text{Br}$ entre 200 °C y 350 °C mostraron una excelente estabilidad en un gran número de ciclos (600 ciclos). No se han observado cambios en las propiedades de almacenamiento (temperaturas de reacción y entalpías). Además, se comprobó que los mecanismos de formación del $\text{Li}_4(\text{OH})_3\text{Br}$ difieren de los comúnmente observados para las estructuras peritéticas, a saber, la reacción peritética y la transformación peritética.

Se demostró que el $\text{Li}_4(\text{OH})_3\text{Br}$ se nuclea y crece directamente a partir de la masa fundida, de modo que se alcanza el 100% de la tasa de conversión, al contrario de lo que ocurre con muchas otras estructuras peritéticas en las que la fase properitética no se consume por completo con, por tanto, un efecto perjudicial en la capacidad de almacenamiento. Además, el dopaje de $\text{Li}_4(\text{OH})_3\text{Br}$ con una cantidad baja (1 % en peso) de nanopartículas de carbono, principalmente fullerenos C60 y MWCNT, mostró un efecto positivo aunque moderado en la capacidad de almacenamiento térmico debido a los efectos interfaciales entre la sal y la superficie de las nanopartículas de carbono. El aumento del contenido de nanopartículas (10 % en peso) tuvo un efecto perjudicial sobre la capacidad de almacenamiento, probablemente debido a la intercalación del Li y a la infiltración de la sal dentro de la estructura de las nanopartículas. Finalmente, el $\text{Li}_4(\text{OH})_3\text{Br}$ presentó varias ventajas, sobre el material de referencia NaNO_3 , como material de almacenamiento para plantas solares DSG de alta presión. Las más importantes son una mayor capacidad volumétrica de almacenamiento de calor latente (+54%) y menores cambios de volumen durante las transiciones de fase (3% frente a 11%), lo que se traduciría en tanques de almacenamiento más pequeños (-33%), intercambiadores de calor de menor tamaño y una mayor vida útil.

Capítulo 5

En este capítulo se realizó el primer estudio de corrosión del compuesto peritético estequiométrico $\text{Li}_4(\text{OH})_3\text{Br}$ para arrojar luz sobre el comportamiento de corrosión de los posibles materiales contenedores con $\text{Li}_4(\text{OH})_3\text{Br}$. En este estudio se ensayaron CS516.Gr70 y SS316. Los ensayos de corrosión cíclica se llevaron a cabo bajo atmósfera de argón y aire a 350 °C aplicando varias duraciones de los ciclos. El acero al carbono demuestra reaccionar con la sal, formando una fase de óxido de hierro y litio (LiFeO_2). La reacción es menos intensa bajo atmósfera de aire. Por lo tanto, la velocidad de corrosión resultante es menor. Debido a la escasa adherencia de la fase LiFeO_2 a los metales, se observó un desprendimiento de la superficie del CS. Se observó que la entalpía de reacción disminuye gradualmente a lo largo del ciclo para el acero al carbono debido a la reacción entre la sal y la muestra de acero. Se registró una mayor pérdida de entalpía después de 600 ciclos para la muestra ensayada bajo Argón con respecto a la atmósfera de aire, particularmente para la sal en contacto directo con el CS. En base a estos resultados, aunque la velocidad de corrosión obtenida mostró la capacidad de este acero para el servicio a largo plazo, debería aplicarse un mayor tiempo de exposición para estudiar el efecto a largo plazo de la corrosión sobre la estabilidad de la sal y

poder evaluar si este acero es adecuado para la exposición a largo plazo con $\text{Li}_4(\text{OH})_3\text{Br}$. El acero inoxidable 316 presentó una mejor resistencia a la corrosión que el CS A516.Gr70 con $\text{Li}_4(\text{OH})_3\text{Br}$ a 350 °C. Este material parece ser una opción muy atractiva para ser utilizado como material contenedor de la sal $\text{Li}_4(\text{OH})_3\text{Br}$. Los resultados preliminares de la corrosión mostraron la capacidad de este acero para el servicio a largo plazo. Deberían realizarse más estudios de corrosión para el SS316 aplicando un tiempo de exposición más largo para definir la velocidad de corrosión de este material y los posibles productos de corrosión a largo plazo.

El Capítulo 6 tiene como objetivo, mitigar la corrosión del $\text{Li}_4(\text{OH})_3\text{Br}$ en condiciones de trabajo duras, así como mejorar las prestaciones de transferencia de calor del material. En este capítulo se desarrollaron materiales compuestos de forma estabilizada a base de $\text{Li}_4(\text{OH})_3\text{Br}$. En primer lugar, se estableció y aplicó una metodología de cribado para la selección del estabilizador de forma más adecuado para el $\text{Li}_4(\text{OH})_3\text{Br}$ peritético entre varios materiales de soporte de óxidos. Los criterios de selección se basaron en i) La compatibilidad termoquímica con la sal peritética. ii) La capacidad antifugas en función de la concentración del material de soporte y iii) La estabilidad cíclica térmica y estructural. El MgO cerámico (nanopartículas sólidas) fue seleccionado como el estabilizador de forma más prometedor. Se sintetizaron, caracterizaron y probaron estructuras porosas de MgO con diversas propiedades estructurales, texturales y morfológicas como materiales de soporte con el objetivo de reducir la cantidad de MgO necesaria para la estabilidad estructural, aumentando así la capacidad de almacenamiento global del material compuesto. La estructura porosa de las partículas sólidas de MgO proporcionaría sitios adicionales para el confinamiento de la sal y mayores fuerzas capilares, aumentando así las prestaciones antifugas del material compuesto a menor carga de óxido. Los resultados mostraron una disminución del 40% de la carga de MgO requerida, proporcionando un rendimiento similar en términos de eficiencia antifugas al utilizar las estructuras porosas de MgO (PMgO) que combinan una superficie específica apreciable y un alto volumen de poros con poros paralelos en forma de placa en el rango de (5-28 nm). El compuesto estabilizado en su forma presentó una buena estabilidad estructural y homogeneidad a lo largo del ciclo, además de una mejora general del 33% en la conductividad térmica del compuesto. Finalmente, a pesar de la pequeña disminución de la entalpía de reacción del compuesto debido al efecto de confinamiento de la sal, el estabilizador de forma PMgO sigue siendo digno de ser considerado para su uso, ya que ayudó a mejorar considerablemente la capacidad de almacenamiento global del compuesto

mediante la disminución de la carga de material de soporte requerido. Deberían llevarse a cabo más investigaciones para mejorar la eficiencia de los compuestos $\text{Li}_4(\text{OH})_3\text{Br}/\text{MgO}$ siguiendo dos puntos 1) Estudio del efecto de las dimensiones y la geometría de los poros sobre las propiedades térmicas del compuesto para poder personalizar las primeras y limitar al máximo el efecto de confinamiento. 2) La adición de materiales de mejora de la conductividad térmica para mejorar las prestaciones generales de transferencia de calor del compuesto en forma estabilizada.

General introduction

In the last few decades, great interest was given to the movement from a harmful and toxic energy system based on fossil fuels toward eco-friendly, clean and sustainable energy system based on renewable energy sources. This transition is mainly due to the fact that the conventional energy sources cause many environmental and health issues. Particularly the greenhouse effect responsible for the climatic change caused by the greenhouse gasses (GHGs) (Carbon dioxide specifically). An average annual increase in CO₂ emission of 1.3 % was reached over 2014 - 2019, with a decrease of 7% [1] of CO₂ emission in the year 2020 due to COVID19 pandemic. Additionally, the extraction of fossil fuels has very bad environmental impacts. Nowadays, thanks to the new environmental policies promoting low-carbon technologies, the movement toward renewable energy sources is slowly increasing. Notably, for the power sector, according to the International Renewable Energy Agency (IRENA), Electricity will be the primary energy carrier by 2050. Indeed, Electricity will represent 50 % of the total final energy consumption by 2050, compared to 21 % today. Moreover, renewable energies (solar power, wind power, geothermal, and hydropower) will supply 90 % of the global electricity needs by 2050, compared to 25 % today. Among the various renewable energy sources, solar energy plays an essential role as a renewable energy sources contributing in the overall energy production. According to the International Energy Agency (IEA), for electricity production, photovoltaic electric generation presented the major part with 2.8 % of the global renewable electricity production in 2019. Concentrating solar power (CSP) presented an appreciable contribution in the total final renewable electricity production considering that is still at a very active development stage. This technology became an attractive research field due to its cost-effectiveness compared to PV technology. Solar energy, like all renewable energy sources, is discontinuous and fluctuates because it is weather dependant, for this reason, the development of thermal energy storage systems is crucial for their implementation.

Thermal energy storage is based on storing the thermal energy in a storage medium to be used later for energy supply. Based on the storage mechanism, thermal energy storage has been exploited into four different storage technologies, sensible heat storage (SHS) using solid or liquid materials, latent heat storage (LHS) using phase change materials, thermochemical heat storage (TCM) using reversible chemical reactions. SHS using molten salts is the current

commercially implemented technology. The success of molten salts lies in the fact that they are relatively cheap and they are stable at high temperatures (up to 560 °C) and therefore can support conventional Rankine steam power cycles. However, they afford a low energy density (30-70 kWh/m³) compared to LHS and TCS materials. For LHS, inorganic anhydrous salts are the most commonly investigated Phase Change Materials (PCMs). The volumetric energy density provided by LHS typically ranges from 80 kWh/m³ to 200 kWh/m³, affording a smaller and potentially cheaper storage system compared to SHS. TCS provides a theoretically outstanding volumetric energy density of 200-600 kWh/m³, five times higher than LHS and ten times that of SHS. However, TCS is still in a very early stage of development and presents some drawbacks which need to be solved such as poor reaction kinetic, low heat and mass transfer ability, materials sintering, complex storage systems and consequent high cost. Peritectic heat storage is a recent innovative technology under development. Thermal energy storage employing the different technologies mentioned above opened a wide range of applications.

For high temperature applications, the development of TES materials and systems has mainly been driven by Concentrated Solar Power (CSP). The most widely implemented TES technology in CSP is the double tank molten salts. TES systems can effectively contribute to the dispatchability of solar power plants and operate conventional thermal power plants in a more flexible manner. Connected to an existing power plant, or as a stand-alone storage system, TES can also contribute to the grid management by load shifting or even replacing peaker-plants. Another significant application is cogeneration, where TES allows decoupling electricity and heat production/use to achieve higher conversion efficiency. Moreover, TES is also used for waste heat recovery. Industrial waste heat is recovered and stored in a TES system and utilized later to reduce the primary energy supply for the same industrial process or transported, if required, to other sites. Among others, cement and concrete, paper industry, foundries, and metallurgical industries are the primary industrial processes implementing the TES systems for waste heat recovery. The development of thermal energy storage systems is conditioned by the development of new thermal storage materials. Indeed, the design of the storage tank and heat exchangers depends on the thermophysical properties of the storage material (Specific heat capacity, energy density, thermal conductivity, volume change, operating temperature range, etc.). Therefore, the development of new and high performant and cost-effective materials for thermal energy storage (TES) at high temperature is becoming a very active research field.

In this regard, this thesis work presents the study of peritectic reactions/transitions for compact thermal energy storage at high temperatures.

These are a novel and very promising class of reactions that can be used for thermal energy storage applications. Peritectic reactions consist of chemical reactions involving the reaction between a solid and a liquid forming a new solid. In respect to their implementation, they would behave like a thermal storage system based on latent heat storage but with an outstanding theoretical effective energy density (200-400 kWh/m³ peritectic reaction, and 400-650 kWh/m³ peritectic reaction + melting) much higher than the currently used phase change materials and comparable to the best gas-solid reactions under development. Additionally, regarding their application, these materials operate at an almost constant temperature at atmospheric pressure leading to simple and compact thermal energy storage systems at an attractive investment cost. For this reasons, these reactions are worth to be studied in detail with the objective to improve their performances and exploit at maximum their potentiality.

Thesis objectives and scope

The main objective of this research work is to develop new materials based on peritectic reactions for thermal energy storage with high performances in terms of energy density, compactness, reversible behaviour, and low cost. The peritectic heat storage concept is based on the release of energy during the formation of chemical compounds during the peritectic reaction/transformation. The thermal energy can be stored by two consecutive processes, an incongruent melting–solidification process (pro-peritectic phase formation) and a liquid-solid chemical reaction (peritectic formation).

The interest towards these reactions is given both to their significantly high theoretical energy densities (200-400 kwh/m³ peritectic reaction, and 400-650 kwh/m³ peritectic reaction + melting) and, regarding their application, the possibility to operate at almost constant temperature at atmospheric pressure leading to simple and compact thermal energy storage systems at an attractive investment cost.

In this work, lithium hydroxide and lithium bromide binary salt system (LiOH-LiBr) has been chosen due to the high theoretical energy density that can be provided by its peritectic reaction/transition (591 kWh/m³) compared to other inorganic salts systems, as well as its

relatively low price compared to metal alloys. The peritectic compound $\text{Li}_4(\text{OH})_3\text{Br}$ was thoroughly investigated to assess its potential utility for TES applications and optimize its performances as high temperature TES material.

To reach the thesis objective, several partial objectives were defined:

1. Investigation of the binary system LiOH-LiBr to elucidate whether the peritectic compound $\text{Li}_4(\text{OH})_3\text{Br}$ can be considered as candidate for compact TES: determination of the phase diagram of the studied system by combining both characterization techniques DSC and XRD. The objective was to provide reliable information about phase transition/reaction temperatures and enthalpies and products of the reactions or phase transitions taking place considering the large discrepancies observed in the literature.
2. Study of the peritectic compound $\text{Li}_4(\text{OH})_3\text{Br}$ as high temperature TES material for concentrating solar power applications by addressing the following points: i) The development and optimization of a suitable synthesis process of the pure peritectic $\text{Li}_4(\text{OH})_3\text{Br}$; ii) Thoroughly characterization of $\text{Li}_4(\text{OH})_3\text{Br}$ in order to elucidate the mechanisms of formation of the peritectic phase on the one hand and to assess its thermal storage performances (transition/reaction temperatures and enthalpies, specific heat, thermal conductivity, and thermal cycling stability) on the other hand.
3. Development of $\text{Li}_4(\text{OH})_3\text{Br/Carbon}$ composites with the aim of enhancing the thermal storage performances of the studied peritectic compound.
4. Study the compatibility between $\text{Li}_4(\text{OH})_3\text{Br}$ and potential storage tank materials (Carbon Steel A516.Gr70 & Stainless Steel AISI 316) under various corrosion conditions.
5. Elaboration and characterization of $\text{Li}_4(\text{OH})_3\text{Br}$ based shape stabilized composites as novel high temperature TES materials in order to mitigate the corrosion phenomena of container materials by $\text{Li}_4(\text{OH})_3\text{Br}$ peritectic salt.

The present thesis work is divided into six chapters

Chapter 1 presents the state-of-the-art in medium and high temperature thermal energy storage, starting with an overview of the current energetic and storage context based on renewable energies, with a special focus on the heat as a primary energy source. In addition, the different typologies of thermal energy storage technologies were described together with the material used in each storage concept. Moreover, this section describes the different high temperature thermal storage applications. Finally, a special focus was devoted to peritectic heat storage materials and technology, highlighting the progress made in this new innovative storage concept, the advantages of these materials and storage technology compared to the other technologies, as well as the aspects to be improved

Chapter 2 presents the materials used in this study as well as the experimental protocols applied for:

- The synthesis of LiOH-LiBr mixtures used to establish the phase diagram of the binary system LiOH-LiBr
- The synthesis of the peritectic compound $\text{Li}_4(\text{OH})_3\text{Br}$. The optimisation of the synthesis protocol of $\text{Li}_4(\text{OH})_3\text{Br}$ is also presented aiming at simplifying the reference protocol by working under air atmosphere instead of using protective argon atmosphere.
- The synthesis protocol of $\text{Li}_4(\text{OH})_3\text{Br}$ /Carbon composites.
- The simple cold-compression route applied for the synthesis of $\text{Li}_4(\text{OH})_3\text{Br}$ based shape stabilized composites
- The experimental protocol followed for synthesizing different MgO samples used as supporting materials with different structural, textural, and morphological properties. Furthermore, a detailed description of the corrosion protocol applied to study the compatibility of container materials (Carbon Steel A516.Gr70 & Stainless Steel AISI 316) with the peritectic salt $\text{Li}_4(\text{OH})_3\text{Br}$ under different atmospheres.
- Finally, the materials characterization techniques (morphological, structural and thermophysical) are presented, notably, the description of the equipment used as well as the description of the measurement conditions and parameters.

Chapter 3 focuses on the determination of the phase diagram of the binary system LiOH-LiBr by means of DSC and XRD experimental analysis to clarify the discrepancies observed compared to previous existing studies relate to temperature values of phase equilibria, the

transition/reaction enthalpy, as well as stoichiometric compounds present in the system. As a conclusion of this chapter, a modified LiOH-LiBr phase diagram is proposed which gives satisfactory explanation to all the disagreements with literature data. In addition, although the enthalpies measured in this work are much lower than the theoretical ones predicted by FactSage 7.3, the peritectic compound $\text{Li}_4(\text{OH})_3\text{Br}$ is still an attractive candidate for TES applications around 300 °C, with an enthalpy of 247 J/g.

Chapter 4 focuses on investigating the peritectic compound $\text{Li}_4(\text{OH})_3\text{Br}$ as high temperature TES material in concentrating solar power applications. A thorough characterization of $\text{Li}_4(\text{OH})_3\text{Br}$ as storage material has been performed by measuring reaction temperatures and enthalpies, specific heat, and thermal conductivity. The effect of the synthesis conditions on the storage properties has been investigated as well. It is concluded that neither the cooling rate applied during the synthesis stage nor the type of atmosphere used (ambient air and protective argon atmosphere) has an influence on the material's performance. The stability of the material to thermal cycling has also been analyzed, showing excellent cycling stability. Moreover, particular attention is paid to the elucidation of mechanisms of formation of $\text{Li}_4(\text{OH})_3\text{Br}$. It is demonstrated that $\text{Li}_4(\text{OH})_3\text{Br}$ needs neither the presence nor contact with the pro-peritectic phase to form. It nucleates and grows directly from the melt so as pure phase $\text{Li}_4(\text{OH})_3\text{Br}$ final microstructure is achieved. An attempt to enhance the storage capacity of the material by the addition of different types of carbon nanoparticles has been carried out. Thermal storage performances of $\text{Li}_4(\text{OH})_3\text{Br}$ for high-pressure DSG solar power plants have been evaluated through comparison with the reference material NaNO_3 .

Chapter 5 is devoted to the study of the corrosion behaviour of Carbon Steel A516.Gr70 & Stainless Steel AISI 316 as potential storage tank materials with the peritectic compound $\text{Li}_4(\text{OH})_3\text{Br}$. Taking into account that the peritectic compound behaves as a phase change material, cycling corrosion experiments were chosen in this study. Different cycling durations were applied, starting by 150 cycles, 300 cycles, and 600 cycles, both under air atmosphere and under protective Argon atmosphere. In order to investigate the corrosion mechanism and evaluate the corrosion rate of the different steel samples, a set of characterization techniques was used, notably SEM, EDS, XRD for the steel samples, combined with DSC and XRD for the peritectic compound.

Chapter 6 is devoted to the study of $\text{Li}_4(\text{OH})_3\text{Br}$ based shape stabilized composites as novel high temperature thermal energy storage materials in order to overcome the corrosion limitation of container materials by the peritectic compound. The first part presents the methodology applied for selecting suitable supporting materials for shape stabilization. The objective is to find proper supporting materials able to shape-stabilize $\text{Li}_4(\text{OH})_3\text{Br}$ during the formation of the melt and after its complete melting, avoiding any leakage, thus obtaining a composite always in the solid-state during the charge and discharge processes. Micro-nanoparticles of MgO , Fe_2O_3 , CuO , SiO_2 , and Al_2O_3 have been tested as candidate supporting materials. The results allowed identifying the most promising composite based on MgO nanoparticles through a deep experimental analysis and characterization including chemical compatibility tests, anti-leakage performance evaluation, structural and thermodynamic properties analysis and preliminary cycling stability study. The second part is devoted to the optimization of $\text{Li}_4(\text{OH})_3\text{Br}/\text{MgO}$ shape stabilized composites. Magnesium oxide (particle size = 100 nm) was selected in the first part as the most promising supporting material for shape stabilization with at a minimum loading of 50 wt. %. In the aim of improving the heat storage capacity of the composite by optimising the MgO concentration required for an optimal structural stability of the composite, $\text{Li}_4(\text{OH})_3\text{Br}/\text{MgO}$ shape stabilized composites were developed using different MgO samples with different structural, textural and morphological properties.

References

- [1] “Global Carbon Project: Coronavirus causes ‘record fall’ in fossil-fuel emissions in 2020 | Carbon Brief.” <https://www.carbonbrief.org/global-carbon-project-coronavirus-causes-record-fall-in-fossil-fuel-emissions-in-2020> (accessed Mar. 24, 2021).

Chapter 1. State of the art in medium and high temperature thermal energy storage

1.1. Energetic and storage contexts overview

The massive population growth over the years has led to a drastic increase in energy demand. Nowadays, more than 70 % of the overall energy production is based on non-renewable energy sources such as coal, petroleum, crude oils, and natural gas [1]. The use of conventional energy resources is the consequence of the industrial revolution during the 19th century, inducing a transition in the energy sources from wood to coal to oil & gas (Figure 1.1). The extraction and consumption of fossil fuels produce waste gas, waste residues, wastewater, and greenhouse gases responsible for global warming, causing severe damages to the environment and human health.

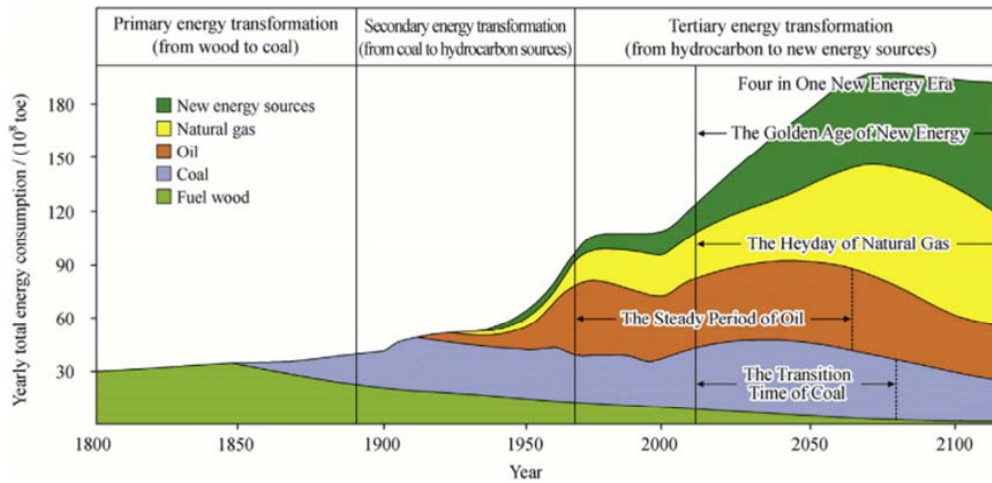


Figure 1.1. Trends and forecasts of global energy consumption. [2]

In order to put an end to the devastating impact of fossil fuels and protect the ecological system, governments and authorities around the world have established new environmental policies and developed future energy roadmaps aiming at decarbonizing energy use in all sectors. The 2030 climate & energy framework established by The European Council targeted to significantly increase renewable energies share in the total energy supply in 2030 with the objective to reduce GHGs [3]. Consequently, the future will bear witness the world's major shift from oil & gas to renewable-based energy systems for a sustainable energy future.

According to the International Renewable Energy Agency (IRENA), renewables (solar power, wind power, geothermal, and hydropower, biomass) represented 11 % of the total final energy consumption in 2018 [4] (Figure 1.2.a) compared to 9.6 % in 2013. This is considered as a moderate increase taking into account the spread of renewable energy deployment worldwide. The share of renewables in final energy demand varies depending on the application sector. Indeed, the power sector represents only 17 % of the total final energy consumption, with the highest share of renewables energies (27.3 % of total final energy consumption (TFEC) in 2018) (Figure 1.2.b).

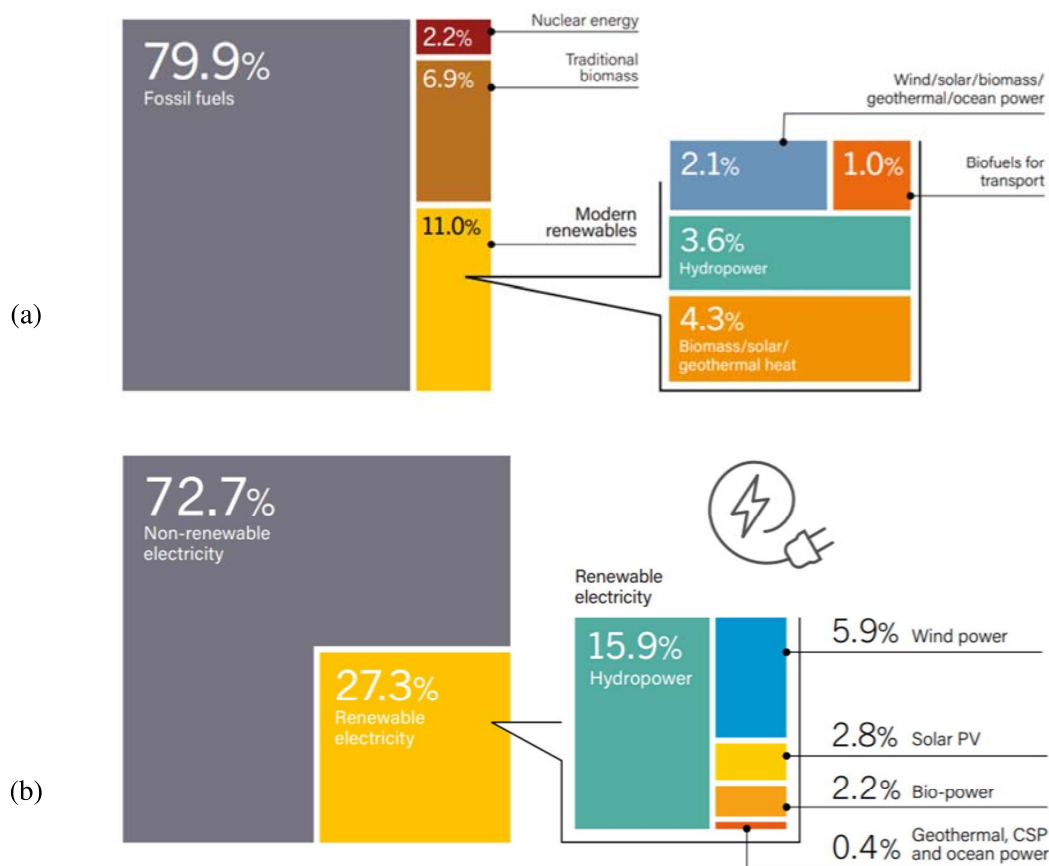


Figure 1.2. (a) Estimated renewable energy share of the total final energy consumption, 2018; (b) Estimated Renewable Energy Share of Global Electricity Production, End-2019 [4]

Solar energy is considered the largest, most abundant, clean, sustainable energy source. The two frequently used solar energy technologies for electricity production are solar PV and concentrated solar power (CSP). As shown in figure 1.2.b, photovoltaic electric generation represented 2.8 % of the global renewable electricity production in 2019. Although

concentrating solar power (CSP), geothermal, and ocean power had a marginal contribution (0.4 %) of the total final renewable electricity production in 2019, its contribution is still appreciable considering that CSP technology is still at a very active development stage and needs technological breakthroughs. Indeed, this energy technology is attracting more interest due to several advantages, namely: i) cost-effective for electricity production compared to solar PV technology. ii) Scalability for low and high temperature applications. iii) High efficiency. iv) Carbon-free. However, despite these advantages, the spread of CSP technology is limited due to two main obstacles: the intermittency of solar energy and the fact that the production sites are far from the consumption region, which requires a supplementary investment cost for energy transportation. The first obstacle is the one to be solved urgently because it affects the operability and limits the economic competitiveness of CSP. Different solutions are proposed: i) the hybridization, which consist of using a back-up power (coal, oil, natural gas) during the periods where there is no solar radiation, for instance, the stations of Nevada Solar One Power Plant and Martin Next Generation Solar Energy Centre and in the USA. ii) Combination of both TES systems and back-up power, for instance, Andasol I Solar Power Plant in Spain; iii) Only TES system [5]. As shown in figure 1.3, thermal energy storage systems are implemented in 45.5 % of the operational CSP plants worldwide, representing 45.1 % of the installed capacity. In comparison, this share reaches 83.3 % of the CSP plants under development. It is worthwhile to highlight the significant increase in the integration of TES systems in this storage technology.

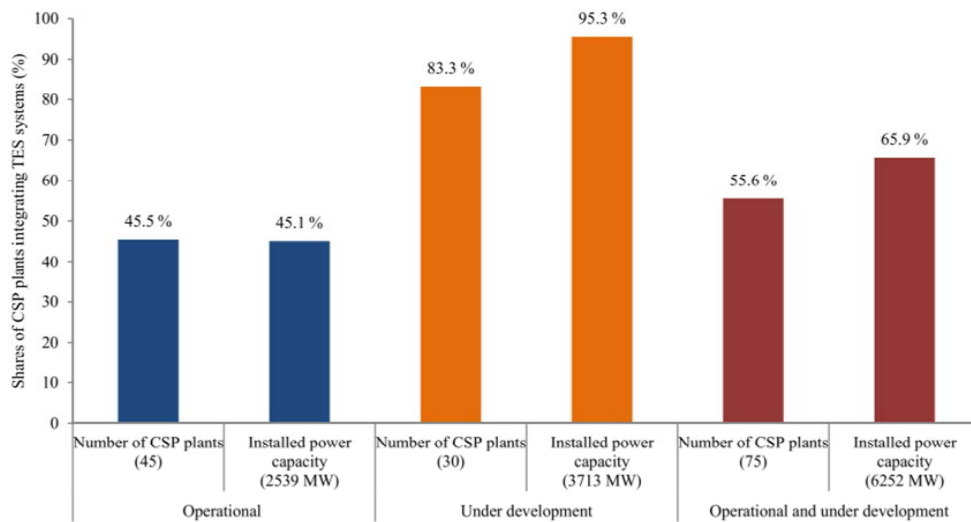


Figure 1.3. Shares of CSP plants integrating TES systems worldwide [5]

1.2. Thermal energy storage (TES)

1.2.1. Definition

Thermal energy storage consists of storing the heat or cold for later use when the energy source is unavailable. The storage cycle consists of three steps, charge, storage, and discharge (figure 1.4) [6]. The integration of thermal energy storage in an energy system ensures the balance between energy demand and supply, improves the thermal reliability and performance of the energy system, and reduces CO₂ emissions. Indeed, during the charging periods (energy supply exceeds the demand), the heat is transferred to the storage media, which will then be released during the discharging periods (no energy source available) (Figure 1.5).

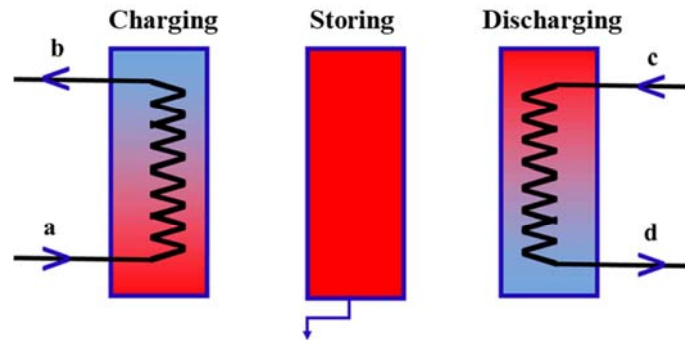


Figure 1.4. Thermal energy storage cycle [6]

Thermal energy storage could be used in multiple applications over a wide range of temperatures. For low temperature applications, the main application is in buildings (domestic water heating, space heating, and cooling). For high temperature applications, TES is used in concentrated solar power for electricity generation from solar energy and for industrial waste heat recovery from heat dissipated from industrial processes. Moreover, thermal energy storage is not only used to tackle the mismatch between the energy supply and demand in CSP plants but also to provide them with greater operational flexibility. In addition, it is also expected that HT-TES provides second life to coal-fired plants, which are being closed for environmental reasons, and that participates as well in the emergence of stand-alone energy storage plants in the grid, where it has a cost advantage over other technologies. In the industrial sector, in addition to the already known uses of recovery and valorization of waste

heat and improvement of the overall efficiency of cogeneration systems or steam boilers, the use of HT-TES is associated with increasing solarization and/or electrification of heat and cold production will be added.

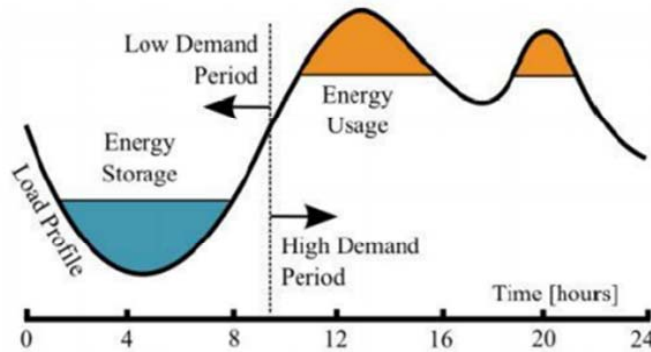


Figure 1.5. Energy storage and usage peaks during 24 hours [7]

1.2.2. Thermal energy storage applications

1.2.2.1. Concentrated solar power plants

CSP is a solar energy technology used for indirect conversion of solar energy to electricity (Rankine cycle) or as a thermal energy source for industrial processes. As shown in figure 1.6, the CSP system is composed mainly of i) solar field, which consists of parallelly aligned receivers (mirrors) through which passes heat collectors (pipes); ii) the Heat transfer fluid (mostly thermal oils such as Therminol VP-1, or molten nitrate salts); iii) tracking device used to track the sun radiation; iv) power block; v) And thermal energy storage system in many CSP plants. Electricity is generated as follows: the heat transfer fluid (HTF) circulating in the pipes is heated by concentrated solar radiation. It is then pumped through the heat exchangers in the power block in order to generate superheated steam, which in turn will generate electricity through a steam turbine generator. Nowadays, CSP is considered a very attractive technology for industrial exploitation owing to the efficient thermal storage system this technology implements, unlike PV, which uses electric storage that is difficult for implementation at a high power level [8].

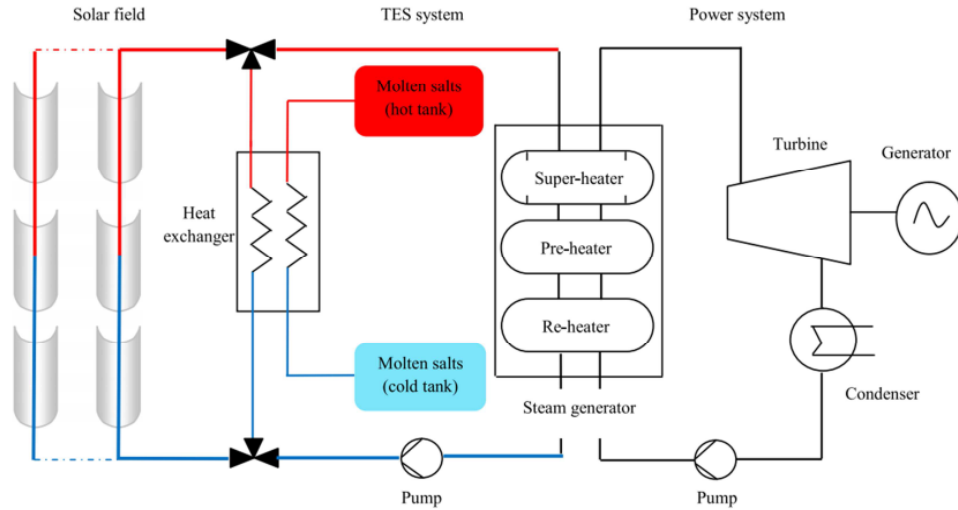


Figure 1.6. Operation principle of CSP a CSP plant [5]

Among several CSP technologies, there are four types of mature CSP plants. They differ from each other based on how the solar radiations are concentrated (type and position of the collector, the shape of the mirror, etc.) [9]–[12]: 1) Parabolic trough collectors (PTC); 2) Solar power tower (SPT); 3) Linear Fresnel reflectors (LFR); 4) And parabolic dish collectors (PDC). PTC and LFR are considered as line focusing collectors because they are equipped with a linear receiver. For this reason, they are relatively less efficient in terms of concentration ratio (300–1000). On the other hand, SPT and PDC are considered as point focusing collectors [13]. For this reason, they are more efficient (concentration ratio 1000–3000) [14]. The most widespread technology is the PCT. As shown in figure 1.7, this technology had the advantages of a high state of maturity, thus lower technical risks and cost-effectiveness [5], [15]. SPT is the second most implemented technology, whereas LFR and PDC are the less implemented technologies.

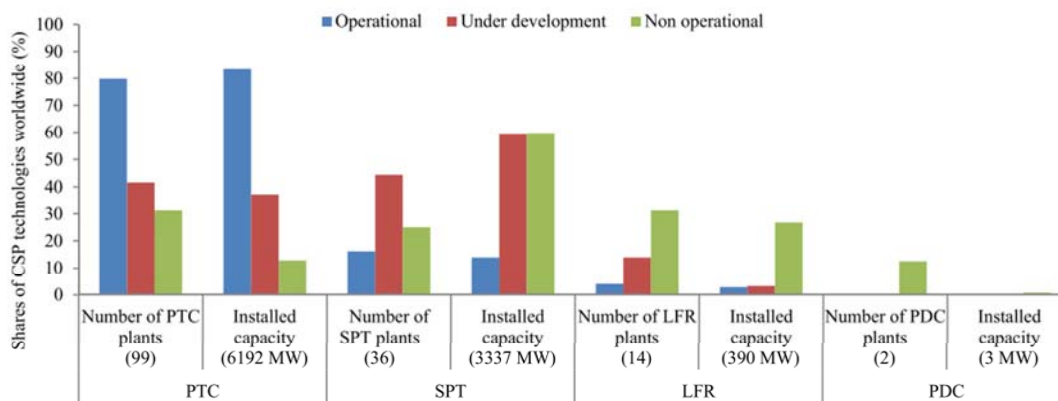


Figure 1.7. Share of different types of CSP plants worldwide [5]

1.2.2. Thermal energy storage technologies

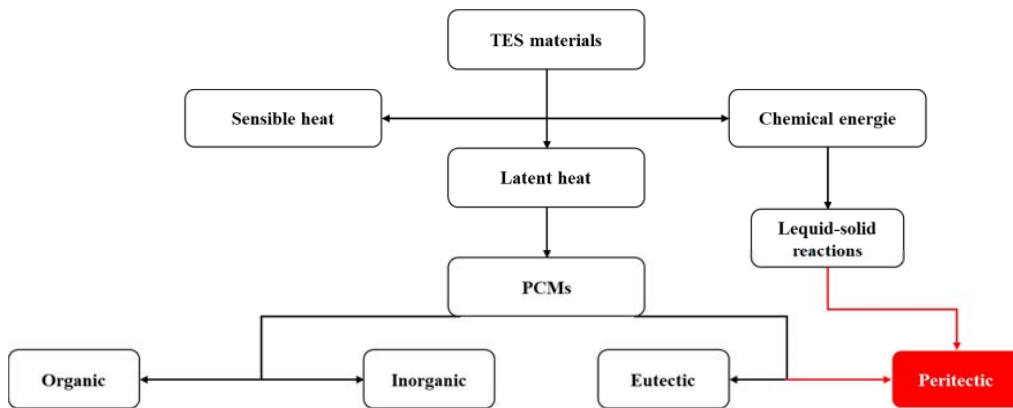


Figure 1.8. TES materials based on the different TES technologies, highlighting the category of the peritectic compounds through a combination of a melting/solidification and liquid/solid chemical reaction storage processes [16].

Thermal energy storage technologies are classified into four different types with different levels of technology maturity: sensible heat storage (SHS), latent heat storage (LHS), and thermochemical heat storage (TCM) [6].

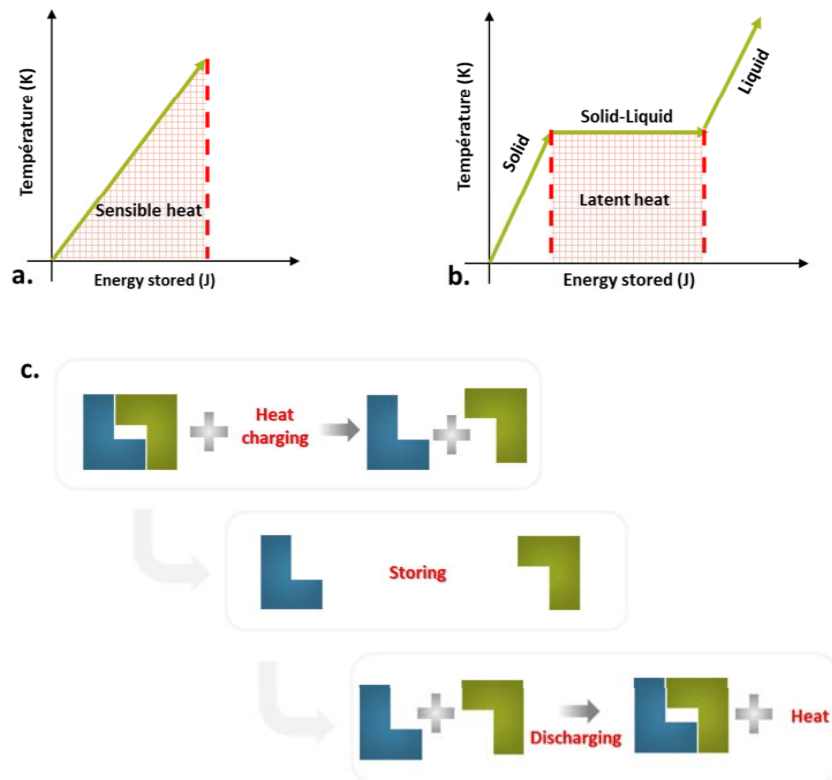


Figure 1.9. Illustration of thermal energy storage technologies: (a) sensible heat storage; (b) latent heat storage; thermochemical heat storage.

1.2.3.1. Sensible heat storage (SHS)

Sensible heat storage consists of storing the heat in a storage media (Solid, liquid, or gaseous) while increasing its temperature and releasing it while decreasing the temperature. The amount of heat stored is calculated according to the following equation (Eq. 1):

$$Q = \int_{t_i}^{t_f} m C_p dt = m \cdot C_p \cdot \Delta T \quad (\text{eq. 1})$$

Where Q is the amount of heat stored in (J), m is the mass of the storage material (kg), C_p is the specific heat of the storage material (J/Kg.K), and ΔT is the temperature variation during the charging and discharging processes. The storage media could be solid such as sand, rock, concrete, metal alloys, and ceramics; a liquid such as water, molten salts, and thermal oils; or gas such as steam and compressed air storage. The amount of heat stored directly depends on the mass of the storage material, its specific heat, and the temperature range. The selection criteria of a suitable SHS material for a particular application are the specific heat of the material, the operational temperature range, the density, the thermal conductivity and diffusivity, the thermochemical cycling stability, the vapor pressure, the compatibility with container materials, the heat transfer properties, safety aspects, and the cost.

For high temperature thermal storage, molten salts in double tank configuration are, by far, the most implemented liquid SHS materials in CSP plants. They are characterized by a large density, a high specific heat capacity, a high boiling point, good thermal stability at high temperature, low vapor pressure, low viscosity, non-toxicity, non-flammability, and low cost. Additionally, molten salts can be used both as TES material and heat transfer fluid. Despite the advantages mentioned above, these materials suffer from several drawbacks, such as the comparatively low thermal conductivity and the high melting temperature, which requires the use of antifreeze protection in order to prevent the solidification of the salts in the pipes, which in turn increases the cost. Molten salts are classified mainly as nitrate, chloride, fluoride, and carbonate-based materials. Nitrate-based salts and their eutectics (Solar salt, Hitec, Hitec XL, LiNaKNO_3 , LiNaKCaNO_3 , $\text{LiNaKNO}_3\text{NO}_2$, etc.) are the most widely used materials [17]–[19]. They are characterized by a relatively low decomposition temperature ($< 600^\circ\text{C}$) adequate for use in parabolic trough collectors (PTC) and linear Fresnel reflectors (LFR) CSP plants. Whereas, the chloride (KMgCl , NaKMgCl , NaMgCaCl , NaKZnCl , KMgZnCl , etc.) [20], fluoride (LiNaKF , NaBF , KBF , KZrF , etc.) [20], [21] and carbonate-based (LiNaKCO_3 , etc.) [22] salts which have higher decomposition temperature ($> 700^\circ\text{C}$)

allow reaching higher operating temperature, they are more adequate for use in solar power tower (SPT) plants.

1.2.3.2. Latent heat storage (LHS)

Latent heat storage consists of storing heat energy during the phase transition of a phase change material at isothermal or quasi-isothermal conditions. In a reversible process, for instance, in the case of solid-liquid transformation, thermal energy is stored during the phase transition from solid to liquid (endothermic transformation). It is then released during the phase transition from liquid to solid (exothermic transformation)(see figure 1.9.b). The advantage of LHS over SHS is the high storage density since the latent heat is excessively higher than the specific heat. For instance, the latent heat of sodium nitrate salt is about 175 kJ/kg, whereas its specific heat is 1.7 kJ/kg K. Additionally, considering the isothermal nature of the phase transition, the heat is stored/released at a constant temperature. The phase transition could be solid \leftrightarrow solid, solid \leftrightarrow liquid, liquid \leftrightarrow gas, or solid \leftrightarrow gas. In addition to the sensible energy stored in the solid and liquid phases, the latent heat stored/released during the phase change of the material also contributes to store the heat. For a solid-liquid LHS material, the amount of thermal energy stored/release depends mainly on the mass and the enthalpy of phase transition of the material, as well as the temperature variation. It is calculated according to the following equation (eq. 2):

$$Q = \int_{T_i}^{T_m} m C_p dT + m \cdot \delta \cdot \Delta H_m + \int_{T_m}^{T_f} m C_p dT \quad (\text{eq. 2})$$

Where m (Kg) is the mass of the PCM, C_p (kJ/kg.K) is the specific heat capacity (solid/liquid), δ is the melted fraction of PCM, ΔH_m (kJ/kg) is the latent heat of fusion, and T_i , T_m , T_f is the initial, melting, and final temperatures respectively.

Solid-solid transition consists of a structural transition that occurs due to modification in the material's crystalline structure. Although this phase transition presents a low volume change during the phase change, it shows a significantly low latent heat compared to other phase transition mechanisms. This drawback limits its use as LHS material. Liquid-gas (Evaporation-Condensation) and solid-gas (Vaporisation- Liquefaction) phase changes have higher latent heat than solid-liquid transitions. However, the considerable volume change they undergo during the phase change complicates the design of LHS system and its implementation in real applications. Solid-liquid (melting-solidification) is the most widely

used phase change process in LHS. This phase transition undergoes a relatively low volume change and possesses a large latent heat, making it very attractive for LHS applications.

The selection of a suitable PCM for a specific application is based on the following criteria: besides the standards requirements requested for any storage material, the PCM material should have a high phase change enthalpy, a low volume change during the phase change, a reversible phase transition, a transition temperature in the range of the working temperature of the TES system both on heating and cooling processes, a good thermal conductivity, a limited and/or controlled phenomena of subcooling, superheating and thermal hysteresis, no/or limited corrosivity.v

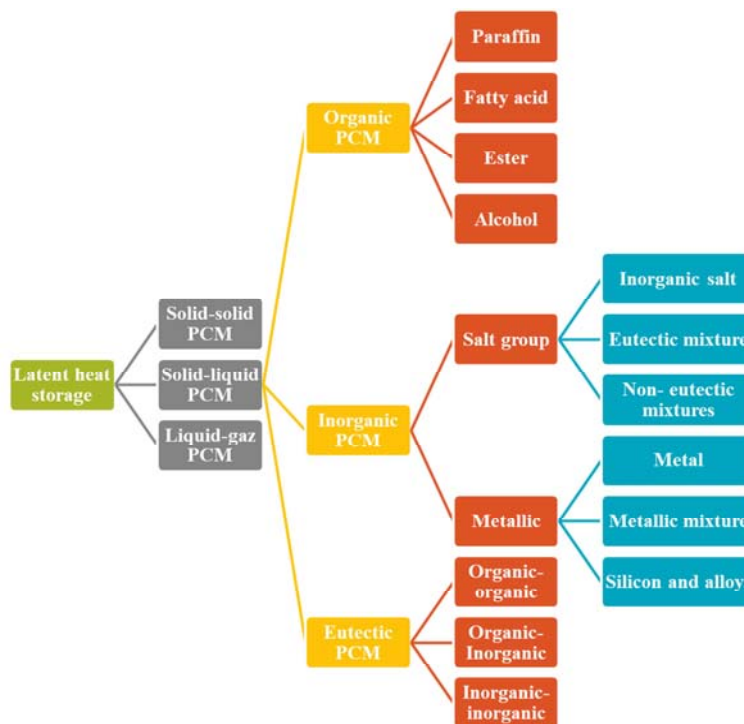


Figure 1.10. Classification of latent heat storage materials

As shown in figure 1.10, solid-liquid PCMs are classified as organic, inorganic, and eutectics. Eutectics are mixtures of organic-organic, inorganic–inorganic or organic–inorganic. Organic PCMs, Mainly paraffin, fatty acids, ester, and sugar alcohols, are adequate for utilization in low to medium temperature applications ($< 250\text{ }^{\circ}\text{C}$) due to their low melting temperature. Whereas inorganics are used for high temperature TES applications (up to $1000\text{ }^{\circ}\text{C}$). The volumetric energy density of inorganics ($250\text{--}400\text{ kg/dm}^3$) is two times higher than that of organic compounds ($128\text{--}200\text{ kg/dm}^3$). This category includes i) Metals (Zn, Mg, Al, etc.) [23]–[25], metal alloys such as Aluminium alloys and Zinc alloys, mixtures of metal

carbonates and alkali halides among which $\text{Li}_2\text{CO}_3/\text{K}_2\text{CO}_3$, $\text{CO}_3/\text{Na}_2\text{CO}_3$, $\text{Li}_2\text{CO}_3/\text{K}_2\text{CO}_3$, $\text{Li}_2\text{CO}_3/\text{Na}_2\text{CO}_3$, as well as $\text{MgCl}_2/\text{NaCl}$, $\text{NaCl}/\text{CaCl}_2$, $\text{LiF}/\text{NaF}/\text{KF}$ [26]–[30]. We can also notice some recent investigations on silicon/boron alloys oriented toward ultra-high temperature TES ($>1200^\circ\text{C}$) for modern thermophotovoltaic conversion. Although less attractive because of higher cost, metal alloys, have been investigated as well and proven to have quite high latent heat of fusion. ii) Inorganic salts (nitrates, carbonates, chlorides, fluorides, and sulfates), salt mixtures ($\text{NaNO}_3\text{--KNO}_3$, $\text{KNO}_3\text{--KCl}$, KF--KCl , $\text{NaF--CaF}_2\text{--MgF}_2$, LiF--NaF , NaF--MgF_2 , $\text{NaF--MgF}_2\text{--KF}$, $\text{KCl--NaF--K}_2\text{CO}_3$, KCl--KF , $\text{KCl--KF--K}_2\text{CO}_3$, NaF--MgF_2 , $\text{Na}_2\text{CO}_3\text{--K}_2\text{CO}_3$, etc.) [31], [32].

1.2.3.3. Thermochemical heat storage (TcHS)

Thermochemical energy storage consists of storing the thermal energy employing reversible chemical reactions between different materials or sorption processes. In the case of TcHS using chemical reactions, the energy is stored upon the endothermic reaction where a compound AB is dissociated into A and B using the heat energy ($\text{AB} + \text{heat Energy} \leftrightarrow \text{A} + \text{B}$). The two reaction products are stored separately, to be combined later to release the heat when it is required (exothermic reaction) [33], [34] (see figure 1.9.c). In case of TcHS using sorption processes, the heat is stored/released through desorption and adsorption/absorption processes. The thermal energy stored/released through the endothermic/exothermic reactions is directly proportional to the mass of the reactive material and reaction enthalpy according to the following equation (eq. 3):

$$Q = m \cdot \Delta H_{\text{reaction}} \quad (\text{eq. 3})$$

Where m is the mass of the storage material (limiting reactant) (kg) and $\Delta H_{\text{reaction}}$ is the reaction enthalpy (kJ/Kg). Although TcHS technology is still at a fundamental laboratory scale and no proven design or material is demonstrated at commercial scale [35], [36], this technology is being intensively investigated owing to the advantages it presents over LHS and SHS technologies. Among these advantages we mention, first, the theoretical energy density in thermochemical heat storage is much higher than in LHS and SHS, which allows smaller storage units volume [37]–[42]. Additionally, the discharging process takes place only when combining the products components regardless of the temperature [43], [44]. This allows long storage durations (e.g., seasonal storage) at ambient temperature and prevents heat loss, thus no need to use expensive thermal insulation systems as in the case of LHS and SHS. Despite

all the above-mentioned advantages, this technology suffers from some drawbacks which limit its exploitation at an industrial scale, such as finding a low cost reaction system with good cyclability, long-term reaction reversibility, and convenient for a specific application in terms of operating temperature and pressure ranges, as well as the complexity of designing reactors and heat exchangers taking into account the mass and heat transfer properties of the reaction. Gas-solid is the most promising thermochemical heat storage reaction [45]. It is based on the chemical reaction between gaseous and solid reactants to store/release thermal energy. They are characterized by the easiness of the separation of the gas released during heat absorption [46]. In addition, adjusting the pressure of the system allows obtaining different charge and/or discharge temperatures because solid-gas reactions take place at constant temperature for a given pressure, and the pressure has an important effect on the reaction temperature [47].

Several gas-solid reaction systems have been explored:

- Hydroxide systems (250-800 °C): this category works on the principle of storing/releasing heat energy through hydration/dehydration reactions. Several reaction couples were investigated in literature, such as CaCl_2 ; SrBr_2 [48]; MgSO_4 [49]; MgCl_2 [50]. The most appropriate ones are $\text{Ca(OH)}_2/\text{CaO}$ [51] and MgO/Mg(OH)_2 thanks to their availability and low cost [52]–[54]. Packed-bed reactors are the most studied configuration for these systems [55], [56].
- Redox systems (600-1000 °C): some examples of these reactions are $\text{Co}_3\text{O}_4/\text{CoO}$ [57]; $\text{Fe}_3\text{O}_4/\text{FeO}$ [58]; $\text{Mn}_2\text{O}_3/\text{Mn}_3\text{O}_4$ [59], [60]; MgO/Mg [58]; BaO_2/BaO [45]; ZnO/Zn [58]; $\text{CuO/Cu}_2\text{O}$ [45]; GeO_2/GeO and SnO_2/Sn [58]. For large scale high temperature applications, redox systems based on metal oxide are considered as the most promising TCHS systems thanks to the fact that: i) they possess high energy density; ii) they achieve high reduction/oxidation temperatures (up to 1100 °C); iii) they provide long storage periods at ambient temperature; iv) air is used both as the HTF and the reactant [61]–[63]. Mixed metal oxides are used because of their improved thermochemical properties compared to pure metal oxides. As for the reactors, these materials are adequate for direct-type reactors [64]. The most attractive system in this category is the cobalt oxide $\text{Co}_3\text{O}_4/\text{CoO}$ owing to its high reaction enthalpy (844 kJ/kg) [61], its good cycling stability [65]. As well as Manganese oxide $\text{Mn}_2\text{O}_3/\text{Mn}_3\text{O}_4$ [63], [66]. The high reaction temperature of these materials (above 900 °C) can be exploited for the new generation of CSP plants, which use volumetric

receivers at atmospheric pressure. However, it can be considered as a limitation for their implementation in current CPS plants working at relatively lower temperatures. Therefore, special focus is being devoted to develop new redox systems with lower redox temperatures, such as doped mixed oxides, perovskite oxides [67], [68], and spinel mixed oxides, for instance $\text{Co}_{3-x}\text{Ni}_x\text{O}_4$ with lower red-ox temperatures compared to pure Co_3O_4 [69].

- Carbonate systems (100-950 °C): two calcination/carbonation reactions were reported in the literature. The cerussite SrCO_3/SrO shows good thermal energy storage density and reaction reversibility [54], [70], [71]. The calcite CaCO_3/CaO [72], [73] or the calcite doped with titanium oxide CaTiO_3 to improve the reaction reversibility [74]. The storage capacity of this system is limited by the particle size of CaO powder which ensures the maximum CO_2 absorption capacity for particle size below 40 μm .
- Metallic hydrides systems (80-400 °C): These materials are characterized by good reaction reversibility and good cyclability at high temperatures leading to efficient long term storage systems. Several types of reactions were reported in literature, such as $\text{NaMgH}_3/\text{NaH}+\text{M}$ [75]; LiH/Li [45], [76], [77]; $\text{Mg}_2\text{FeH}_6/\text{Mg}+\text{Fe}$ [78]; CaH_2/Ca [64], [79], [80]. The Magnesium Hydride System (MgH_2/Mg) [64], [81]–[84] is a very promising material thanks to its high energy density (75 kJ/mol H_2 in a temperature range of 200-500 °C) [78]. Furthermore, CaAl_2 shows to have excellent thermal conductivity and the lowest cost compared to other metal hydrides, which makes it attractive for high temperature TES applications (above 600 °C) [85]. Moreover, $\text{Na}_3\text{AlH}_6/\text{Mg}_2\text{FeH}_6$ couple system has been recently numerically investigated, showing good performances and efficiency (up to 96 % thermal energy recovery) for steam CSP plants [86]. Metallic hydride systems suffer from high operating pressures and flammability, which limit their development at an industrial scale.

1.2.3.4. Peritectic heat storage (materials and technology)

Peritectic heat storage consists of using the chemical reactions leading to the decomposition/formation of the stoichiometric peritectic compounds to store/deliver the thermal energy. The peritectic reactions are reversible reactions that take place at a constant temperature, in which a liquid phase (L) reacts with a solid phase (A) to form a new solid phase (B). The new formed phase (B) can be a solid solution of one of the components, or a new stoichiometric compound. [87]. The idea of using peritectic compounds for TES was

proposed recently, for the first time by Achchaq and Palomo [87]. The heat charge/discharge processes using these materials are described (figure 1.11.b) as follow [87]: Assuming the thermodynamic equilibrium conditions, upon the charging process, at the peritectic temperature (T_P), the solid stoichiometric compound (β) decomposes into the pro-peritectic phase (α) and a liquid phase. The phase (α) melts gradually until reaching the liquidus at (T_L). Upon the discharging process at T_L , the pro-peritectic phase starts to nucleate. The latter continues to grow with the decrease of temperature. Then, when reaching the peritectic temperature, the properitectic phase reacts with the liquid to form the stoichiometric peritectic compound (β) ($L + \alpha \leftrightarrow \beta$). Therefore, the thermal energy is consequently stored/delivered following two consecutive processes: 1) A melting solidification process (incongruent melting). 2) A solid/liquid chemical reaction (peritectic reaction). According to these two storage processes, the peritectic compounds combine both the energies from the latent heat and the reversible chemical reaction (figure 1.8) which gives them the particularity of the outstanding theoretical energy density compared to other materials from the different TES technologies.

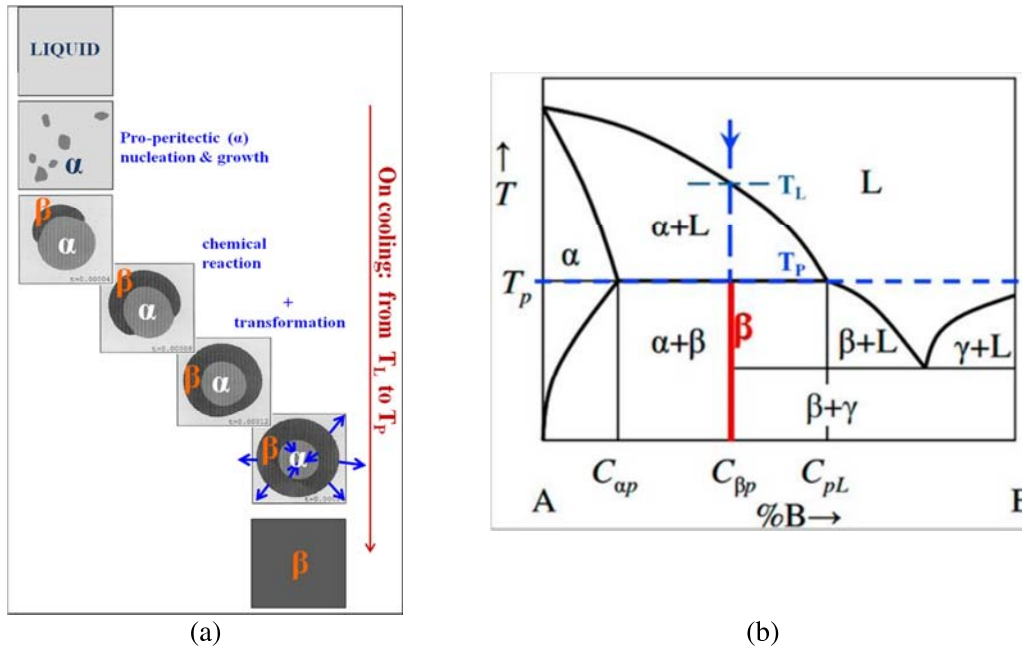


Figure 1.11. (a) Mechanism of formation of a stoichiometric peritectic compound on cooling; (b) phase diagram highlighting the peritectic composition. [87]

Figure 1.11.a describes the mechanism of formation of a peritectic compound. As it can be seen, on cooling, the peritectic reaction ($L + \alpha \leftrightarrow \beta$) occurs at T_P . The reaction is very fast and it is followed by the peritectic thickening which consists of the growth of the peritectic phase.

The thickening is a sluggish process because it takes place by long-term atomic diffusion (slow solid/solid diffusion rate) of the properitectic phase (α) through the formed the peritectic layer to reacts with the liquid phase (L) leading to the formation/growth of the peritectic phase at the interface peritectic/liquid. The process ends when the properitectic phase is completely consumed, which is practically not feasible, leading to the formation of an out of equilibrium peritectic structure. For this reason, lower peritectic reaction enthalpy is expected to be achieved experimentally compared to the theoretical estimated values [87].

Table 1.1. Salt based and mettalic alloys peritectic binary systems and their corresponding thermal storage properties (peritectic temperature (T_p); peritectic reaction enthalpy ΔH ; peritectic energy density (E_p); melting/transition temperature range ($\Delta T_{L \rightarrow P}$); and the energy density corresponding to the formation of both peritectic and pro-peritectic phases [87]

Binary system A/B	TP (°C)	ΔH (J.g ⁻¹)	E_p (kWh.m ⁻³)	$\Delta T_{L \rightarrow P}$ (°C)	$E_{L \rightarrow P}$ (kWh.m ⁻³)
LiBr/LiOH	303.90	803	434	76	591
KOH/LiOH	314.82	535	238	24	283
LiI/LiOH	334.93	308	182	34	253
CsOH/LiOH	373.63	354	214	55	388
Cr/Zn	483.12	118	234	483	679
Mg/Ag	491.94	332	286	6	304
Li/Zn	510.02	304	372	5	565
Mn/Ni	587.35	297	637	493	1642
Ce/Mg	625.22	368	235	4	239
Ca/Zn	642.05	201	224	5	232
Sr/Zn	649.97	167	206	83	349
Li/Si	690.57	1136	377	20	467
CaCl ₂ /CaF ₂	734.94	438	290	98	402

The study carried out by Achchaq et palomo, based on computational thermodynamic, [87] reported several promising peritectic compound of metallic and salt based binary systems with a peritectic temperature in the range of 300 °C to 700 °C, and an outstanding theoretical energy density that can reach 600 kWh/m³ while considering both the enthalpies related to the peritectic reaction and the melting (properitectic phase). The results are presented in table 1.1. The peritectic compound subject of the present study is highlighted in bold.

Table 1.2. Comparison of different thermal storage technologies [88]

	SHS	LHS	TcHS
Mechanism	Temperature gradient	Isothermal phase transition	Reversible chemical reactions

Volumetric energy density	Small ~50 kWh/m ³	Medium ~100 kWh/m ³	High (up to 500 kWh/m ³)
Gravimetric density	Small ~0.02–0.03 kWh/kg	Medium ~0.05–0.1 kWh/kg	High (0.5-1 kWh/kg)
Storage period	Limited due to thermal losses	Limited due to thermal losses	Theoretically unlimited
Storage temperature	charging Temperature (More than T _{cHS})	charging Temperature (More than T _{cHS})	Surrounding temperature (Less than SHS & LHS)
TRL	Industrial-scale	prototypes	Laboratory
Technology	Simple	Medium	Complex
Feedback	Large experimental and commercial feedback	Less experimental and no commercial feedback	No feedback
Flexibility	Less time to switch between charging and discharging	Less time to switch between charging and discharging	Switch between charge and discharge takes a medium time

Table 1.2 presents a comparison between the three TES technologies. Each TES technology has its advantages and limitations as described in previous sections. Sensible heat storage is the most implemented TES technology in commercial CSP plants owing to its attractive efficiency-cost ratio [89]. TcHS systems allow achieving higher thermal storage densities due to their higher reaction enthalpies than LHS, which in turn achieves higher storage densities compared to the SHS storage systems. In addition, the TcHS reactions store heat at an ambient temperature which prevents the thermal losses during the storage period allowing these systems to store thermal energy for more extended periods. This makes TcHS the only technology that enables seasonal storage. As for the technology maturity, unlike SHS and LHS which has a considerable level of maturity, TcHS is still at the fundamental research scale with no experience feedback. The advantages of the peritectic compounds over other materials from the different TES technologies are several. In particular, the outstanding volumetric energy density competing with the ones of gas-solid reactions (compact storage). The simplicity of the storage system where the heat storage/delivering processes takes place at atmospheric pressure similarly to the case of the sensible heat storage technology, and contrary to gas-solid reactions where the reactant have to be separated involving more complex storage systems (Simple technology). Relatively lower investment cost considering the simplicity of the technology and the compactness of the storage (cost-effectiveness TES

solution). These advantages make the peritectic compounds very promising to develop efficient simple cost-effective TES solutions for high temperature applications.

1.5. References

- [1] S. Chu, Y. Cui, and N. Liu, “The path towards sustainable energy,” *Nature Materials*, vol. 16, no. 1. Nature Publishing Group, pp. 16–22, Dec. 20, 2016, doi: 10.1038/nmat4834.
- [2] C. Zou, Q. Zhao, G. Zhang, and B. Xiong, “Energy revolution: From a fossil energy era to a new energy era,” *Natural Gas Industry B*, vol. 3, no. 1, pp. 1–11, Jan. 2016, doi: 10.1016/j.ngib.2016.02.001.
- [3] “2030 climate & energy framework | Climate Action.” https://ec.europa.eu/clima/policies/strategies/2030_en (accessed Apr. 15, 2021).
- [4] REN21, “Renewables 2020 globale status report,” 2020.
- [5] O. Achkari and A. El Fadar, “Latest developments on TES and CSP technologies – Energy and environmental issues, applications and research trends,” *Applied Thermal Engineering*, vol. 167. Elsevier Ltd, p. 114806, Feb. 25, 2020, doi: 10.1016/j.applthermaleng.2019.114806.
- [6] B. Stutz *et al.*, “Storage of thermal solar energy,” *Comptes Rendus Physique*, vol. 18, no. 7–8. Elsevier Masson s.r.l., pp. 401–414, Sep. 01, 2017, doi: 10.1016/j.crhy.2017.09.008.
- [7] S. Sabihuddin, A. Kiprakis, and M. Mueller, “A Numerical and Graphical Review of Energy Storage Technologies,” *Energies*, vol. 8, no. 1, pp. 172–216, Dec. 2014, doi: 10.3390/en8010172.
- [8] “Concentrated Solar Power (CSP) Vs Photovoltaic (PV) – HELIOSCSP.” <https://helioscsp.com/concentrated-solar-power-csp-vs-photovoltaic-pv/> (accessed Apr. 19, 2021).
- [9] “Demonstration Development Project: Solar Thermocline Storage Systems: Preliminary Design Study.” <https://www.epri.com/research/products/1019581> (accessed Apr. 19, 2021).
- [10] E. González-Roubaud, D. Pérez-Osorio, and C. Prieto, “Review of commercial thermal energy storage in concentrated solar power plants: Steam vs. molten salts,” *Renewable and Sustainable Energy Reviews*, vol. 80. Elsevier Ltd, pp. 133–148, 2017, doi: 10.1016/j.rser.2017.05.084.
- [11] D. A. Baharoon, H. A. Rahman, W. Z. W. Omar, and S. O. Fadhl, “Historical development of concentrating solar power technologies to generate clean electricity efficiently – A review,” *Renewable and Sustainable Energy Reviews*, vol. 41. Elsevier Ltd, pp. 996–1027, Jan. 01, 2015, doi: 10.1016/j.rser.2014.09.008.
- [12] T. M. Pavlović, I. S. Radonjić, D. D. Milosavljević, and L. S. Pantić, “A review of concentrating solar power plants in the world and their potential use in Serbia,” *Renewable and Sustainable Energy Reviews*, vol. 16, no. 6. Pergamon, pp. 3891–3902, Aug. 01, 2012, doi: 10.1016/j.rser.2012.03.042.
- [13] M. Liu *et al.*, “Review on concentrating solar power plants and new developments in high temperature thermal energy storage technologies,” *Renewable and Sustainable Energy Reviews*, vol. 53. Elsevier Ltd, pp. 1411–1432, Jan. 01, 2016, doi: 10.1016/j.rser.2015.09.026.
- [14] B. Belgasim, Y. Aldali, M. J. R. Abdunnabi, G. Hashem, and K. Hossin, “The potential of concentrating solar power (CSP) for electricity generation in Libya,” *Renewable and Sustainable Energy Reviews*, vol. 90. Elsevier Ltd, pp. 1–15, Jul. 01, 2018, doi: 10.1016/j.rser.2018.03.045.

- [15] W. Fuqiang, C. Ziming, T. Jianyu, Y. Yuan, S. Yong, and L. Linhua, "Progress in concentrated solar power technology with parabolic trough collector system: A comprehensive review," *Renewable and Sustainable Energy Reviews*, vol. 79, Elsevier Ltd, pp. 1314–1328, Nov. 01, 2017, doi: 10.1016/j.rser.2017.05.174.
- [16] B. Karakashov, "Studies of fibrous carbons for high-temperature thermal energy storage," Dec. 2019, Accessed: Jun. 02, 2021. [Online]. Available: <https://hal.univ-lorraine.fr/tel-02551704>.
- [17] C.-C. Lai, W.-C. Chang, W.-L. Hu, Z. M. Wang, M.-C. Lu, and Y.-L. Chueh, "A solar-thermal energy harvesting scheme: enhanced heat capacity of molten HITEC salt mixed with Sn/SiO_x core-shell nanoparticles," *Nanoscale*, vol. 6, no. 9, pp. 4555–4559, Apr. 2014, doi: 10.1039/C3NR06810B.
- [18] E. González-Roubaud, D. Pérez-Osorio, and C. Prieto, "Review of commercial thermal energy storage in concentrated solar power plants: Steam vs. molten salts," *Renewable and Sustainable Energy Reviews*, vol. 80, pp. 133–148, Dec. 2017, doi: 10.1016/J.RSER.2017.05.084.
- [19] K. Vignarooban, X. Xu, A. Arvay, K. Hsu, and A. M. Kannan, "Heat transfer fluids for concentrating solar power systems – A review," *Applied Energy*, vol. 146, pp. 383–396, May 2015, doi: 10.1016/J.APENERGY.2015.01.125.
- [20] W. Ding, A. Bonk, and T. Bauer, "Molten chloride salts for next generation CSP plants: Selection of promising chloride salts & study on corrosion of alloys in molten chloride salts," *AIP Conference Proceedings*, vol. 2126, Jul. 2019, doi: 10.1063/1.5117729.
- [21] D. F. Williams and K. T. Clarno, "Evaluation of Salt Coolants for Reactor Applications," <http://dx.doi.org/10.13182/NT08-A3992>, vol. 163, no. 3, pp. 330–343, 2017, doi: 10.13182/NT08-A3992.
- [22] T. Wang, D. Mantha, and R. G. Reddy, "Novel high thermal stability LiF–Na₂CO₃–K₂CO₃ eutectic ternary system for thermal energy storage applications," *Solar Energy Materials and Solar Cells*, vol. 140, pp. 366–375, Sep. 2015, doi: 10.1016/J.SOLMAT.2015.04.033.
- [23] K. Dey and N. Sannayellappa, "Numerical simulation and characterization of zinc aluminium 12 alloy for latent heat thermal energy storage application," *AIP Conference Proceedings*, vol. 2274, no. 1, p. 030018, Oct. 2020, doi: 10.1063/5.0022378.
- [24] A. I. Fernández, C. Barreneche, M. Belusko, M. Segarra, F. Bruno, and L. F. Cabeza, "Considerations for the use of metal alloys as phase change materials for high temperature applications," *Solar Energy Materials and Solar Cells*, vol. 171, pp. 275–281, Nov. 2017, doi: 10.1016/J.SOLMAT.2017.06.054.
- [25] J. Q. Sun, R. Y. Zhang, Z. P. Liu, and G. H. Lu, "Thermal reliability test of Al-34%Mg-6%Zn alloy as latent heat storage material and corrosion of metal with respect to thermal cycling," *Energy Conversion and Management*, vol. 48, no. 2, pp. 619–624, Feb. 2007, doi: 10.1016/J.ENCONMAN.2006.05.017.
- [26] L. Sang, M. Cai, Y. Zhao, N. Ren, Y. Wu, and C. Burda, "Mixed metal carbonates/hydroxides for concentrating solar power analyzed with DSC and XRD," *Solar Energy Materials and Solar Cells*, vol. 140, pp. 167–173, Sep. 2015, doi: 10.1016/J.SOLMAT.2015.04.006.
- [27] Y. Jiang, Y. Sun, F. Bruno, and S. Li, "Thermal stability of Na₂CO₃–Li₂CO₃ as a high temperature phase change material for thermal energy storage," *Thermochimica Acta*, vol. 650, pp. 88–94, Apr. 2017, doi: 10.1016/J.TCA.2017.01.002.
- [28] M. Liu, J. Gomez, C. S. Turchi, N. H. S. Tay, W. Saman, and F. Bruno, "Determination of thermo-physical properties and stability testing of high-temperature phase-change materials for CSP applications," 2015, Accessed: Jul. 14, 2021. [Online].

- Available: <http://www.elsevier.com/open-access/userlicense/1.0/>.
- [29] H. Tian, W. Wang, J. Ding, X. Wei, and C. Huang, "Preparation of binary eutectic chloride/expanded graphite as high-temperature thermal energy storage materials," *Solar Energy Materials and Solar Cells*, vol. C, no. 149, pp. 187–194, May 2016, doi: 10.1016/J.SOLMAT.2015.12.038.
 - [30] V. Khokhlov, I. Korzun, V. Dokutovich, and E. Filatov, "Heat capacity and thermal conductivity of molten ternary lithium, sodium, potassium, and zirconium fluorides mixtures," *Journal of Nuclear Materials*, vol. 410, no. 1–3, pp. 32–38, Mar. 2011, doi: 10.1016/J.JNUCMAT.2010.12.306.
 - [31] K. H. Stern, "Molten Salts: Volume 3 Nitrates, Nitrites, and Mixtures: Electrical Conductance, Density, Viscosity, and Surface Tension Data," *A Critical Review Journal of Physical and Chemical Reference Data*, vol. 1, p. 773, 1972, doi: 10.1063/1.3253104.
 - [32] M. M. Kenisarin, "High-temperature phase change materials for thermal energy storage," *Renewable and Sustainable Energy Reviews*, vol. 14, no. 3, pp. 955–970, Apr. 2010, doi: 10.1016/J.RSER.2009.11.011.
 - [33] X. Chen, Z. Zhang, C. Qi, X. Ling, and H. Peng, "State of the art on the high-temperature thermochemical energy storage systems," *Energy Conversion and Management*, vol. 177, pp. 792–815, Dec. 2018, doi: 10.1016/J.ENCONMAN.2018.10.011.
 - [34] D. Liu, L. Xin-Feng, L. Bo, Z. Si-quan, and X. Yan, "Progress in thermochemical energy storage for concentrated solar power: A review," *International Journal of Energy Research*, vol. 42, no. 15, pp. 4546–4561, Dec. 2018, doi: 10.1002/ER.4183.
 - [35] M. Silakhori, M. Jafarian, M. Arjomandi, and G. J. Nathan, "Thermogravimetric analysis of Cu, Mn, Co, and Pb oxides for thermochemical energy storage," *Journal of Energy Storage*, vol. 23, pp. 138–147, Jun. 2019, doi: 10.1016/J.EST.2019.03.008.
 - [36] H. Nazir *et al.*, "Recent developments in phase change materials for energy storage applications: A review," *International Journal of Heat and Mass Transfer*, vol. 129, pp. 491–523, Feb. 2019, doi: 10.1016/J.IJHEATMASSTRANSFER.2018.09.126.
 - [37] J. Cot-Gores, A. Castell, and L. F. Cabeza, "Thermochemical energy storage and conversion: A-state-of-the-art review of the experimental research under practical conditions," *Renewable and Sustainable Energy Reviews*, vol. 16, no. 7, pp. 5207–5224, Sep. 2012, doi: 10.1016/J.RSER.2012.04.007.
 - [38] M. Liu *et al.*, "Review on concentrating solar power plants and new developments in high temperature thermal energy storage technologies," *Renewable and Sustainable Energy Reviews*, vol. 53, pp. 1411–1432, Jan. 2016, doi: 10.1016/J.RSER.2015.09.026.
 - [39] S. Wu, C. Zhou, E. Doroodchi, R. Nellore, and B. Moghtaderi, "A review on high-temperature thermochemical energy storage based on metal oxides redox cycle," *Energy Conversion and Management*, vol. 168, pp. 421–453, Jul. 2018, doi: 10.1016/J.ENCONMAN.2018.05.017.
 - [40] G. Wei *et al.*, "Selection principles and thermophysical properties of high temperature phase change materials for thermal energy storage: A review," *Renewable and Sustainable Energy Reviews*, vol. 81, pp. 1771–1786, Jan. 2018, doi: 10.1016/J.RSER.2017.05.271.
 - [41] L. Miró, J. Gasia, and L. F. Cabeza, "Thermal energy storage (TES) for industrial waste heat (IWH) recovery: A review," *Applied Energy*, vol. 179, pp. 284–301, Oct. 2016, doi: 10.1016/J.APENERGY.2016.06.147.
 - [42] A. Gil *et al.*, "State of the art on high temperature thermal energy storage for power generation. Part 1—Concepts, materials and modellization," *Renewable and Sustainable Energy Reviews*, vol. 14, no. 1, pp. 31–55, Jan. 2010, doi:

- 10.1016/J.RSER.2009.07.035.
- [43] G. Alva, L. Liu, X. Huang, and G. Fang, "Thermal energy storage materials and systems for solar energy applications," *Renewable and Sustainable Energy Reviews*, vol. 68, pp. 693–706, Feb. 2017, doi: 10.1016/J.RSER.2016.10.021.
 - [44] X. Yang, Y. Yuan, N. Zhang, X. Cao, and C. Liu, "Preparation and properties of myristic–palmitic–stearic acid/expanded graphite composites as phase change materials for energy storage," *Solar Energy*, vol. 99, pp. 259–266, Jan. 2014, doi: 10.1016/J.SOLENER.2013.11.021.
 - [45] L. André, S. Abanades, and G. Flamant, "Screening of thermochemical systems based on solid-gas reversible reactions for high temperature solar thermal energy storage," *Renewable and Sustainable Energy Reviews*, vol. 64, pp. 703–715, Oct. 2016, doi: 10.1016/J.RSER.2016.06.043.
 - [46] C. Prieto, P. Cooper, A. I. Fernández, and L. F. Cabeza, "Review of technology: Thermochemical energy storage for concentrated solar power plants," *Renewable and Sustainable Energy Reviews*, vol. 60, pp. 909–929, Jul. 2016, doi: 10.1016/J.RSER.2015.12.364.
 - [47] L. Jiang, L. Wang, R. Wang, F. Zhu, Y. Lu, and A. P. Roskilly, "Experimental investigation on an innovative resorption system for energy storage and upgrade," *Energy Conversion and Management*, vol. 138, pp. 651–658, Apr. 2017, doi: 10.1016/J.ENCONMAN.2017.02.014.
 - [48] F. Marias, P. Neveu, G. Tanguy, and P. Papillon, "Thermodynamic analysis and experimental study of solid/gas reactor operating in open mode," *Energy*, vol. 66, pp. 757–765, Mar. 2014, doi: 10.1016/J.ENERGY.2014.01.101.
 - [49] S. Hongois, F. Kuznik, P. Stevens, and J. J. Roux, "Development and characterisation of a new MgSO₄–zeolite composite for long-term thermal energy storage," *Solar Energy Materials and Solar Cells*, vol. 95, no. 7, pp. 1831–1837, Jul. 2011, doi: 10.1016/J.SOLMAT.2011.01.050.
 - [50] C. Ferchaud, H. Zondag, R. De Boer, and C. Rindt, "Characterization of the sorption process in thermochemical materials for seasonal solar heat storage application," pp. 1–10, 2012, Accessed: Jul. 23, 2021. [Online]. Available: www.tue.nl/taverne.
 - [51] M. Schmidt, A. Gutierrez, and M. Linder, "Thermochemical energy storage with CaO/Ca(OH)₂ – Experimental investigation of the thermal capability at low vapor pressures in a lab scale reactor," *Applied Energy*, vol. 188, pp. 672–681, Feb. 2017, doi: 10.1016/J.APENERGY.2016.11.023.
 - [52] G. Ervin, "Solar heat storage using chemical reactions," *Journal of Solid State Chemistry*, vol. 22, no. 1, pp. 51–61, Sep. 1977, doi: 10.1016/0022-4596(77)90188-8.
 - [53] P. V. Padmanabhan and M. V. Krishna Murthy, "Outward phase change in a cylindrical annulus with axial fins on the inner tube," *International Journal of Heat and Mass Transfer*, vol. 29, no. 12, pp. 1855–1868, Dec. 1986, doi: 10.1016/0017-9310(86)90004-9.
 - [54] Y. Kato, N. Yamashita, K. Kobayashi, and Y. Yoshizawa, "Kinetic study of the hydration of magnesium oxide for a chemical heat pump," *Applied Thermal Engineering*, vol. 16, no. 11, pp. 853–862, Nov. 1996, doi: 10.1016/1359-4311(96)00009-9.
 - [55] Y. Kato, F. uta Takahashi, A. Watanabe, and Y. Yoshizawa, "Thermal analysis of a magnesium oxide/water chemical heat pump for cogeneration," *Applied Thermal Engineering*, vol. 21, no. 10, pp. 1067–1081, Jul. 2001, doi: 10.1016/S1359-4311(00)00103-4.
 - [56] M. Schmidt, C. Szczukowski, C. Roßkopf, M. Linder, and A. Wörner, "Experimental results of a 10 kW high temperature thermochemical storage reactor based on calcium

- hydroxide,” *Applied Thermal Engineering*, vol. 62, no. 2, pp. 553–559, 2014, doi: 10.1016/J.APPLTHERMALENG.2013.09.020.
- [57] C. Agrafiotis, M. Roeb, M. Schmücker, and C. Sattler, “Exploitation of thermochemical cycles based on solid oxide redox systems for thermochemical storage of solar heat. Part 2: Redox oxide-coated porous ceramic structures as integrated thermochemical reactors/heat exchangers,” *Solar Energy*, vol. 114, pp. 440–458, Apr. 2015, doi: 10.1016/J.SOLENER.2014.12.036.
- [58] T. Esence, A. Bruch, S. Molina, B. Stutz, and J. F. Fourmigué, “A review on experience feedback and numerical modeling of packed-bed thermal energy storage systems,” *Solar Energy*, vol. 153, pp. 628–654, Sep. 2017, doi: 10.1016/J.SOLENER.2017.03.032.
- [59] J. Liu, J. Baeyens, Y. Deng, X. Wang, and H. Zhang, “High Temperature Mn₂O₃/Mn₃O₄ and Co₃O₄/CoO Systems for Thermo-chemical Energy Storage,” 2020.
- [60] D. Bielsa, A. Zaki, A. Faik, and P. L. Arias, “Thermochemical heat storage for CSP using Mn₂O₃/Mn₃O₄: Effects of Si doping in cyclability improvement,” *AIP Conference Proceedings*, vol. 2303, no. 1, p. 200001, Dec. 2020, doi: 10.1063/5.0028737.
- [61] S. Tescari *et al.*, “Thermochemical Solar Energy Storage Via Redox Oxides: Materials and Reactor/Heat Exchanger Concepts,” *Energy Procedia*, vol. 49, pp. 1034–1043, Jan. 2014, doi: 10.1016/J.EGYPRO.2014.03.111.
- [62] A. J. Carrillo *et al.*, “Thermochemical energy storage at high temperature via redox cycles of Mn and Co oxides: Pure oxides versus mixed ones,” *Solar Energy Materials and Solar Cells*, vol. 123, pp. 47–57, Apr. 2014, doi: 10.1016/J.SOLMAT.2013.12.018.
- [63] C. Agrafiotis, S. Tescari, M. Roeb, M. Schmücker, and C. Sattler, “Exploitation of thermochemical cycles based on solid oxide redox systems for thermochemical storage of solar heat. Part 3: Cobalt oxide monolithic porous structures as integrated thermochemical reactors/heat exchangers,” *Solar Energy*, vol. 114, pp. 459–475, Apr. 2015, doi: 10.1016/J.SOLENER.2014.12.037.
- [64] P. Pardo *et al.*, “A review on high temperature thermochemical heat energy storage A review on high temperature thermochemical heat energy storage. Renewable and Sustainable Energy Reviews, Elsevier Open Archive TOULOUSE Archive Ouverte (OATAO) A review on high temperature thermochemical heat energy storage,” *Renewable and Sustainable Energy Reviews*, vol. 32, pp. 591–610, 2014, doi: 10.1016/j.rser.2013.12.014.
- [65] G. Flamant, “Thermochimie solaire à hautes températures, résultats expérimentaux. Quelques perspectives d’application,” *Revue de Physique Appliquée*, vol. 15, no. 3, pp. 503–511, 1980, doi: 10.1051/RPHYSAP:01980001503050300.
- [66] A. J. Carrillo, D. P. Serrano, P. Pizarro, and J. M. Coronado, “Thermochemical Heat Storage at High Temperatures using Mn₂O₃/Mn₃O₄ System: Narrowing the Redox Hysteresis by Metal Co-doping,” *Energy Procedia*, vol. 73, pp. 263–271, Jun. 2015, doi: 10.1016/J.EGYPRO.2015.07.686.
- [67] T. Block and M. Schmücker, “Metal oxides for thermochemical energy storage: A comparison of several metal oxide systems,” *Solar Energy*, vol. 126, pp. 195–207, Mar. 2016, doi: 10.1016/J.SOLENER.2015.12.032.
- [68] L. André, S. Abanades, and L. Cassayre, “Mixed Metal Oxide Systems Applied to Thermochemical Storage of Solar Energy: Benefits of Secondary Metal Addition in Co and Mn Oxides and Contribution of Thermodynamics,” *Applied Sciences 2018, Vol. 8, Page 2618*, vol. 8, no. 12, p. 2618, Dec. 2018, doi: 10.3390/APP8122618.

-
- [69] Y. Portilla-Nieto *et al.*, “Development of $\text{Co}_{3-x}\text{Ni}_x\text{O}_4$ materials for thermochemical energy storage at lower red-ox temperature,” *Solar Energy Materials and Solar Cells*, vol. 230, p. 111194, Sep. 2021, doi: 10.1016/J.SOLMAT.2021.111194.
 - [70] Z. H. Pan and C. Y. Zhao, “Gas–solid thermochemical heat storage reactors for high-temperature applications,” *Energy*, vol. 130, pp. 155–173, Jul. 2017, doi: 10.1016/J.ENERGY.2017.04.102.
 - [71] N. R. Rhodes *et al.*, “Solar Thermochemical Energy Storage Through Carbonation Cycles of SrCO_3/SrO Supported on SrZrO_3 ,” *ChemSusChem*, vol. 8, no. 22, pp. 3793–3798, Nov. 2015, doi: 10.1002/CSSC.201501023.
 - [72] R. Barker, “The reactivity of calcium oxide towards carbon dioxide and its use for energy storage,” *Journal of Applied Chemistry and Biotechnology*, vol. 24, no. 4–5, pp. 221–227, Apr. 1974, doi: 10.1002/JCTB.2720240405.
 - [73] K. G. Sakellariou, G. Karagiannakis, Y. A. Criado, and A. G. Konstandopoulos, “Calcium oxide based materials for thermochemical heat storage in concentrated solar power plants,” *Solar Energy*, vol. 122, pp. 215–230, Dec. 2015, doi: 10.1016/J.SOLENER.2015.08.011.
 - [74] J. M. Criado, M. Macias, and A. Macias-Machín, “Analysis of the system $\text{CaO} \square \text{CO}_2 \square \text{H}_2\text{O}$ for storage of solar thermal energy,” *Solar Energy*, vol. 49, no. 2, pp. 83–86, Aug. 1992, doi: 10.1016/0038-092X(92)90141-V.
 - [75] D. A. Sheppard, M. Paskevicius, and C. E. Buckley, “Thermodynamics of Hydrogen Desorption from NaMgH_3 and Its Application As a Solar Heat Storage Medium,” *Chemistry of Materials*, vol. 23, no. 19, pp. 4298–4300, Oct. 2011, doi: 10.1021/CM202056S.
 - [76] Z. Homonnay *et al.*, “Molten Salt Energy Storage System for a DEMO Operated in Pulsed Mode.”
 - [77] M. Olszewski and M. Siman-Tov, “Development of encapsulated lithium hydride thermal energy storage,” *Proceedings of the Intersociety Energy Conversion Engineering Conference*, vol. 6, pp. 2903–2910, 1989, doi: 10.1109/IECEC.1989.74406.
 - [78] F. M and B. B, “High temperature metal hydrides as heat storage materials for solar and related applications,” *International journal of molecular sciences*, vol. 10, no. 1, pp. 335–344, Jan. 2009, doi: 10.3390/IJMS10010325.
 - [79] “Outokumpu HSC Chemistry ® for Windows Chemical Reaction and Equilibrium Software with Extensive Thermochemical Database.”
 - [80] V. A. Kuznetsov, “Eleventh Conference on Energy Conversion and Research on Thermoelectronic Emission in the USA,” *Soviet Atomic Energy 1977* 42:5, vol. 42, no. 5, pp. 485–487, May 1977, doi: 10.1007/BF01120082.
 - [81] B. Bogdanović, T. H. Hartwig, and B. Spliethoff, “The development, testing and optimization of energy storage materials based on the $\text{MgH}_2 \square \text{Mg}$ system,” *International Journal of Hydrogen Energy*, vol. 18, no. 7, pp. 575–589, Jul. 1993, doi: 10.1016/0360-3199(93)90178-D.
 - [82] B. Bogdanović, A. Ritter, and B. Spliethoff, “Active $\text{MgH}_2 \square \text{Mg}$ Systems for Reversible Chemical Energy Storage,” *Angewandte Chemie International Edition in English*, vol. 29, no. 3, pp. 223–234, Mar. 1990, doi: 10.1002/ANIE.199002233.
 - [83] M. Paskevicius, D. A. Sheppard, and C. E. Buckley, “Thermodynamic Changes in Mechanochemically Synthesized Magnesium Hydride Nanoparticles,” *Journal of the American Chemical Society*, vol. 132, no. 14, pp. 5077–5083, Apr. 2010, doi: 10.1021/JA908398U.
 - [84] M. Paskevicius, D. A. Sheppard, K. Williamson, and C. E. Buckley, “Metal hydride

- thermal heat storage prototype for concentrating solar thermal power,” *Energy*, vol. 88, pp. 469–477, Aug. 2015, doi: 10.1016/J.ENERGY.2015.05.068.
- [85] P. A. Ward, J. A. † Teprovich, Y. Lu, J. He, R. Zidan, and † Savannah, “High Temperature Thermal Energy Storage in the CaAl₂ System,” 2017, Accessed: Jul. 23, 2021. [Online]. Available: <http://www.elsevier.com/open-access/userlicense/1.0/>.
- [86] S. Mellouli *et al.*, “Performance analysis of a thermal energy storage system based on paired metal hydrides for concentrating solar power plants,” *Applied Thermal Engineering*, vol. 144, pp. 1017–1029, Nov. 2018, doi: 10.1016/J.APPLTHERMALENG.2018.09.014.
- [87] F. Achchaq and E. P. Del Barrio, “A proposition of peritectic structures as candidates for thermal energy storage,” in *Energy Procedia*, Dec. 2017, vol. 139, pp. 346–351, doi: 10.1016/j.egypro.2017.11.219.
- [88] A. K. Ray, D. Rakshit, and K. Ravikumar, “High-temperature latent thermal storage system for solar power: Materials, concepts, and challenges,” *Cleaner Engineering and Technology*, vol. 4, p. 100155, Oct. 2021, doi: 10.1016/J.CLET.2021.100155.
- [89] “Thermal energy storage: Technology brief,” */publications/2013/Jan/Thermal-energy-storage*, Accessed: Jul. 23, 2021. [Online]. Available: */publications/2013/Jan/Thermal-energy-storage*.

Chapter 2. Materials and characterization techniques

2.1. Materials

2.1.1. Materials and synthesis of LiOH-LiBr mixtures

In order to have a good overview of the LiOH-LiBr phase diagram, 13 compositions were selected and studied within the range of composition from 19 to 84 % mol LiOH. Each composition was analyzed by differential scanning calorimetry (DSC) and X-ray diffraction (XRD) analysis. The materials used in this study are high purity anhydrous Lithium Hydroxide (CAS 1310-65 -2, purity 98%) and Lithium Bromide (CAS 7550-35-8, purity 99+ %), provided by Acros Organics. The preparation of the samples and all the handlings were performed inside a glove box (Brown) under a protective argon atmosphere (0.1 ppm for O₂ and H₂O) to avoid air contamination. A powder mixture of 5 g was prepared for each composition by weighing a specific weight fraction of each component (LiOH and LiBr) using a Sartorius balance (± 0.1 mg). The mixtures were then homogenized by ball milling for 15 minutes using a Spex mixer mill (875 RPM) using stainless-steel vials and stainless-steel balls (3 balls of 3 mm BPR = 0.5) under mild conditions. After the intermixing by ball milling, the powder mixtures were compacted in the form of pellets using a hydraulic press applying a pressure of 3 tons for 1 minute. Using compacted powders helped handle the sample and allowed placing a higher amount of material into the small synthesis crucibles. The synthesis was carried out in a furnace using a hermetically sealed Aluminum DSC crucible (40 μ l) charged with a similar amount of material for each composition (~18 mg). In order to improve the corrosion resistance of the crucibles and avoid leakage of the salt during synthesis, by preventing the creeping phenomena, the crucibles were coated with a low surface energy material (gold) using a sputter coater which deposits a thin film of pure gold (0.4 μ m) onto their inner surface in order to increase the wetting contact angle [1]. For the synthesis, the following temperature program was used: i) a heating ramp at 10 K/min from ambient temperature up to 30 degrees above the melting temperature of the composition under investigation; ii) an isothermal step of 1 hour; iii) a cooling step up to room temperature with a cooling rate of 1.8 K/min. The cooling rate inside the furnace was measured by placing a thermocouple close to the surface of the samples. Each sample was weighed after synthesis in order to detect any weight loss due to leakage during synthesis. For all the compositions

reported in this study, no weight loss was observed, and no leakage of salt outside the crucible occurred. This preparation method avoids any possible deviation from the correct composition, ensuring reliable and accurate results when performing the further characterization of the samples.

2.1.2. Synthesis of peritectic compound $\text{Li}_4(\text{OH})_3\text{Br}$ – Reference protocol

The preparation of the samples and all the handlings were performed inside a glove box (Brown) under a protective argon atmosphere (0.1 ppm for O_2 and H_2O) to avoid air contamination. Powder mixtures of 2 g were prepared by weighing the proper weight fraction of each component (0.75 molar fraction of LiOH and 0.25 molar fraction of LiBr) using a Sartorius balance (± 0.1 mg). The mixtures were then homogenized by ball milling for 15 minutes using a Spex mixer mill (875 RPM) using stainless-steel vials and stainless-steel balls (3 balls of 3 mm BPR = 0.5) under mild conditions. After the intermixing by ball milling, the powder mixtures were poured inside corundum crucibles and placed inside Stainless Steel reactor then sealed under Argon atmosphere. The synthesis was carried out in a muffle furnace according to the following temperature program: i) Heating step at $10^\circ\text{C}/\text{min}$ from ambient temperature up to 30°C above the melting temperature of $\text{Li}_4(\text{OH})_3\text{Br}$; ii) an isothermal step of 1 hour; iii) a free cooling inside the furnace up to room temperature ($\sim 1.8^\circ\text{C}/\text{min}$).

2.1.3. Synthesis of peritectic compound $\text{Li}_4(\text{OH})_3\text{Br}$ –Modified reference protocol

With the aim to investigate the influence of the cooling rate on the final TES performance of $\text{Li}_4(\text{OH})_3\text{Br}$, different samples were prepared by changing the cooling rate of the samples during the synthesis process. The cooling rates tested were 0.5, 1, 1.8 and $50^\circ\text{C}/\text{min}$. Moreover, the possibility of simplifying the synthesis protocol by working under air atmosphere instead of using a protective argon atmosphere was also investigated. Therefore, a sample (2 g approx.) was prepared to modify the reference protocol to this respect. Powder mixture homogenization by ball milling, pellet preparation, and thermal treatment in the oven were carried out under air. Only the first step in which LiOH and LiBr are weighted and mixed in the right proportion was performed inside the glove box under argon atmosphere to avoid LiBr hydration and, therefore, errors in the weighting process.

2.1.4. Synthesis of $\text{Li}_4(\text{OH})_3\text{Br}$ /Carbon composites

Three different types of carbon nanoparticles, already used to enhance thermophysical properties of high-temperature phase change materials [2]–[7], were chosen for this study. They are *i*) reduced graphene oxide (rGO) provided by Graphenea (CAS 7782-42-5, S.ABET:422-499 m^2/g), *ii*) fullerenes C60 provided by Sigma Aldrich (CAS 99685-96-8, purity 98%), and *iii*) multi-walled carbon nanotubes (MWCNTs) provided by Alfa Aesar (CAS 308068-56-6, length 0.5-2 μm , outer diameter $\leq 8\text{nm}$, and inner diameter 2-5 nm). $\text{Li}_4(\text{OH})_3\text{Br}$ /carbon composites were prepared by incorporating carbon nanoparticles in the $\text{Li}_4(\text{OH})_3\text{Br}$ in powder form at different loadings (1 wt. % and 10 wt. % of carbon nanoparticles). The mixture is then physically shacked to ensure homogeneity and melted at 350 °C in an inert atmosphere.

2.1.5. Synthesis of $\text{Li}_4(\text{OH})_3\text{Br}$ based shape stabilized composites

2.1.5.1. Supporting materials for shape stabilization

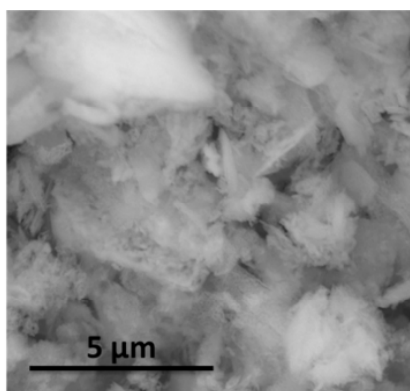
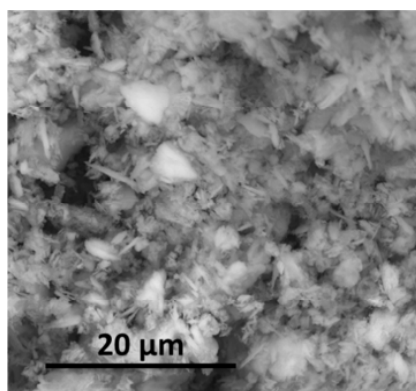
As supporting material for shape stabilization, several commercial oxides have been tested with different particle size (Nano/Micro-particles). General information about the tested materials are presented in table 2.1.

Table 2.1. General information about the tested oxides.

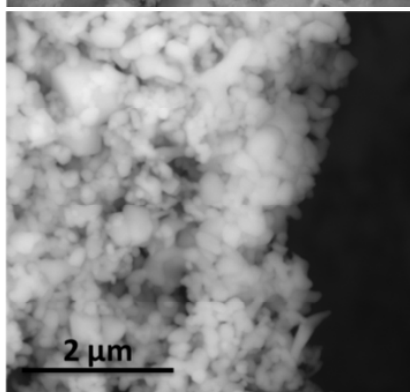
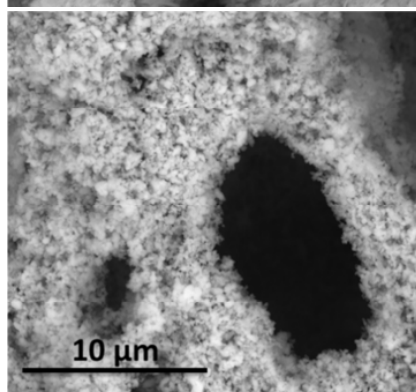
Material	MgO	Fe_2O_3	CuO	SiO_2	Al_2O_3
Supplier	Alfa Aesar	Sigma Aldrich	Alfa Aesar	Sigma Aldrich	Sigma Aldrich
CAS number	1309-48-4	1309-37-1	1317-38-0	7631-86-9	1344-28-1
Purity (%)	99+ %	$\geq 99\%$	99.7 %	$> 95\%$	
Particle size	100 nm	$< 5\ \mu\text{m}$	$< 74\ \mu\text{m}$	12 nm	13 nm
$\rho\ (\text{g}/\text{cm}^3)$	3.58	5.12	6.315	2.2-2.6	3.95

Particles size and morphology of the oxide supporting materials (MgO, Fe_2O_3 , CuO, Al_2O_3 , and SiO_2) were studied by analyzing SEM images of the samples using ImageJ 2.0 software [8]. As can be seen in Figure 2.1, Al_2O_3 and SiO_2 nanopowders formed spherical clusters with well-distributed cluster sizes (Figures 2.1d and 2.1e, respectively); the particle size provided by the supplier was considered in the study. In the case of MgO nanopowder, Figure 2.1a shows crystal agglomerates of MgO with crystal size less than 1 μm . Fe_2O_3 presented spherical powder with uniform distribution of the particle size ($< 13\ \mu\text{m}$).

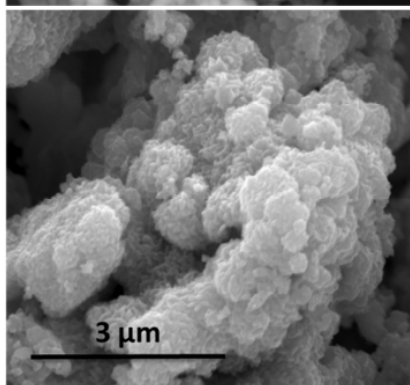
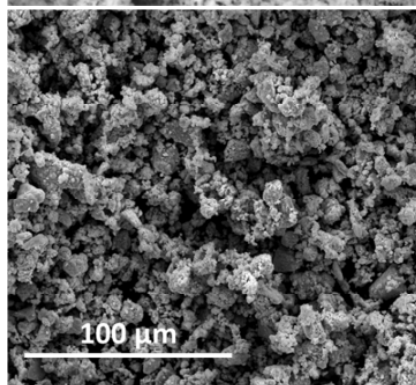
(a)



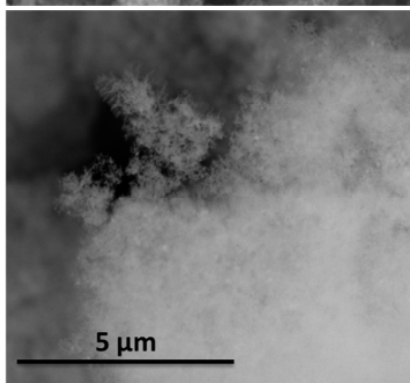
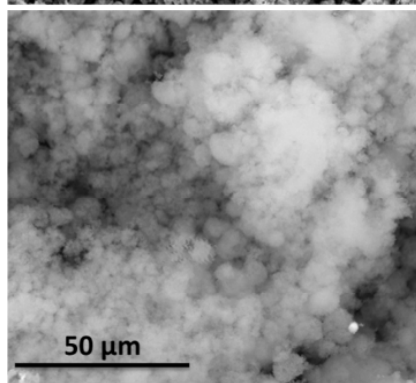
(b)



(c)



(d)



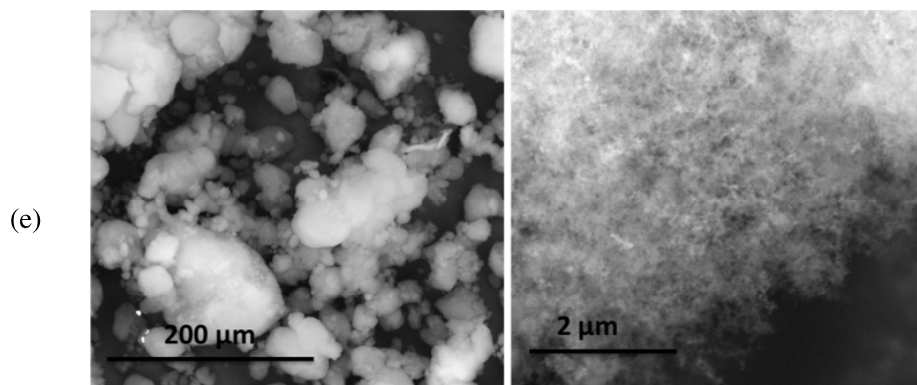


Figure 2.1. SEM images of the tested oxides: (a) MgO; (b) Fe₂O₃; (c) CuO; (d) Al₂O₃; (e) SiO₂.

2.1.5.2. Synthesis of MgO supporting material

Three different Magnesium oxide samples with different structural, textural and morphological properties were tested as supporting materials. The samples were synthesized following different synthesis routes:

- Porous MgO, named PMgO, was synthesized by combustion using Magnesium nitrate (CAS 13446-18-9, ALDRICH), ethylene glycol (CAS 107-21-1, purity 99.8%, SIGMA ALDRICH), and deionized water. 1.28 g of Mg(NO₃)₂ was mixed with 4 mL solution of ethylene glycol and deionized water with a volume ratio of 1:1. The solution was then stirred for 30 min and calcined in a muffle furnace at 600 °C for 2 hours following a heating rate of 2 K/min [9].
- MgO-BMC was synthesized by calcination [10] of basic magnesium carbonate (MgCO₃, CAS 39409-82-0, Sigma-Aldrich) at 400 °C for 2 hours following a heating rate of 2 K/min.
- Nanocrystalline MgO named MgO-BM obtained by the ball-milling process of commercial MgO (CAS 1309-48-4, purity 95 %, particle size [44-105 μm], Alfa Aesar). MgO was subjected to mechanical ball milling for specific time periods (4h, 8h, 16h, 32h, 64h). Spex mixer mill (875 RPM) was used for ball milling using a stainless steel vial and one stainless steel ball of 14 mm diameter with a ball to powder ratio (BPR) of 2:1.

All chemicals used for the synthesis of MgO samples were used as received without further purification.

2.1.5.3. Preparation of Li₄(OH)₃Br based shape stabilized composites

Li₄(OH)₃Br based ss-composites were prepared by uniaxial cold compression route. The storage material Li₄(OH)₃Br was initially grounded and sifted by a 200 μm sieve. Then it was

mixed with the oxide according to specific mass ratios to obtain a total mass of 1 g of composite. The powder mixture was then physically mixed for 20 minutes, using a ball milling (Spex mixer mill 875 RPM) without balls. The purpose of the physical mixing is to ensure the homogeneity of the mixture oxide/salt. Finally, a pellet of 13 mm diameter was made by cold compression of the powder mixture under a pressure of 5 tons for 1 minute. The pellet was then placed in a corundum crucible inside a closed stainless steel reactor under Ar atmosphere and sintered in a muffle furnace over the melting temperature of the salt according to the following temperature program: a first heating step at 10 K/min up to 350 °C, followed by an isothermal step at 350 °C for 1 hour and finally the sample was cooled down to room temperature at around 2 K/min cooling rate. Figure 2.2 demonstrates the preparation steps of $\text{Li}_4(\text{OH})_3\text{Br}$ -based shape stabilized composites

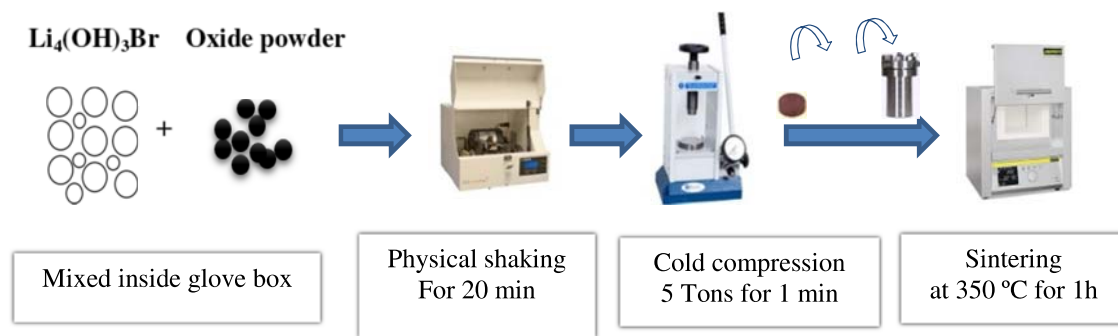


Figure 2.2 Schematic represents the preparation process of shape stabilized composite.

2.1.6. Corrosion test protocol

Table 2.1. Chemical composition of the studied steel samples.

Material	Wt. %								
	Fe	C	Mn	P	S	Cr	Ni	Mo	Si
Carbon steel A516.Gr70	98.28	0.31	0.97	0.04	0.04	-	-	-	0.36
Stainless steel AISI 316	68.41	0.08	0.65	0.05	0.03	17.56	10.45	2.4	0.37

Cycling corrosion tests were carried out in order to evaluate the corrosion resistance of potential container materials used in CSP plants in contact with the studied peritectic compound ($\text{Li}_4(\text{OH})_3\text{Br}$). Two different steel samples were tested in this study, carbon steel A516.Gr70 and stainless steel 316 with dimensions 20 mm X 10 mm X 3 mm. The chemical composition of the tested materials is presented in table 2.2. Steel samples were polished prior

to the corrosion test in order to remove any oxide layer or impurities present in the surfaces (abrasive paper of 400; 600; 800; 1200; 2500). They were then cleaned in an ultrasonic bath with acetone, ethanol, and distilled water.

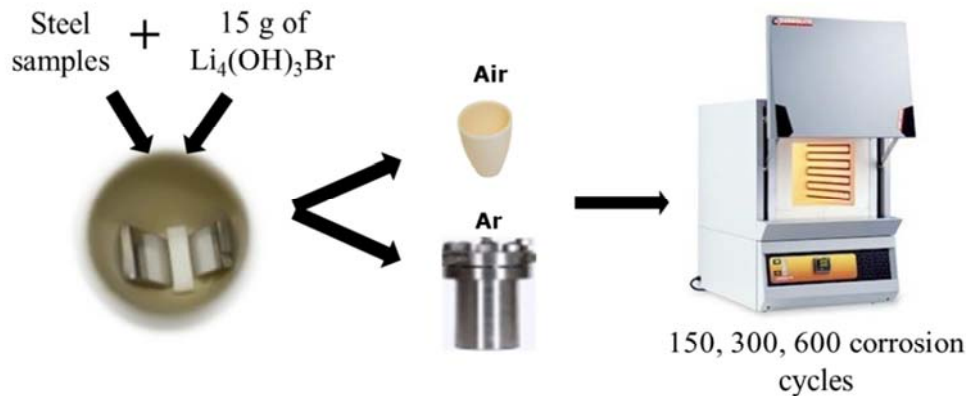


Figure 2.3. Schematic represents the corrosion test protocol

For each steel type, two samples of the same steel were placed inside a corundum crucible and separated by a piece of alumina to avoid their contact. The crucible was then completely filled with $\text{Li}_4(\text{OH})_3\text{Br}$ salt (15 g) in order to ensure the total immersion of the samples. In order to study the effect of the atmosphere on the corrosion behavior of the steel and the stability of the salt, cycling corrosion tests were carried out under two different atmospheres, Air and Ar. In case of the corrosion tests carried out under Argon atmosphere, the Corundum crucible, containing the steel samples, were placed inside stainless steel reactors and sealed under Ar inside the glove box. Corrosion tests were conducted for three different cycle numbers (150 cycles, 300 cycles, and 600 cycles) in order to investigate the evolution of the corrosion upon thermal cycling. The applied corrosion protocol is depicted in figure 2.3. The tests were conducted inside the furnace following the temperature protocol depicted in figure 2.4. The cycling was performed between 250 °C and 350 °C. After the test, steel samples were extracted from the salt (in solid-state) and then washed carefully with distilled water to remove any residue of salt.

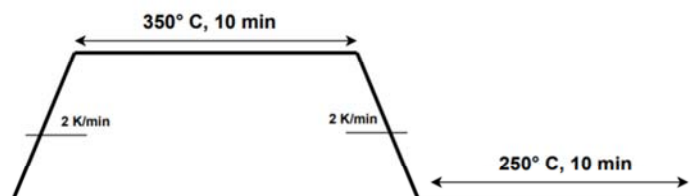


Figure 2.4. Temperature program applied for cycling corrosion test

In order to estimate the corrosion rate, the weight of the steel samples was measured prior to and after the corrosion, test using a Mettler Toledo high precision balance (± 0.001 mg). For Cross-section analysis using SEM + EDS, the samples were prepared as explained in figure 2.5. The resin used is a mixture of 1 ml Aka-Resin and 0.1 ml of Aka-Cure catalyst. The sample embedded inside the resin was cut and polished (abrasive paper of 400; 600; 800; 1200; 2500). This preparation method helps avoid the deterioration or detachment of the corrosion layer from the steel samples giving a more accurate estimation of the thickness of the corrosion layer.

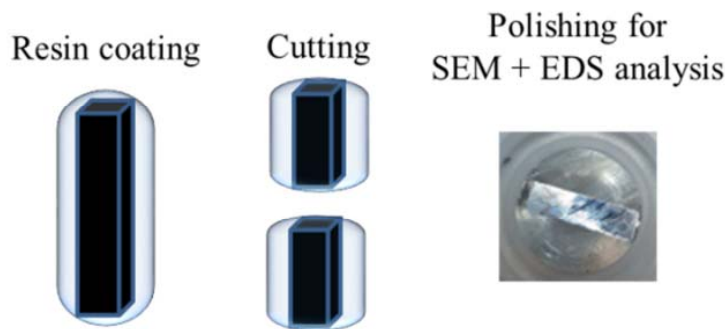


Figure 2.5. Sample preparation for SEM+EDS cross-section analysis

2.2. Characterization techniques

This section is divided into two parts. The first part presents the morphological and structural characterization techniques used in this work, including XRD, SEM, EDS, TEM, gas pycnometer, and BET. The second part presents the thermophysical characterization techniques including DSC and Transient hot disk. The acronyms will be spelled out in the following sections.

2.2.1. Morphological and structural characterization

2.2.1.1. X-ray powder diffraction (XRD)

XRD is the most widely used technique for identifying crystalline phases and cell parameters of crystalline materials. Diffraction patterns are generated from the interaction between the electromagnetic radiations (i.e., X-ray) and the atoms of the crystalline materials.

The X-ray diffractometer functions as follows; first, the X-ray radiations are generated by the X-ray tube. Monochromatic X-rays required for diffraction analysis are then obtained by the monochromator filter. The most used monochromatic radiation in modern powder X-ray diffractometers is Cu $K\alpha$, with a wavelength of 1.5418 \AA . The radiation is then concentrated and targeted toward the sample by collimation [11]. Through the rotation of the sample

holder, the incident radiations are diffracted and reflected by the sample. They are then recorded by a detector and presented in form of diffraction peaks if they satisfy the Bragg law ($n\lambda = 2d \sin\theta$), where n is a positive integer determined by the diffraction order, λ is the wavelength of the X-ray radiation, θ is the incidence angle, and d is the interplanar distance [12]. The diffraction pattern shows the intensity of the generated peaks vs. 2θ ($^\circ$) providing qualitative and quantitative information of the structure-phase and its crystallinity, among other parameters.

In this thesis, XRD measurements were performed by means of a Bruker D8 Discover X-ray diffractometer equipped with a LYNXEYE detector with monochromatic Cu $K\alpha_1$ radiation of $\lambda = 1.54056 \text{ \AA}$. Patterns were recorded at room temperature, in a 2θ angular range ($10 - 120^\circ$), with a step size of 0.02° and a step time of 2 s. A special sample holder was used for powdered air sensitive samples. The structural evolution upon heating was studied by in-situ XRD measurements by using a Bruker Advance D8 instrument with cobalt radiation ($\lambda_{Co\alpha_1} = 1.78886 \text{ \AA}$ / $\lambda_{Co\alpha_2} = 1.79277 \text{ \AA}$). The equipment operated in Bragg-Brentano theta-theta geometry and with an operating power of 30 kV and 50 mA. The samples were placed in a nickel coated high-vacuum chamber designed for use in the range from room temperature up to 1200°C (HTK 1200N) under a high vacuum, inert and reactive atmosphere. The sample was mounted on an alumina sample holder in contact with the temperature sensor. The measurements were carried out under a controlled atmosphere. The obtained diffractograms were analyzed using EVA software to determine the phase compositions and structures of the materials. Additionally, information about the phases formed and their relative percentages, the crystallite sizes, and the microstrain level were obtained by refinement of the diffraction patterns using a full profile fitting procedure [13], [14] based on the Rietveld method [15].

2.2.1.2. Scanning electron microscopy (SEM)

SEM is a characterization technique that allows obtaining microstructural and morphological characteristics of a material. High resolution images are obtained by scanning the sample's surface with a focused beam of accelerated electrons. The interaction of the primary electron beam with the sample surface result in the emission of photons or electrons which are collected by specialized detectors. The collected signals provide information about the morphology, topography, and chemical composition of the sample.

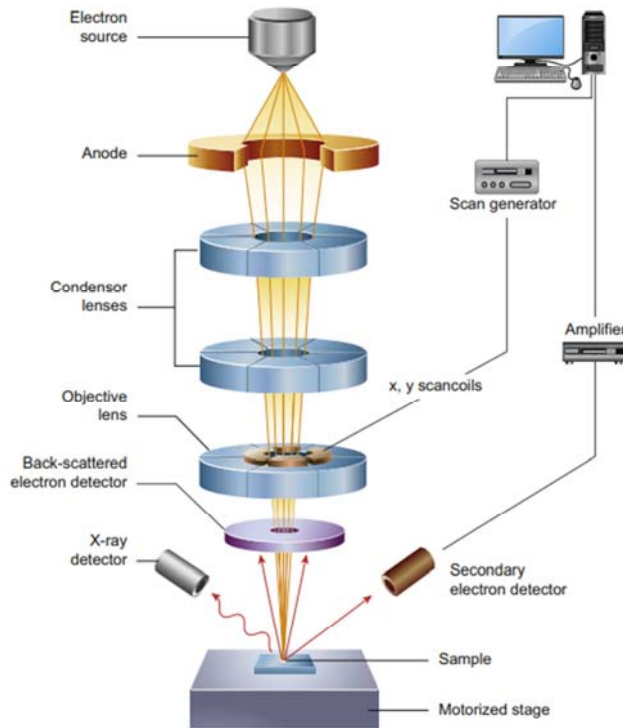


Figure 2.6. Scheme of the core component of SEM microscope. [16]

As shown in Figure 2.6, the electron beam is generated by the electron source (most commonly tungsten filament). It is then focused by the condenser lenses (spot size diameter 0.4–5 nm). The focused beam is deflected by the objective lens in x and y directions. Finally, the deflected beam scans the sample surface in a rectangular zone to produce high resolution images. The electron column serves to prevent contamination and external noises, which increases the resolution of the image. The interaction between the electron beam and the sample results in the emission of secondary electrons (SE) through an inelastic scattering. The latter are produced by energy transmission from the electron to the nucleus of a surface atom allowing this one to jump out of the structure. SE provides topographical information of the sample at very high resolution (less than 1 nm). Excess energy is emitted in form of X-ray characteristic of each element when a SE is diffracted, and a deeper electron jumps to fill its gap. These X-rays can be used for elemental analysis by means of EDS. Back-scattered electrons (BSE) are high energy electrons reflected from the sample by elastic scattering through collisions between the electrons and the atom nucleus. The resolution achieved by BSE (5–10 nm) is low compared to SE because the electrons are extracted from deeper locations than SE. Moreover, the intensity of the BSE is proportional to the atomic number of

the material; consequently, they provide different contrast pattern depends on the composition as well as information about the distribution of different elements in the sample.

In this thesis, the morphology of the materials was studied by a Field Emission Gun Quantum 200 (FEI) SEM operated in high vacuum mode at 30 kV. The micrographs were obtained using the back-scattered electron detector (BSE) and secondary electron detector (ETD). The voltage of the electron beam in this microscope range from 0.2-40 kV, and the maximum resolution is 1-5 nm.

2.2.1.3. Energy dispersive X-ray spectroscopy (EDS)

Energy-dispersive X-ray spectroscopy (EDX or EDS) is a characterization technique that enables the identification and quantification of the chemical composition of a material, as well as the elemental composition mapping. The interaction between the electron beam results in the emission of SE. Consequently, electrons jump from a higher energy state to a lower energy state in order to fill the resulting electron vacancies releasing the difference in energy as an X-ray characteristic of its atom of origin. This allows the identification of the chemical composition of a sample. Same settings as in the SEM were used for the data acquisition in this work.

2.2.1.4. Transmission electron microscopy (TEM)

TEM is a microscopy technique that allows obtaining high resolutions images in the nanoscale range. This technique provides information about the morphology of the sample, crystallization, chemical composition, and even magnetic domains. TEM functions following the basic principle of an optical microscope. However, instead of using visible light, high energy electrons are used. As shown in Figure 2.7, a high energy electron beam (accelerate at ~300 kV) is generated by the electron source (most commonly tungsten filament or lanthanum hexaboride LaB6) [17]. It is then focused on the sample by condenser lenses. The image acquisition is achieved in a phosphorescent screen or charge-coupled device (CCD) camera with the aid of the objective lens and projector lenses, which helps to focus the electron beam through the sample. The magnification of TEM varies from 100X to more than 1000.000X.

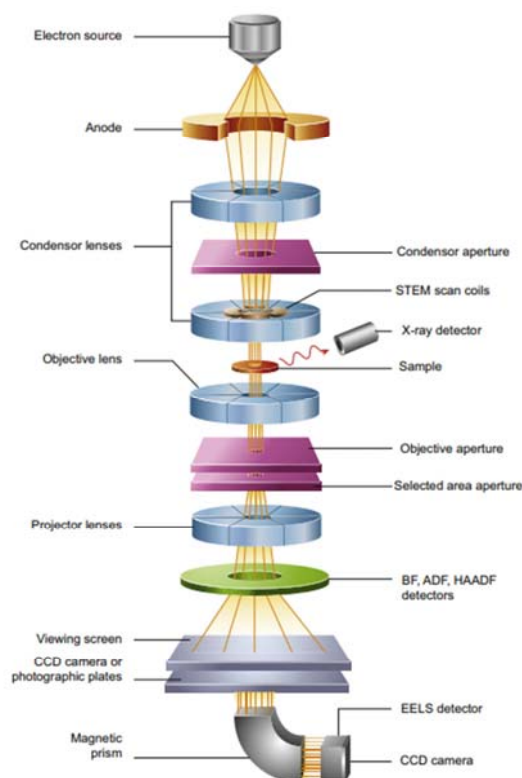


Figure 2.7. Scheme of the core component of TEM microscope. [16]

In this thesis, TEM analysis was performed on Field Emission Gun (FEG) high resolution TEM/STEM, FEI - Tecnai G2 F20 S-TWIN. The used acceleration voltage during image acquisition was 200 kV, and a spot size value of 3 was chosen. Energy Dispersive X-Ray Spectroscopy (EDS) was used for elemental analysis. For sample preparation, solid grid deposition was performed onto a holey carbon film copper grid.

2.2.1.5. Brunauer-Emmett-Teller Analysis (BET)

Gas adsorption/desorption is a widely used characterization technique that enables to determine the specific surface area (SSA) and pore size distribution (PSD) from the adsorption-desorption isotherms [18], [19]. The most widely used gas is Nitrogen adsorption at -195.8°C thanks to its weak interaction with most solids. Thus, it can cover a wide range of pore sizes. However, when the pore size is lower than 1 nm, CO_2 should be used as absorbed gas instead of N_2 because it has a smaller molecules size (2.8 \AA) compared to N_2 (4 \AA) [20]. The SSA is calculated by the physisorption of the gas molecules on the surface of the material. In this thesis, all the samples were characterized by N_2 adsorption/desorption using a Micromeritics ASAP 2460 automated gas adsorption instrument. Nitrogen sorption isotherms of the samples were measured after outgassing of the samples at 250°C under

vacuum for 12 hours. The adsorption isotherm is transformed to a BET plot following the BET equation:

$$\frac{\rho/\rho^\circ}{n(1-\rho/\rho^\circ)} = \frac{1}{nmC} + \frac{C-1}{nmC}(\rho/\rho^\circ) \quad (\text{eq. 2.1})$$

The BET surface area is then calculated from the monolayer capacity following the equation:

$$a_s (BET) = n_m L \sigma_m / m \quad (\text{eq. 2.2})$$

n is the specific amount adsorbed at the relative pressure ρ/ρ°

n_m is the specific monolayer capacity

C is a parameter related to the energy of monolayer adsorption.

L is the Avogadro number

m is the adsorbent (sample) mass.

σ_m is the molecular cross-sectional area occupied by the adsorbate molecule in the monolayer

The Non-Local Density Functional Theory (NLDFT) is a widely implemented model in commercial software that allows having more accurate measurements of the PDS and the SSA by the correlation of an experimental adsorption isotherm with the core of a theoretical adsorption or desorption isotherms. In this thesis, 2D-NLDFT model developed by Jacek Jagiello was used to calculate the SSA and PSD of the samples from the adsorption isotherms using the data reduction software SAIEUS [21].

2.2.1.7. Gas pycnometry

Gas pycnometry technique allows measuring the density and volume of materials based on the Boyle's law, by displacement of gas molecules by a known mass of a sample [22]. An inert gas (Helium / Nitrogen) is used as a displacement medium. Initially, the sealed chamber of the apparatus containing the sample is filled with the inert gas, which will be expanded into a secondary chamber. The density is calculated following the equation:

$$p_1 \cdot V_1 = p_2 \cdot V_2 \quad (\text{eq. 2.3})$$

p_1 and V_1 are the pressure and the gas volume respectively in the measurement chamber containing the sample. p_2 and V_2 are the pressure and the volume of the secondary chamber, respectively.

In this thesis, The skeletal density of the peritectic salt $\text{Li}_4(\text{OH})_3\text{Br}$ was measured at room temperature using helium pycnometer AccuPyc II 1340 instrument from Micromeritics. For the accuracy of the results, 10 measurements for a cylindrical pellet of about 0.25 cm^3 were carried out in a 3 cm^3 cell volume consecutively. The average value was considered as the final density.

2.2.2. Thermophysical characterization

2.2.2.1. Differential scanning calorimetry (DSC)

Differential scanning calorimetry is a characterization technique that enables to measure the thermal and thermodynamic properties of a material during the phase changes it undergoes, such as the transition temperature, the transition enthalpy, and the specific heat capacity. In a heat-flux DSC, the differential heat flow of the material and the reference is measured following the equation:

$$q = -\frac{\Delta T}{R_r} + \Delta T_o \frac{R_r - R_s}{R_r R_s} + (C_r - C_s) \frac{dT_s}{dt} - C_r \frac{d\Delta T}{dt} \quad (\text{eq 2.4})$$

ΔT and ΔT_o are the temperature difference between the sample and the reference and between the sensor and the sample, respectively.

ΔT_o is the temperature control of the sensor. R_r and C_r are the sensor thermal resistance and the sensor heat capacity of the reference, respectively. R_s and C_s are the sensor thermal resistance and the sensor heat capacity of the sample, respectively.

In this thesis, the temperature and enthalpy of the phase transitions or reactions during heating and cooling of the studied materials were determined using a DSC 2500 model. The temperature and enthalpy were calibrated using Sapphire and Indium standards. Argon was used as a purge gas (50mL/min). The accuracy is estimated to be $\pm 1 \text{ K}$ for the transition temperatures and $\pm 3 \text{ J/g}$ for the enthalpies. The sample weight was approximately 18-20 mg. The temperature protocol applying for DSC analysis is the following: i) a heating step of $1 \text{ }^\circ\text{C/min}$ up to $30 \text{ }^\circ\text{C}$ above the melting point of the sample; ii) an isothermal step of 10 minutes; iii) a cooling step at $10 \text{ }^\circ\text{C/min}$ up to room temperature. Sapphire was measured to validate the accuracy before each measurement (error $< 2 \%$). Due to the corrosive nature of the mixture and to avoid any risk of salt leakage during the analysis, only one heating/cooling cycle was applied. It is noteworthy that the good contact between the sample and the crucible was already ensured by a heating/cooling cycle applied in the furnace prior to the DSC analysis. To check the repeatability of the results, three different samples are tested each time.

The phase transition temperatures of isothermal processes were considered as the onset temperature of corresponding endothermic peaks, whereas endset temperatures were used to estimate the temperatures of the liquidus. The enthalpies corresponding to the different transitions were calculated by peaks integration in the heating run.

The specific heat of the peritectic compound $\text{Li}_4(\text{OH})_3\text{Br}$ was measured using the Differential Scanning Calorimetry (TA DSC 2500 model) in direct mode (one single scan measurement) with a heating rate of 1 K/min in the temperature range from 200 °C to 320 °C. Samples of approximately 20 mg were prepared under Argon atmosphere using hermetically sealed Aluminium DSC pans. Before each measurement, the DSC was calibrated using sapphire (according to DIN 51007) in the same temperature range. The uncertainty in specific heat measurements is estimated to be less than 4 %.

2.2.2.2. Transient Plane Source (TPS) Hot Disk technique

The transient hot disk method [29] was used to measure the thermal conductivity of $\text{Li}_4(\text{OH})_3\text{Br}$ at room temperature on a cylindrical-shaped sample (diameter: ca. 13 mm, thickness: ca. 3 mm). The sample was prepared by pressing the peritectic powders in a hydraulic press at 5 tons for 30 seconds. To avoid hydration of the sample, the measurements were carried out in a chamber with a constant flow of nitrogen. A TPS 2500 S instrument equipped with a Kapton sensor of 2 mm in diameter (sensor type 7577) was employed for the measurements. According to the recommendations of Rides et al. [30] and ISO 22007-2:2015 [31], the power applied to the sample was 20 mW during 5 s. To check the reproducibility and quality of the results, several tests have been performed on the same sample using different measuring times (5 to 10 s) and time frames for parameters estimation. The recorded data were processed using the Hot Disk Software (version 7.4.0.10).

2.3. References

- [1] Y. Grosu, L. González-Fernández, U. Nithiyantham, and A. Faik, “Wettability Control for Correct Thermophysical Properties Determination of Molten Salts and Their Nanofluids,” *Energies*, vol. 12, no. 19, p. 3765, Oct. 2019, doi: 10.3390/en12193765.
- [2] Z. Zhang, Y. Yuan, S. Alelyani, X. Cao, and P. E. Phelan, “Thermophysical properties enhancement of ternary carbonates with carbon materials for high-temperature thermal energy storage,” *Solar Energy*, vol. 155, pp. 661–669, Oct. 2017, doi: 10.1016/j.solener.2017.07.010.
- [3] Y. B. Tao, C. H. Lin, and Y. L. He, “Preparation and thermal properties characterization of carbonate salt/carbon nanomaterial composite phase change

- material,” *Energy Conversion and Management*, vol. 97, pp. 103–110, Jun. 2015, doi: 10.1016/j.enconman.2015.03.051.
- [4] F. Ye, Z. Ge, Y. Ding, and J. Yang, “Multi-walled carbon nanotubes added to Na₂CO₃/MgO composites for thermal energy storage,” *Particuology*, vol. 15, pp. 56–60, Aug. 2014, doi: 10.1016/j.partic.2013.05.001.
- [5] Y. Wu, J. Li, M. Wang, H. Wang, and Y. Zhao, “Preparation and Thermophysical Properties of High Thermal Conductive Solar Salt/MWCNTs Composite Materials,” *ChemistrySelect*, vol. 4, no. 15, pp. 4521–4527, Apr. 2019, doi: 10.1002/slct.201900249.
- [6] Y. Wu *et al.*, “Solar salt doped by MWCNTs as a promising high thermal conductivity material for CSP,” *RSC Advances*, vol. 8, no. 34, pp. 19251–19260, 2018, doi: 10.1039/c8ra03019g.
- [7] E. Hamdy, L. Saad, F. Abulfotuh, M. Soliman, and S. Ebrahim, “Enhancement of Molten Nitrate Thermal Properties by Reduced Graphene Oxide and Graphene Quantum Dots,” *ACS Omega*, vol. 5, no. 34, pp. 21345–21354, Sep. 2020, doi: 10.1021/acsomega.0c01291.
- [8] C. T. Rueden *et al.*, “ImageJ2: ImageJ for the next generation of scientific image data,” *BMC Bioinformatics*, vol. 18, no. 1, p. 529, Nov. 2017, doi: 10.1186/s12859-017-1934-z.
- [9] S. Li, “Combustion synthesis of porous MgO and its adsorption properties,” *International Journal of Industrial Chemistry*, vol. 10, no. 1, pp. 89–96, Mar. 2019, doi: 10.1007/s40090-019-0174-7.
- [10] Y. D. Ding, G. Song, X. Zhu, R. Chen, and Q. Liao, “Synthesizing MgO with a high specific surface for carbon dioxide adsorption,” *RSC Advances*, vol. 5, no. 39, pp. 30929–30935, 2015, doi: 10.1039/c4ra15127e.
- [11] H. M. Rietveld, “A profile refinement method for nuclear and magnetic structures,” *Journal of Applied Crystallography*, vol. 2, no. 2, pp. 65–71, Jun. 1969, doi: 10.1107/s0021889869006558.
- [12] W. H. Bragg, “The reflection of X-rays by crystals [3],” *Nature*, vol. 91, no. 2280, Nature Publishing Group, p. 477, 1913, doi: 10.1038/091477b0.
- [13] L. Lutterotti and S. Gialanella, “X-ray diffraction characterization of heavily deformed metallic specimens,” *Acta Materialia*, vol. 46, no. 1, pp. 101–110, Dec. 1998, doi: 10.1016/S1359-6454(97)00222-X.
- [14] J. Rodríguez-Carvajal, “Recent advances in magnetic structure determination by neutron powder diffraction,” *Physica B: Physics of Condensed Matter*, vol. 192, no. 1–2, pp. 55–69, Oct. 1993, doi: 10.1016/0921-4526(93)90108-I.
- [15] H. M. Rietveld, “A profile refinement method for nuclear and magnetic structures,” *Journal of Applied Crystallography*, vol. 2, no. 2, pp. 65–71, Jun. 1969, doi: 10.1107/s0021889869006558.

-
- [16] B. J. Inkson, "Scanning Electron Microscopy (SEM) and Transmission Electron Microscopy (TEM) for Materials Characterization," in *Materials Characterization Using Nondestructive Evaluation (NDE) Methods*, Elsevier Inc., 2016, pp. 17–43.
- [17] C. Y. Tang and Z. Yang, "Transmission Electron Microscopy (TEM)," in *Membrane Characterization*, Elsevier Inc., 2017, pp. 145–159.
- [18] M. Thommes *et al.*, "Physisorption of gases, with special reference to the evaluation of surface area and pore size distribution (IUPAC Technical Report)," *Pure and Applied Chemistry*, vol. 87, no. 9–10, pp. 1051–1069, Oct. 2015, doi: 10.1515/pac-2014-1117.
- [19] K. S. W. Sing *et al.*, "Reporting Physisorption Data for Gas/Solid Systems with Special Reference to the Determination of Surface Area and Porosity," *Pure and Applied Chemistry*, vol. 57, no. 4, pp. 603–619, Jan. 1985, doi: 10.1351/pac198557040603.
- [20] J. Garrido, A. Linares-solano, J. M. Martìn-Martínez, M. Molina-Sabio, F. Rodríguez-Reinoso, and R. Torregrosa, "Use of N₂ vs : CO₂ in the Characterization of Activated Carbons," *Langmuir*, vol. 3, no. 1, pp. 76–81, Jan. 1987, doi: 10.1021/la00073a013.
- [21] J. Jagiello and J. P. Olivier, "2D-NLDFT adsorption models for carbon slit-shaped pores with surface energetical heterogeneity and geometrical corrugation," *Carbon*, vol. 55, pp. 70–80, Apr. 2013, doi: 10.1016/j.carbon.2012.12.011.
- [22] J. B. West, "Robert Boyle's landmark book of 1660 with the first experiments on rarified air," *Journal of Applied Physiology*, vol. 98, no. 1. J Appl Physiol (1985), pp. 31–39, Jan. 2005, doi: 10.1152/jappphysiol.00759.2004.

Chapter 3. Study of the binary system LiOH-LiBr

3.1. Introduction

FactSage software [1] was used by Achchaq et al. [2] for an extensive search and selection of stoichiometric peritectic structures providing energy density above 200 kWh/m³ in the range of temperatures from 300 °C to 700 °C. Out of 635 binary systems analyzed, 145 have shown at least one peritectic structure satisfying those requirements.

At around 300 °C, the peritectic structure Li₄(OH)₃Br appearing in the LiOH-LiBr binary system stands out. According to the calculations carried out, Li₄(OH)₃Br forms at 304 °C, and the theoretical transition enthalpy is as high as 804 J/g (425 kWh/m³) for the stoichiometric composition (0.75 molar fraction of LiOH). These features make Li₄(OH)₃Br a very appealing candidate for TES applications, more specifically for Direct Steam Generation CSP technology working at c.a. 100 bar [3], [4]. It is worth noting that the reference phase change material used for this application is NaNO₃ which melts at 306 °C with an enthalpy of melting of 177 J/g [5]–[7], meaning that Li₄(OH)₃Br has potentially the capacity of reducing the storage volume by almost 5 times. However, in recent experimental work of Achchaq et al. [8], the measured enthalpy of transition for a LiOH-LiBr mixture at 0.75 molar fraction of LiOH is only 170 J/g instead of 804 J/g. There are three different reasons that could explain this significant difference.

1. Achchaq et al. indicate that significant leakage has been observed during Differential Scanning Calorimetry tests, which could partly explain the low value of enthalpy reported.
2. The second reason relates to the mechanism of formation of peritectic structures, where two steps, named peritectic reaction and peritectic transformation, can be distinguished. On cooling, during the peritectic reaction step, the peritectic phase Li₄(OH)₃Br nucleates on the surface of the pro-peritectic phase LiOH(s) and grows through the reaction $\text{LiOH(s)} + \text{Liquid} \rightarrow \text{Li}_4(\text{OH})_3\text{Br}$ forming a peritectic layer that isolates the pro-peritectic phase from the liquid. This step is very fast and takes place at constant temperature. During the so-called peritectic transformation, the growing of

the peritectic layer occurs at the interfaces pro-peritectic/peritectic. This step is characterized by the migration (diffusion) of the atoms from the liquid phase through the peritectic layer up to reach the unreacted LiOH, which is usually a sluggish process that can result in the incomplete conversion of the reactants into the final reaction product $\text{Li}_4(\text{OH})_3\text{Br}$.

3. Last but not least, the reliability of FactSage calculations can be questioned. Indeed, the LiOH-LiBr phase diagram implemented in FactSage is the one proposed by Sangster [9] using the experimental data of Scarpa [10] and Hartwig et al. [12]. As discussed later, there are significant differences between both sets of experimental data regarding not only transition temperature values but also the number of phases present in the LiOH-LiBr system. According to Sangster, the uncertainty in the proposed phase diagram is about 20 °C, which is very high.

This chapter aims to elucidate whether $\text{Li}_4(\text{OH})_3\text{Br}$ can be considered as a candidate for compact TES. To this end, Differential Scanning Calorimetry (DSC) and X-ray analysis are employed to establish the LiOH-LiBr phase diagram while providing reliable information about enthalpy and products of the reactions or phase transitions taking place. The results obtained show significant discrepancies with Sangster's proposal, and a modified phase diagram for the LiOH-LiBr system is depicted in accordance with our observations. It is also shown that, whatever the transition considered, measured enthalpies are much lower than those calculated with FactSage software. Contrary to the case of Achchaq et al., no leakage was observed during DSC tests so as the confidence in enthalpy measurements is high.

Moreover, X-ray analysis indicates that an almost complete conversion of $\text{LiOH(s)} + \text{Liquid}$ into $\text{Li}_4(\text{OH})_3\text{Br}$ is achieved. All this let us think that the phase diagram proposed by Sangster and, therefore, the calculations carried out with FactSage, are likely incorrect. Nevertheless, as shown later, the enthalpy of formation/decomposition of the stoichiometric compound $\text{Li}_4(\text{OH})_3\text{Br}$, though less than initially predicted, is sufficient to make this compound an attractive alternative to NaNO_3 in TES applications.

3.2. State of the art in LiOH/LiBr phase diagram

The phase diagram of LiOH-LiBr system was investigated for the first time by Giuseppe Scarpa [10] in 1915. The thermal analysis carried out indicated the presence of an eutectic

transition taking place at 275 °C and extending from composition $x = 0$ to $x = 0.65$ (x = molar fraction of LiOH). For $x \geq 0.65$, a second isothermal transition was observed at 310 °C approx., whose duration is maximum at $x = 0.75$ and that corresponds to the formation of $\text{Li}_4(\text{OH})_3\text{Br}$ stoichiometric compound. In 1953, Reshetnikov et al. [11] reported a eutectic transition at 250-278 °C with eutectic composition between $x = 0.52$ and $x = 0.725$. They also pointed out the existence of the intermediate compound $\text{Li}_3(\text{OH})_2\text{Br}$, which seems to melt congruently. The phase equilibria of LiOH-LiBr system were examined again by Hartwig et al. [12] in 1981. Differential thermal analysis (DTA) and X-ray investigations were employed to establish the phase diagram. Besides a eutectic transition at 243 °C ($0 < x < 0.5$), they identify two intermediate compounds, $\text{Li}_2(\text{OH})\text{Br}$ and $\text{Li}_4(\text{OH})_3\text{Br}$, both of which melt peritectically according to the authors. The formation of $\text{Li}_4(\text{OH})_3\text{Br}$ was detected at 291 °C for $x \geq 0.59$, whereas $\text{Li}_2(\text{OH})\text{Br}$ appears at 245 °C within the composition range from $x \geq 0.4$ to $x = 0.75$. Similar results have been reported recently by Achchaq et al. [8] (Table 3.1). However, this latter study was conducted by DSC only, and the authors point out significant leakage problems that could compromise the reliability of the results.

Table 3.1. Phase equilibria in LiOH-LiBr system according to currently available experimental data.

	Phase transitions (eutectic, peritectic, peritectoid)	Transition temperature (°C)	Range of existence (molar fraction of LiOH)	Methods	Information provided
Scarpa [10]	Eutectic	275	$x \leq 0.70$ (eutectic point at $x = 0.45$)	Thermal analysis	Table including tested compositions (18) and corresponding transition temperatures
	$\text{Li}_2(\text{OH})\text{Br}$ $\text{Li}_4(\text{OH})_3\text{Br}$	Not reported 310	Not reported $x \geq 0.65$		
Hartwig et al. [12]	Eutectic	243	$x \leq 0.50$ (eutectic point at $x = 0.40$)	DSC & X-ray diffraction	Graphical information including proposed phase diagram with experimental points (13 compositions)
	$\text{Li}_2(\text{OH})\text{Br}$	245	$0.42 \leq x \leq 0.75$		
	$\text{Li}_4(\text{OH})_3\text{Br}$	291	$x \geq 0.59$		
Achchaq et al. [8]	Eutectic	253	Not reported	DSC	Composition (13) – Transition temperatures map
	$\text{Li}_2(\text{OH})\text{Br}$	254	Not reported		
	$\text{Li}_4(\text{OH})_3\text{Br}$	290	Not reported		

Despite the significant discrepancies in available experimental data as well as in their interpretation (summarized in Table 3.1), a theoretical phase diagram for LiOH-LiBr system

was proposed by Sangster [9] in 2000. Through careful analysis of all available liquidus data at that time [10], [12], Sangster concludes that the reported “eutectic” at 243 or 250 °C is actually the subsolidus transition temperature of $\text{Li}_2(\text{OH})\text{Br}$ compound. For the calculation of the phase diagram, the existence of intermediate compounds $\text{Li}_4(\text{OH})_3\text{Br}$ (melting peritectically) and $\text{Li}_2(\text{OH})\text{Br}$ (decomposing in the subsolidus) was assumed. On the contrary, Sangster considers that there is no independent evidence for the $\text{Li}_3(\text{OH})_2\text{Br}$ compound existence and, therefore, it was not included in the calculation of the phase diagram. As can be seen in Figure 3.1, the phase diagram shows a calculated eutectic at 267 °C (eutectic composition, $x = 0.423$), the peritectic reaction of $\text{Li}_4(\text{OH})_3\text{Br}$ at 304 °C ($x = 0.625$), and $\text{Li}_2(\text{OH})\text{Br}$ compound with a transition temperature at 244 °C. According to Sangster, an uncertainty of ± 20 °C may be assigned to the calculated diagram, which is very high. This is the phase diagram currently implemented in FactSage 7.3 [1].

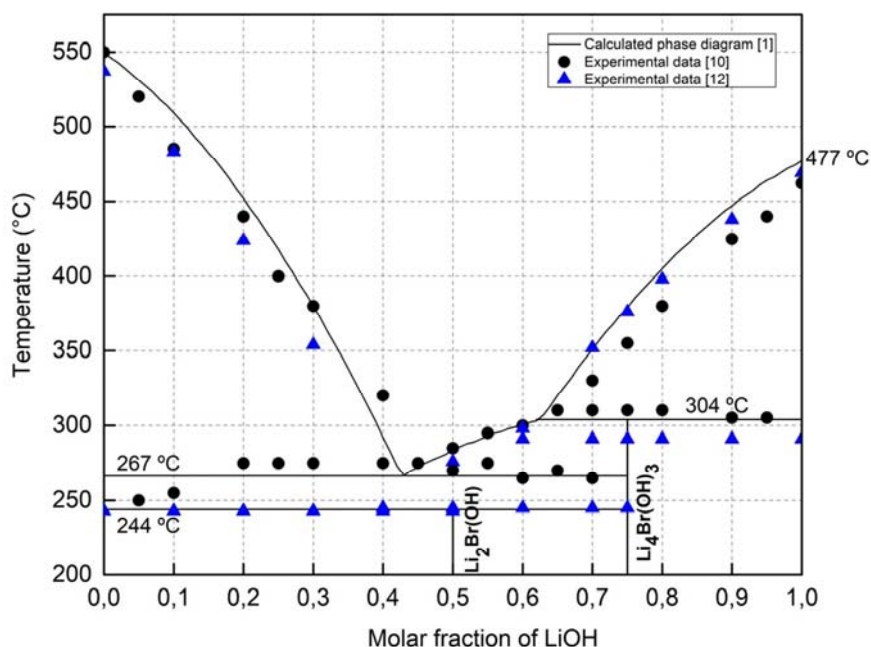


Figure 3.1. LiOH-LiBr phase diagram proposed by Sangster [1] based on the experimental data obtained by Scarpa [10] (black circles) and Hartwig et al. [12] (blue triangles).

3.3. Experimental estimation of the phase diagram of the binary system LiOH-LiBr

The experimental investigation of the LiOH-LiBr system has been carried out through Differential Scanning Calorimetry (DSC) and X-ray diffraction. Thirteen LiOH-LiBr mixtures with LiOH molar fraction ranging from $x = 0.19$ to $x = 0.84$ have been investigated.

3.3.1. Thermal Characterization of LiOH-LiBr mixtures

The DSC thermograms obtained upon heating are displayed in Figure 3.2, whereas the transition temperature values are reported in Table 3.2. We remind that prior to DSC tests, the samples were already subjected to a first heating/cooling run in an oven (section 2.2.2.1). Also, at least three samples for each composition have been prepared and tested to check the repeatability of the results. Figure 3.2 and Table 3.2 show a first endothermic event that occurs at 230 °C approx. In the range of composition from 0.56 to 0.84 molar fraction of LiOH. This solid-state transition (named T_1) is not predicted in the phase diagrams known so far [9], [10], [12] and will be discussed furtherly later. The second and third endothermic events occur between 243 - 250 °C and 246 - 254 °C, respectively. According to Hartwig et al. [12], the endothermic event observed at 243 - 250 °C corresponds to a eutectic transition line, whereas that appearing at 246 - 254 °C relates to the formation of the stoichiometric phase $\text{Li}_2(\text{OH})\text{Br}$, which melts peritectically. On the contrary, Sangster [9] states that $\text{Li}_2(\text{OH})\text{Br}$ results from a peritectoid reaction and that the event observed at 243 - 250 °C is actually the subsolidus decomposing temperature of such compound. A zoom of DSC thermograms for compositions $x = 0.19$ to $x = 0.62$ between 240-260 °C is provided in Figure 3.3. Firstly, it can be seen that both endothermic peaks are visible throughout the range of tested compositions from 0.19 to 0.62 mole fraction of LiOH, which means that $\text{Li}_2(\text{OH})\text{Br}$ cannot be a peritectic compound as it extends beyond any reasonable value of possible peritectic composition. According to Hartwig's postulates, the intersection of the peritectic line with the liquidus line (peritectic composition) occurs at about $x = 0.42$ so that the endothermic peak corresponding to the formation of $\text{Li}_2(\text{OH})\text{Br}$ should disappear for compositions with lower LiOH content ($x < 0.42$), which is not the case. It can also be seen that the intensity of the endothermic event at the lowest temperature (c.a. 250 °C) increases with the LiOH content of the mixture up to $x = 0.50$, where the intermediate compound $\text{Li}_2(\text{OH})\text{Br}$ is placed, and a maximum intensity value is observed. Together with the previous observation, this likely indicates that $\text{Li}_2(\text{OH})\text{Br}$ forms through a peritectoid reaction at 250

°C approx. Regarding the endothermic event at the highest temperature (c.a. 254 °C), it shows the maximum intensity at $x = 0.48$ which is compatible with the existence of a eutectic transition with eutectic point close to $x = 0.43$ as reported by Hartwig et al. [12] (eutectic point at $x = 0.40$). Moreover, no endothermic events have been observed at the temperature of the eutectic transition proposed by Sangster [9] (267 °C), while the liquidus line indicates the existence of such type transition. According to our experimental results, neither Hartwig nor Sangster's conclusions seem to be correct. What we observe fits better with the formation of compound $\text{Li}_2(\text{OH})\text{Br}$ at 250 °C through a peritectoid transformation and the existence of a eutectic transition at 254 °C approx., both extending over the compositional range from $x = 0$ to $x = 0.62$ approx.

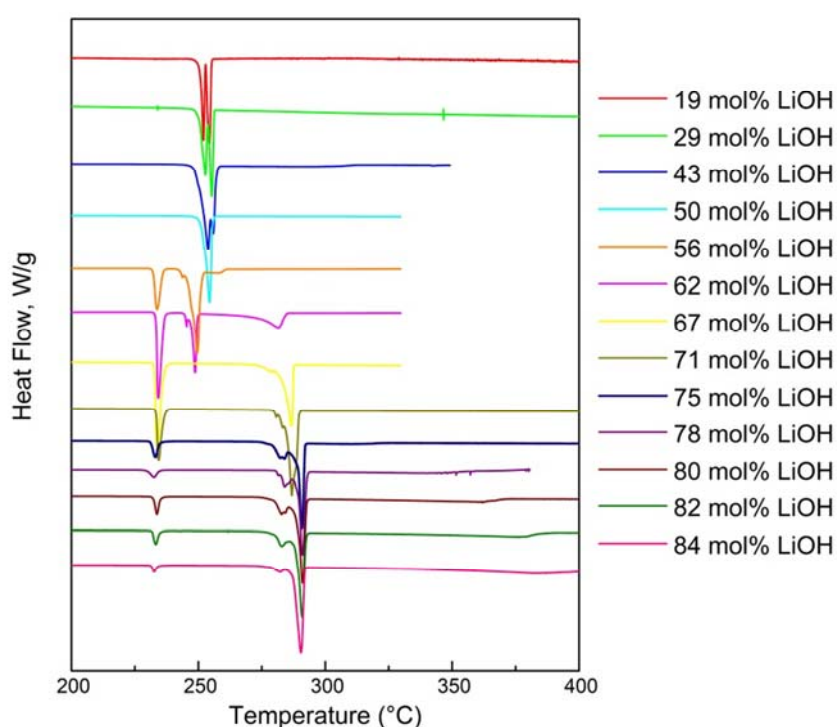


Figure 3.2. DSC thermograms upon heating (heating rate = 1 K/min) of LiOH-LiBr samples with different compositions from 0.19 to 0.84 molar fraction of LiOH.

Table 3.2. Phase transition temperatures of LiOH-LiBr mixtures obtained from DSC analysis.

Composition (%mol LiOH)	Transition temperatures (°C)					
	T ₁	Peritectoid	Eutectic line	T ₂	Peritectic	Liquidus Line
84	231	-	-	278	287	403
82	231	-	-	280	288	389
80	232	-	-	280	289	372
78	230	-	-	280	289	378
75 Li ₄ (OH) ₃ Br	231	-	-	279	289	321
71	233	-	-	280	284	
67	232	-	-	274	283	
62	233	245	247	273	-	
56	232	243	246	-	-	Not detectable
50 Li ₂ (OH)Br	-	246	251	-	-	
43	-	249	251	-	-	
29	-	250	254	-	-	
19	-	250	254	-	-	

Coming back to Figure 3.2 and Table 3.2, another endothermic event is observed at c.a. 289 °C for molar fractions of LiOH greater or equal to $x = 0.62$, which is preceded by a less energetic transition at 280 °C approx. (named T₂). As shown in Table 3.3 and Figure 3.4, the maximum value of the reaction enthalpy associated to those endothermic peaks is reached at $x = 0.75$, where the peritectic compound Li₄(OH)₃Br is located. Again, our experimental results are in good agreement with those of Hartwig et al. [12], showing a peritectic transition/reaction at 289 °C approx. which is very close to the value proposed by Hartwig (291 °C) and 15 °C below the value calculated by Sangster [9] (304 °C). The transition T₂ preceding the peritectic reaction has not been reported before and will be discussed later. Regarding the liquidus line, it is hardly visible for compositions below $x = 0.75$, whereas the values of liquidus temperature observed beyond $x = 0.75$ are in very good agreement with those reported by Scarpa [10] and are 10-20 °C below those proposed by Hartwig et al. [12].

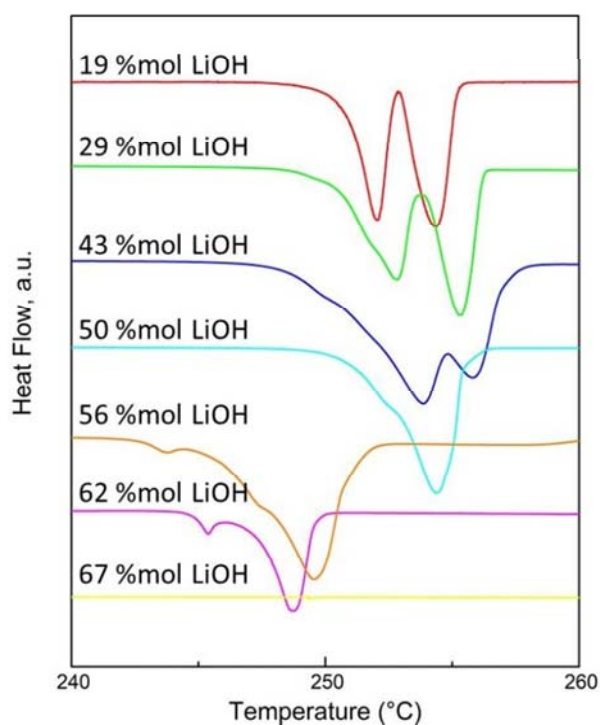


Figure 3.3. Zoom on DSC thermograms for LiOH-LiBr samples with composition within 0.19 and 0.67 molar fraction of LiOH.

Table 3.3. Enthalpies of phase transition of LiOH-LiBr mixtures obtained from DSC analysis.

Composition (% mol LiOH)	Enthalpy of phase transition (J/g)			
	T_1	Eutectic transition + Peritectoid reaction	T_2 transition + Peritectic reaction	Melting
84	9		195	175
82	17		195	159
80	21		206	131
78	19		233	117
75 $\text{Li}_4(\text{OH})_3\text{Br}$	29		247	50
71	61		202	
67	107		128	
62	80	52		62
56	40	138		
50 $\text{Li}_2(\text{OH})\text{Br}$		156		
43		126		
29		77		
19		32		

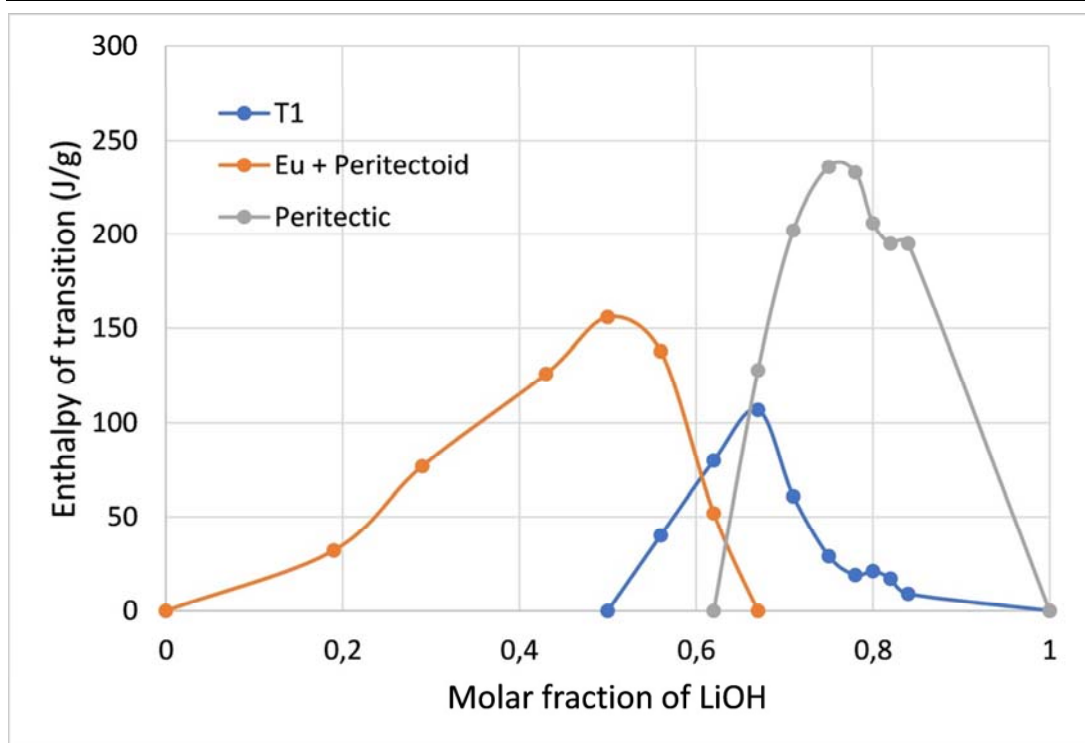


Figure 3.4. Measured enthalpies for transition T_1 (blue line), eutectic + peritectoid reaction (orange line) and peritectic reaction (grey line).

The composition-transition temperature data from our DSC analysis have been reported on the phase diagram proposed by Hartwig et al. [12] together with their experimental results (Figure 3.5). Except for the transitions T_1 and T_2 (not reported before) and interpretation about $\text{Li}_2(\text{OH})\text{Br}$ formation mechanism (peritectoid vs. peritectic), Figure 3.5 shows a quite good agreement between our experimental results and Hartwig's phase diagram. They are also in good agreement with the transition temperatures proposed by Achchaq et al. [8] for the eutectic line and the plateaux where intermediate compounds $\text{Li}_2(\text{OH})\text{Br}$ and $\text{Li}_4(\text{OH})_3\text{Br}$ form. All this leads us to think that the phase diagram proposed by Sangster [9] and implemented in FactSage 7.3, as well as Scarpa's data [10], is probably incorrect. The transition enthalpies observed also point in this direction. Whatever the transition considered (Figure 3.4, Table 3.3), the measured phase change enthalpies are much lower than those predicted by FactSage 7.3. For instance, the measured enthalpies corresponding to the eutectic transition are approximately one-third lower than those calculated with FactSage. The same applies to the peritectic transformation leading to the formation of the compound $\text{Li}_4(\text{OH})_3\text{Br}$. FactSage predicts an enthalpy of 804 J/g, while the measured enthalpy is only 247 J/g. Even considering that the transformation can be produced outside the thermodynamic equilibrium, following for example a Scheil-Gulliver scheme, FactSage's prediction (450 J/g) remains

quite above what is actually observed. In a recent paper by Legros et al. [13], the authors suggest that the structure form close to 290 °C with related enthalpy of phase transition of 250 J/g approx. is a potential $\text{Li}_4(\text{OH})_3\text{Br}$ polymorph that is systematically obtained because thermodynamically more stable than the $\text{Li}_4(\text{OH})_3\text{Br}$ described by Hönnerscheid et al. [14].

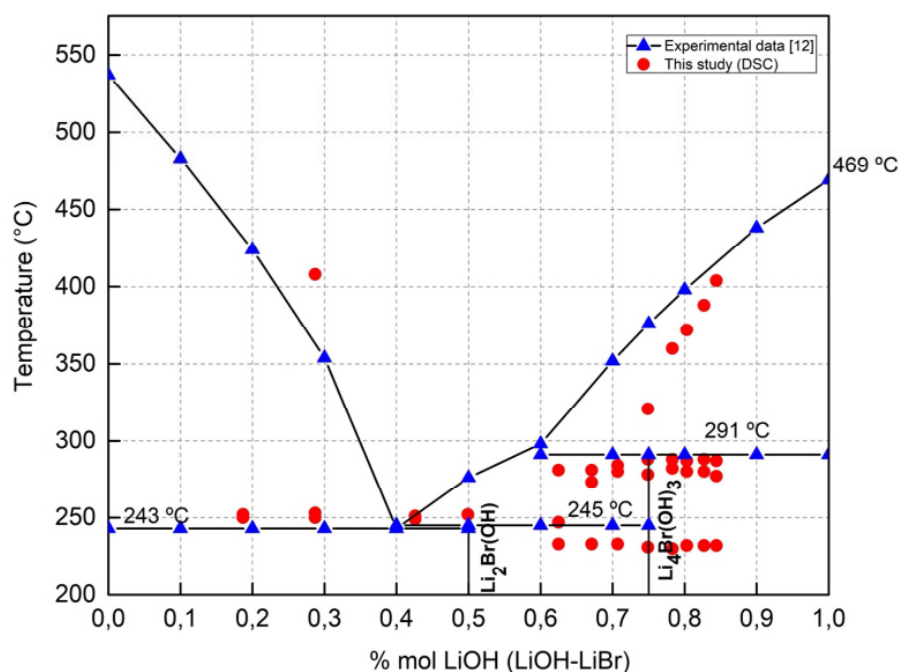


Figure 3.5. LiOH-LiBr phase diagram proposed by Hartwig et al. [12] and experimental data obtained by DSC in this work (red symbols) and by Hartwig (blue symbols).

3.3.2. Structural characterization of LiOH-LiBr mixtures

3.3.2.1. X-ray diffraction analysis of LiOH-LiBr mixtures

In Figure 3.6, the X-ray diffraction patterns at room temperature for some selected compositions are shown. For the compositions studied, the reaction products correspond to those predicted in the phase diagrams proposed so far [9], [10], [12]. In samples with LiOH molar fraction below 0.5, the phases identified are LiBr and $\text{Li}_2(\text{OH})\text{Br}$. In the compositional range from 0.5 to 0.75, they are $\text{Li}_2(\text{OH})\text{Br}$ and $\text{Li}_4(\text{OH})_3\text{Br}$. Beyond $x = 0.75$, only $\text{Li}_4(\text{OH})_3\text{Br}$ and LiOH are present. Moreover, the quantitative analysis carried out (see Table 3.4) also indicates a quite good agreement between experimental observations and calculations carried out with FactSage 7.3, based on Sangster's phase diagram. It is worth to note too that 100% $\text{Li}_2(\text{OH})\text{Br}$ and 100% $\text{Li}_4(\text{OH})_3\text{Br}$ are obtained for samples with

compositions $x = 0.5$ and $x = 0.75$, respectively, meaning that both the peritectoid and peritectic reactions seems have been completed.

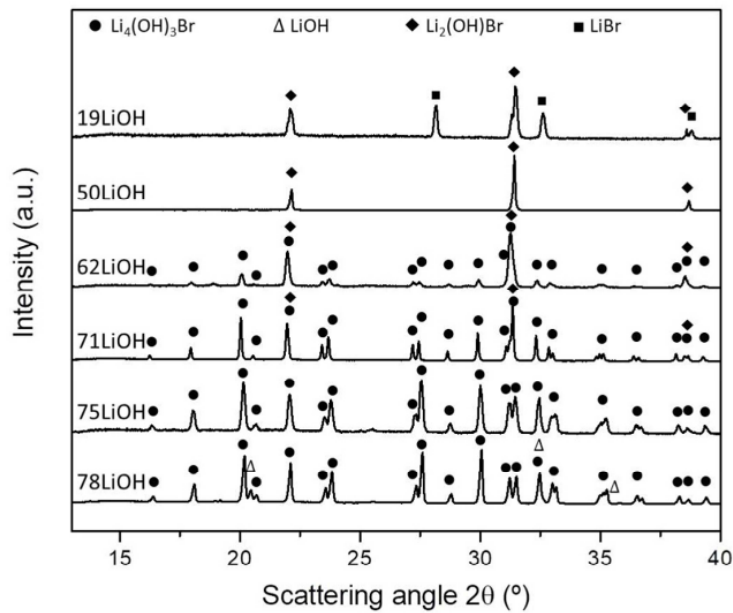


Figure 3.6. XRD results for some LiOH-LiBr selected compositions

Table 3.4. XRD quantitative analysis results – Experimental data have been obtained by fitting x-ray diffraction profiles by Rietveld method. Calculations have been performed using FactSage 7.3 based on the phase diagram proposed by Sangster [9].

Composition (mol. %)	Experimental data (wt. %)	Calculations (wt. %)
78LiOH-22LiBr	87 $\text{Li}_4(\text{OH})_3\text{Br}$ 13 LiOH	91 $\text{Li}_4(\text{OH})_3\text{Br}$ 9 LiOH
75LiOH-25LiBr	100 $\text{Li}_4(\text{OH})_3\text{Br}$	100 $\text{Li}_4(\text{OH})_3\text{Br}$
71LiOH-29LiBr	82 $\text{Li}_4(\text{OH})_3\text{Br}$ 18 $\text{Li}_2(\text{OH})\text{Br}$	78 $\text{Li}_4(\text{OH})_3\text{Br}$ 22 $\text{Li}_2(\text{OH})\text{Br}$
62LiOH-38LiBr	46 $\text{Li}_4(\text{OH})_3\text{Br}$ 54 $\text{Li}_2(\text{OH})\text{Br}$	42 $\text{Li}_4(\text{OH})_3\text{Br}$ 58 $\text{Li}_2(\text{OH})\text{Br}$
50LiOH-50LiBr	100 $\text{Li}_2(\text{OH})\text{Br}$	100 $\text{Li}_2(\text{OH})\text{Br}$

3.3.2.2. In-situ XRD analysis for investigation of novel phase transition

To investigate the nature of transitions T_1 and T_2 , several quenching and in-situ XRD experiments were carried out at the composition showing the maximum energy related to the transition T_1 (67 mol% LiOH). The quenching experiments were carried out in a homemade small cylindrical oven (internal diameter 15 mm; depth 10 mm). A similar sample holder as

the one used for the DSC measurements was used for the experiments. The sample holder was suspended in the oven thanks to the two wires of a type K thermocouple. In this configuration, the junction between the two wires is insured by the metallic sample holder itself (separated contact thermocouple configuration), allowing a better control of the holder temperature. The oven was coupled to the thermocouple through a data acquisition card and a relay system to regulate the temperature of the sample. Thus, the sample was heated to the targeted temperature, held at that temperature for 10 minutes, and then quenched in liquid Nitrogen. Figure 3.7 shows the XRD patterns after quenching at 240 °C and 260 °C (both after T_1). In both cases, the XRD patterns show the presence of a new crystalline phase (labeled as N in the graph) as well as less than 5% of a second unknown phase (labeled as U).

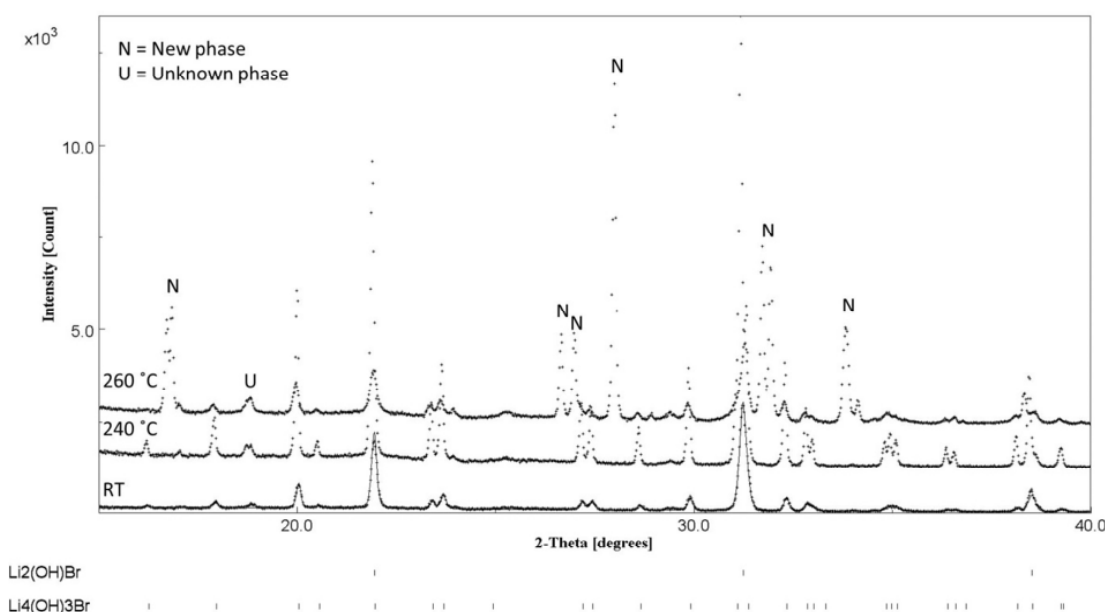


Figure 3.7. XRD patterns after quenching a sample of composition 67 mol. % LiOH at 240 °C and 260 °C.

Due to the corrosive nature of the salt and to avoid possible damage to the in-situ cell, the in-situ XRD measurements were performed only up to 240 °C. In this case, the sample (67 mol% LiOH) was heated from room temperature up to 230 °C and 240 °C respectively, then cooled down at 230 °C and finally at room temperature with a heating rate of 10 K/min. In this experiment, the XRD patterns were registered, at the selected temperature, after a stabilization time of 30 minutes to ensure stable conditions with no temperature fluctuation during the measurements. In order to help in the comparison of the XRD results, it should be kept in mind that the XRD analysis of the quenched samples was performed using Copper radiation

($\lambda_{\text{Cu K}\alpha 1} = 1.54056 \text{ \AA}$). In contrast, the in-situ analyses were performed using Cobalt radiation ($\lambda_{\text{Co}\alpha 1} = 1.78886 \text{ \AA} / \lambda_{\text{Co}\alpha 2} = 1.79277 \text{ \AA}$). The XRD patterns obtained are shown in Figure 3.8.

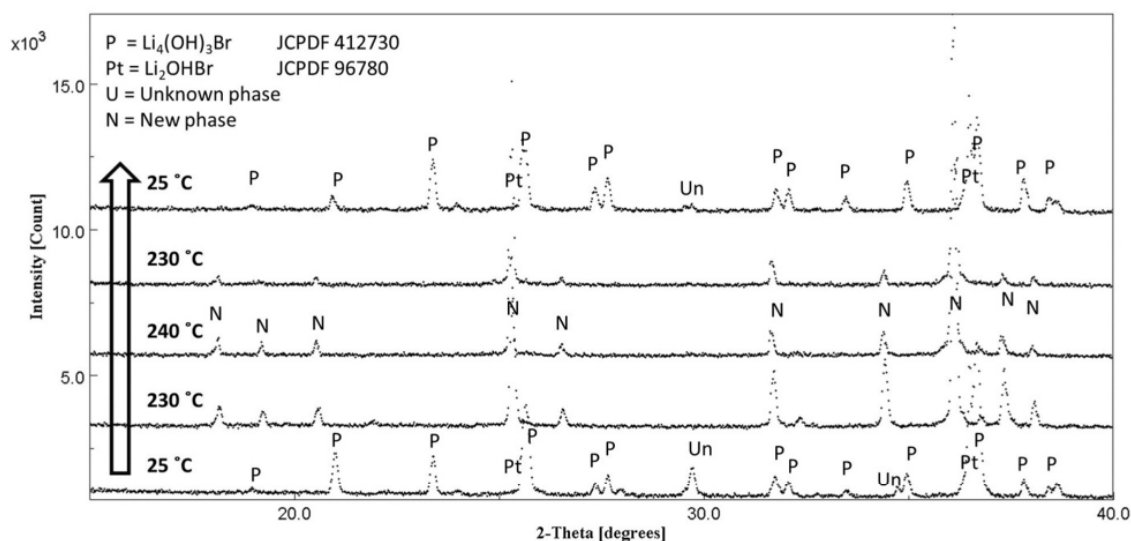


Figure 3.8. In-situ XRD results of the sample 67mol. % LiOH after synthesis.

As expected, the room temperature pattern in Figure 3.8 shows the presence of the peritectic phase $\text{Li}_4(\text{OH})_3\text{Br}$ and the peritectoid phase $\text{Li}_2(\text{OH})\text{Br}$. The results at temperatures 230 °C and 240 °C substantially confirm what was observed in the DSC experiments. At 230 °C there is a solid-state transformation with the formation of a new crystalline phase (labeled N) for the moment unknown. This transformation is completed at 240 °C and is reversible, as shown in the XRD after cooling at 25 °C (upper part in the figure following the direction of the arrow). The formation of this new phase N corresponds to the disappearance of the peritectic phase from the pattern, while the peritectoid phase is still well visible. For this last phase, at high temperature, the Rietveld refinement shows cell parameter higher than the one relevant to the room temperature phase ($a = 0.409 \text{ nm}$ versus 0.406 nm) due to the volume expansion upon heating. It is worth noting that upon heating, the second unknown phase identified (labeled as Un) in the pattern at room temperature (at 2θ around 30°) also disappears and appears again after cooling. This suggests that this peak also belongs to the peritectic crystalline phase. It is worth noting that the new phase N detected in the in-situ experiments doesn't show the same reflections of the phases identified after the quenching experiment. This difference is probably due to the non-equilibrium conditions of the samples subjected to quenching not allowing reaching the more stable structure.

3.3.3. Proposition of new phase diagram for LiOH-LiBr binary system

Although further studies are necessary to clarify the nature of phase transitions T_1 and T_2 , the in-situ XRD results, together with enthalpy measurements (Fig. 4) and observations from [26], give some hints about them. According to DSC measurements, the solid-state transition T_1 takes place at 230 °C, which is the temperature at which the new crystalline phase N appears in in-situ XRD spectra and the peritectic compound $\text{Li}_4(\text{OH})_3\text{Br}$ disappears completely. On the other hand, Figure 3. 4 shows that the enthalpy linked to phase transition T_1 reaches its maximum value at composition $x = 0.67$, which approximately coincides with the 1:2 molar composition corresponding to the stoichiometric compound $\text{Li}_3(\text{OH})_2\text{Br}$ mentioned by Reshetnikov et al. [11]. Therefore, we could assume that the transition T_1 represents a reversible reaction on heating between solids $\text{Li}_4(\text{OH})_3\text{Br}$ and $\text{Li}_2(\text{OH})\text{Br}$ with $\text{Li}_3(\text{OH})_2\text{Br}$ as reaction product ($\text{Li}_4(\text{OH})_3\text{Br} + \text{Li}_2(\text{OH})\text{Br} \rightarrow 2 \text{Li}_3(\text{OH})_2\text{Br}$). Accordingly, the transition T_2 , appearing just before the peritectic reaction, should correspond to the decomposition (on heating) of the stoichiometric compound $\text{Li}_3(\text{OH})_2\text{Br}$ into $\text{Li}_4(\text{OH})_3\text{Br}$ and a liquid phase with 0.5 molar fraction of LiOH ($2 \text{Li}_3(\text{OH})_2\text{Br} \rightarrow \text{Li}_4(\text{OH})_3\text{Br} + \text{LiOH(l)} + \text{LiBr(l)}$).

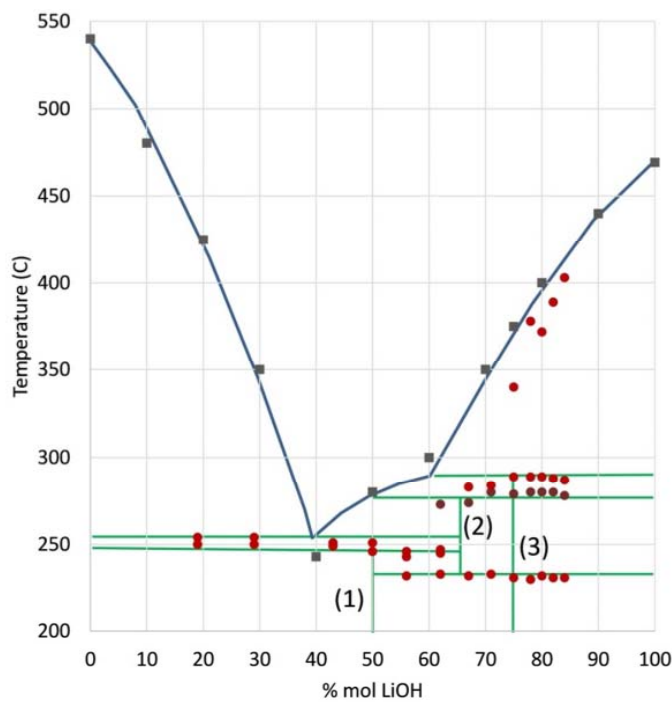


Figure 3.9. Sketch of possible LiOH-LiBr phase diagram according to the experimental analysis carried out, showing two peritectic compounds (2 – $\text{Li}_3(\text{OH})_2\text{Br}$ & 3 – $\text{Li}_4(\text{OH})_3\text{Br}$), one peritectoid (1 – $\text{Li}_2(\text{OH})\text{Br}$) and eutectic transition at 254 °C.

Considering the set of experimental results obtained, as well as the analyses made of them, the phase diagram of the LiOH-LiBr system could probably be the one drawn by hand in Figure 3.9. It encompasses three stoichiometric compounds:

1. $\text{Li}_2(\text{OH})\text{Br}$, which forms through a peritectoid reaction at 250 °C approx. over the compositional range $x \leq 0.66-0.67$;
2. $\text{Li}_3(\text{OH})_2\text{Br}$, which is the product of the reaction between solids $\text{Li}_4(\text{OH})_3\text{Br}$ and $\text{Li}_2(\text{OH})\text{Br}$ at 230 °C and melts peritectically at 280 °C approx., with peritectic point at $x = 0.5$;
3. iii) $\text{Li}_4(\text{OH})_3\text{Br}$, which forms through a peritectic reaction at 289 °C approx. at compositions $x \geq 0.62$. The eutectic transition occurs at 254 °C approx. and extends over the composition range $x > 0$ to $x = 0.66-0.67$, with eutectic point at $x = 0.40$.

3.4. Conclusion

In this chapter, LiOH-LiBr binary system was thoroughly investigated by means of DSC and XRD experimental analysis. Significant discrepancies compared to previous existing studies were observed. They relate to temperature values of phase equilibria as well as stoichiometric compounds present in the system. From our experimental results, a modified LiOH-LiBr phase diagram was proposed which gives satisfactory explanation to all observations carried out. It includes stoichiometric compounds $\text{Li}_2(\text{OH})\text{Br}$ (peritectoid plateau at 250 °C, $x \leq 0.666$), $\text{Li}_3(\text{OH})_2\text{Br}$ (stable between 230 °C and 280 °C, melting peritectically for $x \geq 0.5$) and $\text{Li}_4(\text{OH})_3\text{Br}$ (peritectic plateau at 289 °C, $x \geq 0.5$). It also displays a eutectic transition at 254 °C approx., which extends over the composition range $x > 0$ to $x = 0.66-0.67$, with eutectic point at $x = 0.40$.

The disagreements with previous studies also concern the enthalpies of transition. Whatever the transition considered; the enthalpies measured in this work are much lower than those predicted by FactSage 7.3, where LiOH-LiBr phase diagram proposed by Sangster in 2000 is implemented. Given the reliability of our DSC measures and taking into account that the identified peritectic and peritectoid reactions are completed (checked by XRD), these differences can only be attributed to the proven shortcomings of the Sangster's phase diagram.

In spite of much lower energy density than a priori expected, the peritectic compound $\text{Li}_4(\text{OH})_3\text{Br}$ is still an attractive candidate for TES applications around 300 °C. With a reaction enthalpy of 247 J/g at 289 °C, it can compete with phase change material NaNO_3 , that melts at 306 °C with 175 J/g of latent heat, which is the reference material for TES applied to high pressure (100 bar) DSG technology. Full characterization of the thermo-physical properties of $\text{Li}_4(\text{OH})_3\text{Br}$ (transition temperature, reaction enthalpy, thermal conductivity, specific heat capacity), as well as thermal cycling stability analysis and corrosion studies will be discussed in the next chapters.

3.5. References

- [1] C. W. Bale *et al.*, “FactSage thermochemical software and databases, 2010-2016,” *Calphad: Computer Coupling of Phase Diagrams and Thermochemistry*, vol. 54, pp. 35–53, Sep. 2016, doi: 10.1016/j.calphad.2016.05.002.
- [2] F. Achchaq and E. P. Del Barrio, “A proposition of peritectic structures as candidates for thermal energy storage,” in *Energy Procedia*, Dec. 2017, vol. 139, pp. 346–351, doi: 10.1016/j.egypro.2017.11.219.
- [3] W. D. Steinmann and R. Tamme, “Latent heat storage for solar steam systems,” in *Journal of Solar Energy Engineering, Transactions of the ASME*, Feb. 2008, vol. 130, no. 1, pp. 0110041–0110045, doi: 10.1115/1.2804624.
- [4] D. Laing, C. Bahl, T. Bauer, D. Lehmann, and W. D. Steinmann, “Thermal energy storage for direct steam generation,” *Solar Energy*, vol. 85, no. 4, pp. 627–633, Apr. 2011, doi: 10.1016/j.solener.2010.08.015.
- [5] “EASE/EERA Energy Storage Technology Development Roadmap towards 2030 | EASE: Why Energy Storage? | EASE.” <https://ease-storage.eu/publication/easeeera-energy-storage-technology-development-roadmap-towards-2030/> (accessed Oct. 20, 2020).
- [6] T. Bauer, D. Laing, and R. Tamme, “Characterization of sodium nitrate as phase change material,” *International Journal of Thermophysics*, vol. 33, no. 1, pp. 91–104, Jan. 2012, doi: 10.1007/s10765-011-1113-9.
- [7] A. Lomonaco, D. Hailot, E. Pernot, E. Franquet, and J. P. Bédécarrats, “Sodium nitrate thermal behavior in latent heat thermal energy storage: A study of the impact of sodium nitrite on melting temperature and enthalpy,” *Solar Energy Materials and Solar Cells*, vol. 149, pp. 81–87, May 2016, doi: 10.1016/j.solmat.2015.12.043.
- [8] F. Achchaq, E. Palomo del Barrio, E. Lebraud, S. Péchev, and J. Toutain, “Development of a new LiBr/LiOH-based alloy for thermal energy storage,” *Journal of Physics and Chemistry of Solids*, vol. 131, pp. 173–179, Aug. 2019, doi: 10.1016/j.jpcs.2019.04.001.
- [9] J. Sangster, “Thermodynamics and phase diagrams of 32 binary common-ion systems of the group Li,Na,K,Rb,Cs//F,Cl,Br,I,OH,NO₃,” *Journal of Phase Equilibria*, vol. 21,

- no. 3, pp. 241–268, 2000, doi: 10.1361/105497100770340048.
- [10] “1915Sca1_G. Scarpa_Atti Real. Accad. Lincei, Sez. II, 1915, vol. 24, p. 476 (in Italian).pdf.” .
 - [11] N. A. Reshetnikov and G. M. Unzhakov, “No Title,” *Izv. Fiz.-Khim. Nauch.-Issled. Inst. Irkutsk. Gosud. Univ*, vol. 2, p. 23, 1953.
 - [12] P. Hartwig, A. Rabenau, and W. Weppner, “Lithium hydroxide halides: phase equilibria and ionic conductivities,” *Journal of The Less-Common Metals*, vol. 78, no. 2, pp. 227–233, Apr. 1981, doi: 10.1016/0022-5088(81)90132-6.
 - [13] P. Legros, E. Lebraud, M. Duquesne, and F. Achchaq, “Li₄Br(OH)₃ microstructure monitoring over its synthesis to tackle the lithium-based salts exploitation challenges as advanced phase change materials for storage technologies,” *Materials and Design*, vol. 196, p. 109160, Nov. 2020, doi: 10.1016/j.matdes.2020.109160.
 - [14] A. Hoennerscheid, J. Nuss, C. Muehle, and M. Jansen, “The Crystal Structures of the Lithium Hydroxide Halides Li₄(OH)₃Br and Li₄(OH)₃I,” *ChemInform*, vol. 34, no. 19, May 2003, doi: 10.1002/chin.200319010.

Chapter 4: Study of the peritectic compound $\text{Li}_4(\text{OH})_3\text{Br}$ as high temperature TES material in concentrating solar power applications

4.1. Introduction

In this chapter, the thermal and structural properties of $\text{Li}_4(\text{OH})_3\text{Br}$ are thoroughly investigated. The synthesis method and experimental techniques employed are described in sections 2.1 and 2.2. The characterization of $\text{Li}_4(\text{OH})_3\text{Br}$ as storage material is conducted by measuring transition temperatures and enthalpies, specific heats, and thermal conductivity. The effect of the synthesis conditions (i.e., thermal treatment, atmosphere used) on the storage properties, as well as the stability of the material to thermal cycling. Moreover, particular attention is paid to the study of subcooling phenomena and elucidation of mechanisms of formation of $\text{Li}_4(\text{OH})_3\text{Br}$ by combining DSC (Differential Scanning Calorimetry) with X-ray diffraction and TEM (Transmission Electron Microscopy). The study also includes a first attempt to enhance the performance of the storage material by addition of different types of carbon nanoparticles, such as fullerene C_{60} , reduced graphene oxide and multi-walled carbon nanotubes. At last, the performance of $\text{Li}_4(\text{OH})_3\text{Br}$ for TES in DSG solar power application is discussed and compared to that of commonly used phase change storage material sodium nitrate.

4.2. Mechanism of formation of the peritectic compound $\text{Li}_4(\text{OH})_3\text{Br}$

The term peritectic usually refers to reactions in which a liquid phase reacts with at least one solid phase at a defined temperature, T_p (peritectic temperature), to form one new solid phase. According to the phase diagram in Figure 3.9, the peritectic reaction leading to the intermediate compound $\text{Li}_4(\text{OH})_3\text{Br}$ takes place at $T_p = 289^\circ\text{C}$ and writes as: $\text{LiOH(s)} + \text{liquid} \rightarrow \text{Li}_4(\text{OH})_3\text{Br}$. Under thermodynamic equilibrium conditions, the pro-peritectic phase LiOH(s) nucleates on cooling at the liquidus temperature then grows until the peritectic temperature is reached. At this point, the liquid composition is that of the so called peritectic point ($x = 0.62$ according to Figure 3.9), and the liquid reacts with LiOH(s) to give $\text{Li}_4(\text{OH})_3\text{Br}$. The conversion into $\text{Li}_4(\text{OH})_3\text{Br}$ is 100% for composition $x = 0.75$ that we are going to investigate, which corresponds to that of stoichiometric compound $\text{Li}_4(\text{OH})_3\text{Br}$.

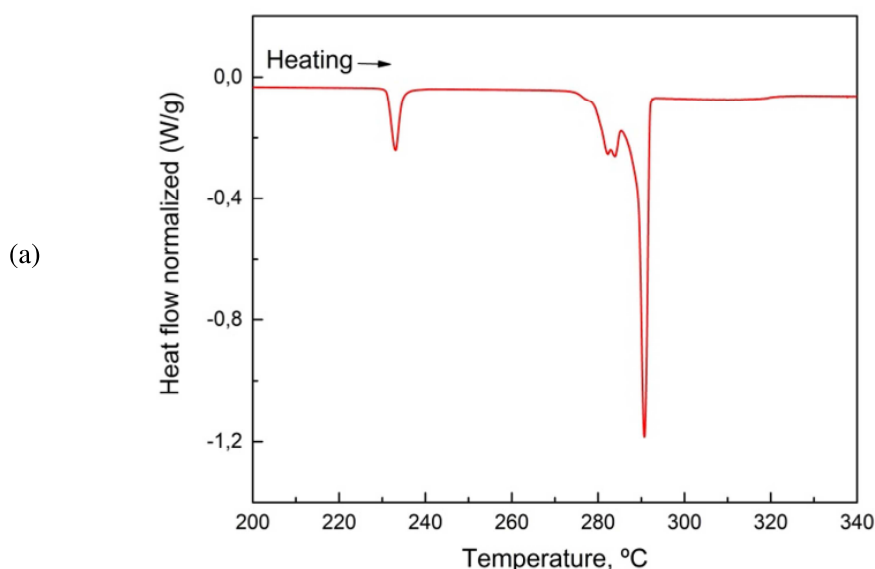
Peritectic structures usually form by means of at least three mechanisms [1]–[3]:

- *Peritectic reaction.* The reaction starts with the nucleation of the peritectic phase at the pro-peritectic/liquid interface. Then, lateral growth of the peritectic phase around the pro-peritectic phase takes place at the triple junction (pro-peritectic, peritectic, and liquid), readily forming a layer that isolates the pro-peritectic phase from the liquid. The peritectic reaction ends once the pro-peritectic phase is enwrapped by the peritectic phase. This mechanism occurs through short-range diffusion so as the reaction is usually fast and isothermal.
- *Peritectic transformation.* In contrast to peritectic reaction, the peritectic transformation occurs through a long-range diffusion mechanism, where atoms migrate through the peritectic layer to form peritectic solid at the pro-peritectic/peritectic and peritectic/liquid interfaces. The diffusion process through the peritectic layer depends on the atoms diffusion rate, the shape of the phase diagram and the cooling rate. In case of systems where the peritectic phase has a limited composition (c.f. stoichiometric peritectic compounds as $\text{Li}_4(\text{OH})_3\text{Br}$), the mechanism of peritectic transformation is highly unlikely.
- *Direct precipitation.* Direct precipitation of the peritectic phase from the melt (or from the pro-peritectic phase) can occur when a peritectic reaction or peritectic transformation is sluggish, as is often the case, and enough undercooling below the peritectic temperature (T_p) occurs.

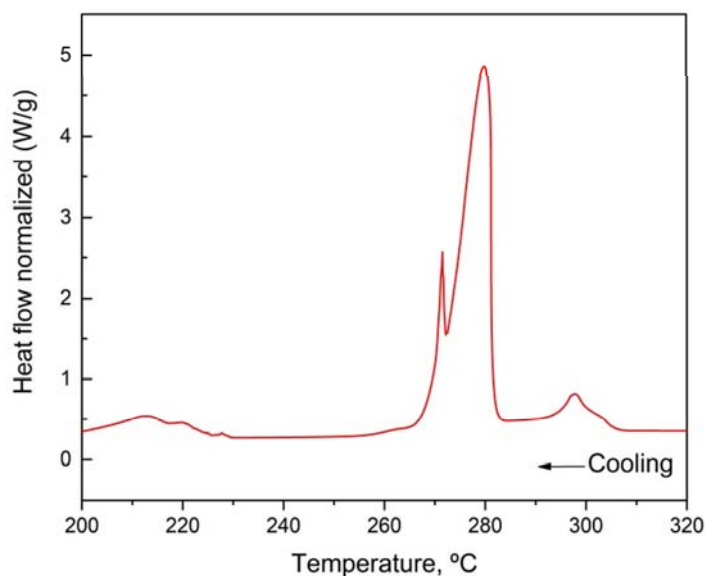
Due to the sluggishness of long-range solid-state diffusion, peritectic transformation could not proceed completely, leading to the existence of pro-peritectic phase in the final microstructure after peritectic solidification. However, although less common, the peritectic reaction can also occur by a mechanism different from that described above. In fact, due to surface tension conditions [2], the peritectic phase can nucleate and grow in the liquid without contact with the pro-peritectic phase, which will gradually dissolve. In such a case, as observed in Al-Mn [4] and Ni-Zn [5] systems, nearly phase-pure peritectic phase is achieved after the solidification process. Moreover, almost 100% pure peritectic-phase has also been reported during the solidification of highly undercooled peritectic alloys [6]–[8]. It is shown that, in such conditions, the peritectic phase directly solidifies from the undercooled melt by completely suppressing the nucleation and growth of the pro-peritectic phase, even in the case of peritectic stoichiometric compounds [9].

4.3. Phase change behavior and thermophysical characterization of the peritectic compound $\text{Li}_4(\text{OH})_3\text{Br}$

Three samples of LiOH-LiBr mixture with 0.75 molar fraction of LiOH composition were prepared under argon atmosphere as described in section 2.1.1. As already explained, they were submitted to the following thermal treatment in an oven to synthesize $\text{Li}_4(\text{OH})_3\text{Br}$: i) a heating ramp at 10K/min from ambient temperature up to 30°C above the melting temperature of $\text{Li}_4(\text{OH})_3\text{Br}$; ii) an isothermal step of 1 hour; iii) a cooling step up to room temperature with a cooling rate of 1.8 K/min . Their subsequent DSC analysis was performed at a heating rate of 1 K/min up to 320°C , whereas the cooling rate was 10°C/min up to room temperature. The DSC thermograms obtained are almost identical for the three samples. As shown in Figure 4.1.a, three endothermic peaks are clearly visible during the heating stage. The onset temperatures of the first and second peaks are 231°C and 279°C , respectively. As explained in chapter 3, these transitions are related to the formation and decomposition of intermediate compound $\text{Li}_3(\text{OH})_2\text{Br}$. It forms at the expense of $\text{Li}_4(\text{OH})_3\text{Br}$ through the solid-state reaction $\text{Li}_4(\text{OH})_3\text{Br} \rightarrow \text{Li}_3(\text{OH})_2\text{Br} + \text{LiOH}$, whereas it decomposes into $\text{Li}_4(\text{OH})_3\text{Br}$ through the reverse reaction. The third peak corresponds to the peritectic melting of $\text{Li}_4(\text{OH})_3\text{Br}$, which occurs at 289°C giving a liquid solution ($x = 0.62$) and solid-phase LiOH . The melting of LiOH is hardly visible on heating, but its solidification is clearly appreciated on cooling (Figure 4.1.b). As discussed later, the liquidus temperature is estimated to be $\geq 340^\circ\text{C}$. The enthalpy values corresponding to observed transitions are reported in Table 4.1.



(b)

Figure 4.1. DSC thermograms of a sample of $\text{Li}_4(\text{OH})_3\text{Br}$: (a) heating stage; (b) cooling stage.Table 4.1. Temperatures and enthalpies of phase transitions/reactions of LiOH-LiBr mixture at composition $x = 0.75$ on heating.

	Transition temperature (°C)	Enthalpy of transition/reaction (J/g)
Formation of $\text{Li}_3(\text{OH})_2\text{Br}$	231	29
Decomposition of $\text{Li}_3(\text{OH})_2\text{Br}$	279	247 ^(*)
Peritectic decomposition of $\text{Li}_4(\text{OH})_3\text{Br}$	289	
End of melting	≥ 340	50

(*) This value corresponds to the addition of the enthalpy of the decomposition of $\text{Li}_3(\text{OH})_2\text{Br}$ at 279 °C and that of $\text{Li}_4(\text{OH})_3\text{Br}$ at 289 °C.

Subcooling phenomena have been qualitatively analyzed, not only because they can limit the use of the material in thermal storage applications but also because they can provide some understanding of the mechanisms of $\text{Li}_4(\text{OH})_3\text{Br}$ formation. To this end, ten new samples were prepared as described in section 2.1.1. Each sample was submitted to a DSC test with a heating rate of 1 °C/min, whereas the cooling rate used was 50 °C/min for three of them and 10 °C/min for the rest. The DSC thermograms achieved on cooling are displayed in Figure 4.3 (cooling rate = 50 °C/min) and Figure 4.3 (cooling rate = 10 °C/min). At the highest cooling rate (Figure 4.2), the nucleation of the pro-peritectic phase LiOH(s) occurs at temperatures between 290 °C and 300 °C. The peritectic reaction and eventual transformation leading to $\text{Li}_4(\text{OH})_3\text{Br}$ are observed at 280 °C, which is 9 °C below the equilibrium temperature

determined on heating. The transition temperatures related to the formation/decomposition of $\text{Li}_3(\text{OH})_2\text{Br}$ are also shifted to lower temperatures. They are 266 °C and 222 °C approx. respectively (instead of 279 °C and 231 °C). At the lower cooling rate (Figure 4.3), two different behaviours are observed. There are at least two samples in which there is no evidence of the pro-peritectic phase formation (LiOH nucleation and growth). Indeed, the first exothermic event on cooling occurs at 273-276 °C where the peritectic phase seems to directly precipitate from the metastable melt. On the contrary, there are five samples in which the exothermic peak corresponding to the nucleation and growth of LiOH(s) is clearly visible at temperatures ranging from 340 °C to 278 °C. In these cases, the exothermic peak corresponding to the formation of $\text{Li}_4(\text{OH})_3\text{Br}$ appears at temperatures ranging from 270 °C to 282 °C (19-7 °C below the equilibrium temperature). For all the samples, the peak related to the transition leading to $\text{Li}_3(\text{OH})_2\text{Br}$ on cooling often overlaps with the exothermic peak related to $\text{Li}_4(\text{OH})_3\text{Br}$ formation. However, the last transition at 210-228 °C is clearly visible and corresponds to the decomposition of previously formed $\text{Li}_3(\text{OH})_2\text{Br}$.

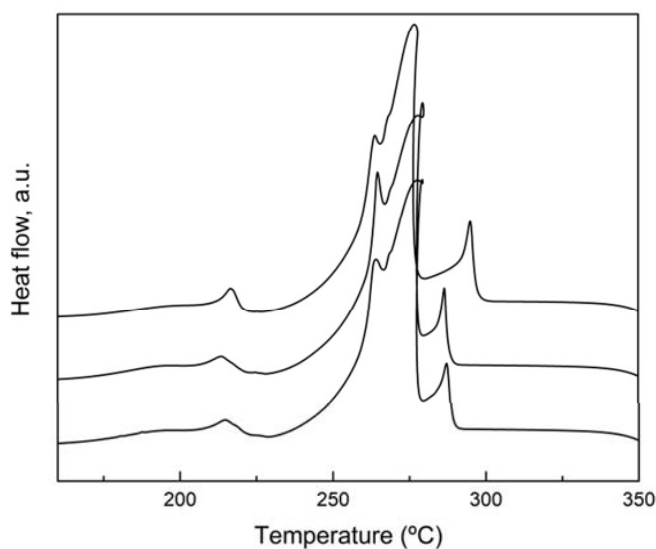


Figure 4.2. DSC thermograms (on cooling) with a cooling rate of 50 °C/min for LiOH-LiBr mixtures at $x = 0.75$ LiOH .

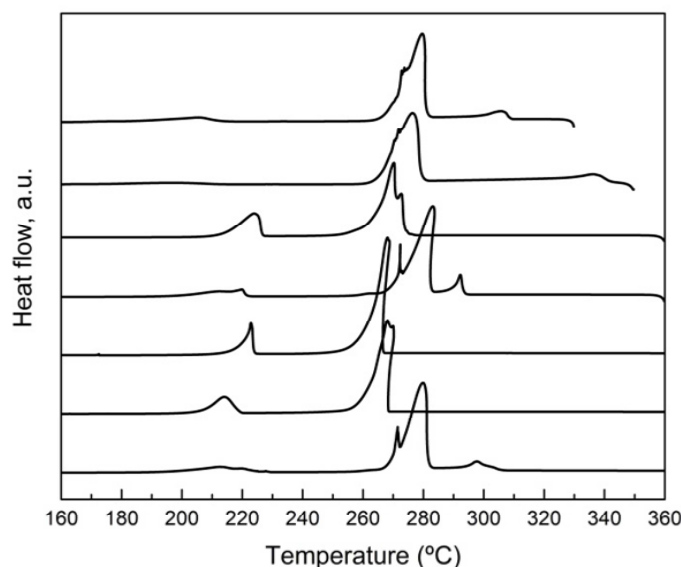


Figure 4.3. DSC thermograms (on cooling) with a cooling rate of 10 °C/min for LiOH-LiBr mixtures at $x = 0.75$ LiOH.

4.4. The effect of the synthesis conditions on the storage properties of the peritectic compound $\text{Li}_4(\text{OH})_3\text{Br}$

4.4.1. Effect of synthesis cooling rate

The effect of changing the cooling rate during the synthesis of the peritectic phase $\text{Li}_4(\text{OH})_3\text{Br}$ has also been analyzed by DSC. A priori, increasing the cooling rate could lead to metastability phenomena translating into different final microstructures and, therefore, different phase transition properties. It can also lead to a finer-grained pro-peritectic phase, which could facilitate the peritectic reaction if it occurs at the triple pro-peritectic/peritectic/liquid junction. Figure 4.4 displays the DSC thermograms obtained for samples prepared under argon atmosphere at cooling rates of 0.5, 1, 1.8, and 50 °C/min. It can be seen that whatever the cooling rate used during the synthesis stage, almost identical thermograms are obtained. $\text{Li}_4(\text{OH})_3\text{Br}$ formation is always observed at 289 °C, and no significant differences in enthalpy values are obtained (Table 4.2). According to these results, we can conclude that changing the cooling rate in the synthesis process has no significant influence on the final microstructure of the sample, neither on the reactivity and degree of conversion into peritectic phase $\text{Li}_4(\text{OH})_3\text{Br}$. This suggests again that the mechanism of formation of $\text{Li}_4(\text{OH})_3\text{Br}$ likely differs from the most common one in which the peritectic

phase nucleates at the pro-peritectic/liquid interface and grows around the pro-peritectic phase forming a layer that isolates the latter phase from the liquid.

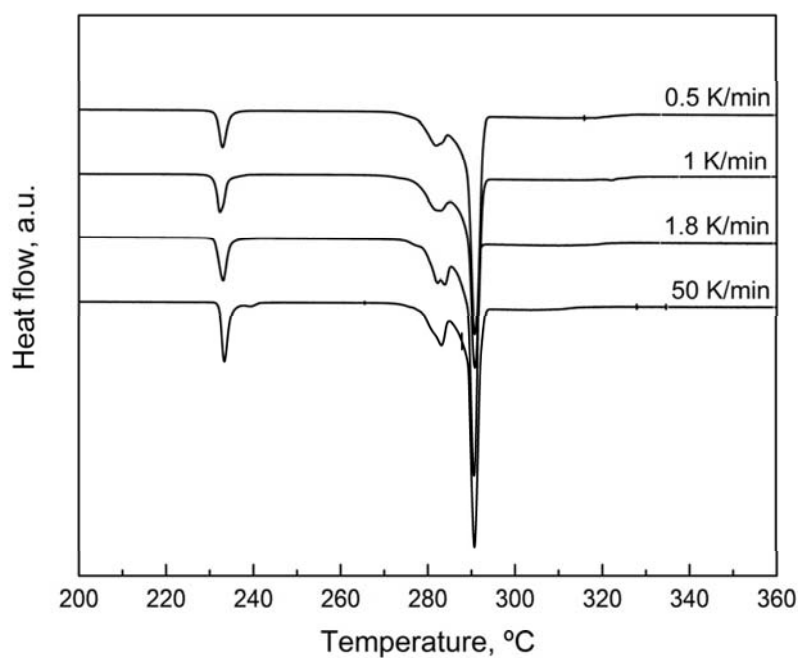


Figure 4.4. DSC thermograms (on heating, heating rate = 1 °C/min) for LiOH-LiBr mixtures at $x = 0.75$ LiOH prepared under argon atmosphere using different cooling rates during the synthesis stage.

Table 4.2. Peritectic reaction temperatures and enthalpies corresponding to the samples prepared using different cooling rates during the synthesis stage.

Cooling rate (°C/min)	temperature (°C)	Enthalpy (J/g) (*)
0.5	289	248
1.0	289	235
1.8	289	247
50	289	243

(*) This value corresponds to the addition of the enthalpy of the decomposition of $\text{Li}_3(\text{OH})_2\text{Br}$ at 279 °C and that of $\text{Li}_4(\text{OH})_3\text{Br}$ at 289 °C.

4.4.2. Effect of synthesis atmosphere

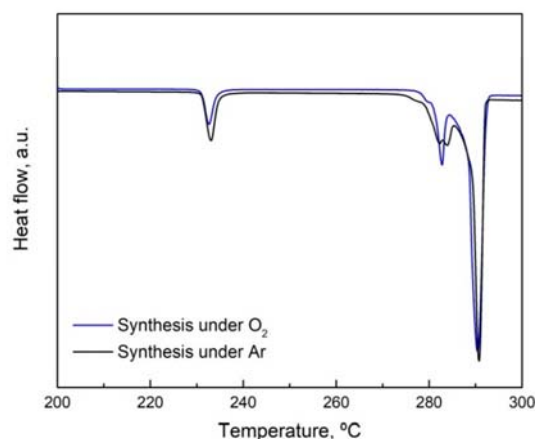
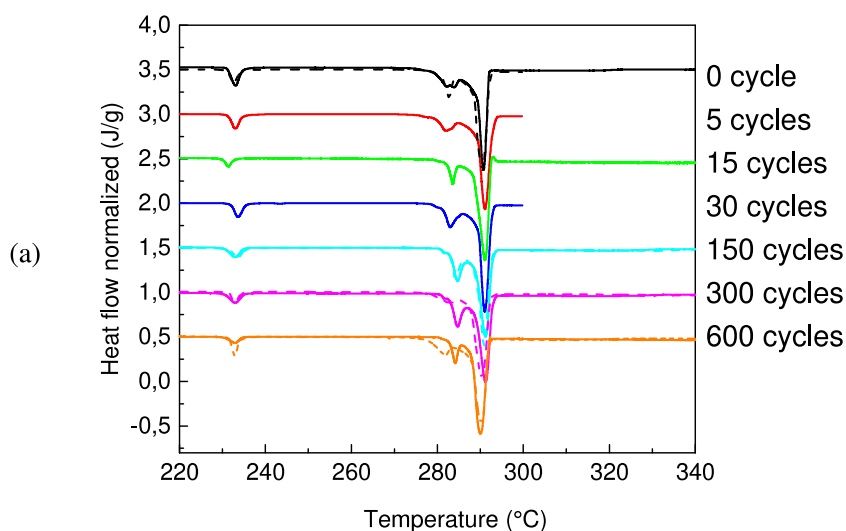


Figure 4.5. DSC thermograms (on heating, heating rate = 1 °C/min) for LiOH-LiBr mixtures at $x = 0.75$ LiOH prepared under different atmospheres (argon and air).

The possibility of simplifying the synthesis protocol by working under ambient air instead of using a protective argon atmosphere has also been investigated. To this end, a sample ($x = 0.75$) was prepared by modifying the reference protocol to this respect (thermal treatment in the oven was carried out under air). Figure 4.5 shows that there are no differences in the thermal behaviour of the sample prepared under air and that prepared using argon as a protective atmosphere.

4.5. Thermal cycling stability of the peritectic compound $\text{Li}_4(\text{OH})_3\text{Br}$



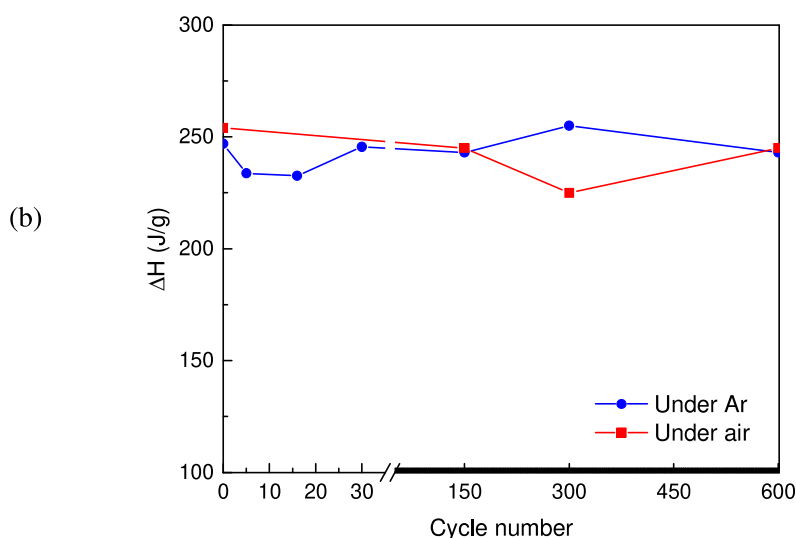


Figure 4.6. Thermal cycling of $\text{Li}_4(\text{OH})_3\text{Br}$ under Argon and Air: (a) heating DSC curves (solid line represents test under Ar / dashed line represents test under Air); (b) evolution of the enthalpy (T_2 + Peritectic) upon cycling.

To check the thermal cycling stability of the studied material, $\text{Li}_4(\text{OH})_3\text{Br}$ samples have been submitted to several heating/cooling cycles between 200 °C and 350 °C in a muffle furnace under both inert atmosphere and Air. The heating DSC curves depicted in figure 4.6.a shows that the temperature related to the peritectic reaction remains unchanged over 600 cycles both under Argon and Air atmospheres. Additionally, the evolution of the enthalpy related to the transition (T_2 + Peritectic) presented in figure 4.6.b shows as well good stability of the enthalpy over 600 cycles, both under Ar and Oxygen. It can be concluded that the peritectic $\text{Li}_4(\text{OH})_3\text{Br}$ owns excellent thermal cycling stability over 600 heating/cooling cycles with no sensitivity to the atmosphere.

4.6. Specific heat capacity and thermal conductivity of the peritectic compound $\text{Li}_4(\text{OH})_3\text{Br}$

The specific heat and thermal conductivity of $\text{Li}_4(\text{OH})_3\text{Br}$ have been measured. Figure 4.7 shows the specific heat values measured by DSC direct method, whereas the numerical values are reported in Table 4.3.

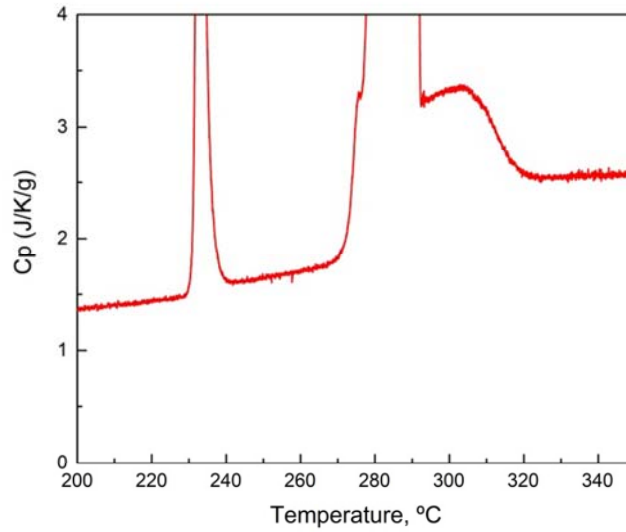


Figure 4.7. Variation of the specific heat (C_p) with temperature obtained by DSC direct method.

Table 4.3. Constant pressure specific heat values obtained by DSC direct method.

Temperature range (°C)	Specific heat values (J/g/K)	Slope of the regression line (mJ/g/K ²)
200 - 230	1.28 – 1.40	3.45
240 - 270	1.569 – 1.686	3.90
320 - 350	2.523 – 2.546	negligible

Table 4.4 presents the thermal conductivity values of $\text{Li}_4(\text{OH})_3\text{Br}$ at room temperature with good reproducibility of the tests.

Table 4.4. Thermal conductivity values of $\text{Li}_4(\text{OH})_3\text{Br}$

Test	k (W/m/K)	Average (W/m/K)	Standard deviation (W/m/K)
1	0.4740	0.4716	0.0018
2	0.4713		
3	0.4695		

4.7. Structural characterization of the peritectic compound $\text{Li}_4(\text{OH})_3\text{Br}$

As already explained, the peritectic structures form by at least two mechanisms, namely peritectic reaction and peritectic transformation [1]–[3]. The peritectic reaction starts by the

nucleation of the peritectic phase ($\text{Li}_4(\text{OH})_3\text{Br}$) at the pro-peritectic/liquid interface ($\text{LiOH(s)}/\text{Liquid}$). Then, lateral growth of the peritectic phase around the pro-peritectic phase takes place, readily forming a layer that isolates the pro-peritectic phase from the liquid. This mechanism occurs through short-range diffusion so as the reaction is usually fast and isothermal. In contrast to peritectic reaction, the peritectic transformation occurs through a long-range diffusion mechanism, where atoms migrate through the peritectic layer to form peritectic solid at the pro-peritectic/peritectic and peritectic/liquid interfaces. The atoms diffusion through the peritectic layer usually is a sluggish process so as the peritectic transformation is rarely completed. This is especially true for peritectic structures with a limited range of composition, the limit case being peritectic stoichiometric compounds where the necessary gradient of concentration for diffusion to take place is zero. Therefore, the reaction $\text{LiOH(s)} + \text{Liquid} \rightarrow \text{Li}_4(\text{OH})_3\text{Br}$ is expected to be incomplete, leading to metastable microstructures containing pro-peritectic phase LiOH(s)

The investigation of the phases present in the different samples studied by DSC has been carried out by X-ray diffraction analysis at room temperature. Figure 4.8 shows the diffraction pattern of $\text{Li}_4(\text{OH})_3\text{Br}$ synthesized following the reference protocol. It can be seen that the only phase present is $\text{Li}_4(\text{OH})_3\text{Br}$. Indeed, all the reflections corresponding to $\text{Li}_4(\text{OH})_3\text{Br}$ and no others are observed. The same results have been obtained for the samples produced with different cooling rates (0.5, 1 and 50 °C/min) as well as for the sample prepared under ambient air instead of using argon atmosphere. These results are in apparent contradiction with the mechanisms of peritectic structure formation. The fact that the pure-phase $\text{Li}_4(\text{OH})_3\text{Br}$ is achieved after the solidification process, and this regardless of the cooling rate applied, suggests that the mechanisms of formation of this compound differ from the usual ones. Although less common, it has also been reported that the peritectic phase can also nucleate and grow in the liquid without contact with the pro-peritectic phase, which will gradually dissolve. In such a case, as observed in Al-Mn [4] and Ni-Zn [5] systems, nearly phase-pure peritectic phase is achieved after the solidification process. Moreover, almost 100% pure peritectic-phase has also been reported during the solidification of highly undercooled peritectic alloys [59]–[61]. It is shown that, in such conditions, the peritectic phase directly solidifies from the undercooled melt by completely suppressing the nucleation and growth of the pro-peritectic phase, even in the case of peritectic stoichiometric compounds [9].

The results obtained by X-ray diffraction as well as those from subcooling analysis point together in these two directions. The subcooling analyses show two situations: *i*) the most frequently observed, in which the formation of $\text{Li}_4(\text{OH})_3\text{Br}$ is preceded by the nucleation and growth of the pro-peritectic phase LiOH , and *ii*) a less frequent one, in which the nucleation and growth of the pro-peritectic phase are suppressed and $\text{Li}_4(\text{OH})_3\text{Br}$ directly forms from the metastable liquid. Presumably, as already observed in other peritectic systems, $\text{Li}_4(\text{OH})_3\text{Br}$ needs neither the presence nor contact with the pro-peritectic phase to form. It nucleates and grows directly in the liquid.

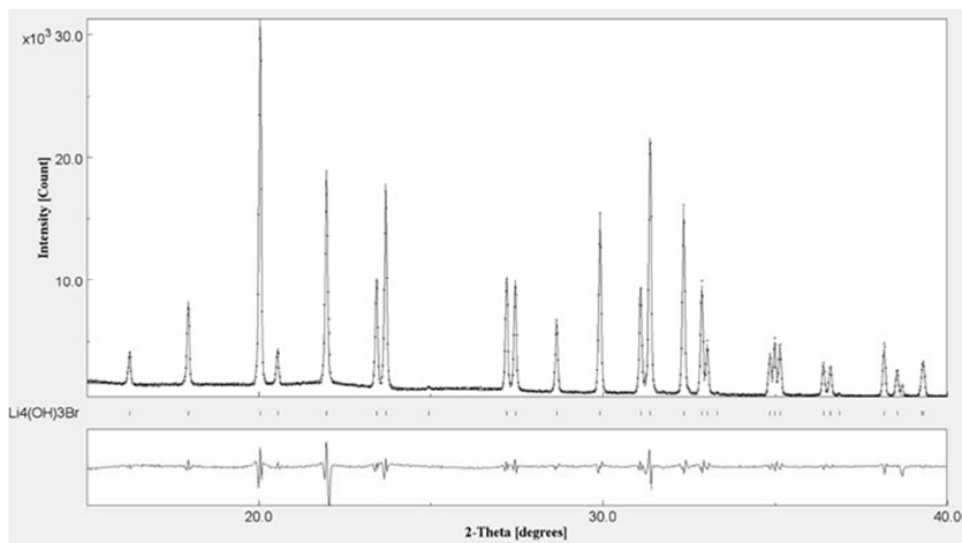


Figure 4.8. X-ray diffraction spectrum obtained at room temperature for a sample (0.75 molar fraction of LiOH).

Additional arguments in this sense are provided by TEM images (Figure 4.9), where there is no evidence of the typical microstructure expected when the peritectic compound forms following common steps of peritectic reaction and peritectic transformation. In this case, the microstructure usually has at least two clearly distinguishable phases, one of which (peritectic phase) enwraps the other one (pro-peritectic phase). As shown in Figure 4.9, this feature is not observed in our sample. Although the sample seems heterogeneous, with lighter and darker areas, these could be the result of optical effects due to the lack of flatness of the sample. To investigate the chemical composition of the sample, EDS experiments were carried out at different points of the sample, trying to quantify the O/Br atomic ratio. The results achieved reveal O/Br ratios ranging from c.a. 5/1 (darker zones) to c.a. 1/1 (lighter zones), meaning that the chemical composition of the sample is likely not homogeneous. However, this result is in

apparent contradiction with the results of X-ray analysis, which indicate the existence of a single phase ($\text{Li}_4(\text{OH})_3\text{Br}$) in the sample. Although these discrepancies would deserve to be analyzed in more detail, we tend at the moment to give greater confidence to the results of X-rays, which are much more accurate and reliable than those of EDS.

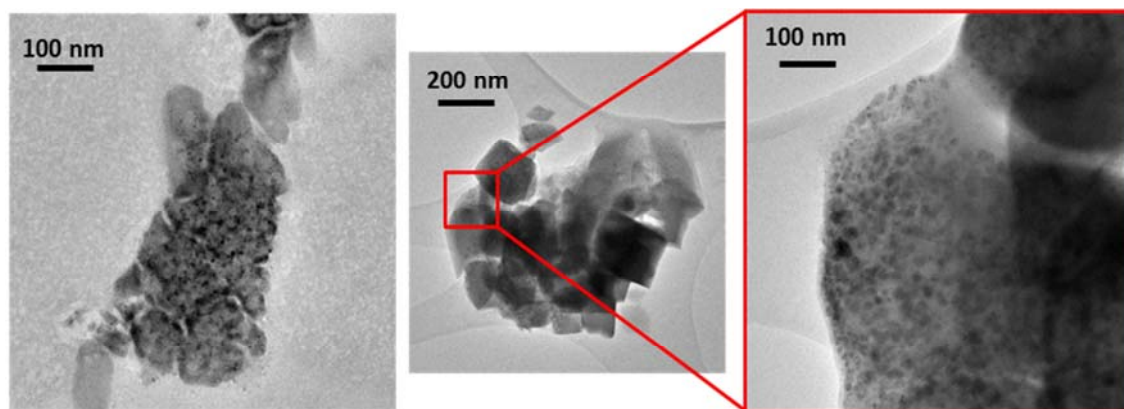


Figure 4.9. TEM images of a sample (0.75 molar fraction of LiOH) prepared by the reference protocol described in section 2.1.

4.8. Assessment of $\text{Li}_4(\text{OH})_3\text{Br}$ as storage material in solar power applications

Among solar energy technologies, high-pressure (c.a. 100 bar) Direct Steam Generation (DSG) is the one with heat storage requirements that best matches the characteristics of $\text{Li}_4(\text{OH})_3\text{Br}$. In DSG solar thermal power plants, the availability of isothermal storage capacity is a precondition for the effective operation of storage systems. Indeed, since a significant share of the energy is transferred at constant temperature (steam condensing/water evaporation), nearly isothermal storage and release of energy is advantageous. Systems based on sensible heat storage, which are developed for today's parabolic trough power plants using thermal oil as a heat transfer medium in the absorbers, are unemployable since this concept would require a significant variation of the steam pressure between storage and discharge. A straightforward and often proposed solution for isothermal energy storage is the use of energy related to phase transition, usually between solid and liquid states [10], [11]. Here, condensing steam from the solar field is used to liquefy the storage material during the charging cycle, while the storage provides steam during the discharging process by solidification of the storage material. The melting temperature of the storage material lies between the saturation temperature of the steam from the solar field and the saturation temperature in the steam cycle. In high-pressure (c.a. 100 bar) DSG power plants, transition

temperatures close to 300 °C are hence required. Table 4.5 includes a list of phase change materials that have already been considered for this application, although sodium nitrate is the only one that have been thoroughly investigated [12], [13] and used in relevant-scale prototypes [11].

Table 4.5. Phase change materials with melting point in the temperature range from 280 °C to 310 °C and enthalpy of melting above 150 J/g (data from Ref. [14]).

Material	Melting point (°C)	Enthalpy of melting (J/g)
NaNO_3	310	174
NaNO_2	282	180
$\text{NaOH}/\text{Na}_2\text{CO}_3$ (7.2 %)	283	340
$\text{NaCl}(5.7\%)/\text{NaNO}_3(85.5\%)/\text{Na}_2\text{SO}_4$	287	176
$\text{NaCl}/\text{NaNO}_3$ (5 %)	284	171
$\text{KNO}_3(10\ %)/\text{NaNO}_3$	290	170

Compared to the materials in Table 4.5, $\text{Li}_4(\text{OH})_3\text{Br}$ results are very competitive because it provides a specific latent heat storage capacity of 247 J/g in a narrow temperature range from 280 °C to 289 °C. Only the eutectic mixture $\text{NaOH}/\text{Na}_2\text{CO}_3$ (7.2 %) is able to provide higher storage capacity, but it contains a high amount of NaOH, which is very hygroscopic and corrosive. Considering that NaNO_3 is the reference material for TES in DSG application, Table 4.6 provides a more detailed comparison with $\text{Li}_4(\text{OH})_3\text{Br}$. It can be seen that energy density is the main asset of $\text{Li}_4(\text{OH})_3\text{Br}$ compared to NaNO_3 . Indeed, the volumetric latent heat storage capacity of $\text{Li}_4(\text{OH})_3\text{Br}$ (141 kWh/m³) is 54% higher than that of NaNO_3 , meaning that $\text{Li}_4(\text{OH})_3\text{Br}$ offers the opportunity of reducing significantly the volume of the storage tank (35 % approx. for same storage capacity). Low expansion/shrinkage of the material during the peritectic reaction/transdition is another remarkable feature of $\text{Li}_4(\text{OH})_3\text{Br}$. Whereas the volume expansion on melting of NaNO_3 is quite high (almost 11%), that of $\text{Li}_4(\text{OH})_3\text{Br}$ is only 3 %. This has two kinds of advantages: on the one hand, the dead volume needed to accommodate the volumetric expansion of the storage material is lower (3 % vs. 11 %); on the other hand, the mechanical stress on the construction elements of the storage

system (e.g., tank, heat exchanger) is also lower and, therefore, they may have a longer lifetime. On the contrary, the price per kWh of $\text{Li}_4(\text{OH})_3\text{Br}$ is 42% higher than NaNO_3 (14.6 \$/kWh vs. 10.3 \$/kWh). and the thermal conductivity is lower (0.59 W/m/K vs. 0.47 W/m/K). However, contrary to what might be thought, this does not necessarily have a negative impact on the cost of investment. On the one hand, as already mentioned, the volume of the storage tank can be 35% approx. lower in the case of $\text{Li}_4(\text{OH})_3\text{Br}$ - based systems due to the higher volumetric energy density of the peritectic compound. On the other hand, although the thermal conductivity is lower, the surface of the heat exchanger can be reduced by 10% approx. in $\text{Li}_4(\text{OH})_3\text{Br}$ -based systems because of less volume of storage material required for the same storage capacity and power. To illustrate this point, let us consider a TES system with storage capacity Q and charging/discharging time t_{ch} . To simplify the analysis, we assume a parallel plates TES system configuration so as the charging time and storage capacity can be approached by [15]:

$$t_{ch} = (\rho \Delta H e^2) / (4k \Delta T) \quad \& \quad Q = S \rho \Delta H e \quad (eq. 4.1)$$

ρ , ΔH and k represent the density, the latent heat, and the thermal conductivity of the storage material, respectively. S is the surface of the heat exchanger, and e represents the thickness of the storage material plates (the distance between the plates of the heat exchanger). From the equations above and thermophysical properties of NaNO_3 and $\text{Li}_4(\text{OH})_3\text{Br}$ in Table 6, it follows that:

$$\frac{S_{\text{NaNO}_3}}{S_{\text{Li}_4(\text{OH})_3\text{Br}}} = \left(\frac{(\rho \Delta H k)_{\text{Li}_4(\text{OH})_3\text{Br}}}{S(\rho \Delta H k)_{\text{NaNO}_3}} \right)^{1/2} \approx 1.1$$

Considering that the storage tank and the heat exchanger usually account for more than 60% of the total investment cost of the storage system, the reduction of in tank volume (35 % approx.) and heat exchanger size (10 % approx.) in $\text{Li}_4(\text{OH})_3\text{Br}$ -based systems compared to NaNO_3 -based systems can likely compensate the higher specific price of $\text{Li}_4(\text{OH})_3\text{Br}$.

Table 4.6. Physical properties and price of NaNO_3 [12], [13], [16], and $\text{Li}_4(\text{OH})_3\text{Br}$.

	NaNO_3	$\text{Li}_4(\text{OH})_3\text{Br}$
Melting/transition temperature ($^{\circ}\text{C}$)	306	280-289
Enthalpy of melting/transition (J/g)	175	247
Thermal conductivity (s) (W/m/K)	0.59	0.47
Thermal conductivity (l) (W/m/K)	0.51 – 0.57	n.a
Specific heat (s) (J/g/K)	1.78	1.68
Specific heat (l) (J/g/K)	1.61 – 1.82	2.52
Density (l) (g/cc)	1.89 – 1.93	2.06 ^(*)
Volume expansion (%)	10.7	3.0
Volumetric energy density (kWh/m^3)	92	141
Cycling stability	Proven	Proven
Corrosivity	Moderate	Moderate
Price (\$/kg) ^(**)	0.5	1.0
Price (\$/kWh)	10.28	14.6

^(*) Not measured. Calculated from LiOH-LiBr phase diagram implemented in FactSage 7.3. software.

^(**) Wholesale market prices from Alibaba.

4.9. $\text{Li}_4(\text{OH})_3\text{Br}$ /Carbon composites

Carbon nanoparticles have already been used to enhance the thermophysical properties of high-temperature phase change materials (PCM), such as carbonate mixtures [17]–[19] and nitrate mixtures [20]–[22]. The addition of a small amount of carbon nanoparticles to the PCM usually leads to increased values of thermal conductivity. Sometimes, other beneficial effects have also been observed, such as increased values of specific heat or enthalpy of melting. Often, improvement of the cycling stability of the material has been reported as well. In this part, the effect of adding different types of carbon nanoparticles on the storage capacity of the studied peritectic salt has been investigated. The carbon nanoparticles employed are fullerenes C_{60} , multi-walled carbon nanotubes (MWCNT), and reduced graphene oxide (rGO).

The nanocomposites were prepared as described in section 2.1.4, with nanoparticles loading of 1 wt. % and 10 wt. % and submitted to 15 heating/cooling cycles between 200 $^{\circ}\text{C}$ and 350 $^{\circ}\text{C}$ in a muffle furnace under an inert atmosphere. DSC tests were performed every 5 cycles to

analyze the eventual evolution of the storage properties of the material. The results achieved are reported in Figure 4.10 and Table 4.7. The values of transition temperature reported in Table 4.7 correspond to the onset temperature of the endothermic peak related to the peritectic reaction (3rd peak in the DSC thermograms), whereas the values of enthalpies of transition in Table 4.7 and Figure 4.10 include both the enthalpy of melting of $\text{Li}_4(\text{OH})_3\text{Br}$ at 289 °C (3rd peak in the DSC thermograms) and that of the decomposition of $\text{Li}_3(\text{OH})_2\text{Br}$ at 279 °C (2nd peak in the DSC thermograms).

Table 4.7. Peritectic temperature (T_p) and enthalpy (ΔH) of nanocomposites obtained by addition of carbon nanoparticles (C60: fullerene C60; MWCNT: multi-walled carbon nanotubes; rGO: reduced graphene oxide) to the salt.

	Before cycling		After cycling		Calculated
	T_p (°C)	ΔH (J/g)	T_p (°C)	ΔH (J/g)	ΔH_{cal} (J/g)
Without nanoparticles	289	247	289	243	247
1 wt. % C ₆₀	288	250	288	246	245
10 wt. % C ₆₀	288	233	287	206	223
1 wt. % MWCNT	288	250	288	252	245
10 wt. % MWCNT	286	204	280	188	223
1 wt. % rGO	288	246	288	242	245
10 wt. % rGO	287	196	287	174	223

Calculated values in the last column are: $\Delta H_{\text{cal}} = \Delta H \cdot f$ (eq 4.2)

Where f represents the mass fraction of salt within the composite.

As shown in Table 4.7, before cycling, the addition of nanoparticles does not involve significant changes in the peritectic temperature value (286 - 288 °C) compared to that of pure salt (289 °C). The slight depression observed (1 - 3 °C) can be due to the infiltration of part of the salt into the nanoparticle structure, which is in all the cases characterized by small pore size able to induce Gibbs-Thomson effects. After cycling, the peritectic temperature remains unchanged for all composites except for the composite with 10 wt. % MWCNT, where an additional shift of – 6 °C is observed in T_p . This suggests that the infiltration of the salt into the MWCNT has been increasing over cycles.

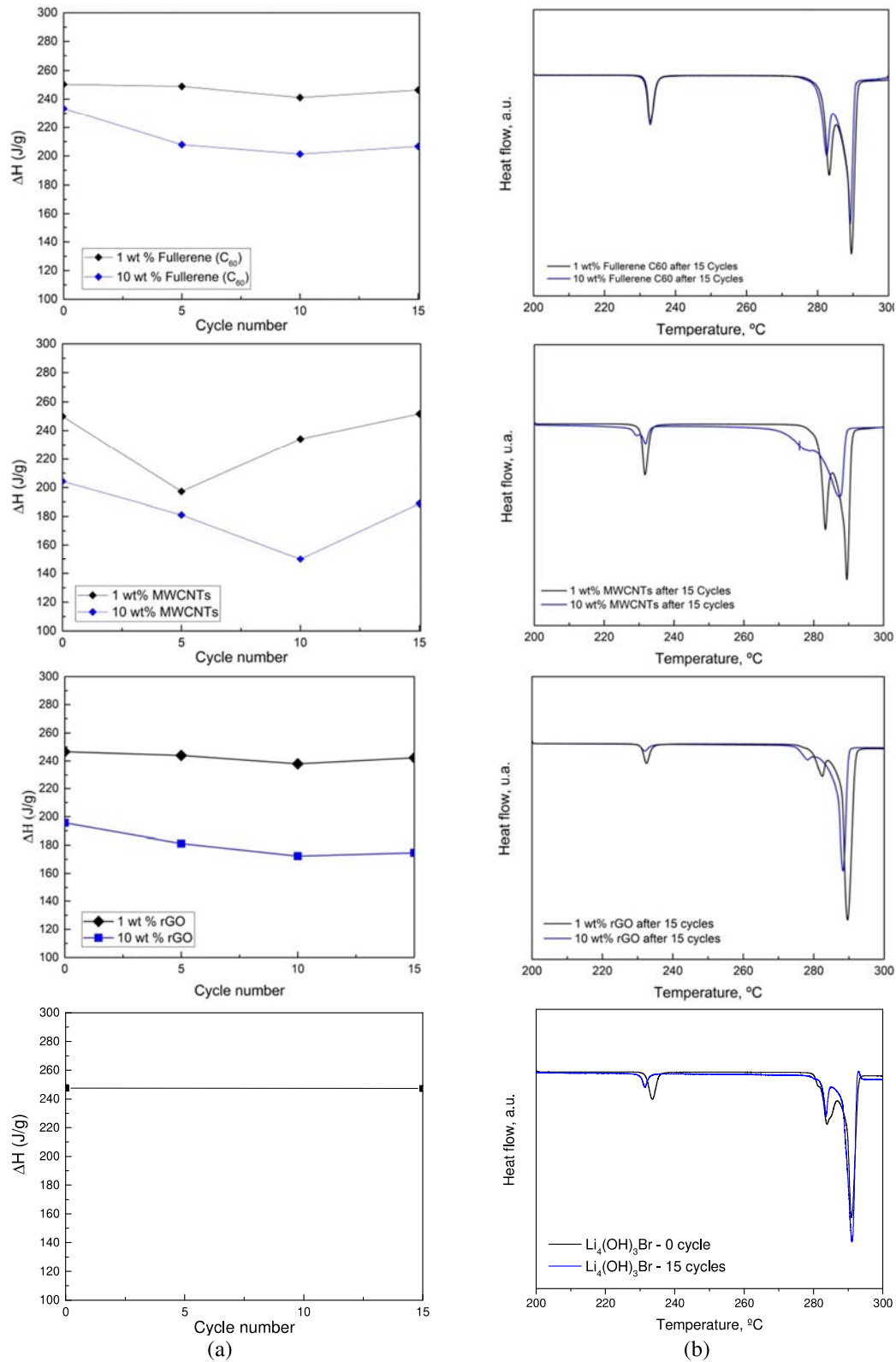


Figure 4.10. Effect of adding carbon nanoparticles on the cycling behavior of the storage material at $x = 0.75$ LiOH: (a) variation of the enthalpy of peritectic reaction over cycling; (b) Heating DSC thermograms after cycling.

Regarding enthalpy values, the composites with 1 wt. % nanoparticle loading shows quite good performances. Their values of the reaction enthalpy range from 246 J/g (rGO) to 250 J/g (C60) before cycling and remain almost unchanged after 15 thermal cycles and close to $\Delta H_{\text{cal}} = 245 \text{ J/g}$. However, we can notice that measured ΔH is 6-10 J/g higher than ΔH_{cal} for composites with nanoparticles C60 and MWCNT, suggesting the existence of interfacial effects favouring the nucleation and ordering of the crystalline phase of the salt on the surface of the carbon nanoparticles. Indeed, the fundamental work by Radhakrishnan et al. [23], [24] and Alba-Simionesco et al. [25] about confinement effects on freezing and melting processes shows that strongly attractive walls materials (e.g., carbon nanoparticles C60 and MWCNT studied in this work), promote the heterogeneous nucleation of the crystalline phase and can lead to increased latent heats provided that the subsequent growth of the crystal is not constrained by the geometry of the pore, thus achieving a highly ordered crystalline phase. This effect is not apparent in the case of rGO-based composites likely because of the chemistry of its surface (80-87% of C and 13-17% of O according to the supplier), which makes it less hydrophobic than pure carbon C60 and MWCNTs particles.

Contrary to composites with 1 wt. % nanoparticle loading, the composites with higher nanoparticles content (10 wt. %) show poor performances. The values of the reaction enthalpy range from 196 J/g (rGO) to 233 J/g (C60) before cycling, and they are reduced by 7.5 % (MWCNT) to 11.5 % (C60) after 15 thermal cycles. At the end of the cycling process, the reaction enthalpy of all composites is not only below that of the pure salt (247 J/g) but also below the expected value taking into account the salt content of the composites ($\Delta H_{\text{cal}} = 223 \text{ J/g}$). This means that there is either a problem of chemical compatibility between the nanoparticles and the salt or, more likely, some kind of interaction between both that modifies the thermodynamic equilibria of the salt, such as strong confinement of part of the salt into the porous structure of the nanoparticles which suppresses, totally or partially, the phase transitions. In fact, as discussed below, there is a close relationship between the enthalpy changes observed and the geometry characteristics of the different carbon nanoparticles used.

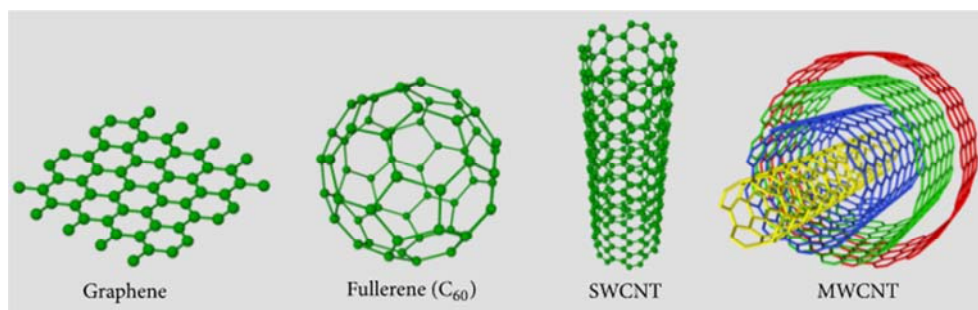


Figure 4.11. Carbon-based nanotubes: Graphene, Fullerene C₆₀, and MWCNT [26]

Fullerene C60 has a closed-cage polyhedral structure composed of 60-80 carbons disposed in pentagon and hexagon configuration (Figure 4.11). C60 is 0.7 nm in diameter so as its volume over surface ratio is $V/S = 0.116 \text{ nm}$ approx. C-C and C=C bonds lengths are 0.1455 Å and 0.1391 Å [27], respectively, resulting in a C-hexagons diagonal of 0.291 nm. This means that neither LiOH (ionic radius: 0.2-0.3 nm) nor LiBr (ionic radius: 0.217 nm) can penetrate into the C60 structure. On the contrary, lithium has an ionic radius of 0.09 nm so as its intercalation into C60 structure may occur. Indeed, carbon-based nanostructures are usual materials for electrodes in batteries and capacitors due to their ability of lithium insertion and diffusion. Therefore, we can consider that lithium intercalation into C60 nanoparticles is taking place when $\text{Li}_4(\text{OH})_3\text{Br}$ is in the molten state, thus leading to a reduction of the reaction enthalpy because of the modification of the salt composition. Obviously, the enthalpy reduction increases with the nanoparticle loading, as shown in Figure 4.10.a. In addition, the process of lithium insertion progresses through the melting/solidification cycles until saturation of C60 nanoparticles is reached. Thus, the reaction enthalpy of the material progressively decreases, then stabilizes from the tenth cycle onwards at 206 J/g approx. for the composite with a 10 wt.% loading of nanoparticles (Figure 4.10.a).

Reduced graphene oxide (rGO) is a multilayered structure with 0.8-1.09 nm interlayer spacing [28]. Carbon atoms of the layers are disposed in hexagon configuration, with bonds length of 0.142 nm. The number of carbon layers of the rGO used in this work has been determined by XRD according to the method proposed by Scherrer [29] as follow:

According to Scherrer equation:

$$B(2\theta) = \frac{K \lambda}{L \cos \theta} \quad [29] \quad (\text{eq 4.3})$$

- B is the peak width at half maximum.
- 2θ is the angle of the incident beam
- L is the crystallite size (L)
- λ is the wavelength
- K is the Scherrer constant: it depends on how the width is determined, the shape of the crystal, and the size distribution. As proposed by Warren et al. [30] different K values refer to different crystal's orientation. Indeed, $K = 0.94$ for crystalline domain in the dimension normal to the layers (called L_c)

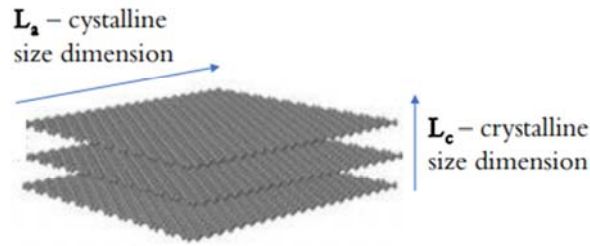


Figure 4.12. Multilayer graphene

Thus, from eq 4.3 we have
$$L_c = \frac{0.94 \lambda}{B \cos \theta} \quad (\text{eq 4.4})$$

According to the XRD results of the tested rGO and Bragg's law $2d \sin \theta = n\lambda$ (eq 4.5):

- $B = 8.902753^\circ = 0.155 \text{ rad}$
- Peak position $2\theta = 23.734^\circ = 0.414 \text{ rad}$
- $\lambda = 1.5406 \text{ \AA}$
- $d = 3.7458$

$$\text{Thus, } L_c = \frac{0.94 \times 1.5406}{0.155 \cos 0.207} = 9.34$$

The number of rGO layers = $(L_c / d\text{-spacing}) + 1 = (9.34 / 3.7458) + 1 = 3.49$ [31]

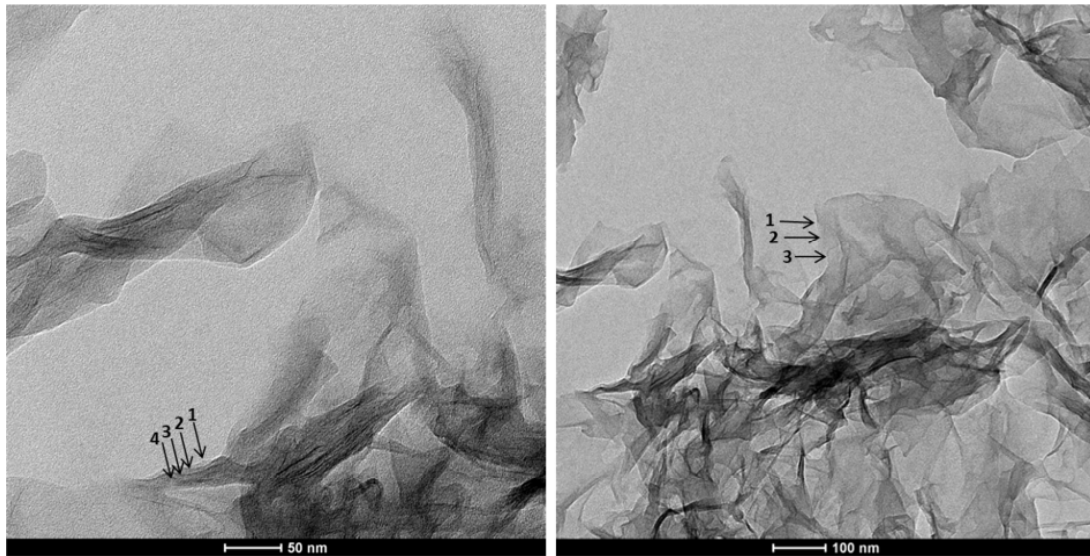


Figure 4.13. TEM image of the tested rGO sheets

The tested rGO particles are formed of 3-4 layers (see figure 4.13). Taking into account the interlayer spacing of rGO (0.8-1.09 nm), as well as the ionic radius of LiOH (0.2-0.3 nm) and LiBr (0.217 nm), it is possible that, in addition to lithium insertion, there is a phenomenon of

salt infiltration into the structure of the rGO which explains why the enthalpy loss is higher in the rGO-based compounds than in the C60-based compounds. On the one hand, the interlayer spacing of the carbon layers of rGO is only 2-3 times higher than the size of LiOH and LiBr so as the solidification of infiltrated salt is likely suppressed. On the other hand, the volume over surface ratio of rGO is much higher ($V/S = 0.8 - 1.68 \text{ nm}$, depending on the interlayer spacing) than that of C60 ($V/S = 0.116 \text{ nm}$), meaning a much higher capacity for lithium insertion and salt infiltration. Again, we observe that the salt infiltration into the rGO structure is not instantaneous but takes place progressively along the heating/cooling cycles. As shown in Figure 4.10.a, the saturation of rGO (maximum allowed salt infiltration within the rGO structure) is reached at the 10th cycle for the composite with 10 wt.% of nanoparticles.

CNTs are cylindrical shaped carbon nanostructures with carbon atoms arranged in hexagon configuration. They are divided into two kinds, SWCNT (single-walled carbon nanotubes) and MWCNTs (multi-walled carbon nanotubes), SWCNT is a single rolled graphene sheet with the edges stitched together, and MWCNT is several graphene tubes binded together by weak Van der Waals forces (see figure 4.11). MWCNTs have been chosen in this study because they can be produced in industrial scale. According to the supplier, the external diameter of MWNCT used is about 8 nm, while the internal diameter is 3-5 nm. This leads to a volume over a surface ratio of $V/S = 0.28 - 0.78 \text{ nm}$, which is close to the lower limit value of rGO. Compared to the size of LiOH and LiBr molecules, the internal diameter of MWCNTs is large enough for salt infiltration takes place as it was the case for rGO. However, because of the less V/S ratio, the capacity to host salt into the carbon structure for the same nanoparticles loading is less than in rGO case and, consequently, the loss of enthalpy is a bit lower as well (Figure 4.10.a). Contrary to C60-based and rGO-based composites, in which the enthalpy smoothly decreases along with the cycling processes, erratic behavior is observed for MWCNT-based composites (Figure 4.10.a). TEM has been used to investigate whether this erratic behavior could be related to changes in the microstructure of the composites along cycles. However, no substantial differences in TEM images have been appreciated before and after cycling. On the contrary, as shown in Figure 4.14, MWCNT distribution in the composites is quite heterogeneous in all cases. The left side of Figure 4.14 allows clearly appreciating dark and light zones corresponding to regions with higher and less salt content, respectively. On the other hand, the magnification on the right side shows MWCNTs forming tangles embedded into the salt. These structural features are promoted by the high form factor of MWCNT nanoparticles (length = 0.5 - 2 μm , diameter <

8 nm), and it is not observed in C60-based and rGO-based composites, where the distribution of nanoparticles is quite homogeneous. Therefore, the erratic changes of enthalpy values observed during the cycling process of MWCNT-based composites are likely related to the sampling which is done on the composite to get proper samples for DSC analyses.

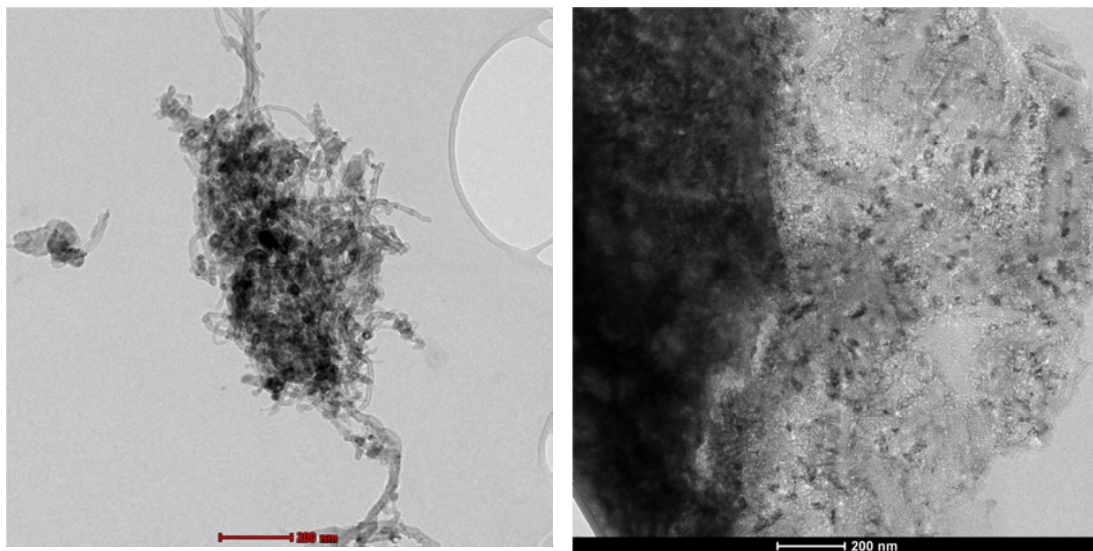


Figure 4.14. TEM images of MWCNT-based composite with 10 wt. % nanoparticle loading.

4.10. Conclusion

In this chapter, the thermal and structural properties of the peritectic stoichiometric compound $\text{Li}_4(\text{OH})_3\text{Br}$ have been thoroughly investigated. This encompasses the characterization of $\text{Li}_4(\text{OH})_3\text{Br}$ as a storage material for applications close to 300 °C by measuring transition temperatures (280-289 °C), reaction enthalpies (247 J/g), specific heats (c.a. 1.68 J/g/K in solid, 2.52 J/g/K in liquid) and thermal conductivity (0.47 W/m/K at room temperature). The effect of the synthesis conditions on the storage properties has been investigated as well. It is concluded that neither the cooling rate applied during the synthesis stage nor the type of atmosphere used (ambient air and protective argon atmosphere) has an influence on the material's performance. The stability of the material to thermal cycling has also been analyzed, showing good cycling stability. Moreover, particular attention is paid to the study of subcooling phenomena and elucidation of mechanisms of formation of $\text{Li}_4(\text{OH})_3\text{Br}$ by combining DSC with X-ray diffraction and TEM. It is shown that the mechanism of formation of $\text{Li}_4(\text{OH})_3\text{Br}$ differs from the most common one consisting of so-called peritectic reaction followed by peritectic transformation. As already observed in other peritectic systems, $\text{Li}_4(\text{OH})_3\text{Br}$ needs neither the presence nor contact with the pro-peritectic phase to

form. It nucleates and grows directly from the melt resulting in a pure-phase $\text{Li}_4(\text{OH})_3\text{Br}$. A first attempt to enhance the storage capacity of the material by the addition of different types of carbon nanoparticles, such as fullerene C60, reduced graphene oxide and multi-walled carbon nanotubes, has been carried out. It is shown that the addition of a low amount of carbon nanoparticles (1 wt. %) can lead to a slight increase of the reaction enthalpy due to interfacial effects between the salt and the surface of the nanoparticle. However, increasing further the amount of carbon nanoparticles (10 wt. %) has a detrimental impact on the reaction enthalpy, likely due to the infiltration of part of the salt into the nanoporous structure of the nanoparticles and subsequent partial or total suppression of phase transitions. In any case, from a practical point of view, the addition of carbon nanoparticles does not represent a clear advantage in terms of latent heat storage capacity: at best, an increase of 5 J/g over 247 J/g (< 2 %) has been observed. $\text{Li}_4(\text{OH})_3\text{Br}$ has been assessed as a storage material for high-pressure DSG solar power plants through comparison with reference material NaNO_3 . The main advantages of $\text{Li}_4(\text{OH})_3\text{Br}$ are higher volumetric latent heat storage capacity (+ 54%) and lower volume changes during phase transitions (3 % vs. 11 %), which would translate into smaller storage tanks (-33 %), lower size heat exchangers and longer lifetime.

4.11. References

- [1] G. P. H.E. Exner, *Peritectic Structures, Metallography and Microstructures*, Vol 9, *ASM Handbook, American Society for Metals*. 1985.
- [2] H. Fredriksson, *Solidification of Peritectics. Casting, Metals Handbook, 9th ed., ASM International*. 1988.
- [3] H. W. Kerr, J. Cisse, and G. F. Bolling, "On equilibrium and non-equilibrium peritectic transformations," *Acta Metallurgica*, vol. 22, no. 6, pp. 677–686, Jun. 1974, doi: 10.1016/0001-6160(74)90077-7.
- [4] H. Fredriksson and T. Nylen, "Mechanism of peritectic reactions and transformations," *Metal Science*, vol. 16, no. 6. Taylor & Francis, pp. 283–294, Jun. 01, 1982, doi: 10.1179/030634582790427370.
- [5] H. E. E. G. Petzow, *Zur Kenntnis Peritektischer Umwandlungen, Radex Rundsch* 3-4. 1967.
- [6] W. Löser, M. Leonhardt, H. G. Lindenkrenz, and B. Arnold, "Phase selection in undercooled binary peritectic alloy melts," *Materials Science and Engineering A*, vol. 375–377, no. 1-2 SPEC. ISS., pp. 534–539, Jul. 2004, doi: 10.1016/j.msea.2003.10.138.
- [7] G. Phanikumar, K. Biswas, O. Funke, D. Holland-Moritz, D. M. Herlach, and K. Chattopadhyay, "Solidification of undercooled peritectic Fe-Ge alloy," *Acta Materialia*, vol. 53, no. 13, pp. 3591–3600, Aug. 2005, doi: 10.1016/j.actamat.2005.03.053.
- [8] W. Zhai and B. Wei, "Direct nucleation and growth of peritectic phase induced by substantial undercooling condition," *Materials Letters*, vol. 108, pp. 145–148, Oct.

- 2013, doi: 10.1016/j.matlet.2013.06.084.
- [9] P. Lü and H. P. Wang, "Direct formation of peritectic phase but no primary phase appearance within $\text{Ni}_{83.25}\text{Zr}_{16.75}$ peritectic alloy during free fall," *Scientific Reports*, vol. 6, no. 1, pp. 1–7, Mar. 2016, doi: 10.1038/srep22641.
 - [10] W. D. Steinmann and R. Tamme, "Latent heat storage for solar steam systems," in *Journal of Solar Energy Engineering, Transactions of the ASME*, Feb. 2008, vol. 130, no. 1, pp. 0110041–0110045, doi: 10.1115/1.2804624.
 - [11] D. Laing, C. Bahl, T. Bauer, D. Lehmann, and W. D. Steinmann, "Thermal energy storage for direct steam generation," *Solar Energy*, vol. 85, no. 4, pp. 627–633, Apr. 2011, doi: 10.1016/j.solener.2010.08.015.
 - [12] T. Bauer, D. Laing, and R. Tamme, "Characterization of sodium nitrate as phase change material," *International Journal of Thermophysics*, vol. 33, no. 1, pp. 91–104, Jan. 2012, doi: 10.1007/s10765-011-1113-9.
 - [13] A. Lomonaco, D. Haillot, E. Pernot, E. Franquet, and J. P. Bédécarrats, "Sodium nitrate thermal behavior in latent heat thermal energy storage: A study of the impact of sodium nitrite on melting temperature and enthalpy," *Solar Energy Materials and Solar Cells*, vol. 149, pp. 81–87, May 2016, doi: 10.1016/j.solmat.2015.12.043.
 - [14] M. M. Kenisarin, "High-temperature phase change materials for thermal energy storage," *Renewable and Sustainable Energy Reviews*, vol. 14, no. 3, Pergamon, pp. 955–970, Apr. 01, 2010, doi: 10.1016/j.rser.2009.11.011.
 - [15] V. Alexiades and A. D. Solomon, "MATHEMATICAL MODELING OF MELTING AND FREEZING PROCESSES," 1976.
 - [16] R. Tamme, T. Bauer, J. Buschle, D. Laing, H. Müller-Steinhagen, and W.-D. Steinmann, "Latent heat storage above 120°C for applications in the industrial process heat sector and solar power generation," *International Journal of Energy Research*, vol. 32, no. 3, pp. 264–271, Mar. 2008, doi: 10.1002/er.1346.
 - [17] Z. Zhang, Y. Yuan, S. Alelyani, X. Cao, and P. E. Phelan, "Thermophysical properties enhancement of ternary carbonates with carbon materials for high-temperature thermal energy storage," *Solar Energy*, vol. 155, pp. 661–669, Oct. 2017, doi: 10.1016/j.solener.2017.07.010.
 - [18] Y. B. Tao, C. H. Lin, and Y. L. He, "Preparation and thermal properties characterization of carbonate salt/carbon nanomaterial composite phase change material," *Energy Conversion and Management*, vol. 97, pp. 103–110, Jun. 2015, doi: 10.1016/j.enconman.2015.03.051.
 - [19] F. Ye, Z. Ge, Y. Ding, and J. Yang, "Multi-walled carbon nanotubes added to $\text{Na}_2\text{CO}_3/\text{MgO}$ composites for thermal energy storage," *Particuology*, vol. 15, pp. 56–60, Aug. 2014, doi: 10.1016/j.partic.2013.05.001.
 - [20] E. Hamdy, L. Saad, F. Abulfotuh, M. Soliman, and S. Ebrahim, "Enhancement of Molten Nitrate Thermal Properties by Reduced Graphene Oxide and Graphene Quantum Dots," *ACS Omega*, vol. 5, no. 34, pp. 21345–21354, Sep. 2020, doi: 10.1021/acsomega.0c01291.
 - [21] Y. Wu, J. Li, M. Wang, H. Wang, and Y. Zhao, "Preparation and Thermophysical Properties of High Thermal Conductive Solar Salt/MWCNTs Composite Materials," *ChemistrySelect*, vol. 4, no. 15, pp. 4521–4527, Apr. 2019, doi: 10.1002/slct.201900249.
 - [22] Y. Wu *et al.*, "Solar salt doped by MWCNTs as a promising high thermal conductivity material for CSP," *RSC Advances*, vol. 8, no. 34, pp. 19251–19260, 2018, doi: 10.1039/c8ra03019g.
 - [23] R. Radhakrishnan, K. E. Gubbins, A. Watanabe, and K. Kaneko, "Freezing of simple fluids in microporous activated carbon fibers: Comparison of simulation and

- experiment,” *Journal of Chemical Physics*, vol. 111, no. 19, pp. 9058–9067, Nov. 1999, doi: 10.1063/1.480261.
- [24] R. Radhakrishnan and K. E. Gubbins, “Free energy studies of freezing in slit pores: An order-parameter approach using Monte Carlo simulation,” *Molecular Physics*, vol. 96, no. 8, pp. 1249–1267, 1999, doi: 10.1080/00268979909483070.
- [25] C. Alba-Simionesco *et al.*, “Effects of confinement on freezing and melting,” *Journal of Physics Condensed Matter*, vol. 18, no. 6. IOP Publishing, p. R15, Feb. 15, 2006, doi: 10.1088/0953-8984/18/6/R01.
- [26] M. L. Casais-Molina, C. Cab, G. Canto, J. Medina, and A. Tapia, “Carbon Nanomaterials for Breast Cancer Treatment,” *Journal of Nanomaterials*, vol. 2018, 2018, doi: 10.1155/2018/2058613.
- [27] W. I. F. David *et al.*, “Crystal structure and bonding of ordered C_{60} ,” *Nature*, vol. 353, no. 6340, pp. 147–149, 1991, doi: 10.1038/353147a0.
- [28] T. Liu, L. Tian, N. Graham, B. Yang, W. Yu, and K. Sun, “Regulating the Interlayer Spacing of Graphene Oxide Membranes and Enhancing their Stability by Use of PACl,” *Environmental Science and Technology*, vol. 53, no. 20, pp. 11949–11959, Oct. 2019, doi: 10.1021/acs.est.9b04418.
- [29] “P. Scherrer, ‘Bestimmung der Grösse und der inneren Struktur von Kolloidteilchen mittels Röntgenstrahlen,’ *Nachr. Ges. Wiss. Göttingen* 26 (1918) pp 98-100. - Recherche Google.”
[https://www.google.com/search?q=P.+Scherrer%2C+“Bestimmung+der+Grösse+und+der+inneren+Struktur+von+Kolloidteilchen+mittels+Röntgenstrahlen%2C”+Nachr.+Ges.+Wiss.+Göttingen+26+\(1918\)+pp+98-100.&rlz=1C1GCEU_fr&oq=P.+Scherrer%2C+“Bestimmung+der+Grösse+und+der+inneren+Struktur+von+Kolloidteilchen+mittels+Röntgenstrahlen%2C”+Nachr.+Ges.+Wiss.+Göttingen+26+\(1918\)+pp+98-100.&aqs=chrome..69i57.183j0j4&sourceid=chrome&ie=UTF-8](https://www.google.com/search?q=P.+Scherrer%2C+“Bestimmung+der+Grösse+und+der+inneren+Struktur+von+Kolloidteilchen+mittels+Röntgenstrahlen%2C”+Nachr.+Ges.+Wiss.+Göttingen+26+(1918)+pp+98-100.&rlz=1C1GCEU_fr&oq=P.+Scherrer%2C+“Bestimmung+der+Grösse+und+der+inneren+Struktur+von+Kolloidteilchen+mittels+Röntgenstrahlen%2C”+Nachr.+Ges.+Wiss.+Göttingen+26+(1918)+pp+98-100.&aqs=chrome..69i57.183j0j4&sourceid=chrome&ie=UTF-8) (accessed Mar. 31, 2021).
- [30] B. E. Warren, P. Bodenstein, and IUCr, “The diffraction pattern of fine particle carbon blacks,” *urn:issn:0365-110X*, vol. 18, no. 2, pp. 282–286, Feb. 1965, doi: 10.1107/S0365110X65000609.
- [31] B. E. Warren and P. Bodenstein, “The diffraction pattern of fine particle carbon blacks,” *Acta Crystallographica*, vol. 18, no. 2, pp. 282–286, Mar. 1965, doi: 10.1107/s0365110x65000609.

Chapter 5: Corrosion of container materials for CSP with $\text{Li}_4(\text{OH})_3\text{Br}$ peritectic salt

5.1. Introduction

In TES field, the corrosion study of the container material with the storage media allows determining the lifetime of the storage unit on the one hand and contributing to the design of the storage system on the other hand. Based on the corrosion rate, it is possible to measure the thickness of the heat exchangers and the storage tank for operating for a defined period of time. Besides, the results allow identifying the optimal operating conditions and environmental parameters to limit the corrosion issue as much as possible. The objective of this chapter is to provide first experimental results to shed a light about the corrosion behaviour of potential container materials with the peritectic $\text{Li}_4(\text{OH})_3\text{Br}$. Two steel samples extensively considered as TES containers with molten salts for CSP plants were tested, namely carbon Steel A516.Gr70 and Stainless Steel 316. Cycling corrosion tests were carried out at 350 °C under both air and protective Argon atmosphere. Cycling corrosion tests were chosen in this study since they are more adequate to the intended application of this material considering that the mechanism of the peritectic reaction/transformation involves a melting/solidification processes. The applied corrosion protocol is described in subchapter 2.2.1.6. To avoid any possible interference of impurities that may affect the corrosion phenomena, high purity anhydrous Lithium Hydroxide (purity 98%) and Lithium Bromide (purity 99+ %) were used for the synthesis of the peritectic compound $\text{Li}_4(\text{OH})_3\text{Br}$. Different aspects of the corrosion study have been addressed, including i) identification of corrosion products. ii) Characterization of the morphology of the corrosion layer and surface degradation. iii) Study of the effect of different working conditions (cycle number, atmosphere) on the corrosion mechanism. iv) Determination of the corrosion rate based on statistical cross-section analysis after the corrosion test. v) Characterization of $\text{Li}_4(\text{OH})_3\text{Br}$ salt after the corrosion tests to check its stability under different test conditions and to verify whether there is any salt degradation due to dissolution of impurities and corrosion products. Different characterization techniques were used for the investigations including X-ray

Diffraction (XRD) analysis, Microscopy (SEM) and Energy Dispersive X-ray Spectroscopy (EDX).

5.2. Corrosion of Carbon Steel A516.Gr70 with $\text{Li}_4(\text{OH})_3\text{Br}$

Figure 5.1 presents cleaned and dried CS samples after the corrosion tests. The corrosion layer formed at the surface of the sample is black and uniform. The colour is getting darker while increasing the number of cycles. Macroscopically, no differences are noticed in colour or the surface state of the samples tested under Air and Argon. It is noticed a shiny surface appearance in some parts of the samples.

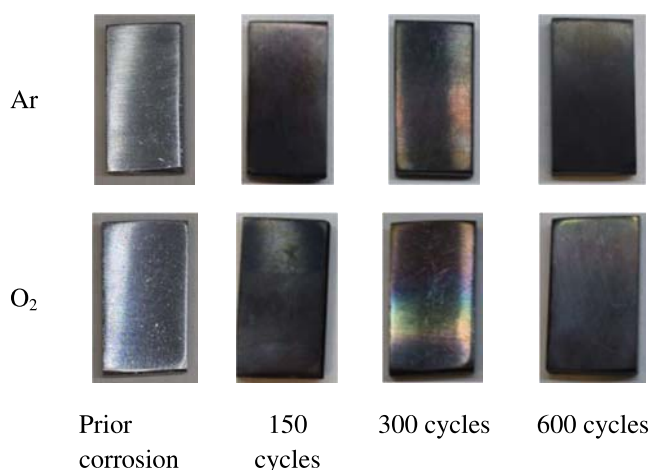
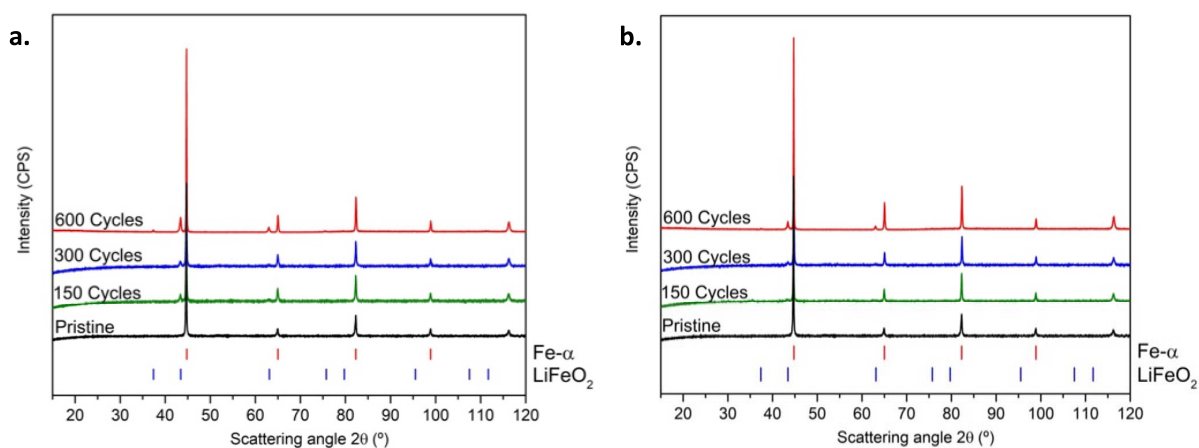


Figure 5.1. Images of CS samples before and after corrosion tests for different cycle numbers under different atmospheres.

5.2.1. Analysis of Carbon steel

5.2.1.1. X-ray diffraction analysis



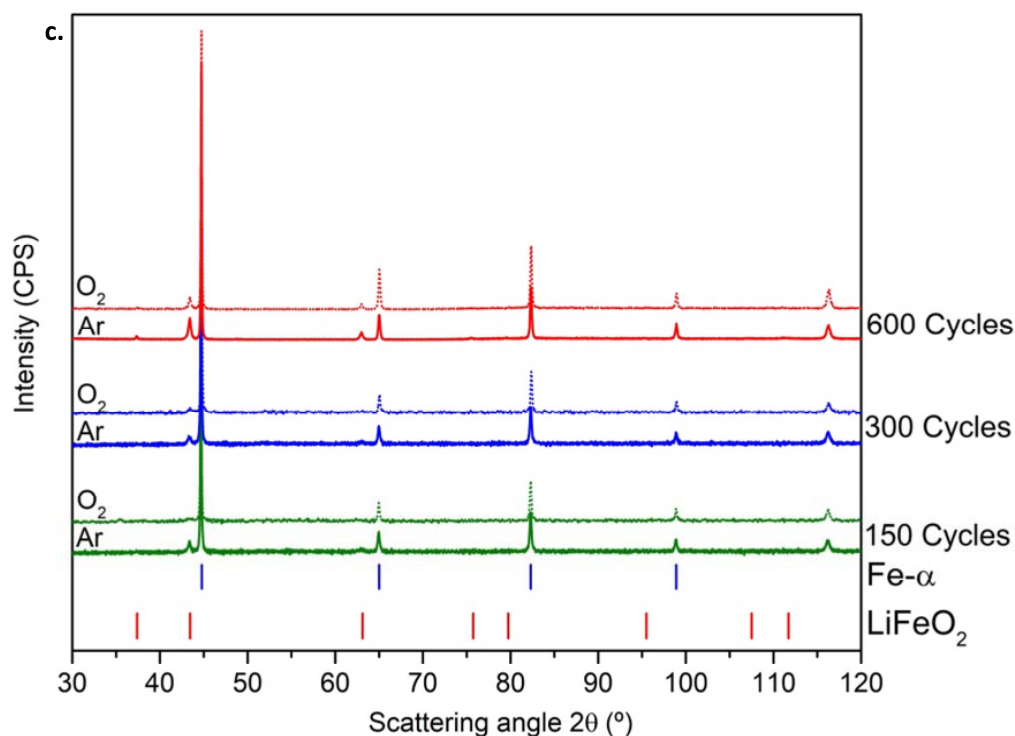
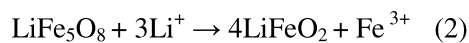


Figure 5.2. XRD patterns of the surface of CS after corrosion tests at 350 °C for different cycle numbers: a) under Ar; b) under air; c) superposition of both patterns.

The surfaces of CS A516.Gr70 samples were analyzed by XRD in order to determine the nature of the corrosion layer. Patterns were recorded in a 2θ angular range between 10° and 120° . Figure 5.2.a and 5.2.b show the patterns of the samples cycled under Argon atmosphere and air atmosphere, respectively. In each figure, four patterns are presented corresponding to the samples cycled for 150, 300, and 600 cycles, additionally to the pattern of the pristine material. Figure 5.2.c depicts the superposition of the patterns undergoing the same number of cycles under different atmospheres in order to highlight any possible modification of the peaks intensities and positions. Regardless to the atmosphere, the Iron phase was observed in all the samples similarly to the pristine material. A simple normalization of the patterns is applied in order to qualitatively compare the various results. For all the samples tested both under air and Argon atmosphere, the formed corrosion layer consists of a Lithium iron oxide phase LiFeO_2 . One can observe that, the peaks of LiFeO_2 phase are hardly visible for the CS cycled under air atmosphere for 150 cycles, particularly the most representative peaks at 37° , 43° and 63° are absent. This observation indicates that the thickness of the corrosion layer formed in this sample is below the sensitivity of the XRD ($< 2\mu\text{m}$). Additionally, regardless to the atmosphere, the intensities of the peaks related to LiFeO_2 phase increase with the increase

of the cycling duration, indicating the growth of the corrosion reaction over cycling. Moreover, the relatively high intensities of the iron phase observed for the CS samples after the corrosion tests can be a sign of the low thickness of the corrosion layer where the X-ray beam can penetrate and amply reach the iron phase. Furthermore, as it can be clearly noticed in figure 5.2.c, for the same cycle number, the intensities of the peaks related to LiFeO₂ phase are more pronounced for samples tested under Ar compared to the ones tested under air. These results indicate that the corrosion reaction of the carbon steel with Li₄(OH)₃Br salt is more active under Argon atmosphere. Overall, the corrosion process using Carbon steel A516.Gr70 is not only affected by the exposure time (cycle number) factor but also by the type of atmosphere present during the test.

The formation of the Lithium iron oxide phase (LiFeO₂) presumably takes place through an oxidation followed by lithiumization of the iron oxide phase. The lithiumization takes place through inward Lithium cation diffusion into Fe₂O₃ phase at the interface Fe₂O₃/Salt thanks to the small ionic radius of the latter (0.09 nm). This corrosion mechanism is common in lithium containing salts (LiNaKNO₃; Li₂CO₃-Na₂CO₃-K₂CO₃) [1] due to high basicity of the lithium components. The lithiumization takes place as previously reported by Cheng et al. [2] following reaction (1) where LiFe₅O₈ is formed through Li⁺ diffusion into Fe₂O₃ phase. LiFeO₂ is formed following reaction (2) coating the spinel phase. The growth of LiFe₅O₈ is ended by the total consumption of the iron oxide phase. Similarly, LiFe₅O₈ phase will be consumed by the inward growth of LiFeO₂. the iron oxide phase formed on the surface of carbon steel is very thin [3], thereby it will be consumed rapidly. For this reason it was observed in the XRD pattern. Following this mechanism, the growth of lithium iron oxide phase is expected to be more important under air atmosphere due to the presence of oxygen with promote the CS oxidation. This expectation is in disagreement with the obtained results, where more intense corrosion reaction was observed for the sample tested under Argon.



The formation of LiFeO₂ in addition to its polymorphs resulting from the corrosion of carbon steel in contact with LiOH in aqueous solution under hydrogen was also reported by Graydon et Kirk [7] where LiFeO₂ showed to form through lithium intercalation into the iron hydroxide structure Fe(OH)₃.

5.2.1.2. Cross-section analysis of the corrosion layer using SEM / EDS

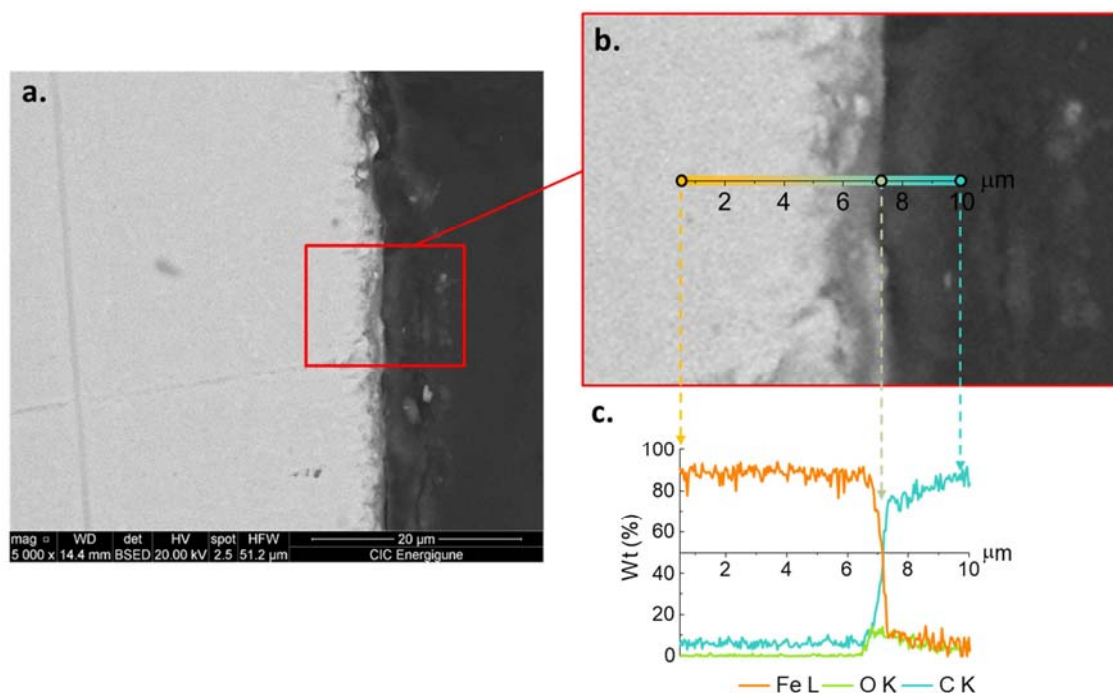
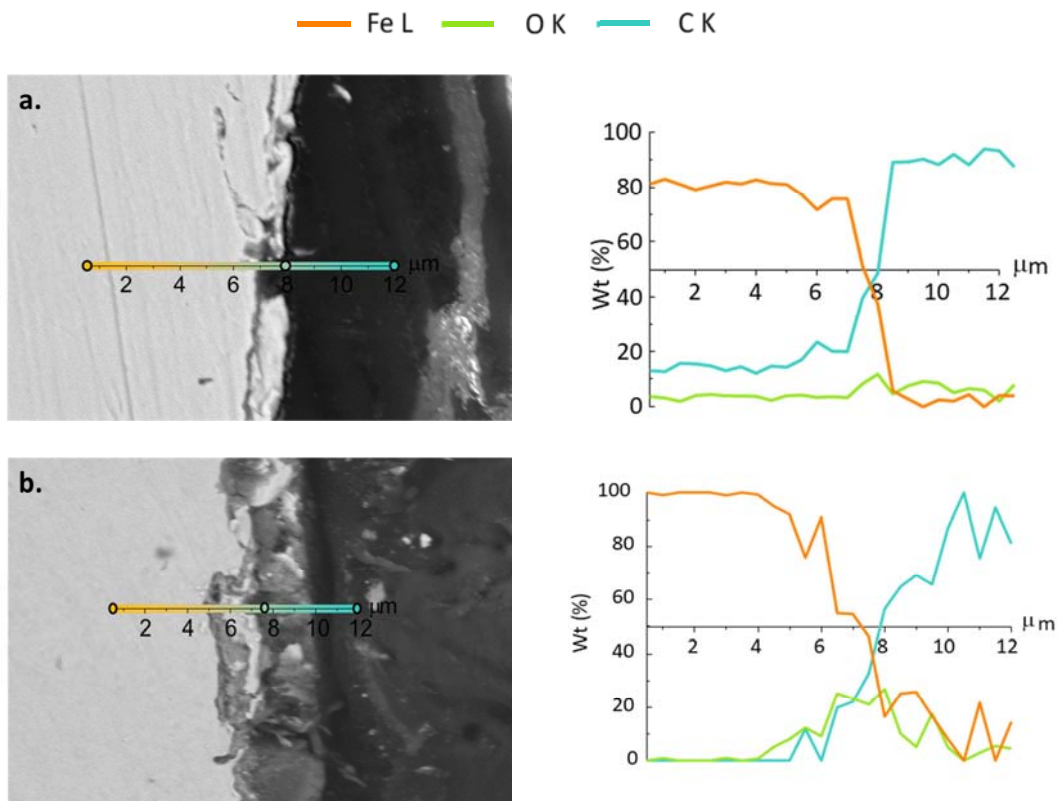


Figure 5.3. Cross-sectional analysis of the carbon steel tested under Ar after 150 corrosion cycle. a) SEM micrograph of the cross-section; b) enlargement of the region where the EDS is performed; c) EDS profile (Iron in orange line, Oxygen in green line, and Carbon in blue line).

In order to elucidate the mechanism of corrosion and to evaluate the depth of the corrosion attack, the elemental distribution of the principal elements together with the SEM imaging of the cross-section were carried out. Figure 5.3 shows an example of the cross-section analysis of Carbon steel with $\text{Li}_4(\text{OH})_3\text{Br}$ salt after 150 corrosion cycles under Argon atmosphere. Carbon steel samples tested under both Argon atmosphere and air atmosphere for 150, 300 and 600 cycles were analyzed and presented in a similar way. The EDS profiles of the cross-section and the corresponding SEM images of the samples are presented in figure 5.4. For the samples tested under Argon, after 150 cycles, there is no evidence of the corrosion layer according to the cross-section micrograph. After 300 cycles, evidence of corrosion starts to appear. The cross-section micrograph show a roughness of the surface with presence of cracks and surface peeling due to the detachment of the lithium iron oxide phase formed as product of the corrosion. After 600 cycles, the cross-section micrograph shows a sever roughness and deterioration of the surface state of the CS. The thickness of LiFeO_2 phase increased over cycling and due to the poor adherence of the latter, the peeling phenomena is more important in this sample. The EDS analyses of the samples undergoing 300 and 600 cycles show a step in the Carbon appearing before reaching the interface between the metallic samples and the

resin simultaneously with a gradual decrease of the Iron concentration and a jump in the Oxygen concentration. These results confirm the presence of the corrosion layer LiFeO_2 detached from the surface of the carbon steel causing the roughness of the surface. The resin penetrated the holes and surface defects created by the detached corrosion layer which manifested as a gradual increase of the carbon as shown in figure 5.5. However, considering the sensitivity of the EDS technique, the concentration of the element can't be determined accurately.

For the samples tested under air, the corrosion layer is not visible after 150 and 300 cycles. Meanwhile, after 600 cycles, the cross-section micrograph shows a roughness of the sample due to corrosion attack and formation of LiFeO_2 phase. The thickness of the corrosion layer was carried out by a statistical cross-section analysis. The results are presented in table 5.3.



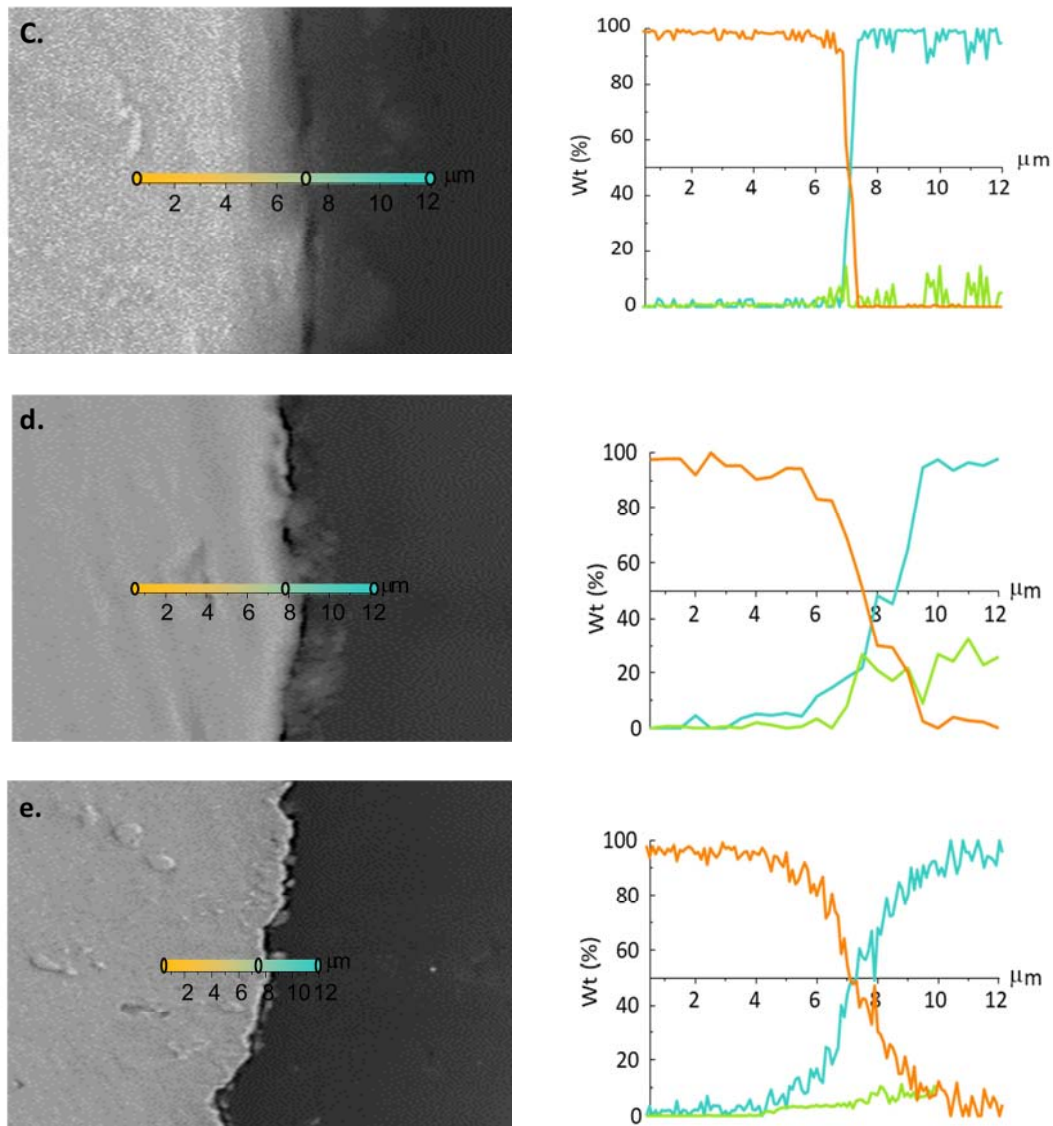
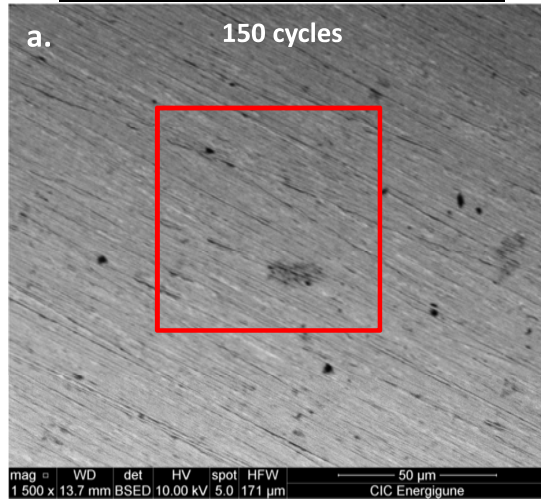


Figure 5.4. SEM-EDS cross-sectional analysis of the carbon steel samples tested under: Argon atmosphere (a) 300 cycles; (b) 600 cycles. Air atmosphere (c) 150 cycles; (d) 300 cycles; (e) 600 cycles.

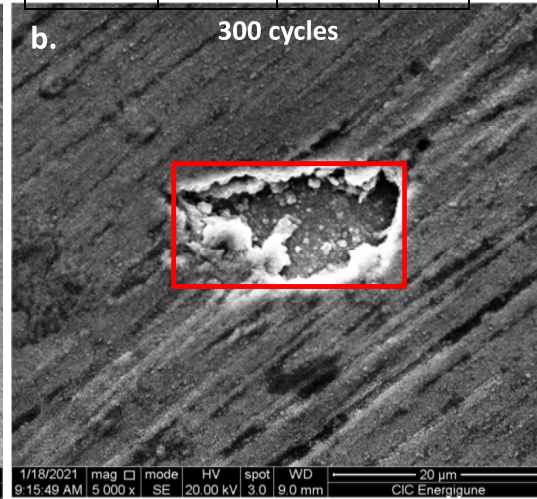
5.2.1.3. Surface analysis and morphology of the corrosion products formed on carbon steel

5.2.1.3.1. Carbon Steel tested under Argo

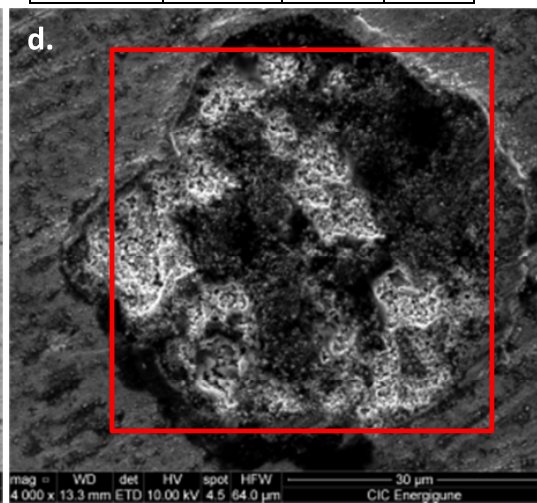
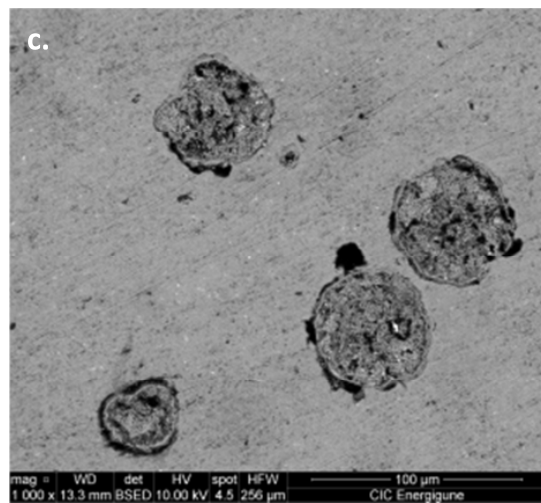
Element	C	O	Fe
Wt %	00.19	04.17	95.64



Element	C	O	Fe
Wt %	00.00	06.71	93.29



Element	C	O	Fe
Wt %	10.01	28.33	61.66



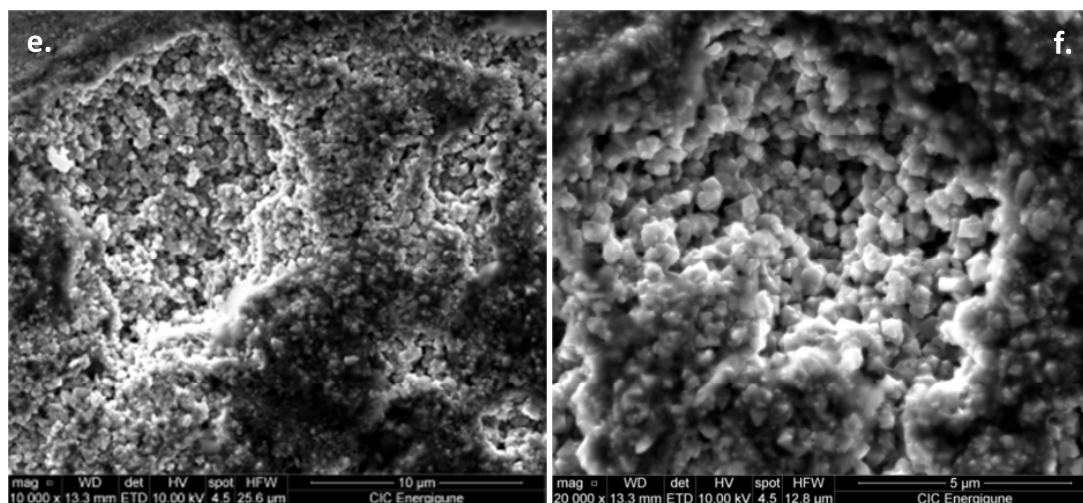


Figure 5.5. SEM images combined with EDS analysis of the surface of the carbon steel after corrosion test with $\text{Li}_4(\text{OH})_3\text{Br}$ salt at 350°C under Argon: a) After 150 cycles; b) after 300 cycles; c,d,e,f) after 600 cycles at different magnifications;

For all the samples cycled under Argon atmosphere, regardless to the number of cycles they have undergone, the localised EDS analysis shows the presence of oxygen in variable concentrations. Considering that Lithium is not detectable, this is an indication of the formation of the Lithium ferrite (LiFeO_2) corrosion layer as detected by XRD analysis. Regarding the surface morphology, the surface of CS tested under Argon atmosphere was analyzed by SEM as shown in Figure 5.5. The sample cycled for 150 cycles shows a homogenous surface morphology with absence of any surface defect or surface peeling (figure 5.5.a). Analysing the surface of CS after 300 cycles (figure 5.5.b), the morphology shows the presence of surface defect scattered all over the surface due to corrosion. The density of defects present in the surface drastically increased for the CS cycled for 600 cycles compared to the sample subjected to 300 cycles. As it is shown in figure 5.5.c,d, circular spots with a diameter ranging from 34 to 54 μm were observed. These spots have a non-homogeneous distribution all over the surface of the sample and are the results of the detachment of the corrosion product LiFeO_2 from the surface of the CS which results in holes with different sizes and corrosion penetration rates. This result is in correlation with the cross-section results presented above (section 5.2.1.2) where the observed roughness and the deterioration of the surface of the samples tested under Argon can be confirmed by the detachment of the corrosion layer LiFeO_2 due to its poor adherence to the surface of the steel. The high magnification of the surface defects presented in figure 5.5.e,f show a cubic-like morphology with an average cube diameter of 400 nm, which corresponds to the typical morphology of lithium iron oxide [8], [9]. The high corrosion penetration observed for the CS

after 600 cycles compared to the sample cycled over 300 times is due to the high degree of corrosion which is expressed by the important oxygen concentration obtained for this sample.

5.2.1.3.2. Carbon Steel tested under air

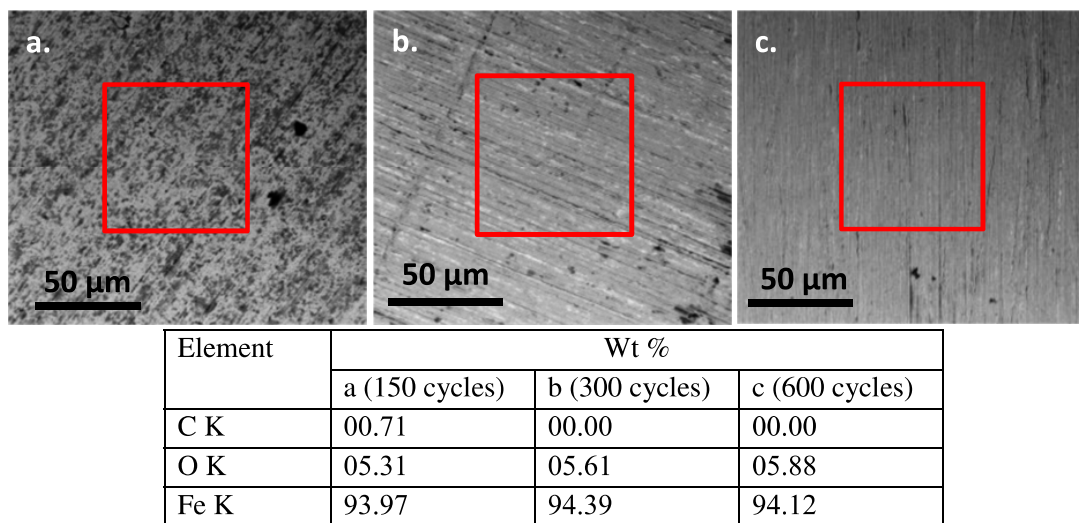


Figure 5.6. SEM micrographs combined with EDS analysis of the surface of carbon steel samples tested under air: a) after 150 corrosion cycles; b) after 300 corrosion cycles; c) after 600 corrosion cycles.

The surface analyses of the CS samples cycled under air atmosphere and the corresponding EDS elemental results are presented in figure 5.6. Unlike the CS cycled under Argon atmosphere, there is no evidence of surface defects. The surface morphology is homogeneous. The EDS results show the presence of oxygen as a sign of the presence of the corrosion layer LiFeO_2 . Taking into account the accuracy of EDS analysis, the oxygen concentrations presented in table 5.6 gives only a rough idea about the evolution of the corrosion layer. The results show no increase of the corrosion layer over cycling.

5.2.2. Analysis of the peritectic salt $\text{Li}_4(\text{OH})_3\text{Br}$

5.2.2.1. Thermal analysis

In order to study the thermal behaviour of $\text{Li}_4(\text{OH})_3\text{Br}$ while in contact with the different steel samples under various working conditions (atmosphere, exposure time), and to check for any degradation phenomena, the salt was analyzed by DSC technique. After each corrosion test, carried out under Argon or air, cycled for 150, 300, or 600 times, salt samples were analyzed after extraction from two different zones of the crucible. One is the salt which was on the top of the crucible, distant from the steel sample, and second is the salt which was in

direct contact with the steel sample. This protocol was followed considering the fact that the corrosion test was static and the salt composition would change heterogeneously due to possible corrosion effect. It is noteworthy that, when the salt samples extracted from different zones of the same test crucible present similar values of enthalpy and temperature of the peritectic reaction, an average of the enthalpy is presented in table 5.1. Otherwise, the values of both samples are presented as well as both DSC curves. The DSC curves of the salt samples obtained upon heating (at 1 K/min) are presented in figure 5.7 together with the reference samples corresponding to the salt cycled without being in contact with the steel samples. The temperatures and enthalpies related to the peritectic reaction of the corrosion salt samples, the reference samples and the pristine salt are reported in table 5.1. All the depicted heating DSC curves present three endothermic peaks regardless to the atmosphere (argon, air) during the corrosion test. Similarly to the pristine salt, the first and second peaks occur at 230-231 °C and 279 °C, respectively, corresponding to the formation/decomposition of the intermediate compound $\text{Li}_3(\text{OH})_2\text{Br}$. The third peak appears at 288-289 °C corresponding to the peritectic reaction ($\text{Li}_4(\text{OH})_3\text{Br} \rightarrow \text{LiOH (s)} + \text{L}$). The liquidus is hardly visible and it was estimated to be ≥ 340 °C. It is important to note that the enthalpy values reported in this chapter include both the enthalpy of melting of $\text{Li}_4(\text{OH})_3\text{Br}$ at 289 °C (3rd peak in the DSC thermograms) and that of the decomposition of $\text{Li}_3(\text{OH})_2\text{Br}$ at 279 °C (2nd peak in the DSC thermograms), whereas the reaction temperature corresponds to the onset temperature of the endothermic peak related to the peritectic reaction.

As explained in the subchapter 4.5, $\text{Li}_4(\text{OH})_3\text{Br}$ presents an excellent thermal cycling stability with no sensitivity to the working atmosphere. Analysing the results reported in table 5.1 and the DSC curves, it can be observed that the temperature related to the peritectic reaction remains unchanged regardless to the exposure time (cycling duration), the working atmosphere, and the zone from which the salt is extracted. Regarding the reaction enthalpy, different thermal behaviours were observed in respect to the atmosphere presents during the test. For the salt samples tested under Argon atmosphere, a gradual decrease of the enthalpy was recorder while increasing the cycling duration. Taking into account the experimental error of the DSC equipment, an average enthalpy loss of about 2% was recorded after 150 cycles when compared to the one of the reference salt. For the salt undergoing 300 cycles, the enthalpy loss was twice higher for the salt in contact with the CS (9 %), compared to the salt distant from the steel sample (4%). Similar observations were reported for the salt undergoing 600 cycles with a larger enthalpy loss (13% for the salt in contact with CS). The expected gradual enthalpy loss observed over cycling is related to the corrosion reaction which impacts

the salt composition, more drastically the salt in direct contact with the steel sample. In the case of the salt tested under air atmosphere, the reaction enthalpy remains homogeneously stable for over 300 cycles. For the sample undergoing 600 cycles, the salt distant from the CS shows a stable enthalpy (+ 1%), whereas the salt in contact with the CS shows a decrease of the enthalpy by 8%. This result shows that the chemical reaction between the Lithium hydroxide and the iron phase impact in the first place the salt in contact with CS resulting in the change of its composition. The results reported in this section are in correlation with the analysis of the CS samples.

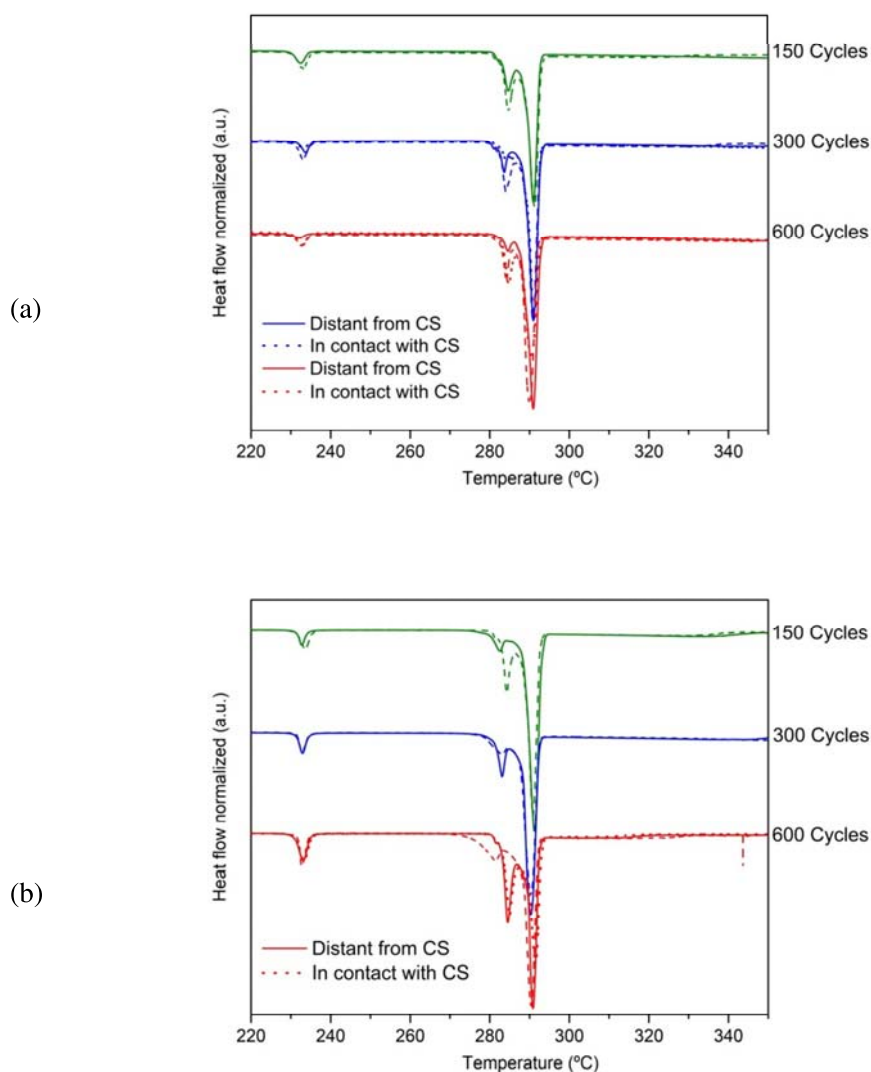


Figure 5.7. Heating DSC curves obtained on cooling at (1 K/min) of $\text{Li}_4(\text{OH})_3$ extracted after corrosion tests with Carbon steel for different cycle numbers: a) under Ar; b) under air; (solid line represents the corrosion sample; dash line represents the reference sample).

Table 5.1. Temperatures and enthalpies corresponding to the peritectic reaction of $\text{Li}_4(\text{OH})_3\text{Br}$ after corrosion tests with CS under Argon and air compared to reference values.

Cycle number	Corrosion under Ar				Corrosion under O_2			
	T_P (°C)	$T_{\text{Reference}}$ (°C)	ΔH_P^* (J/g)	$\Delta H_{\text{Reference}}^*$ (J/g)	T_P (°C)	$T_{\text{Reference}}^*$ (°C)	ΔH_P^* (J/g)	$\Delta H_{\text{Reference}}^*$ (J/g)
0 Cycle	289		251		289		251	
150 Cycles	289	289	236	243	289	289	246	245
300 Cycles	289 ^a 289 ^b	289	242 ^a 230 ^b	255	288	287	246	250
600 Cycles	288 ^a 288 ^b	288	223 ^a 209 ^b	243	289 ^a 289 ^b	288	251 ^a 222 ^b	245

* These values correspond to the addition of the enthalpy of the decomposition of $\text{Li}_3(\text{OH})_2\text{Br}$ at 279 °C and that of $\text{Li}_4(\text{OH})_3\text{Br}$ at 289 °C.

^a Sample distant from CS

^b Sample in direct contact with CS

5.2.2.2. Microstructural analysis

As explained before, the corrosion tests using CS carried out both under air and Argon atmospheres show the formation of the corrosion layer LiFeO_2 on the surface of the samples. Particularly, for the CS sample tested under Argon and cycled 600 times, the corrosion layer tend to detach from the surface of the CS inducing surface defects (see figure 5.5). $\text{Li}_4(\text{OH})_3\text{Br}$ salt was analyzed by SEM-EDS to investigate the possible presence of residue of the detached part of the corrosion layer LiFeO_2 within the salt.

The SEM images of the salt samples undergoing 600 cycles and the corresponding EDS results are presented in figure 5.8. Considering that the cycling corrosion tests carried out were static, two parts of the salt were analyzed. The solidified salt situated on the top of the crucible, distant from the steel sample. And the salt in direct contact with the CS sample. The results presented in figure 5.8 are in correlation with the results of the cross-section analysis and the surface analysis of the CS. Indeed, For the CS samples cycled under air atmosphere, the EDS analysis of both salt samples (in contact with CS, and the distant from CS) presented in figure 5.8.C&d only shows the presence of oxygen and Bromine, components of $\text{Li}_4(\text{OH})_3\text{Br}$. A total absence of Iron was noticed. This result is supported by the absence of surface peeling mechanism for CS tested under air. Consequently, no lithium iron oxide phase residues were expected to be detected in the salt. The composition of the salt in contact with the CS is expected to change and it is confirmed by the enthalpy loss observed for the salt tested under Oxygen over 600 cycles. For the CS cycled under Argon atmosphere, the EDS

analysis of the salt sample which was in direct contact with the CS, presented in figure 5.8.b, shows, in addition to the expected Oxygen and Bromine (components of the salt), the presence of Iron in small concentration. Considering that Lithium is not detectable by EDS technique, the presence of Iron is related to the residue of the corrosion layer LiFeO_2 detached from the surface of CS after 600 cycles under Argon.

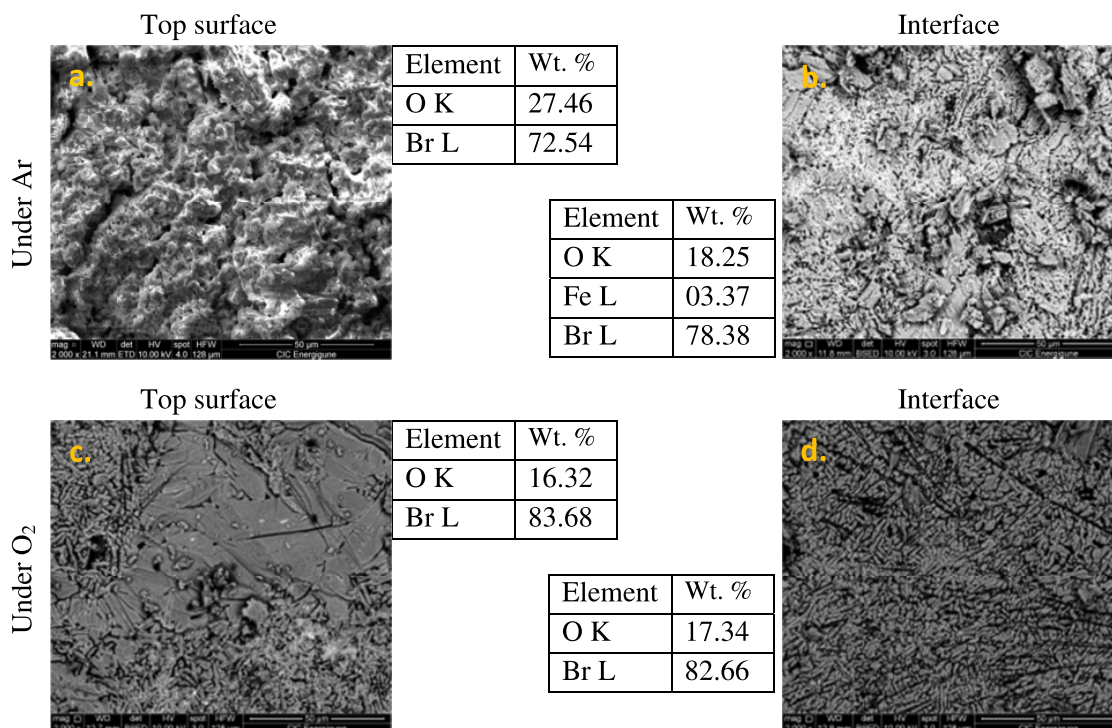


Figure 5.8. SEM and EDX analyses of the salt $\text{Li}_4(\text{OH})_3\text{Br}$ after 600 corrosion cycles with the carbon steel: (a,b) under Ar; (c,d) under O_2 ; (a,c) the salt situated on the top of the corrosion crucible ; (b,d) the salt in contact with the metallic sample.

5.3. Corrosion of Stainless steel AISI 316L with $\text{Li}_4(\text{OH})_3\text{Br}$

Figure 5.9 presents cleaned and dried SS316 samples after the corrosion tests. The corrosion layer formed at the surface of the sample has a golden uniform colour. The colour is more pronounced for the samples tested under air. It is noticed a shiny surface appearance for all the samples.

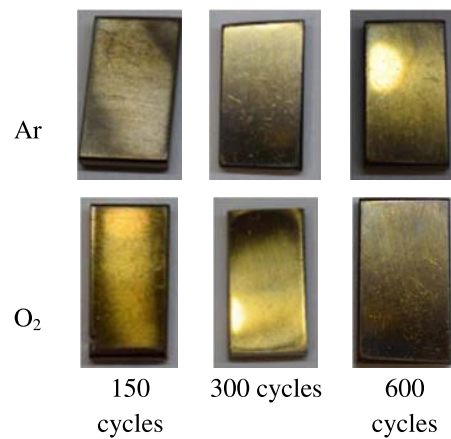
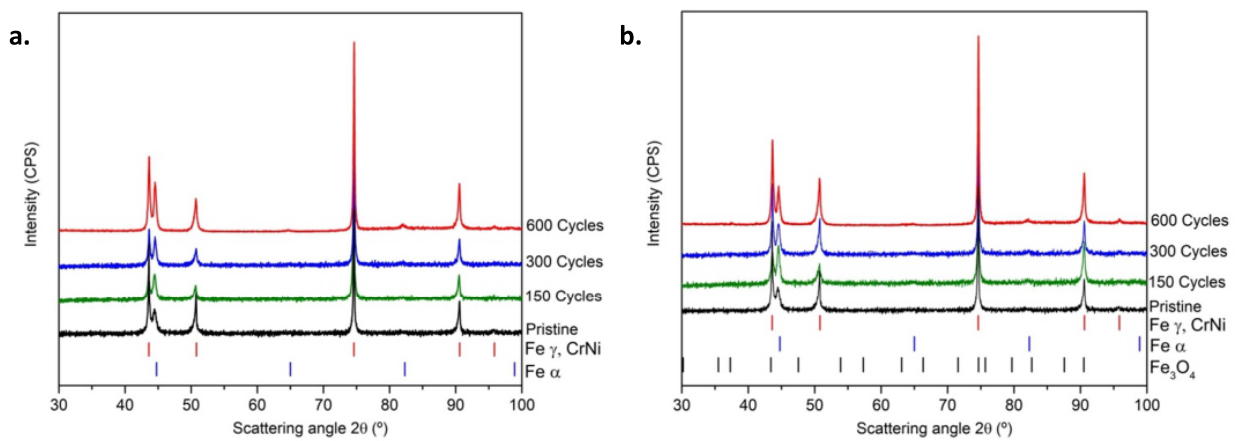


Figure 5.9. Images of SS samples after corrosion tests for different cycle numbers under different atmospheres

5.3.1. Analysis of stainless steel 316

5.3.1.1. X-ray diffraction analysis



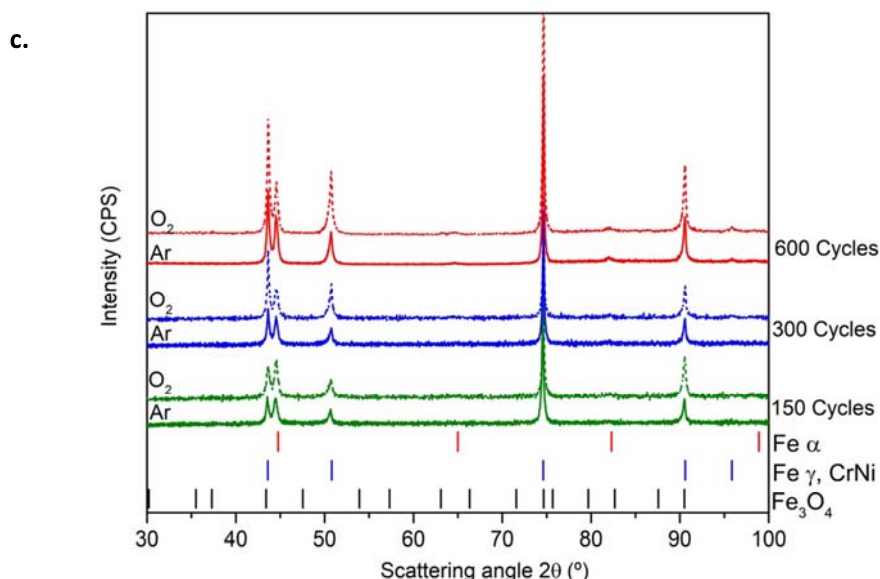


Figure 5.10. XRD patterns of the surface of SS 316 after corrosion tests at 350 °C for different cycle numbers: a) under Ar; b) under air; c) superposition of both patterns. The surface of SS 316 samples was analyzed by XRD in order to determine the nature of the corrosion layer. Figure 5.10.a and 5.11.b show the patterns of the samples cycled under Argon atmosphere and air atmosphere, respectively. In each figure, four patterns are presented corresponding to the samples cycled for 150, 300, and 600 cycles, additionally to the pattern of the pristine material. Figure 5.10.c depicts the superposition of the patterns undergoing the same number of cycles under different atmospheres in order to highlight any possible modification of the peaks intensities and positions. For the SS samples tested under Argon atmosphere, regardless to the number of the cycles applied, no corrosion layer was detected by XRD analysis. Only the phases corresponding to the pristine material were detected including Iron, Chromium, and Nickel phases with no evidence of oxide layer (or below XRD sensitivity). The absence of the oxide layer after 600 heating/cooling cycles is a sign of good compatibility of the SS 316 with $\text{Li}_4(\text{OH})_3\text{Br}$ salt while working under Argon atmosphere. In the case of the SS 316 samples tested under air atmosphere, the presence of iron, chromium and nickel phases were reported for all the samples.). No lithium based phase was formed as an indication of the absence of a chemical reaction between the salt and the steel sample. Particularly for the sample undergoing 600 cycles, one can notice the appearance of very low intensity peaks related to an iron oxide phase (magnetite Fe_3O_4). Overall, the results show that the compatibility of the SS 316 with $\text{Li}_4(\text{OH})_3\text{Br}$ is good while working under argon atmosphere. On the other hand, although iron oxide was detected after 600 cycles while working under oxygen, the low degree of oxidation of the SS 316 already gives insights about the suitability of this steel for use with the salt under air.

5.3.1.2. Cross-section analysis of the corrosion layer using SEM / EDS

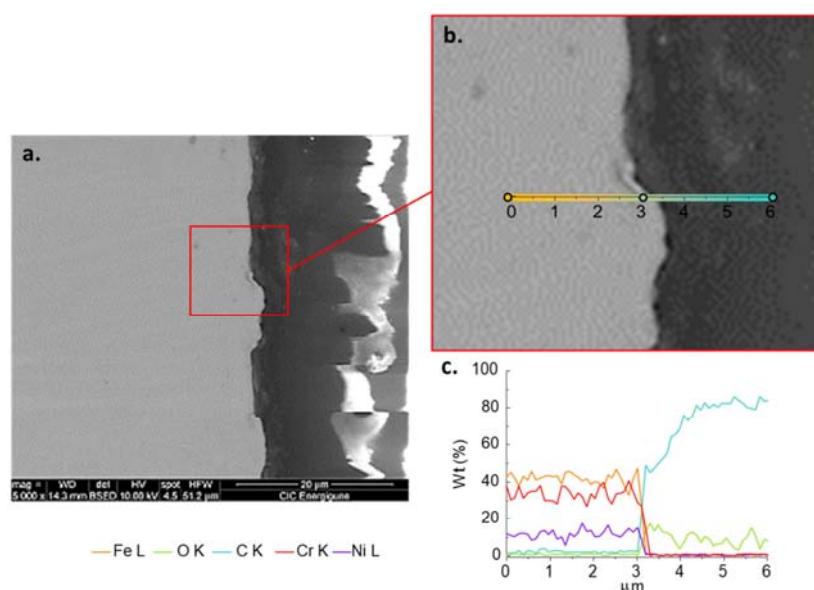
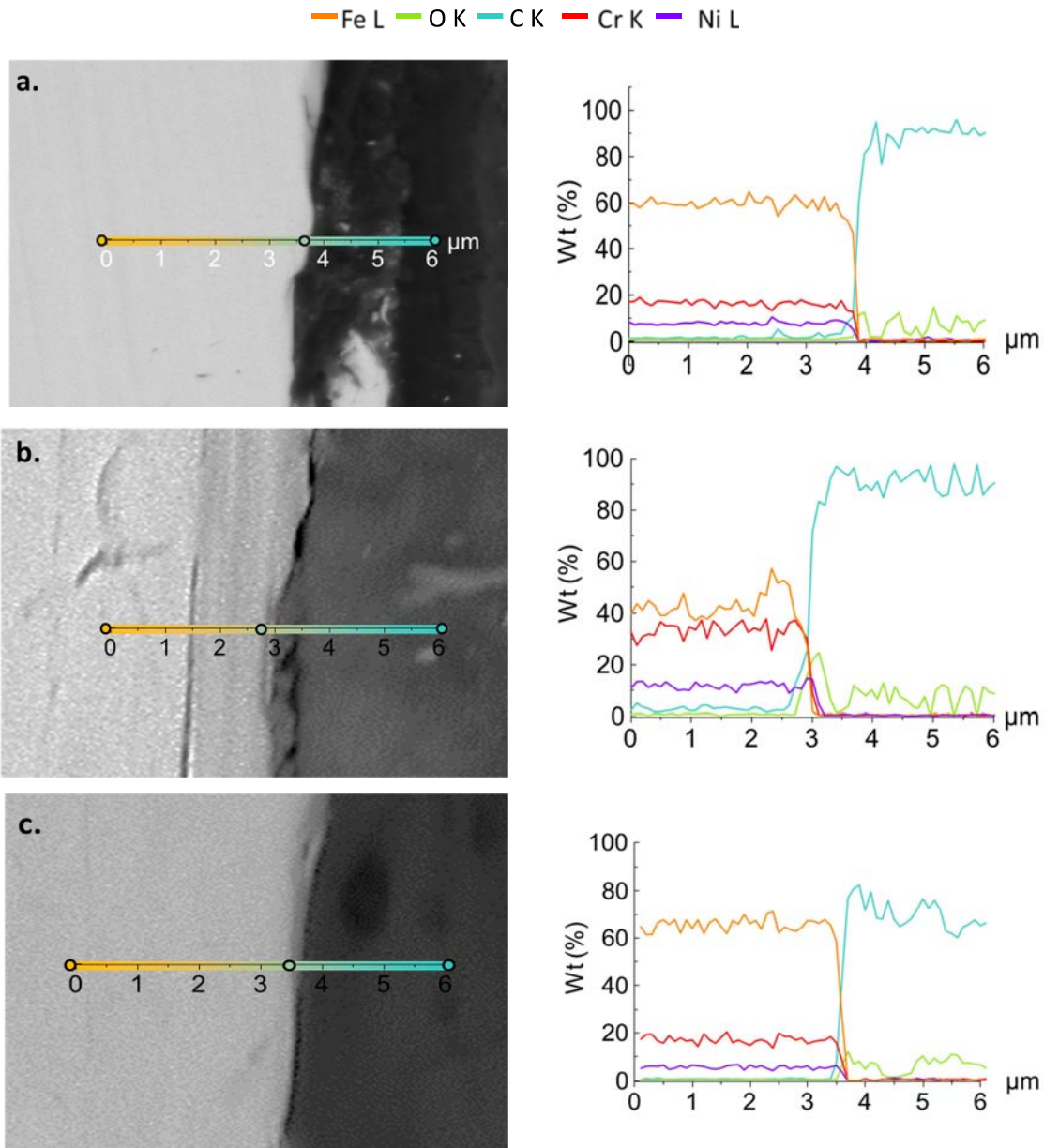


Figure 5.11. Cross-sectional analysis of the SS 316 tested under Ar after 150 corrosion cycle. a) SEM micrograph of the cross-section; b) enlargement of the region where the EDS is performed; c) EDS profile (Iron in orange line, Oxygen in green line, Carbon in blue line, Chromium in red line, and Nickel in purple line).

Figure 5.11 shows an example of the cross-section analysis of SS 316 with $\text{Li}_4(\text{OH})_3\text{Br}$ salt after 150 corrosion cycles under Argon atmosphere. The SS 316 tested under both Argon and air for 150, 300 and 600 cycles was analyzed and presented in a similar way. The EDS profiles of the cross-section and the corresponding SEM images of the samples are presented in figure 5.12.

For the samples tested under Argon, there is no evidence of the corrosion layer even after 600 heating/cooling cycles as shown in figure 6.13. These observations are confirmed by the EDS profile of the cross-section presented in figure 6.14, where it can be seen that the drastic jump in oxygen concentration is synchronized with the severe increase in carbon concentration (resin components) and the severe reduction in iron concentration. These observations are a sign of absent of the iron oxide layer. Similar behaviour was observed for the samples tested under air atmosphere undergoing 150 and 300 heating/cooling cycles. More precise characterization techniques, such as the XPS-depth profiling, should be applied to accurately estimate the possible oxide layer formed which couldn't be detected neither by XRD nor by EDS profile of the cross section. For the sample tested under air over 600 cycles, the corrosion product consists of iron oxide phase (Fe_3O_4). Moreover, for this steel, the thickness

of the corrosion layer couldn't be estimated by cross-sectional statistical analysis since no oxide layer is evident in SEM cross-section micrographs.



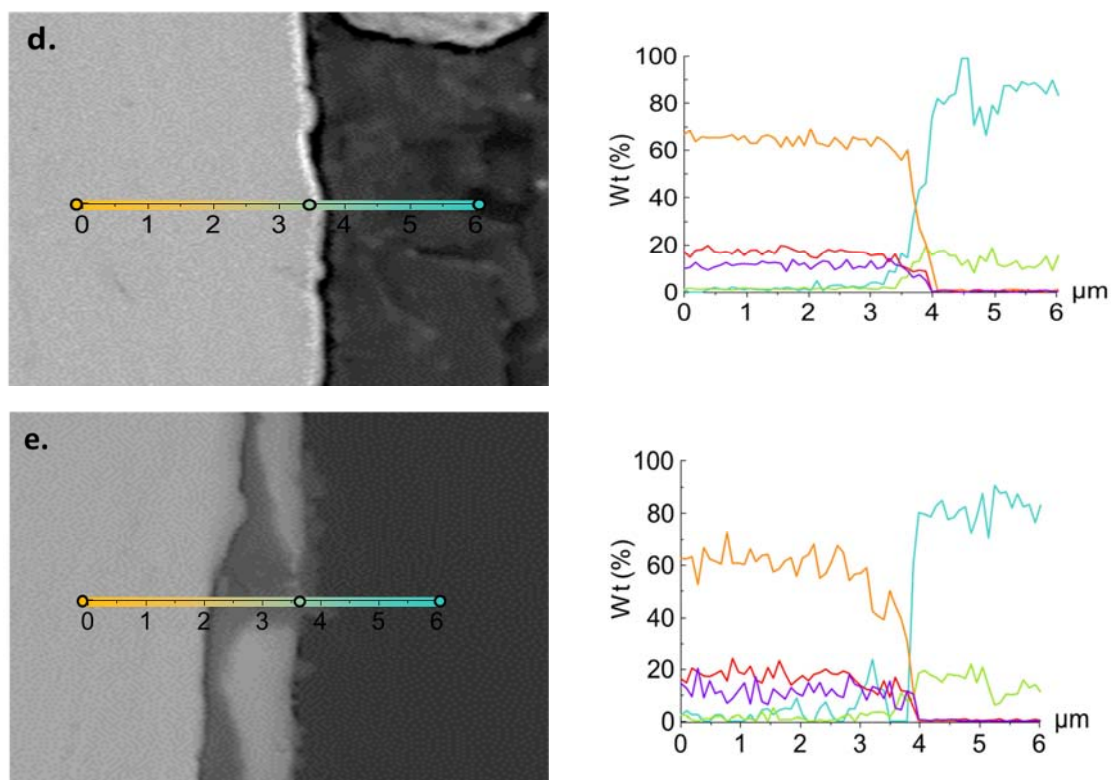
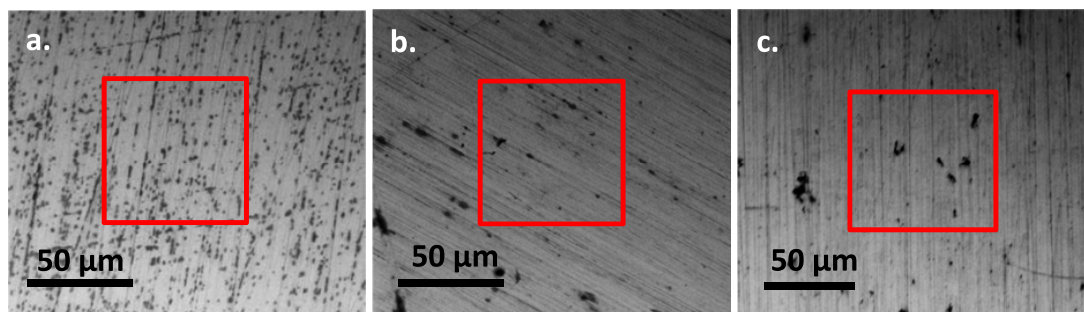


Figure 5.12. SEM-EDS cross-sectional analysis of the SS 316 samples tested under: Argon atmosphere (a) 300 cycles; (b) 600 cycles. Air atmosphere (c) 150 cycles; (d) 300 cycles; (e) 600 cycles.

5.3.1.3. Surface analysis of SS 316 after corrosion

5.3.1.3.1. SS 316 tested under Argon

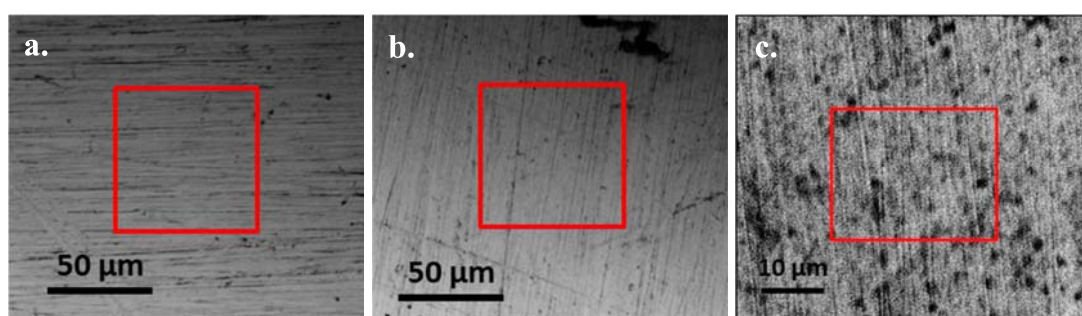


Element	Wt %			
	Pristine	a (150 cycles)	b (300 cycles)	c (600 cycles)
O K	0.86	00.84	00.57	00.52
Mo L	03.61	01.87	02.06	01.86
Ni L	09.97	06.09	05.84	04.62
Cr K	38.49	19.15	18.84	18.20
Fe K	44.65	72.06	73.19	74.79

Figure 5.13. SEM micrographs combined with EDS analysis of the surface of SS 316 samples tested under Ar: a) after 150 corrosion cycles; b) after 300 corrosion cycles; c) after 600 corrosion cycles.

The surface analyses of the SS 316 samples cycled under Argon atmosphere and the corresponding EDS elemental results are presented in figure 5.13. The overall surface morphology is homogeneous with no surface defects. Although the oxide layer was not detected by XRD as shown in section 5.3.1.1, the EDS results show the presence of oxygen in minimal concentrations similarly to the pristine material as an indication of the presence of the iron oxide layer on the surface of the stainless steel with negligible thickness. Taking into account the similarities of the oxygen concentrations for samples cycled for 150, 300 and 600 cycles, it can be concluded that the degree of oxidation didn't increase with cycling.

5.3.1.3.2. SS 316 tested under air



Element	Wt %			
	Pristine	a (150 cycles)	b (300 cycles)	c (600 cycles)
O K	0.86	00.79	00.74	01.89
Mo L	03.61	02.34	02.22	00.00
Ni L	09.97	06.01	05.32	12.24
Cr K	38.49	18.64	18.66	16.85
Fe K	44.65	72.22	73.07	69.02

Figure 5.14. SEM micrographs combined with EDS analysis of the surface of SS 316 samples tested under air: a) after 150 corrosion cycles; b) after 300 corrosion cycles; c) after 600 corrosion cycles.

The surface analyses of the SS 316 samples cycled under air atmosphere and the corresponding EDS elemental results are presented in figure 5.14. The overall surface morphology is homogeneous with no surface defects. The EDS results show the presence of oxygen in minimal concentrations for the samples undergoing 150 and 300 cycles as an indication of the presence of very thin iron oxide layer (not detectable by XRD analysis) on the surface of the stainless steel. Meanwhile for the sample undergoing 600 cycles, there is a slight increase of the concentration of oxygen. This means that the degree of oxidation of the sample increased while increasing the number of cycles and it manifest in the increase of the

thickness of the oxide layer (slightly detected by XRD). The EDS analysis of the surface of the samples confirmed the EDS results of the cross-section carried out in section (5.3.1.2).

5.3.2. Analysis of the peritectic salt $\text{Li}_4(\text{OH})_3\text{Br}$

5.3.2.1. Thermal analysis

The DSC curves of the salt samples obtained upon heating (at 1 K/min) are presented in figure 5.15 together with the reference samples corresponding to the salt cycled without being in contact with the SS316. The temperatures and enthalpies related to the peritectic reaction of the corrosion salt samples, the reference samples and the pristine salt are reported in table 5.2. Three endothermic peaks were recorded for all the samples similarly to the pristine salt (subchapter 4.5). Analysing the results reported in table 5.2 and the DSC curves, it can be observed that the temperature related to the peritectic reaction remains unchanged regardless to the exposure time (cycling duration), the working atmosphere, and the zone from which the salt is extracted. Regarding the enthalpy related to the peritectic reaction, different thermal behaviours were observed in respect to the atmosphere presents during the test. For the salt samples tested under Argon atmosphere, taking into account the experimental error of the DSC equipment, the enthalpy of the salt remains homogeneously stable regardless to the cycling duration, except for the salt in contact with the SS316 cycled over 600 times where a slight decrease of the enthalpy of about 1% was obtained. For the tests carried out under air atmosphere which promotes the oxidation of the steel, for short-term cycling durations (150 and 300 cycles) a good stability of the enthalpy with a slight improvement up to 5% was recorded homogeneously. Whereas, after 600 cycles, unlike the salt distant from the steel sample which show a stable reaction enthalpy, the salt in contact with SS316 presents an enthalpy loss of 5%. Overall, the stability of the reaction temperatures and enthalpies for the salt samples tested under argon atmosphere in contact with SS316 is an indication of the absence of any chemical reaction between both materials. While working under air, the small enthalpy loss observed after 600 cycles exceptionally for the salt in direct contact with the steel is related to the formation of the iron oxide phase (Fe_3O_4) as confirmed by the EDS analysis of the surface of SS316 sample. To get a better understanding of mechanism occurring between both materials, the elemental composition of the salt was investigate by EDS analysis and presented in the following section.

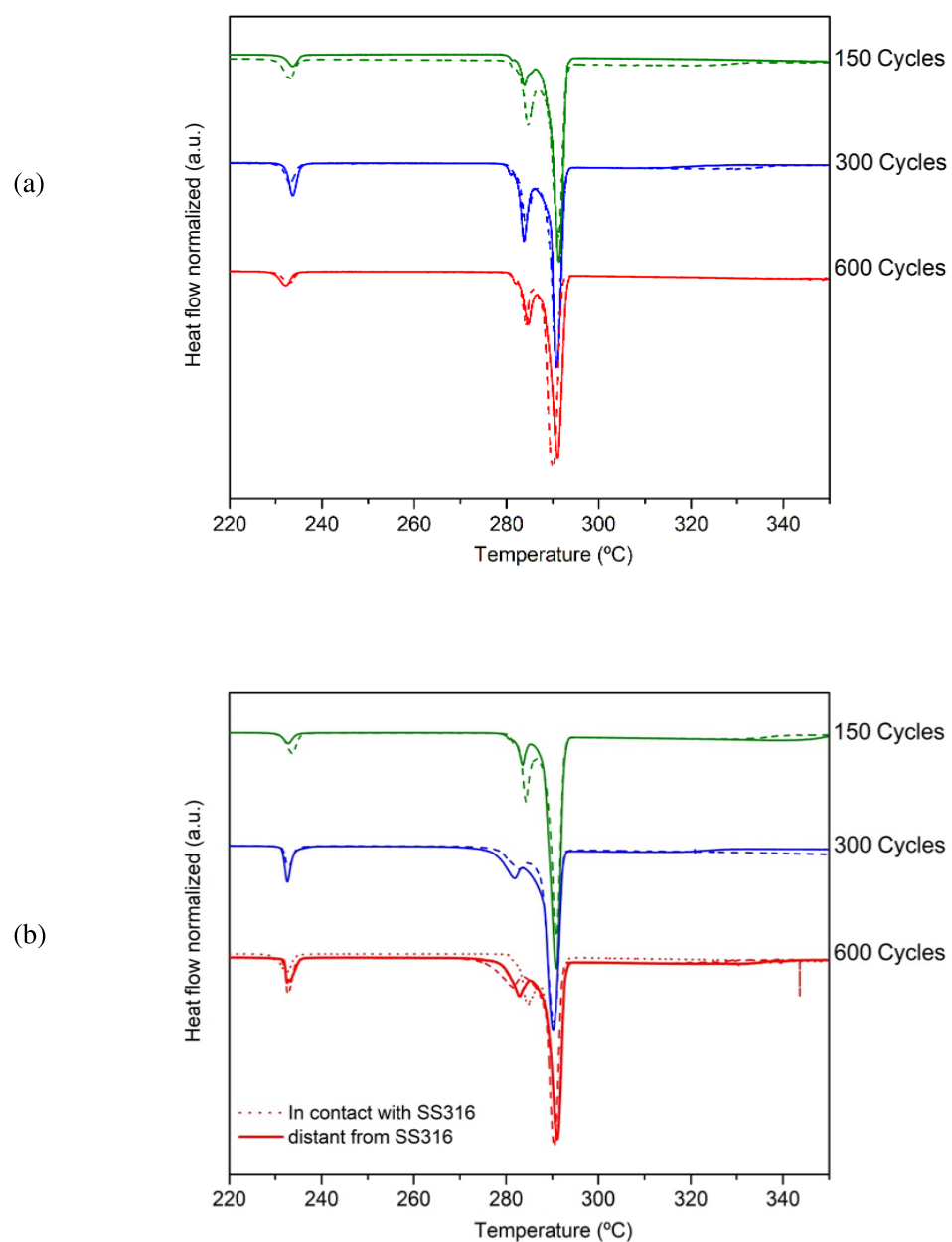


Figure 5.15. Heating DSC curves obtained at (1 K/min) of $\text{Li}_4(\text{OH})_3\text{Br}$ extracted after corrosion tests with SS 316 for different cycle numbers: a) under Ar; b) under air; (solid line represents the corrosion sample; dash line represents the reference sample).

Table 5.2 Temperatures and enthalpies corresponding to the peritectic reaction of $\text{Li}_4(\text{OH})_3\text{Br}$ after corrosion tests with SS 316 under Argon and air atmospheres compared to reference values

Cycle number	Corrosion under Ar				Corrosion under O_2			
	T_P (°C)	$T_{\text{Reference}}$ (°C)	ΔH_P^* (J/g)	$\Delta H_{\text{Reference}}^*$ (J/g)	T_P (°C)	$T_{\text{Reference}}^*$ (°C)	ΔH_P (J/g)	$\Delta H_{\text{Reference}}^*$ (J/g)
0 Cycle	289		251		288		254	
150 Cycles	289	289	241	243	288	289	259	245
300 Cycles	289	289	258	255	288	287	255	250
600 Cycles	289	288	239	243	289 ^a 288 ^b	288	243 ^a 229 ^b	245

* These values correspond to the addition of the enthalpy of the decomposition of $\text{Li}_3(\text{OH})_2\text{Br}$ at 279 °C and that of $\text{Li}_4(\text{OH})_3\text{Br}$ at 289 °C.

^a Sample distant from SS316

^b Sample in direct contact with SS316

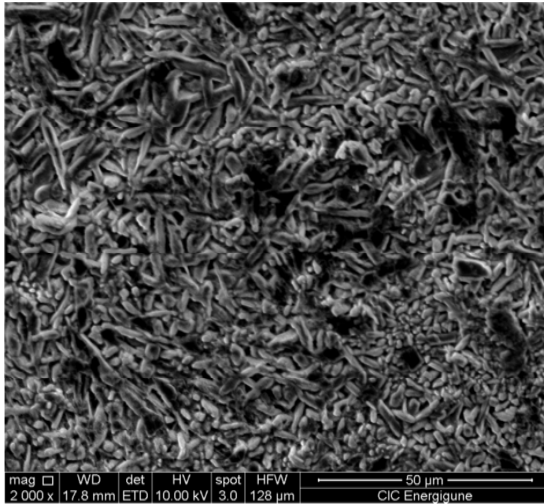
5.3.2.2. Microstructural analysis

In order to elucidate the corrosion mechanism, and to investigate the effect of the corrosion products on the initial salt composition, EDS analysis of the salt, which was in direct contact with the steel sample undergoing 600 cycles, was carried out. The SEM images of the salt samples and the corresponding EDS results are presented in figure 5.16. For the salt tested under Argon atmosphere, only bromine and oxygen were detected corresponding to the studied salt.. None of the SS316 alloying elements was detected within the salt. This result is in good agreement with EDS, and XRD analysis of the SS316 where no oxide layer was observed over 600 Heating/cooling cycles. For the sample tested under air atmosphere, oxygen and bromine were expectedly corresponding to salt components LiOH and LiBr . Additionally, the presence of Chromium was reported in relatively low concentrations (about 5 wt. %). The presence of Cr in the post-corrosion salt sample can be presumably due to the dissolution of chromium compounds in the salt. Chromium dissolution due to corrosion of SS316 and high Cr content steel in molten carbonates and nitrates salt was extensively reported in previous studies [1], [10], [11] as a result of the transformation of chromia (Cr_2O_3) to highly soluble chromates (CrO_4) and dichromates (Cr_2O_7) [12]–[15]. This phenomenon showed to appear at early corrosion stages and manifested in an increase of chromium content in the salt after the corrosion. Chromium showed to improve the corrosion resistance of steel. Cheng et al. [2], and Miguel et al. [1], on the study of corrosion of high Cr content steels by lithium containing salts, reported lower corrosion rates for steel with higher Cr content. These studies showed the formation of passivation iron-chromium oxides (spinel

$(\text{Fe Cr})_3\text{O}_4$; FeCr_2O_4) as the inner corrosion layer. These oxides form through an inward diffusion of lithium anion and outward diffusion of iron anions (Fe^{3+}). They are insoluble and act as corrosion inhibitor by blocking the iron diffusion from the substrate. The formation of lithium iron oxide phase (LiFeO_2) as the outer corrosion layer was also reported [16], [17].

In this work, the analysis of SS316 tested under air didn't report the presence of iron chromium oxide on the surface of the steel. Solely Cr was detected in the salt sample. This result means that no passivation layer was formed at the applied cycle number. The potential lithiumization of the iron oxide formed on the surface of steel is presumable over long-term cycling considering the high temperature of the test and the basic nature of the alkali hydroxide LiOH . One can conclude that the corrosion mechanism, over short-term cycling (600 cycles), manifests through oxidation and chromium dissolution in the salt due to the presence of oxygen atmosphere as well as the high temperature of the test (350°C). Longer exposure time through the increase of the cycling duration should be applied for this steel, and the following point should be investigated in order to determine the utility of this steel as a container material with $\text{Li}_4(\text{OH})_3\text{Br}$ at 300°C . 1) Define the complete corrosion mechanism of this steel with $\text{Li}_4(\text{OH})_3\text{Br}$ through the determination of the eventual corrosion products and check whether they involve lithium containing phases. 2) Investigate the effect of the eventual corrosion product on the stability of the salt. 3) Evaluate the long-term corrosion rate.

Under Ar



Element	Wt. %
O K	17.44
Br L	82.56

Under O_2

Element	Wt. %
O K	11.34
Br L	83.84
Cr K	04.82

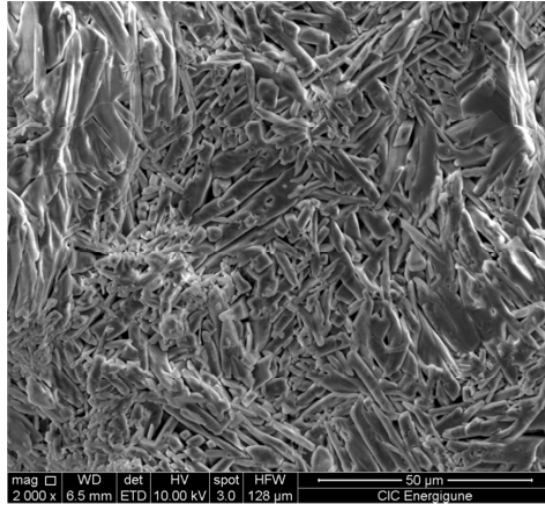


Figure 5.16. SEM and EDX analyses of $\text{Li}_4(\text{OH})_3\text{Br}$ salt in the interface with SS 316 after 600 corrosion cycles, both under Ar and air.

5.4. Corrosion rate estimation

The corrosion rate can be determined following several approaches under the assumption of uniform corrosion. 1) The weight loss (mg/cm^2) after a decaling process of the sample according to ASTM G1-03 protocol [7]. 2) Quantitative analysis of the weight gain of the sample (mg/cm^2). 3) Evolution of the thickness of the corrosion layer with time (mm/yr). In this work the corrosion rate was estimated based on the evaluation of the corrosion layer thickness over cycling by cross-section analysis. A summary of the obtained results is reported in table 5.3.

Table 5.4 which represent the reference corrosion rates allowing operability of CS in the industry. According to the obtained corrosion rate for the CS under air atmosphere, this steel is recommended for long-term service with $\text{Li}_4(\text{OH})_3\text{Br}$ salt at 300°C under air atmosphere.

Table 5.3. Average corrosion attack thickness (μm) measured by SEM cross-sectional analysis and the corresponding corrosion rates related to CS A516.Gr70 tested under both air and argon atmosphere at 350°C over various cycle numbers.

	Atmosphere	150 cycles	300 cycles	600 cycles
Thickness (μm)	Ar	NA	2.5	5.3
	O_2	NA	NA	0.4
Corrosion rate (mm/ye)	Ar	NA	0.040	0.042
	O_2	NA	NA	0.003

For the SS316, analysing the cross section, no evidence of the corrosion layer was detected in all the samples regardless the atmosphere and the number of cycles applied. Besides, no

weight gain was detected after the corrosion tests. For these reasons, the estimation of the corrosion rate of this steel couldn't be carried out neither by statistical cross-section analysis nor by quantitative weight gain analysis

Table 5.4. Industrial operability of A516 Gr70 according to the corrosion rate [19]

Corrosion rate ($\mu\text{m}/\text{yr}$)	Recommendation
> 1275	Completely destroyed within days
127–1274	Not recommended for service greater than 1 month
64–126	Not recommended for service greater than 1 year
14–63	Caution recommended, based on the specific application
0.4–13	Recommended for long-term service
< 0.3	Recommended for long-term service, no corrosion, other than as a result of surface cleaning, was evidenced

5.5. Conclusion

The compatibility of Carbon Steel A516 and Stainless Steel 316 with $\text{Li}_4(\text{OH})_3\text{Br}$ under various corrosion conditions has been investigated through cycling corrosion experiments.

Regarding the Carbon steel, for both samples tested under air and Argon atmosphere, the composition of the corrosion layer consists mainly of a Lithium iron oxide phase LiFeO_2 with poor adherence to the metal. A continuous growth of the corrosion layer with cycling was observed. It is noteworthy that the corrosion process is not only affected by the time factor but also by the type of atmosphere present during the test. Indeed, the corrosion reaction of the carbon steel with $\text{Li}_4(\text{OH})_3\text{Br}$ salt is more active under Argon atmosphere. Concerning the salt stability, unlike the salt distant from the CS, salt samples in direct contact with CS showed a gradual decrease in the reaction enthalpy. This is explained by the reaction between the Lithium and the metallic sample leading to the formation of LiFeO_2 through lithiumization of the iron oxide phase. The corrosion rate obtained for this steel showed its ability to operate for long-term service in contact with $\text{Li}_4(\text{OH})_3\text{Br}$, nevertheless, longer exposure time should be applied to investigate the effect of the corrosion product on the degradation of the salt.

Regarding the stainless steel, the XRD results show no corrosion in case of the samples cycled 600 times under Argon atmosphere. This is probably due to the small amount of oxide layer not detectable by XRD. However, the samples cycled in air show the presence of an iron oxide phase (Fe_3O_4) in the corrosion layer, especially evident in the sample cycled 600 times.

No localized corrosion has been found throughout the section. The analysis of the salt samples confirms its stability during the corrosion tests carried out both under Argon and air. No modification of the reaction enthalpy or the melting temperature was detected except for the sample tested under air after 600 cycles where a slight decrease in the reaction enthalpy was observed, due to the formation of the iron oxide corrosion layer. The corrosion rate for this steel couldn't be estimated after 600 heating/cooling cycles. Overall, Stainless steel 316 seems to be a very attractive option to be used as container material for $\text{Li}_4(\text{OH})_3\text{Br}$ salt at 350 °C. This steel performed better corrosion resistance than CS A516. Nevertheless, it is recommended to perform the corrosion study applying longer exposure time in order to define the corrosion rate of this material and to check whether lithium containing phases will be formed over longer cycling durations.

References

- [1] M. T. de Miguel, V. Encinas-Sánchez, M. I. Lasanta, G. García-Martín, and F. J. Pérez, "Corrosion resistance of HR3C to a carbonate molten salt for energy storage applications in CSP plants," *Solar Energy Materials and Solar Cells*, vol. 157, pp. 966–972, Dec. 2016, doi: 10.1016/J.SOLMAT.2016.08.014.
- [2] W. J. Cheng, D. J. Chen, and C. J. Wang, "High-temperature corrosion of Cr–Mo steel in molten $\text{LiNO}_3\text{--NaNO}_3\text{--KNO}_3$ eutectic salt for thermal energy storage," *Solar Energy Materials and Solar Cells*, vol. 132, pp. 563–569, Jan. 2015, doi: 10.1016/J.SOLMAT.2014.10.007.
- [3] R. Y. Chen and W. Y. D. Yuen, "Review of the High-Temperature Oxidation of Iron and Carbon Steels in Air or Oxygen," *Oxidation of Metals* 2003 59:5, vol. 59, no. 5, pp. 433–468, Jun. 2003, doi: 10.1023/A:1023685905159.
- [4] L. N. Dinh, C. M. Cecala, J. H. Leckey, and M. Balooch, "The effects of moisture on LiD single crystals studied by temperature-programmed decomposition," *Journal of Nuclear Materials*, vol. 295, no. 2–3, pp. 193–204, Jun. 2001, doi: 10.1016/S0022-3115(01)00548-7.
- [5] E. Garlea *et al.*, "Identification of lithium hydride and its hydrolysis products with neutron imaging," *Journal of Nuclear Materials*, vol. 485, pp. 147–153, Mar. 2017, doi: 10.1016/J.JNUCMAT.2016.12.012.
- [6] L. N. Dinh, W. McLean, M. A. Schildbach, J. D. LeMay, W. J. Siekhaus, and M. Balooch, "The nature and effects of the thermal stability of lithium hydroxide," *Journal of Nuclear Materials*, vol. 317, no. 2–3, pp. 175–188, May 2003, doi: 10.1016/S0022-3115(03)00084-9.
- [7] J. W. Graydon' and D. W. Kirk', "THE CORROSION OF CARBON STEEL IN AQUEOUS LITHIUM HYDROXIDE UNDER A HYDROGEN BLANKET," 1990.
- [8] Y. Yang, D. Li, G. Wan, F. Lv, D. Li, and X. Wang, "Hydrothermal Stripping Synthesis of- LiFeO_2 Nanoparticles from Qinghai Salt Lake Brine," doi: 10.1051/06090.
- [9] S.-P. Guo, Z. Ma, J.-C. Li, and H.-G. Xue, "First investigation of the electrochemical performance of $\gamma\text{-LiFeO}_2$ micro-cubes as promising anode material for lithium-ion

- batteries,” *Journal of Materials Science* 2016 52:3, vol. 52, no. 3, pp. 1469–1476, Oct. 2016, doi: 10.1007/S10853-016-0441-3.
- [10] K. L. Summers and D. Chidambaram, “Corrosion Behavior of Structural Materials for Potential Use in Nitrate Salts Based Solar Thermal Power Plants,” *Journal of The Electrochemical Society*, vol. 164, no. 8, p. H5357, Aug. 2017, doi: 10.1149/2.0501708JES.
- [11] R. W. Bradshaw and S. H. Goods, “Corrosion resistance of stainless steels during thermal cycling in alkali nitrate molten salts,” Sep. 2001, doi: 10.2172/1020472.
- [12] A. G. Fernández, H. Galleguillos, E. Fuentealba, and F. J. Pérez, “Corrosion of stainless steels and low-Cr steel in molten $\text{Ca}(\text{NO}_3)_2\text{--NaNO}_3\text{--KNO}_3$ eutectic salt for direct energy storage in CSP plants,” *Solar Energy Materials and Solar Cells*, vol. 141, pp. 7–13, Oct. 2015, doi: 10.1016/J.SOLMAT.2015.05.004.
- [13] R. W. Bradshaw and R. W. Carling, “A Review of the Chemical and Physical Properties of Molten Alkali Nitrate Salts and Their Effect on Materials Used for Solar Central Receivers *,” *ECS Proceedings Volumes*, vol. 1987–7, no. 1, p. 959, Jan. 1987, doi: 10.1149/198707.0959PV.
- [14] S. Guillot *et al.*, “Corrosion effects between molten salts and thermal storage material for concentrated solar power plants,” *Applied Energy*, vol. 94, pp. 174–181, Jun. 2012, doi: 10.1016/J.APENERGY.2011.12.057.
- [15] P. Biedenkopf, M. Spiegel, and H. J. Grabke, “High temperature corrosion of low and high alloy steels under molten carbonate fuel cell conditions,” *Materials and Corrosion*, vol. 48, no. 8, pp. 477–488, Aug. 1997, doi: 10.1002/MACO.19970480803.
- [16] P. Biedenkopf, M. Spiegel, and H. J. Grabke, “The corrosion behaviour of iron and chromium in molten $(\text{Li}_{0.62}\text{K}_{0.38})_2\text{CO}_3$,” *Electrochimica Acta*, vol. 44, no. 4, pp. 683–692, Sep. 1998, doi: 10.1016/S0013-4686(97)10191-8.
- [17] P. Biedenkopf, M. Spiegel, and H. J. Grabke, “The corrosion behavior of Fe-Cr alloys containing Co, Mn, and/or Ni and of a Co-base alloy in the presence of molten (Li,K)-carbonate,” *Materials and Corrosion*, vol. 48, no. 11, pp. 731–743, Nov. 1997, doi: 10.1002/MACO.19970481103.
- [18] “ASTM International - ASTM G1-03(2011) - Standard Practice for Preparing, Cleaning, and Evaluating Corrosion Test Specimens | Engineering360.” <https://standards.globalspec.com/std/3846071/astm-g1-03-2011> (accessed Sep. 04, 2021).
- [19] F. J. Ruiz-Cabañas, C. Prieto, V. Madina, A. I. Fernández, and L. F. Cabeza, “Materials selection for thermal energy storage systems in parabolic trough collector solar facilities using high chloride content nitrate salts,” *Solar Energy Materials and Solar Cells*, vol. 163, pp. 134–147, Apr. 2017, doi: 10.1016/J.SOLMAT.2017.01.028.

Chapter 6: $\text{Li}_4(\text{OH})_3\text{Br}$ based shape stabilized composites

6.1. Introduction

$\text{Li}_4(\text{OH})_3\text{Br}$, like most inorganic salts, suffers from corrosivity and low thermal conductivity ($< 1 \text{ W/m/K}$). Corrosion involves using expensive corrosion-resistant materials for the storage tank and heat exchanger, while low thermal conductivity has to be compensated by oversizing the latter, thus increasing investment cost. To mitigate the corrosion issue, different techniques for encapsulating high-temperature salts are being investigated. They can be classified into two main categories, namely core-shell microencapsulation [1]–[5], where the shell acts as a container to prevent liquid leakage, and the so-called shape-stabilized composite materials (ss-composites) [2], [3], [5]–[7], where a porous supporting material encapsulates the salt and retain the liquid phase by capillary forces and surface tension. Compared with core-shell microencapsulation, ss-composites have clear advantages regarding production cost and performance. Indeed, they are generally produced by simple melting infiltration in porous support or by cold compression of a mixture of the micro-nanoparticles supporting materials and salt powders. Moreover, they usually have the ability of self-management of the volume changes of the salt during phase transitions, which is one of the major concerns of core-shell microencapsulation, and they lead to higher apparent thermal conductivity enhancement.

This chapter is divided into two parts: The first part addresses the selection methodology of suitable supporting materials for $\text{Li}_4(\text{OH})_3\text{Br}$ based ss-composites obtained by cold-compression route, which is the most advantageous from an economic point of view. Candidate supporting materials considered are micro and/or nanoparticles of MgO , Fe_2O_3 , CuO , SiO_2 and Al_2O_3 . The experimental screening carried out included the study of the chemical compatibility between the candidates supporting material and $\text{Li}_4(\text{OH})_3\text{Br}$, the anti-leakage performance and maximum salt loading evaluation as well as the thermal cycling stability of corresponding ss-composites,

The second part of this chapter focuses on $\text{Li}_4(\text{OH})_3\text{Br}/\text{MgO}$ shape stabilized composites. In the first part of this study, magnesium oxide was selected, among several metal oxides, as the most promising supporting material for shape stabilization of the peritectic salt. The ceramic MgO Nano-powder with a particle size of 100 nm affords good structural stability of the composite at a minimum loading of 50 wt. %. This loading is high and will considerably decrease the storage capacity of the composite. Therefore, the optimization of MgO concentration needed for a good structural stability and storage capacity of the composite is required. In this context, $\text{Li}_4(\text{OH})_3\text{Br}/\text{MgO}$ shape stabilized composites were developed using different porous MgO samples with different structural, textural, and morphological properties. The purpose of using porous MgO as supporting materials for the shape stabilization is to combine the benefits of the mesoporosity present within the MgO particles in leakage prevention thanks to the strong capillary forces it generates, with the benefits of the mechanical lock and liquid bridge force responsible for structural stability in the ss-composites prepared by cold compression. This combination will help decrease the amount of supporting material required for the structural stability of the composite. The pore size was targeted to be dominantly in the mesoporous range (2-50 nm) because, on the one hand, macropores (> 50 nm) not only can't provide sufficient capillary force for molten salt retention, but also their synthesis is not feasible considering the characteristic of our powder. On the other hand, micropores (<2 nm) provide stronger capillary forces. However, they are too small that the solidification of the infiltrated salt will most probably be suppressed, which will affect the thermal energy of the peritectic salt. Consequently, mesoporosity is found to be a good compromise, with strong capillary forces and pore volume sufficient for salt solidification. Three porous MgO samples were synthesized/treated and used in this study as supporting materials, i) Porous MgO (named PMgO) synthesized by combustion using Magnesium nitrate $\text{Mg}(\text{NO}_3)_2$, ethylene glycol, and deionized water, giving a BET surface area of $40 \text{ m}^2/\text{g}$ and a pore volume of $0.217 \text{ cm}^3/\text{g}$. ii) Porous MgO synthesized by calcination of basic magnesium carbonate (named MgO-BMC), giving a higher BET surface area of $129 \text{ m}^2/\text{g}$ and a pore volume of $0.294 \text{ cm}^3/\text{g}$. iii) Commercial MgO micro-powder (Particle size in the range of [44-105 μm]) treated by ball milling process (named MgO-BM) in order to obtain a nanocrystalline structure, giving a BET surface area of about $55 \text{ m}^2/\text{g}$ and pore volume of $0.088 \text{ cm}^3/\text{g}$. The synthesis methods of MgO samples and the composite materials are described in chapter 2, section 2.1.5.2 and 2.1.5.3, respectively.

6.2. Selection of the most convenient supporting materials

The selection of the supporting material is critical for succeeding ss-composites [6]. The thermal stability in the planned working temperature range and the chemical compatibility with encapsulated salt are the most basic requirements, which directly determine the usability of the supporting material. Good wettability with loaded salt and high specific surface area is also of great importance because it determines maximum salt loading and, therefore, the latent heat storage capacity of the final material. To a lesser extent, high thermal conductivity is also advisable to reduce the size of heat exchangers or, alternatively, to maximize the size of pellets/grains in fixed packed-bed storage systems. Obviously, economic and safety aspects are also relevant so as safe (non-corrosive, non-flammable, non-explosive), cheap, easy to obtain, and process supporting materials are required as well.

Supporting material used in ss-composites studied so far can be classified into three main groups:

- Carbon based supporting materials such as expanded graphite and graphite foams [8]–[22]. They prove to be compatible with nitrites and chlorides and have a high salt absorption capacity (> 85 wt. %). Besides, they are excellent in heat transfer enhancement because of their high thermal conductivity (up to 100 W/m/K reported). However, they are characterized by poor wettability with salts, and they also tend to oxidize at a temperature above 600 °C approx. ss-composites using expanded graphite are usually prepared by uniaxial or isostatic cold-compression route, whereas vacuum-assisted melting infiltration method is used in the preparation of graphite foam-based composites;
- Clay mineral supporting materials such as expanded perlite, expanded vermiculite, and diatomite [3], [23]–[30]. They demonstrate chemical compatibility with nitrites, chlorides, and sulfates as well as high salt absorption capacity (> 85 wt. % for expanded perlite and vermiculite; 55-70 wt. % for diatomite). Moreover, the wettability with molten salts is good, and they can support temperatures above 1000 °C. However, they have low values of thermal conductivity (< 0.15 W/m/K), and a melting infiltration route is needed for ss-composites preparation, which is more expensive than cold compression method. Another type of clay minerals used as an additive for PCM composites is the natural halloysite nanoclay. These materials are characterized by good thermal stability, a high adsorption capacity, and low cost.

Halloysite nanoclay are used generally as a nucleating agent to mitigate the subcooling phenomena of the hydrate PCMs and applied for cold storage [31], [32];

- Other supporting materials including refractory oxides (MgO , Al_2O_3 , SiO_2 , mullite), SiC , and $\text{Ca}(\text{OH})_2$ [7], [33]–[53]. The compatibility and good wettability with nitrates, carbonates, chlorides, and sulfates have been proven for most of them. Maximum salt loading is lower than in previous cases but still significant (up to 70 wt. %). On the contrary, they show excellent thermal stability up to 1400-1600 °C (only 570 °C for calcium hydroxide). In addition, they have relatively high thermal conductivity (3-65 W/m/K), and corresponding ss-composites are prepared by cold-compression route.

6.2.1. Screening methodology of the most convenient supporting material for shape stabilization of $\text{Li}_4(\text{OH})_3\text{Br}$

The experimental screening carried out to select the best supporting material focuses on fundamental aspects such as chemical compatibility of the supporting material with $\text{Li}_4(\text{OH})_3\text{Br}$, the anti-leakage performance of corresponding ss-composite, and maximum salt loading allowed as well thermal properties and thermal cycling stability of final composites. A three steps methodology was established to discard either useless or poorly performant supporting material progressively:

1. Chemical compatibility test. It consists in preparing a mixture of 90 wt. % $\text{Li}_4(\text{OH})_3\text{Br}$ and 10 wt. % Oxide. The powder mixture is then subjected to a heating process up to 400 °C ($T_{\text{m,salt}} + 60$ °C) during 24 hours inside closed stainless-steel reactors under Ar atmosphere. After these extreme heating conditions, chemical compatibility is investigated by means of Differential Scanning calorimetry (DSC) analysis and X-ray diffraction analysis to detect eventual side reactions or changes/degradations in the storage properties of $\text{Li}_4(\text{OH})_3\text{Br}$.
2. Anti-leakage performance analysis and maximum salt loading allowed. Pellets of $\text{Li}_4(\text{OH})_3\text{Br}$ /Oxide composite materials with different oxide loadings are prepared following a cold-compression method. They are then submitted to the following thermal treatment: heating step at 10 K/min up to 350 °C, followed by an isothermal step at 350 °C for 1 hour, and finally a cooling step at around 2 K/min up to room temperature. The effectiveness of the composite in retaining the liquid phase of $\text{Li}_4(\text{OH})_3\text{Br}$ was qualified by visual inspection of the pellets during the test. Those

composites allowing higher salt content while displaying good anti-leakage performance are moved to the last step.

3. Stability of the composites under thermal cycling conditions. In this step, the phase transition properties of composites that have passed previous tests are determined before and after 50 heating and cooling cycles. Thermal cycling tests were carried out in a muffle furnace under Argon atmosphere, between 250 °C and 350 °C, applying heating/cooling rates of 10 K/min and 2 K/min, respectively. Both cycling and storage properties determination are carried out using differential scanning calorimetry (TA DSC 2500 model). The composite which shows better stability and heat storage capacity is finally selected as supporting material.

6.2.1.1. Chemical compatibility of the supporting material with molten $\text{Li}_4(\text{OH})_3\text{Br}$

Upon heating, as described in the previous chapters, $\text{Li}_4(\text{OH})_3\text{Br}$ undergoes different reversible phase transitions. The first solid state transformation at around 230 °C. The second solid state transition at 279 °C and finally the peritectic reaction at 289 °C. All these transformations are reflected in the DSC curve depicted in figure 4.1. These curves are considered as the reference in terms of transition temperature and reaction enthalpy, which will be taken into consideration when analyzing the compatibility and performance of the different supporting materials. The values assigned to the peritectic reaction in this work represent the sum of both the second solid state transition and the peritectic reaction.

As already mentioned in section 6.1.1 (step 1 of the screening), different $\text{Li}_4(\text{OH})_3\text{Br}$ /Oxide mixtures were prepared using 10 wt. % of support materials reported in Table 2.1 and heated at 400 °C during 24 hours inside closed stainless-steel reactors under Ar atmosphere. Afterward, all the samples were subjected to structural analysis using X-ray diffraction in order to test the compatibility with the salt and detect possible side products formed due to the reaction between the salt and the oxide. The DSC curves of different mixtures ($\text{Li}_4(\text{OH})_3\text{Br}$ + 10 wt. % oxide) after compatibility tests obtained both upon heating and cooling are reported in Figure 6.1.

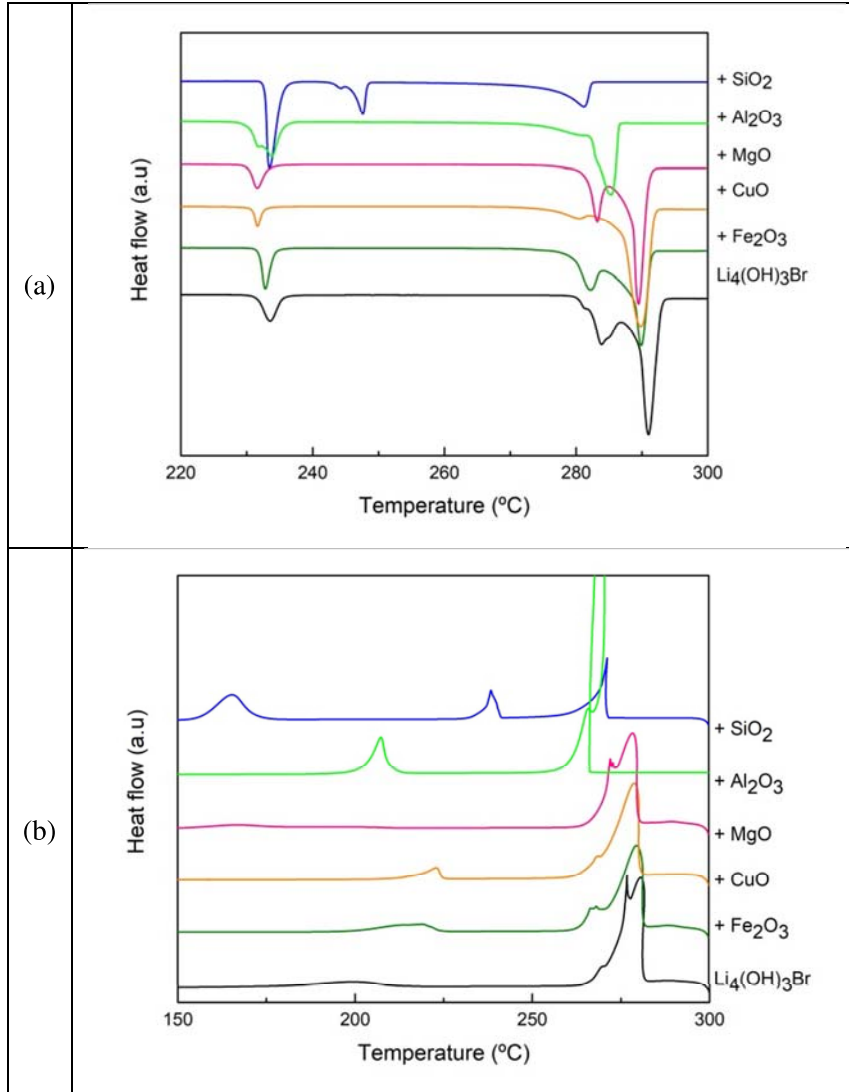


Figure 6.1. DSC curves of $\text{Li}_4(\text{OH})_3\text{Br}$ /oxide mixtures after compatibility tests recorded at 1°C/min: a- upon heating; b- upon cooling.

The temperatures and enthalpies of the reaction corresponding to the different composites are presented in Table 6.1. The enthalpy of the peritectic reaction relative to the mass fraction of the salt in the composite $\Delta H_{\text{calculated}}$ is calculated as follow:

$$\Delta H_{\text{calculated}} = \Delta H_{\text{Li}_4(\text{OH})_3\text{Br}} \cdot X_{\text{Li}_4(\text{OH})_3\text{Br}}, \quad (\text{eq. 1})$$

Where $X_{\text{Li}_4(\text{OH})_3\text{Br}}$ represents the mass fraction of the salt and $\Delta H_{\text{Li}_4(\text{OH})_3\text{Br}}$ is the enthalpy of the pure peritectic salt.

Table 6.1. Temperatures and enthalpies corresponding to the peritectic reaction of different $\text{Li}_4(\text{OH})_3\text{Br}$ /oxide mixtures after compatibility tests.

Composition	T_{onset} (°C)	$\Delta H_{\text{Experimental}}^*$ (J/g)	$\Delta H_{\text{Calculated}}^*$ (J/g)	Enthalpy loss (%)
Pure $\text{Li}_4(\text{OH})_3\text{Br}$	289	247	247	
90 $\text{Li}_4(\text{OH})_3\text{Br}$ -10 Fe_2O_3	288	197		10
90 $\text{Li}_4(\text{OH})_3\text{Br}$ -10 CuO	287	215	222	3
90 $\text{Li}_4(\text{OH})_3\text{Br}$ -10 MgO	288	209		6
90 $\text{Li}_4(\text{OH})_3\text{Br}$ -10 Al_2O_3	282	137		34

* These values correspond to the addition of the enthalpy of the decomposition of $\text{Li}_3(\text{OH})_2\text{Br}$ at 279 °C and that of $\text{Li}_4(\text{OH})_3\text{Br}$ at 289 °C.

Analyzing Figure 6.1.a, the DSC curves of sample 90 $\text{Li}_4(\text{OH})_3\text{Br}$ -10 SiO_2 show a narrowing of the peak at the peritectic transition temperature together with the broadening of the first peak, besides the appearance of a new DSC peak at 246 °C. The three thermal events are reversible upon cooling (see figure 6.1.b). This behaviour is an indication of a chemical reaction between the salt and the silica nanopowder. For this reason, the Silicon dioxide was discarded at this level. Alumina nanopowder was also discarded due to the huge loss of the enthalpy of the peritectic reaction (- 34%), as shown in Table 6.1. In addition, the DSC heating curve shows the displacement of both the second solid-state reaction and the peritectic reaction to lower temperatures (- 7 °C). The reason for this phenomenon can be due to the very small particle size of Al_2O_3 powder. In fact, the use of nanometric power (13 nm) with a very high specific surface area will create a large number of cavities inside the composite pellet, and this leads to the possible confinement of a quantity of the peritectic salt inside these cavities inducing the Gibbs-Thomson effect. Additionally, the salt trapped inside the cavities and the vacancies can cause a total or partial suppression of the peritectic reaction which may be the reason of the significant decrease in the peritectic reaction enthalpy. In case of CuO , MgO , and Fe_2O_3 oxides, good thermal stability of the composites has been noticed. The temperature of the peritectic reaction remains unchanged. Considering the systematic error (± 3 J/g), the enthalpy of the peritectic reaction is stable in case of $\text{Li}_4(\text{OH})_3\text{Br}/\text{CuO}$ composite. However, it shows a slight decrease (6 % loss) in case of MgO and (10 % loss) for Fe_2O_3 composite. CuO , MgO , and Fe_2O_3 metal oxides have been selected for further investigation (Shape stability performance and thermal cycling stability).

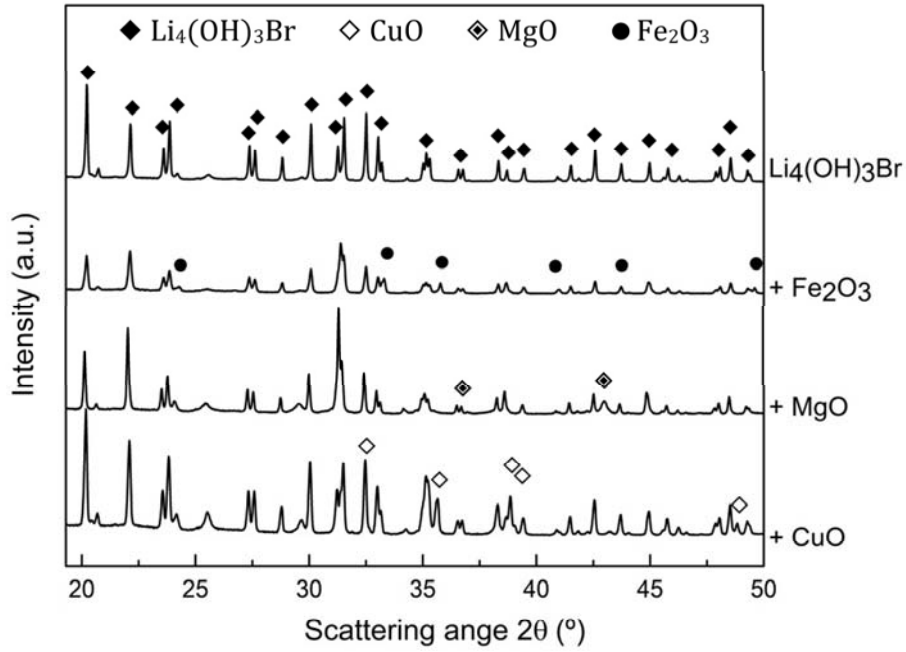


Figure 6.2. XRD results of $\text{Li}_4(\text{OH})_3\text{Br}$ /oxide mixtures after compatibility tests

Analyzing the XRD results of $\text{Li}_4(\text{OH})_3\text{Br}$ and the composite materials reported in Figure 6.2, it can be clearly seen that the patterns corresponding to the samples $90\text{Li}_4(\text{OH})_3\text{Br}-10\text{Fe}_2\text{O}_3$, $90\text{Li}_4(\text{OH})_3\text{Br}-10\text{MgO}$, $90\text{Li}_4(\text{OH})_3\text{Br}-10\text{CuO}$ show only the peaks related to the peritectic salt plus the Fe_2O_3 , MgO and CuO respectively. No new peaks associated with the formation of new phases were detected despite the harsh conditions applied for the compatibility tests, which indicates good chemical compatibility between the salt and the tested oxides.

6.2.1.2. Anti-leakage effectiveness and maximum salt loading

Capillary forces are mainly responsible for retaining the liquid salt during the phase change process. The parameters which determine the capillary effect are the size and topology of the pores, as well as the adhesion forces between the liquid salt and the pore wall. The latter is estimated by the effective contact angle between the liquid salt and the supporting material (higher is the liquid adhesion, lower is the effective contact angle) [54]-[55]. Considering that the work required displacing a liquid tube outside a cylindrical pore is given by:

$$dW \equiv \Delta P_c \times dV = \frac{2\gamma_{lv}\cos\theta}{r} dV = S_p \gamma_{lv} \cos\theta dV \quad (\text{eq. 2})$$







where ΔP_c is the capillary pressure, dV is the infinitesimal volume of the liquid tube displaced along the axis of a cylindrical pore of radius r . γ_{lv} is the liquid-vapor surface tension, $S_p = 2/r$ represents the surface area per unit of pore volume and θ is the effective contact angle. It can be concluded that the greater is the wettability, and the higher is the surface area (smaller pore size for same total porosity), the better is the anti-leakage efficiency.

From this, it follows several conclusions of practical interest for the interpretation of the results of leakage tests performed:

1. Decreasing the size of the oxide particles at constant oxide loading improves anti-leakage efficiency of the ss-composite;
2. The same happens when increasing the oxide loading at constant particles size although at the expense of losing storage capacity;
3. For equal oxide loading and particles size, oxides with higher wettability with the salt lead to ss-composites with better anti-leakage efficiency.

The anti-leakage performance of composites $\text{Li}_4(\text{OH})_3\text{Br}/\text{MgO}$, $\text{Li}_4(\text{OH})_3\text{Br}/\text{CuO}$, and $\text{Li}_4(\text{OH})_3\text{Br}/\text{Fe}_2\text{O}_3$ has been analyzed as described in section 6.2.1 (step 2 of the screening). For each composite, different pellet (13 mm in diameter, 5 mm in thickness) with oxide content ranging from 20 wt. % to 60 wt. % were prepared in order to determine the maximum salt loading allowed.

Table 6.2. $\text{Li}_4(\text{OH})_3\text{Br}$ -based ss-composites with different oxide loading after sintering showing salt leakage assessment.

wt. % Oxide	20	30	40	50	60
$\text{Li}_4(\text{OH})_3\text{Br}/\text{MgO}$					
leakage assessment		Serious	Minor	No	No
$\text{Li}_4(\text{OH})_3\text{Br}/\text{CuO}$					
leakage assessment		Serious	Serious	Minor	No
$\text{Li}_4(\text{OH})_3\text{Br}/\text{Fe}_2\text{O}_3$					
leakage assessment	Serious	No	No	No	

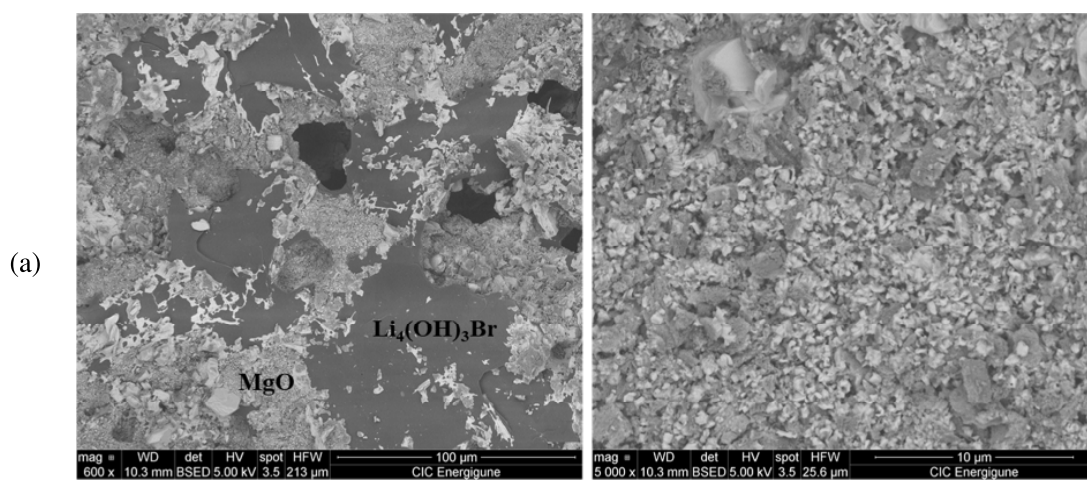
As it is shown in Table 6.2:

- $\text{Li}_4(\text{OH})_3\text{Br}/\text{MgO}$ composite shows a minor salt leakage at 30-40 wt.% content of MgO. Sample with 50 wt. % MgO present no sign of salt leakage. The pellet shape is perfectly preserved, showing a smooth surface without cracks. Sample with 60 wt. % MgO shows good structural stability without salt leakage. However, the pellet has cracked after sintering which could be due to the high amount of MgO nanoparticles and the less amount of the salt, which ensures the structural bonding after solidification. The advantages expected of using nanostructures MgO powder with 100 nm particle size was to have the shape stabilization at a small loading of MgO thanks to the high specific surface area of MgO nanopowder which generate a high surface tension between the salt and MgO. However, despite the nanometric particle size used, the form stability was ensured at a minimum content of 50 wt. % MgO unlike $\text{Li}_4(\text{OH})_3\text{Br}/\text{Fe}_2\text{O}_3$, this could be due to the wettability of MgO by the molten salt is not as high as in the case of Fe_2O_3 micro-powder.
- $\text{Li}_4(\text{OH})_3\text{Br}/\text{Fe}_2\text{O}_3$ composite presents a significant salt leakage at 20 wt. % of Fe_2O_3 . Sample with 30-40-50 wt. % Fe_2O_3 presents excellent structural stability without any sign of salt leakage. Even though nanostructure supporting materials prove to afford a good anti-leakage efficiency of ss-composite at less content compared to materials with micrometric particle size, Fe_2O_3 with particle size $< 5 \mu\text{m}$ shows excellent structural stability at only 30 wt. % loading compared to 50 wt. % MgO with a particle size of 100 nm. This can indicate the excellent wettability of Fe_2O_3 microparticles by the molten salt. In order to afford the maximum reaction enthalpy, the minimum content of 30 wt. % Fe_2O_3 was chosen for further investigations.
- $\text{Li}_4(\text{OH})_3\text{Br}/\text{CuO}$ composite shows a constant improvement of the structural stability and no leakage sign while increasing the content of the CuO from 30 to 60 wt.%. Samples with 30-40 wt. % of CuO show a significant amount of salt leakage with segregation of salt after sintering, which could be due to the difference in density of the two components. At 50 wt. % CuO, a small leakage of the salt can be observed. While increasing the CuO loading up to 60 wt. % the shape stabilization is perfectly ensured, no salt leakage was observed. The high CuO loading (60 wt. %) required for the shape stability of the composite could be explained by i) the big particle size of this material ($< 74 \mu\text{m}$) giving a less surface area, thus less surface tension between the molten peritectic salt and CuO required for salt retention at liquid state inside the structure of the composite. ii) and/or the modest wettability of CuO by the molten salt.

60 wt. % CuO is the minimum loading required to guarantee the shape stabilization of the composite, however, at the expense of the salt loading. This relatively large amount of the supporting material will considerably decrease the storage capacity of the composite. The result was not satisfactory from a thermal storage application point of view. For this reason, CuO was discarded at this level.

6.2.1.3. Thermal and microstructural characterization and stability of $\text{Li}_4(\text{OH})_3\text{Br}$ based shape stabilized composites

The composites ($70\text{Li}_4(\text{OH})_3\text{Br}-30\text{Fe}_2\text{O}_3$; $50\text{Li}_4(\text{OH})_3\text{Br}-50\text{MgO}$), which satisfied the criterion of form stabilization, were characterized by DSC. The objective was to investigate the influence of shape stabilization on the thermal properties of the salt. The morphology of the ss-composites was investigated by SEM. Figure 6.3. a,b presents the microstructures of $50\text{Li}_4(\text{OH})_3\text{Br}-50\text{MgO}$ and $70\text{Li}_4(\text{OH})_3\text{Br}-30\text{Fe}_2\text{O}_3$ composites, respectively. In both cases, it can be seen that $\text{Li}_4(\text{OH})_3\text{Br}$ salt is embedded in the oxide particles. This morphology prevents the leakage of the molten salt outside the structure of the composite by capillary force and surface tension. Analyzing the SEM images, two regions can be distinguished, one region with a smooth surface presenting smooth lamellar undulations corresponding to the peritectic salt, and another region with granular morphology corresponding to the oxide particles. Both structures of the composites present an open porosity



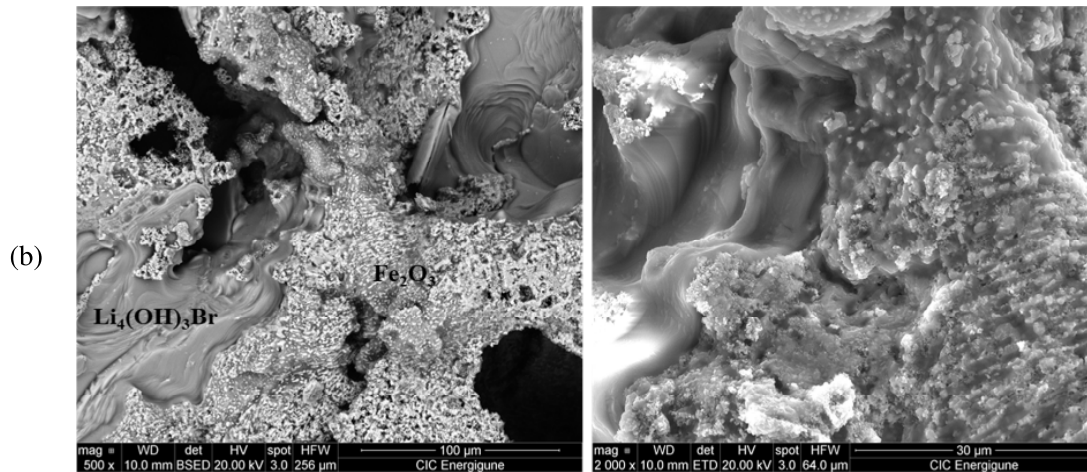


Figure 6.3. SEM images of the ss-composite: (a) $50\text{Li}_4(\text{OH})_3\text{Br}-50\text{MgO}$; (b) $70\text{Li}_4(\text{OH})_3\text{Br}-30\text{Fe}_2\text{O}_3$

The results of the DSC in terms of transition temperatures and reaction enthalpies are reported in Table 6.3. Both DSC curves of $70\text{Li}_4(\text{OH})_3\text{Br}-30\text{Fe}_2\text{O}_3$ presented in Figure 6.4 and of $90\text{Li}_4(\text{OH})_3\text{Br}-10\text{Fe}_2\text{O}_3$ presented in Figure 6.1 show a shift in the peritectic reaction to lower temperatures; the shift increases with increasing Fe_2O_3 content (peritectic reaction temperature is 288°C and 281°C for $90\text{Li}_4(\text{OH})_3\text{Br}-10\text{Fe}_2\text{O}_3$ and $70\text{Li}_4(\text{OH})_3\text{Br}-30\text{Fe}_2\text{O}_3$, respectively). This can be explained by the possible salt confinement in the interparticle voids of the composites (thanks to the great wettability of Fe_2O_3 by the molten salt), which increases with the augmentation of the salt loading. A drop in the enthalpy of the peritectic reaction is also noticed, showing a higher loss for the sample with higher Fe_2O_3 loading (10% and 17% enthalpy loss for $90\text{Li}_4(\text{OH})_3\text{Br}-10\text{Fe}_2\text{O}_3$ and $70\text{Li}_4(\text{OH})_3\text{Br}-30\text{Fe}_2\text{O}_3$, respectively). This can be explained by the fact that the salt trapped inside the interparticle voids of the composite does not contribute to the total reaction enthalpy. Considering the high surface area of MgO compared to Fe_2O_3 (particle size is 100 nm and $<5\text{ }\mu\text{m}$ for MgO and Fe_2O_3 , respectively), the aforementioned phenomena are expected to be more pronounced; however, due to the moderate wettability of MgO by the molten salt, the Gibbs–Thomson effect is less likely to occur.

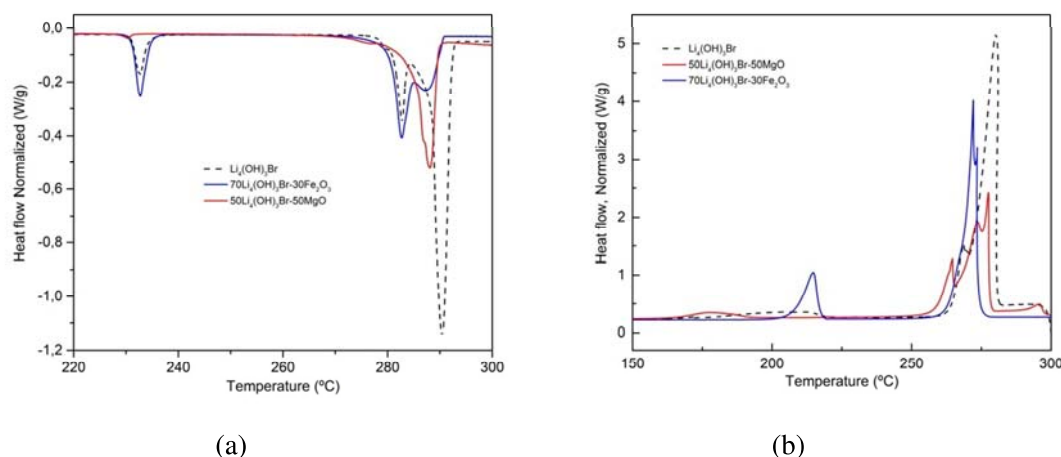


Figure 6.4. DSC curves of $\text{Li}_4(\text{OH})_3\text{Br}$ -based shape stabilized composites: (a) Upon heating; (b) Upon cooling.

Table 6.3. Temperatures and enthalpies corresponding to the peritectic reaction of different $\text{Li}_4(\text{OH})_3\text{Br}$ based ss-composites before and after thermal cycling.

Composition	T_{onset} (°C)	$\Delta H_{\text{Experimental}}$ (J/g)	$\Delta H_{\text{Calculated}}$ (J/g)	Enthalpy loss (%)
Pure $\text{Li}_4(\text{OH})_3\text{Br}$	289	247	247	
70 $\text{Li}_4(\text{OH})_3\text{Br}$ -30 Fe_2O_3 -0Cycle	281	132	173	17
70 $\text{Li}_4(\text{OH})_3\text{Br}$ -30 Fe_2O_3 -50Cycles	282	93	173	33
50 $\text{Li}_4(\text{OH})_3\text{Br}$ -50 MgO -0Cycle	285	114	124	4
50 $\text{Li}_4(\text{OH})_3\text{Br}$ -50 MgO -50Cycles	287	123	124	0.5

* These values correspond to the addition of the enthalpy of the decomposition of $\text{Li}_3(\text{OH})_2\text{Br}$ at 279 °C and that of $\text{Li}_4(\text{OH})_3\text{Br}$ at 289 °C.

Analyzing Table 6.3, the most promising material is the composite with MgO as support. A slight enthalpy loss is observed, 4 % compared to the 17 % for the composite with Fe_2O_3 . The enthalpy loss observed could be a sign of inhomogeneity of the composites structure, which means that the sample analyzed by DSC contained more supporting material than the active material (Salt). The composites with the best performances (with 50 wt.% of MgO and 30 wt.% of Fe_2O_3) were subjected to a cycle life analysis test (up to 50 cycles) to determine the reactivity and shape stabilization performance after prolonged charge-discharge cycles. The results of these experiments are reported in Figure 6.5. No leaks of the salt outside the composite were observed after 50 charge/discharge cycles for both samples. These results are very promising; the number of cycles applied could indeed be considered representative

regarding the stability of the shape stabilized composite. When considering the chemical stability, both composites confirm the trend already observed after one cycle.

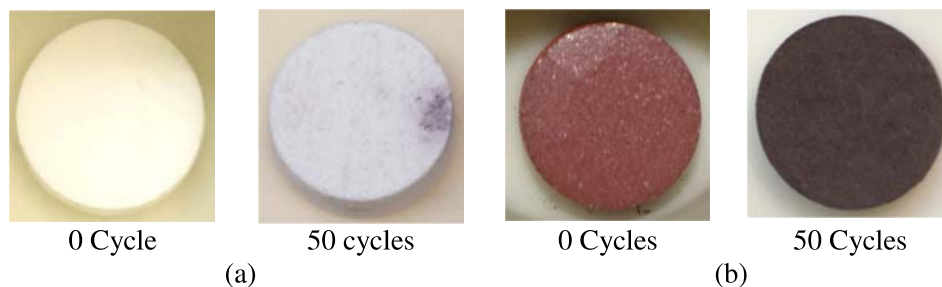


Figure 6.5. Images of the composite of $\text{Li}_4(\text{OH})_3\text{Br}$ based shape stabilized composite before and after thermal cycling tests: (a) $50\text{Li}_4(\text{OH})_3\text{Br}-50\text{MgO}$; (b) $70\text{Li}_4(\text{OH})_3\text{Br}-30\text{Fe}_2\text{O}_3$.

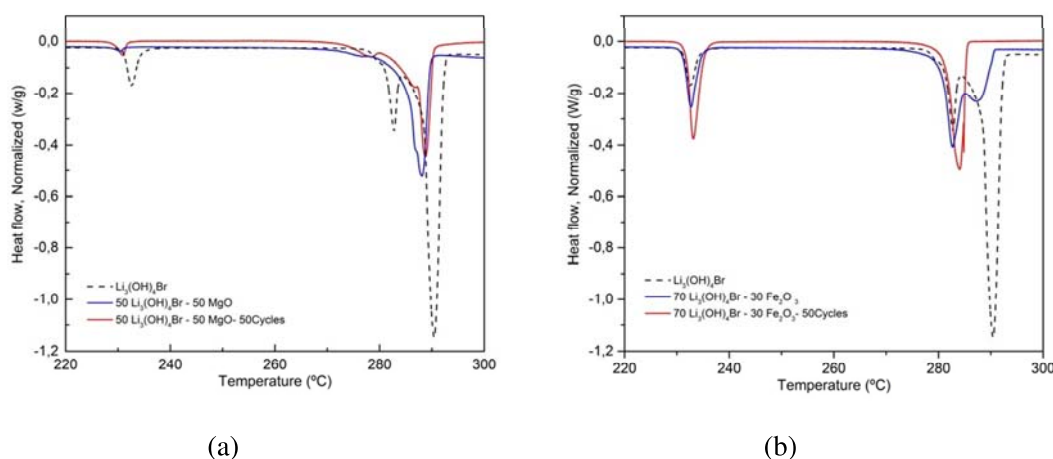


Figure 6.6. DSC curves of $\text{Li}_4(\text{OH})_3\text{Br}$ -based shape stabilized composites after cycling stability tests: (a) $50\text{Li}_4(\text{OH})_3\text{Br}-50\text{MgO}$; (b) $70\text{Li}_4(\text{OH})_3\text{Br}-30\text{Fe}_2\text{O}_3$.

MgO based composite is stable and inert, as confirmed by the results relevant to the reaction energy after 50 cycles (see Table 6.3) with enthalpy loss of only 0.5 %. The heating DSC curves of $50\text{Li}_4(\text{OH})_3\text{Br}-50\text{MgO}$ present good reproducibility as shown in Figure 6.6.a. On the other side, the Fe_2O_3 based composite shows a significant decrease in the reaction energy of 33 %, excluding its possible further utilization. This result is probably due to a slow and progressive reaction of the salt with the oxide, responsible for the strong interaction between the two materials, ending with the gradual degradation of the salt. This is manifested by a change in the heating DSC curves presented in Figure 6.6.b after 50 heating/cooling cycles.

6.3. $\text{Li}_4(\text{OH})_3\text{Br}/\text{MgO}$ shape stabilized composites

6.3.1. Characterization of as-prepared MgO samples

6.3.1.1. Nano-crystalline MgO prepared by ball milling process (MgO-BM)

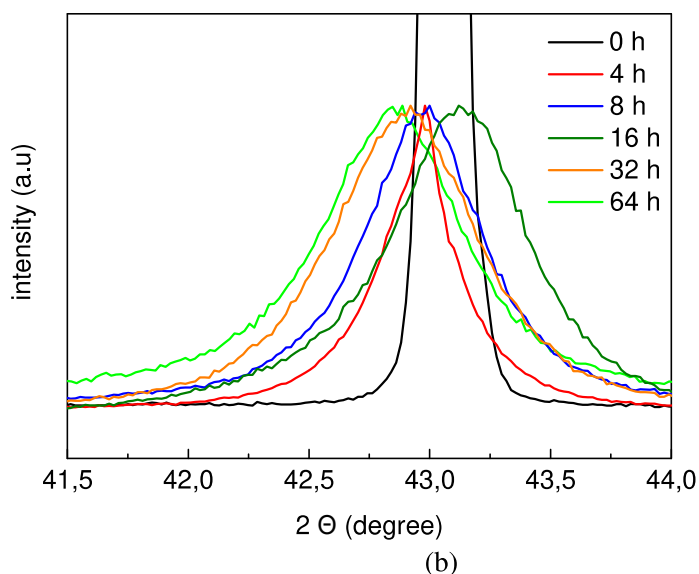
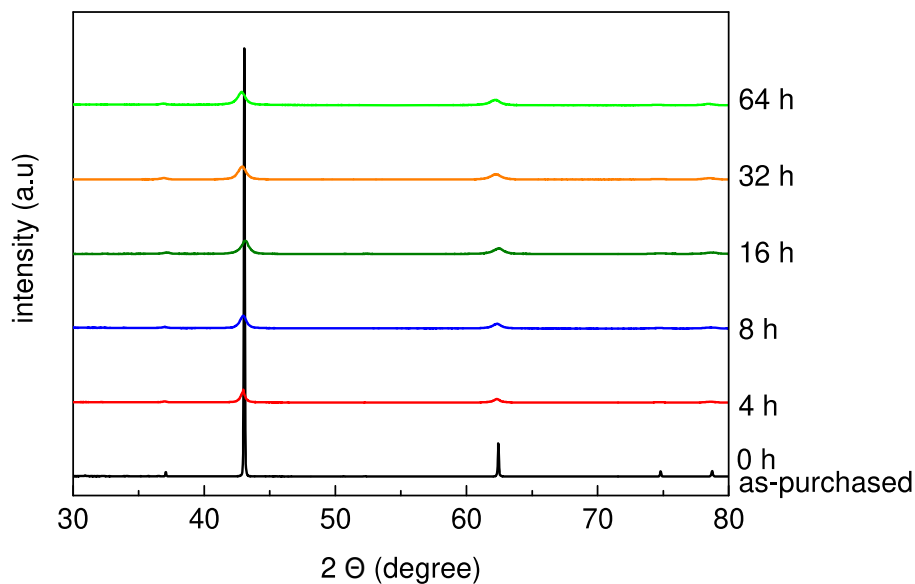


Figure 6.7. XRD patterns of milled MgO powders with milling time from 0 h to 64 h. MgO-BM samples were obtained by mechanical ball-milling treatment of commercial MgO powder with particle size in the range of (44-105 μm). The applied ball-milling protocol is described in chapter 2, section 2.1.5.2. In the context of our study, the ball-milling process

was applied in order to obtain a nanocrystalline porous structure. The porosity is obtained by particles fragmentation due to the collision energy during the ball-milling process. XRD analyses were carried out in order to study the effect of the milling time on the crystal structure of MgO-BM samples and to see whether there is a relationship between the crystalline size of the material and the antileakage performances. Figure 6.7 presents the XRD patterns of MgO as purchased and after different milling times. It can be seen clearly that the peaks become significantly broader and less intense after 4 hours of milling time. Increasing the milling time, from 4 hours to 64 hours, leads to an increase of the broadening of the peaks due to the formation of a highly disordered nanocrystalline phase, reflected by the decrease of the crystallite size and the increase in the lattice strain, as shown in figure 6.8. Particularly, the crystallite size rapidly decreased after 4 hours of ball-milling from ≈ 1064 nm to ≈ 20 nm. After that, it kept decreasing gradually, reaching 10 nm after 64 hours of ball-milling. On the other hand, the lattice strain has an opposite trend showing an increase from 0.06 % to 0.54 %, with the rise of milling time from 0 h to 64 h. The strain increase is due to the severe plastic deformation generated by the high collision energy during the ball-milling process, which causes the distortion of the lattice structure of MgO and lattice defects such as vacancies, dislocations, grain boundaries step, kink, corner atoms, etc. Additionally, as explained before, the collision energy generates the apparition of minor porosity with pore size in the range of 2 to 28 nm with a pore volume of $0.088 \text{ cm}^3/\text{g}$. For all the samples treated, neither the apparition of impurities nor the formation of new phases was observed after the ball-milling process.

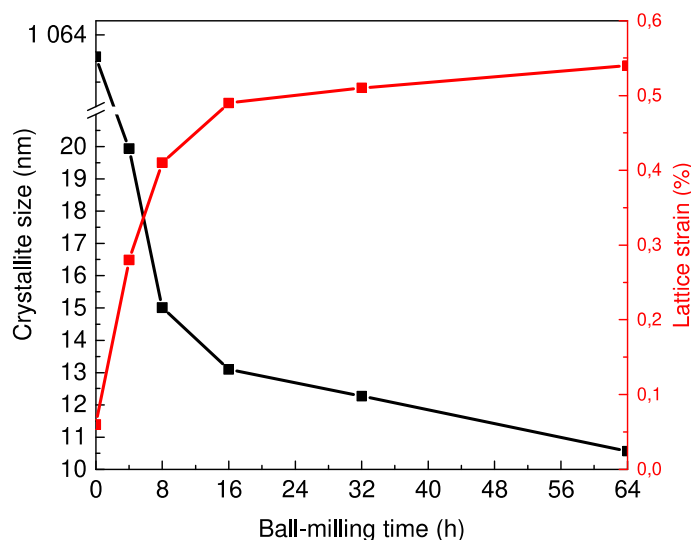


Figure 6.8. Variation of crystalline size and lattice strain of milled MgO as a function of ball-milling time

The anti-leakage performance of $\text{Li}_4(\text{OH})_3\text{Br}/\text{MgO-BM}$ ss-composites has been analyzed as described in section 6.2.1 (step 2 of the screening). For each composite, pellets of 13 mm in diameter and 5 mm in thickness were prepared using MgO-BM samples treated applying different milling times (MgO-BM-0h; MgO-BM-4h; MgO-BM-8h; MgO-BM-32h; MgO-BM-64h). The same MgO-BM loading of 30 wt. % was used for all the samples. It should be highlighted that according to the leakage tests carried out, 30 wt. % is the minimum loading achieved by the sample MgO-BM64h. Figure 6.9 present the different MgO-BM samples after the thermal treatment for salt leakage assessment. MgO-BM0h shows a serious salt leakage at 30 wt. % loading. The salt leakage is because the MgO sample before ball-milling treatment presents high particle size (44-105 μm) and no pores or surface defects or cavities (strain $\sim 0.02\%$) which results in the low specific surface area. The samples MgO-BM4h and MgO-BM8h present as well a severe salt leakage. It can be seen that the salt has leaked outside the structure of the composite and filled completely the bottom of the Corundum crucible. The lattice strain increased up to 0.28 % and 0.41 %, and the crystalline size decreased up to 20 nm and 15 nm for MgO-BM4h and MgO-BM8h, respectively. These structural modifications indicate the increase in the density of pore cavities and defects created by ball-milling, besides the augmentation of the density of grain boundaries. Both phenomena contribute to the rise of the specific surface area. However, according to the leakage test (figure 6.9), specific surface area and mesopores obtained after 8 hours of ball-milling are insufficient to prevent salt leakage. In the case of MgO-BM32h, a serious leakage occurs after the heat treatment; however, it can be noticed that the pellet didn't completely lose its shape, which is a sign of a beginning of salt retention. MgO-BM64h sample shows excellent structural stability at 30 wt. % loading. No salt leakage, cracks or breakages of the pellet were observed. It can be concluded that the nanocrystalline structure characteristic of the different MgO-BM samples impacts the structural stability of the composite through the modification of the structural properties of the material (increase the density of grain boundaries, and the density of pores and cavities within the structure). Moreover, the particularities of the sample MgO-BM64h, which allowed it to reach structural stability apart from the crystalline size, consist of its specific textural and morphological properties. Prolonged milling time (64 hours) will help to i) generates certain mesoporosity to the structure (pore volume = 0.088 cm^3/g) as confirmed by N_2 adsorption/desorption analysis (section 6.3.1.3). ii) Increases the density of defects within the structure. iii) Considerably decreases the particle size of the initial powder, as shown in figure 6.10 and table 6.4, MgO-BM64h has narrower particle size distribution compared to MgO-BM32h. The average

particle size is about $4\ \mu\text{m}$ compared to $10\ \mu\text{m}$ for MgO-BM32h and $44\text{--}105\ \mu\text{m}$ for the initial powder. All these specific morphological and textural properties generated by prolonged ball-milling treatment contributed in increasing the specific surface area of MgO-BM64h , and since the higher is the specific surface area the better is the antileakage efficiency, the structural stability was obtained particularly for the sample MgO-BM64h submitted to prolonged milling time.

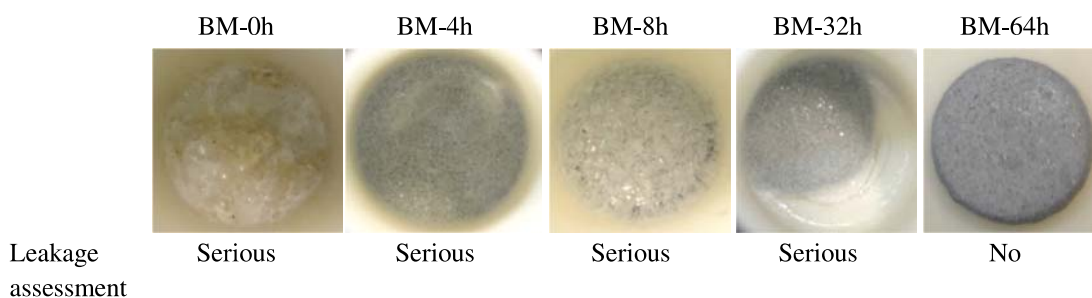
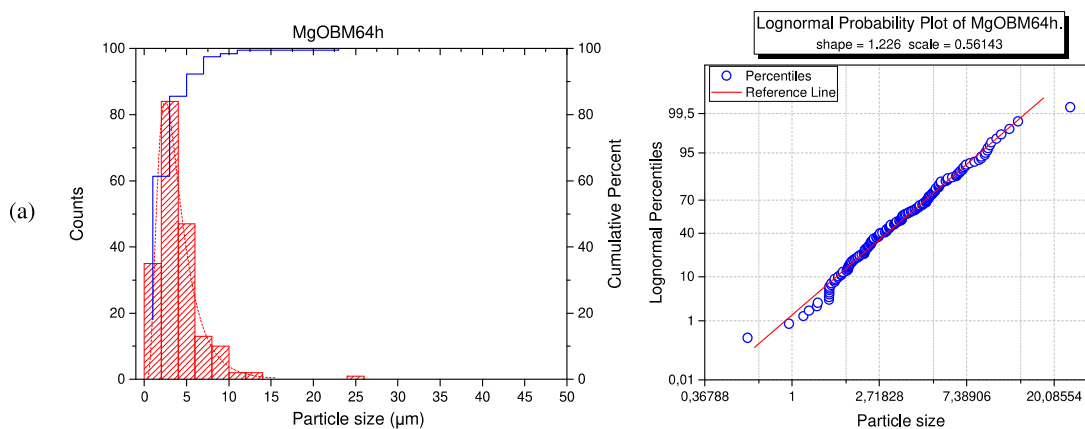
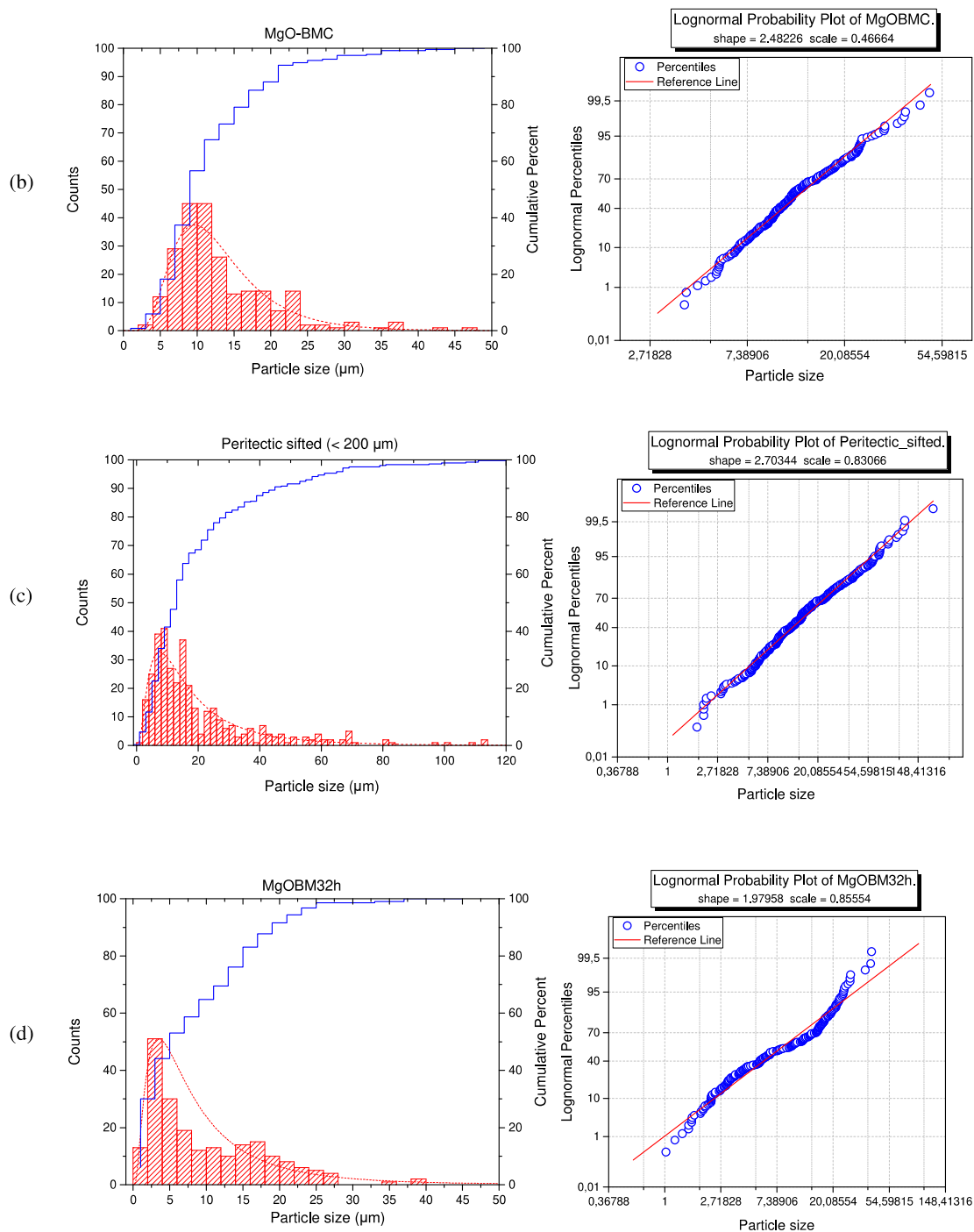


Figure 6.9. $70\text{Li}_4(\text{OH})_3\text{Br}/30\text{MgO-BM}$ ss-composites with milling time from 0 h up to 64 h after sintering showing salt leakage assessment.

6.3.1.2. Particle size distribution of as-prepared MgO samples





(e)

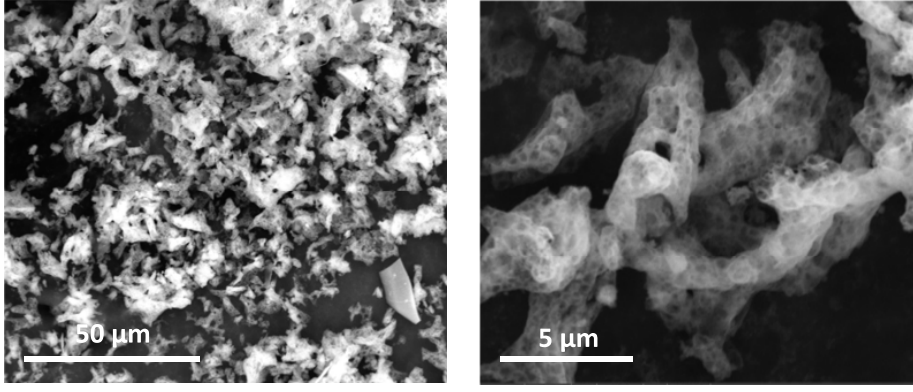


Figure 6.10. Histogram and cumulative probabilities of particle size distribution, and Lognormal probability plot of particle size of (a) MgO-BM64h; (b) MgO-BMC; (c) Sifted peritectic salt powder; (d) MgO-BM32h; (e) SEM micrographs of as prepared PMgO after physical shaking process

Particles size distribution of the as-prepared MgO samples (PMgO, MgO-BMC, MgO-BM64h, MgO-BM32h) and the sifted powder of the peritectic $\text{Li}_4(\text{OH})_3\text{Br}$ was assessed by analyzing SEM images of the samples using the software ImageJ2.0. At least 150 measurements were performed for each sample. Figure 6.10 shows the histograms of the particle size and the lognormal probability plots of (a) MgO-BM64h, (b) MgO-BMC, (c) the sifted peritectic powder, (d) MgO-BM32h, and (e) SEM micrographs of as prepared PMgO used for particle size estimation. In case of MgO-BM32h, MgO-BM64h MgO-BMC and sifted peritectic, the particle size distribution follows a lognormal distribution given by the following probability density function:

$$f(x) = \frac{1}{x\sigma\sqrt{2\pi}} \exp\left(-\frac{(\ln(x)-\mu)^2}{2\sigma^2}\right) \quad (eq. 1)$$

μ (shape scale parameter) is the mean

σ (the scale parameter) is the standard deviation of the natural logarithm of the variable

The arithmetic mean particle size is calculated following equation 2:

$$Mean = \exp\left(\mu + \frac{\sigma^2}{2}\right) \quad (2)$$

The arithmetic standard deviation is calculated following equation 3:

$$\text{Standard deviation} = \sqrt{[\exp(\sigma^2) - 1]\exp(2\mu + \sigma^2)} \quad (3)$$

The average particle size and the standard deviation of the different MgO samples are presented in Table 6.4. According to the results, MgO-BM64h presents a narrow particle size distribution with an average particle size of 4 μm in the range of 0 to 16 μm and a span of up to 26 μm . MgO-BMC has a relatively wider particle size distribution in the range of 2 to 48 μm with an average size of 13 μm . The wide particle size distribution of MgO-BMC sample will help to obtain a compact pellet. The wide particle size distribution of sifted peritectic salt is found to extend in the range of 0 to 170 μm with a predominant size of 0.6 – 21 μm . In the case of PMgO, after the physical shaking of the mixture $\text{Li}_4(\text{OH})_3\text{Br}/\text{PMgO}$, the foam-like structure of PMgO is destroyed, giving particles with random particle size and irregular geometric shape. For this reason, the longest length between two cutting edges was measured, representing this sample's particle size distribution. The predominant particle size was found to extend in the range from 0.6 μm to 21 μm . It is worth noting that even though MgO-BM64h, MgO-BMC and PMgO have very close particle size values. The latter still has an impact on the specific surface area of the samples besides the other textural properties. It is noteworthy that a supporting material with a small particle size combined with a broad particle size distribution can be beneficial for antileakage efficiency by increasing the SSA and the compactness of the pellet.

Table 6.4. The mean particle size and standard deviation of MgO samples

Sample	Mean particle size (μm)	Standard deviation (μm)
MgO-BM32h	10.44	10.84
MgO-BM64h	3.99	2.43
MgO-BMC	13.35	6.58
Sifted peritectic	21.08	21.02
PMgO	0.6 - 21	-

6.3.1.3. Porous structure of as-prepared MgO samples

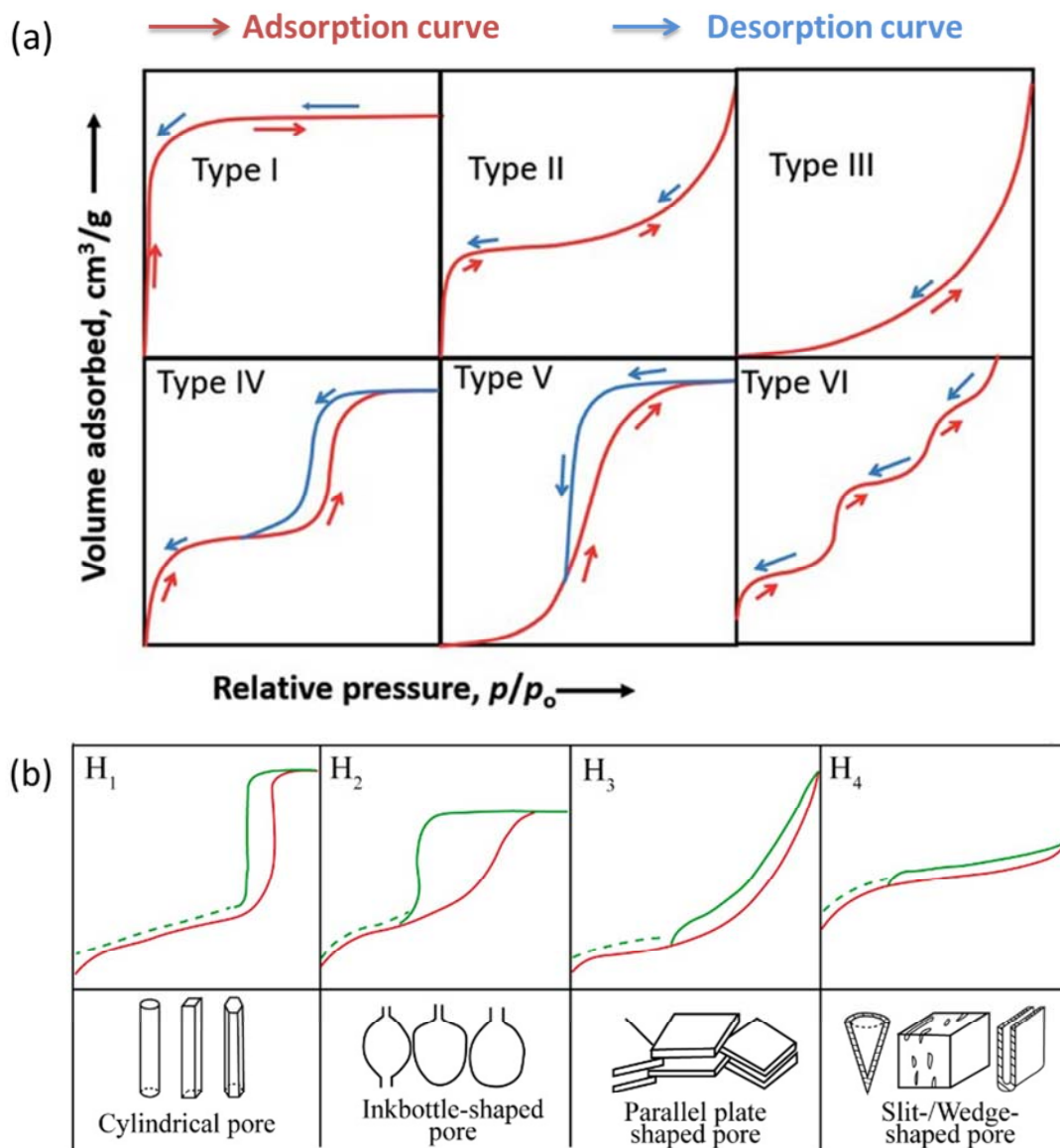


Figure 6.11. (a) Different types of adsorption isotherms according to IUPAC classification;
 (b) Different types of hysteresis patterns and the corresponding pore geometry [56]-[58]

The purpose of synthesizing porous MgO samples (PMgO, MgO-BM and MgO-BMC) was to benefit from the advantage of the mesoporosity in improving the antileakage efficiency of the ss-composites. No specifications of the BET surface area, the total pore volume, pore size distribution, pore shape, nanocrystalline size, and surface morphology of MgO particles were defined a priori.

The textural properties of the as-prepared porous MgO samples were investigated by means of N_2 adsorption/desorption isotherms. The International Union of Pure and Applied Chemistry (IUPAC) [56], [57] classified the adsorption isotherms, based on their nature, mainly into six different types (see figure 6.11.a). Some of the isotherms exhibit hysteresis, which can be obtained in different types (see figure 6.11.b). The hysteresis loop provides important information about the geometry of the pores. It should be highlighted that, according to the IUPAC, there are three main types of pores: micropores (< 2 nm), mesopores (2-50 nm), and macropores (> 50 nm). In this thesis, N_2 adsorption/desorption isotherms were obtained using a Micromeritics ASAP 2460 automated gas adsorption instrument. The equipment used and the experimental protocol applied are described in detail in chapter 2, section 2.2.1.5. The specific surface area of the samples was calculated using the Brunauer-Emmett-Teller (BET) model over the range of relative pressure (P/P_0) between 0.05 and 0.35. The pore size distribution was calculated applying the 2D-NLDFT model. And the total pore volume was determined for $P/P_0 = 0.98$.

Figure 6.12.a presents Nitrogen adsorption-desorption isotherms of the different MgO samples (PMgO; MgO-BMC; MgO-BM64h). The three isotherms saturate gradually with the increase of relative pressure. According to the IUPAC classification, MgO-BMC (green curve) exhibits type IV profile isotherm related to mesoporous materials. In the case of PMgO (blue curve) and MgO-BM64h (red curve), the isotherms display a profile between type II and type IV. Due to the noticeable hysteresis loops, they are associated to mesoporous materials as well. To sum up, the three MgO samples exhibit a type IV profile, proof of their mesoporous nature. In this regard, the shape of the isotherms can be explained as follows: i) At low relative pressures, the isotherms show a small steep uptake of Nitrogen due to the rapid saturation of the micropores, indicating the negligible amount of the latter. ii) Following that, it shows a quasi-plateau over a broad relative pressure range due to capillary condensation in mesopores. This phenomenon proves that these materials are predominantly mesoporous. iii) At high relative pressure ($P/P_0 > 0.5$), the MgO-BMC isotherm shows a sharp increase of N_2 adsorption compared to the other two samples, which might indicate that MgO-BMC owns a highly porous structure compared to PMgO and MgO-BM64h. This result correlates with the values of the total pore volume estimated, which show that MgO-BMC has the highest total pore volume. On the other hand, MgO-BM64h exhibits low N_2 adsorption compared to MgO-BMC and PMgO as an indication of low porosity structure. This result is

confirmed by the total pore volume of this sample which shows the lowest value compared to the other two samples.

Regarding the pore geometry, the three isotherms present different types of hysteresis, indicating that each sample has a specific pore shape. MgO-BMC isotherms show an H2-type hysteresis loop. The latter is characterized by the apparition of an inflection point around a relative pressure $P/P_0 = 0.5$ in the desorption isotherm inducing a wider hysteresis. The typical pore shape associated to this type of hysteresis is called inkbottle-shaped pore, and it has a large body with a narrow bottleneck shape open on one side or both sides, as shown in figure 6.11.b. This type is also characterized by a disordered distribution of pores. In addition to H2-type hysteresis, it can be noticed the presence of H1-type hysteresis loop in the range of relative pressure from 0.8 to 0.98. This type is characterized by a narrow hysteresis besides to a rapid increase of the adsorption isotherm at high $P/P_0 = 0.9$. The typical pore shape of this type corresponds to tubular-shaped or cylindrical pores open on both sides. To sum it up, according to IUPAC classification, the isotherms show that MgO-BMC sample has inkbottle-shaped pores combined with cylindrical pores. As shown in figure 6.12.a, PMgO isotherms show H3-type hysteresis loop. The hysteresis is narrow and appears in the relative pressure region between 0.5 and 0.98. This type of hysteresis is characteristic of parallel plate-shaped pores, as shown in figure 6.11.b. Regarding MgO-BM64h, the isotherms show H4-type hysteresis loop characteristic of slit-shaped pores.

As shown in table 6.5, MgO-BMC shows to have the highest pore volume ($0.294 \text{ cm}^3/\text{g}$), followed by PMgO ($0.217 \text{ cm}^3/\text{g}$), which has a slightly lower value, followed by MgO-BM64h ($0.088 \text{ cm}^3/\text{g}$), which has a very low pore volume, three times lower than that of MgO-BMC, this low pore volume is anticipated because, unlike MgO-BMC, MgO-BM64h was tailored to be used as nanocrystalline material and not a porous one. The porosity this material has is the product of the ball milling process, which impacts the shape stabilization efficiency of the composite material advantageously. The total pore volume values are reflected in the N_2 adsorption/desorption isotherms, as explained above. Indeed, the highest pore volume is reflected by the highest adsorption amount of Nitrogen and vice versa. Regarding the pore size distribution, as shown in figure 6.12.b, MgO-BMC has a narrow pore size distribution that extends from 2 to 7 nm with one peak at 4 nm. PMgO and MgO-BM64h have a wider and almost similar pore size distribution represented by two broad peaks at 10 and 22 nm for PMgO and in the range from 5 to 28 nm, with the main peak at 22 nm for MgO-BM64h. The calculated BET specific surface area is $40 \text{ m}^2 \text{ g}^{-1}$ and $55 \text{ m}^2 \text{ g}^{-1}$ for PMgO and MgO-BM64h, respectively. Meanwhile, MgO-BMC has a specific surface area of 129 m^2

g^{-1} , three times higher than the one of PMgO and MgO-BM64h. In fact, MgO-BMC has a higher specific surface area than PMgO even though they have almost the same total pore volume and particle size is because the former has a smaller pore size, as shown in figure 6.12. In addition, this high SSA is the result of the highly porous structure of the sample as expressed by the high Nitrogen adsorption at very high relative pressure and the fuzz-like surface morphology of MgO-BMC particles. Moreover, it is essential to highlight that the reason why MgO-BM64h has an appreciable specific surface area (slightly higher than that of PMgO), even though it doesn't have a remarkable porosity, is owing to the rough surface morphology of the particles due to particle agglomerations creating cavities, besides to the surface defects and reduction of the particle size due to the ball milling process.

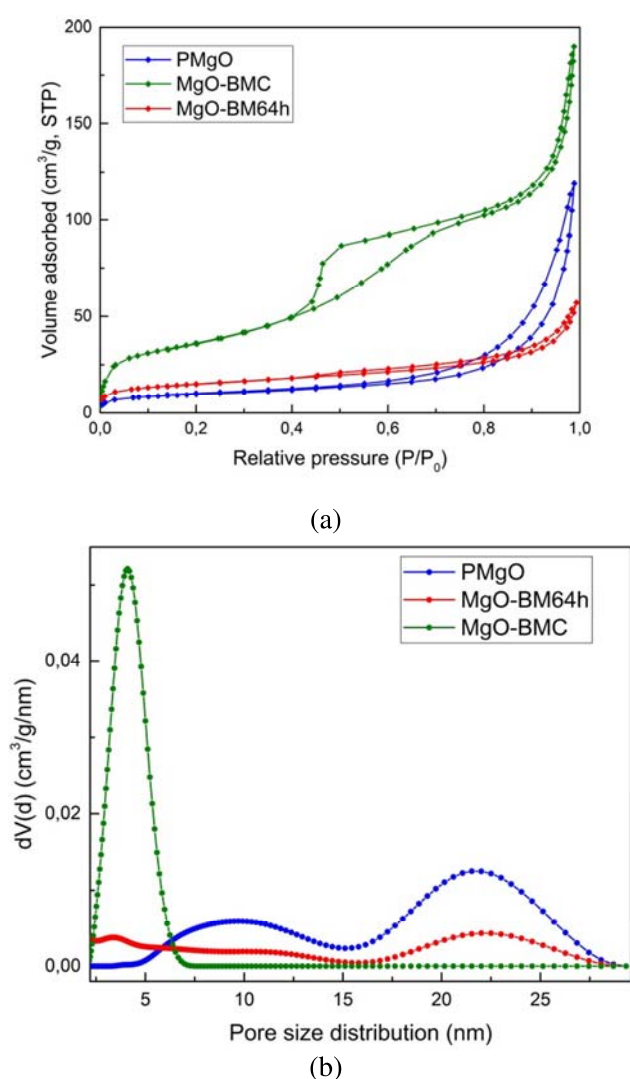


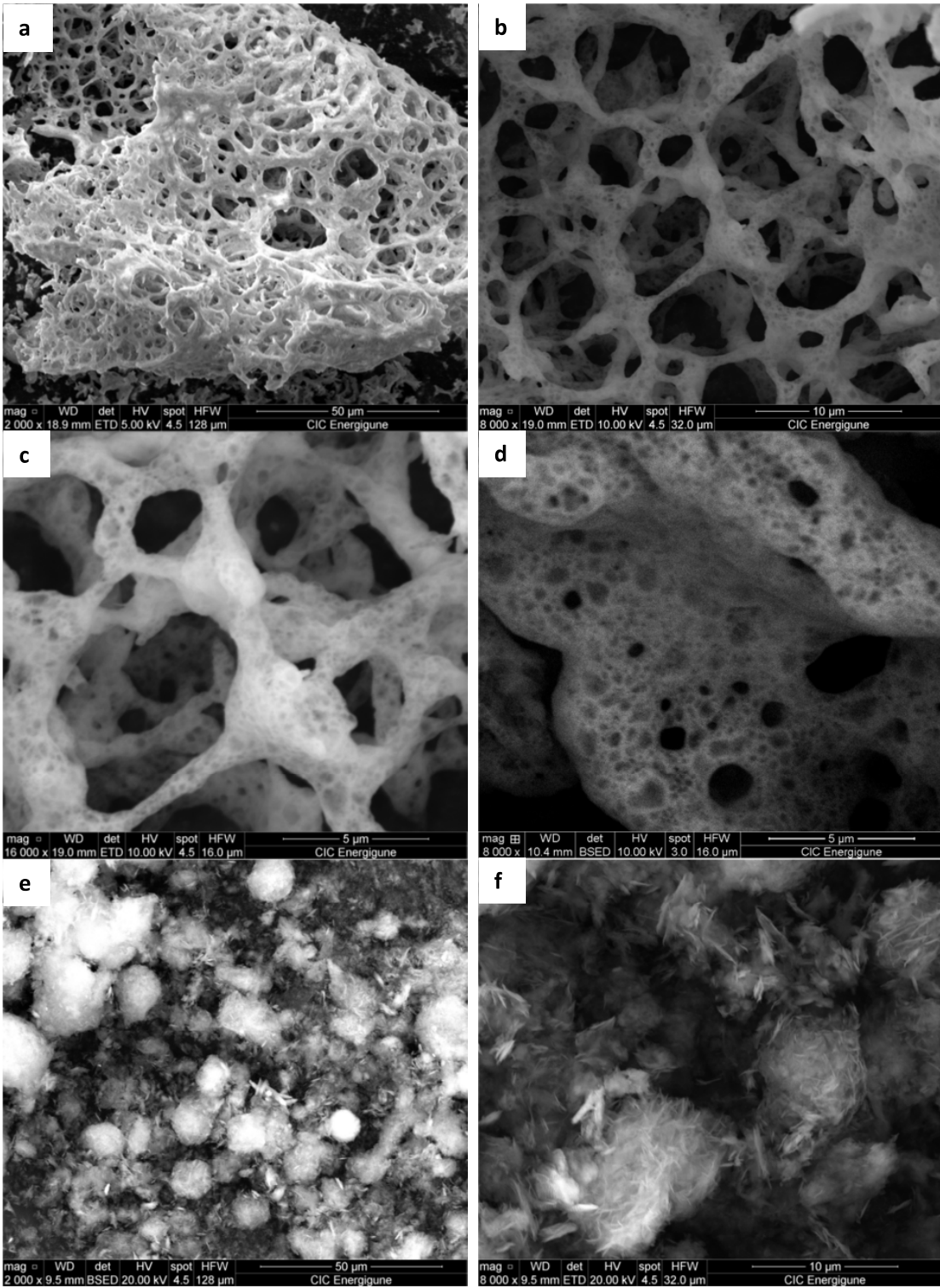
Figure 6.12. a) N_2 adsorption-desorption isotherms of as-prepared Porous MgO; b) Pore size distributions of as-prepared porous MgO.

Table 6.5. BET surface areas and pore volume of different MgO samples determined from nitrogen adsorption-desorption isotherm

Sample	Surface area (m^2/g)	Pore volume (cm^3/g)
MgO-nm	> 7.3	Non-porous
PMgO	40.1	0.217
MgO-BMC	129.1	0.294
MgO-BM64h	54.5	0.088

6.3.1.4. Microstructural analysis of the as-prepared MgO samples

Figure 6.13 presents the SEM images of the three porous MgO samples. The as-prepared PMgO sample shows a sponge-like morphology with interconnected holes of different sizes ranging from $0.5\ \mu\text{m}$ to $20\ \mu\text{m}$. Besides the presence of an interconnected open porosity within the walls of the sponge-like structure. The pores are on the scale of tens of nanometers, as confirmed by BET results. It should be noted that the sponge-like morphology property is not beneficial for the antileakage performance of the composite, as it is destroyed after the physical shaking of the mixture $\text{Li}_4(\text{OH})_3\text{Br}/\text{PMgO}$ during the synthesis process because the synthesized porous MgO is a fluffy-like powder and has no mechanical resistance. On the other hand, the presence of nanoporosity will help to limit the salt leakage phenomena by the capillary forces it induces. For this sample, the particle size is not a key parameter for the structural stability of the composite because it changes drastically during the synthesis process. In fact, the estimation of the average particle size of PMgO after the physical shaking step was found to be in the range from $0.6\ \mu\text{m}$ to $21\ \mu\text{m}$. Regarding the MgO-BMC sample, the morphology exhibits spherical particles with a fuzz-like structure on its surface. The average particle size is found to be $13\ \mu\text{m}$. In the case of MgO-BM64h sample, the microstructure shows the aggregation of MgO particles due to the ball-milling process exhibiting irregular shape aggregates with different sizes. The surface morphology shows a rough surface due to the attachment of small particles to the surface of larger aggregates, besides to the cracks, pores, and defects created by the collision forces. The average aggregate size is estimated to be around $4\ \mu\text{m}$.



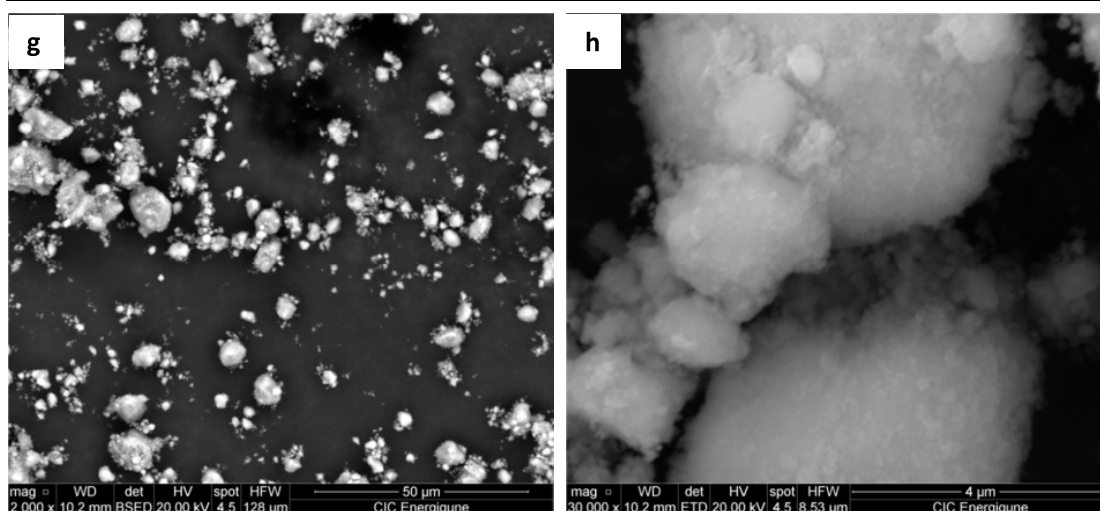


Figure 6.13. SEM images of (a-b-c-d) PMgO; (e-f) MgO-BMC; (g-h) MgO-BM64h

6.3.2. Characterization of $\text{Li}_4(\text{OH})_3\text{Br}/\text{MgO}$ composites

6.3.2.1. Anti-leakage effectiveness and maximum salt loading

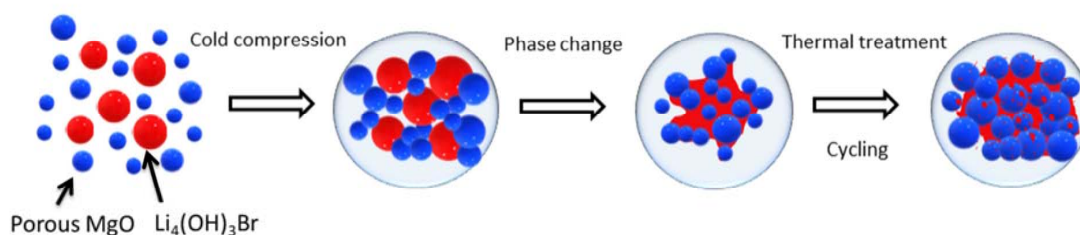


Figure 6.14. Schematic represents the microstructural evolution of $\text{Li}_4(\text{OH})_3\text{Br}/\text{porous-MgO}$ composite upon fabrication process and after cycling

Wt. %
MgO

50

30

30

30

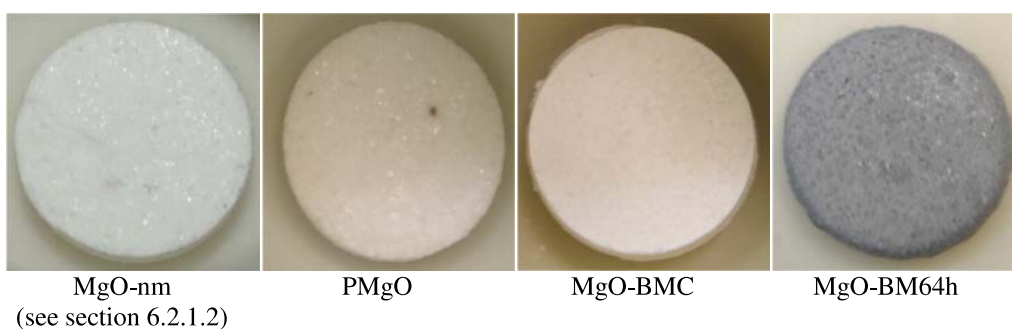


Figure 6.15. $\text{Li}_4(\text{OH})_3\text{Br}/\text{MgO}$ ss-composites with different MgO samples after sintering

In the first part of this chapter, MgO nanopowder (100 nm) has shown its ability to afford the shape stabilization of the peritectic salt $\text{Li}_4(\text{OH})_3\text{Br}$ at a minimum loading of 50 wt. % (see section 6.1.1.2). Considering that MgO as supporting material for the ss-composite doesn't

contribute to the enthalpy of the $\text{Li}_4(\text{OH})_3\text{Br}/\text{MgO}$ composite, it is necessary to decrease the amount of supporting material, required for optimal structural stability, as much as possible in order to enhance the storage capacity of the composite. For this purpose, antileakage tests were carried out using the three previously characterized porous MgO samples with different structural, textural and morphological properties. Initially, pellets were prepared by applying the synthesis protocol described in chapter 2, section 2.1.5.3. MgO content was decreased from a concentration of 50 wt. % until reaching the minimum amount required to ensure the structural stability of the composite after thermal treatment. Figure 6.15 shows the pellets after thermal treatment of the composites highlighting the minimum MgO loading achieved by each sample. It should be noted that for MgO loading less than 30 wt. %, PMgO, MgO-BMC, and MgO-BM64h show salt leakage.

It is plain to see that the three MgO samples achieved the same minimum oxide loading (30 Wt. %) even though they possess fully and completely different structural and textural properties. The common property to all the samples is the presence of mesoporosity. The latter plays the main role in improving the structural stability at a loading less than the one needed in the case of non-porous MgO-nm nanoparticles (50 wt. %). The three composite samples ($70\text{Li}_4(\text{OH})_3\text{Br}$ -30PMgO, $70\text{Li}_4(\text{OH})_3\text{Br}$ -30MgO-BMC, and $70\text{Li}_4(\text{OH})_3\text{Br}$ -30MgO-BM64h) were synthesized by cold compression route. Their structural stability is guaranteed by the two following mechanisms:

1) The standard mechanism responsible for the structural stability in the case of shape stabilized composites prepared by cold compression route [27], [53], [58]. Following this mechanism, the structural stability at the solid state is ensured through both the mechanical locks created by the external compression pressure and the bonding created by the solidified peritectic salt. At the liquid state, the structural stability of the composite is ensured by the interfacial energy between the porous MgO and the molten salt. For a detailed explanation of the mechanism, a description of the microstructural evolution of the composite before and after thermal treatment is proposed in figure 6.14. First, the compression pressure creates cavities, holes, and interparticle voids inside the pellet through mechanical locks between MgO particles while ensuring the compactness of the pellet. Then, during the thermal treatment, when the temperature exceeded the melting temperature of $\text{Li}_4(\text{OH})_3\text{Br}$ salt (350 °C), both the pressure difference created by the volume change of the peritectic salt (~3%) during the phase change, the interfacial energy between the liquid salt and MgO particles, and

the gravitational force, push the liquid salt to flow into the voids forming a liquid bridge. The structure of the composite in the multiphase state will be maintained thanks to the formed liquid bridge, capillary force and surface tension between the liquid salt and MgO particles. The above-described mechanism will also help to manage the volume expansion of the melted salts

2) Mesoporosity presents within the MgO nanoparticles. Besides to the interparticle pores present in the pellet, mesopores will contribute to the structural stability of the composite by preventing salt leakage through the strong capillary force and surface tension they provide. Several studies reported the advantages of using mesoporosity over macroporosity and microporosity for preventing PCM leakage [59]–[64]. In fact, microporosity offers stronger capillary forces compared to mesopores, hence better liquid retention. However, they present a higher confinement effect compared to mesopores, which can affect the reaction temperature and enthalpy of the composite. For this reason, the presence of only small microporosity within the tested porous MgO samples can be accepted. On the other hand, macropores are more appropriated for higher salt loading in the case of solid foam-like porous supporting materials, which is not the concern of our study. Besides, macropores provide weaker capillary force, unable to ensure liquid retention. For these reasons, macropores can't be beneficial for our study. Finally, it can be concluded that unlike non-porous MgO used in the first part of this chapter, which benefits only from the first mechanism to ensure its structural stability, the porous MgO combined both the first and second mechanism, which allows to considerably decrease the amount of MgO required for the same antileakage efficiency.

Section 6.2.1.2 listed the primary characteristics of an oxide supporting material (massive powder) that affect the salt loading. These characteristics are the oxide particles size, the surface area of the oxide powder, and the wettability of the oxide by the melted salt. It was concluded that the antileakage efficiency of the composite is optimal when using a supporting material with a combination of good wettability and a large surface area (small particle size). In this part, other characteristics related to mesoporous oxide particles were evaluated. They consist of the pore shape, the pore size, the pore size distribution, the total pore volume, the surface morphology of the particle, and the crystalline size). It was found that structural stability is ensured while combining two or more of these characteristics for one objective, which is to afford as high specific surface area as possible. For instance, the structural

stability in the case of $\text{Li}_4(\text{OH})_3\text{Br}/\text{MgO-BMC}$ composite is ensured, besides to the mechanism (1) described above, thanks to the high specific surface area of Mg-BMC ($129.1 \text{ m}^2/\text{g}$) afforded by the combination of the high pore volume of the sample ($0.294 \text{ cm}^3/\text{g}$), small pore size (nm) and fuzzy-like surface morphology of the porous particles. Basically, the high surface area generates higher interfacial energy between the salt and MgO-BMC, which ensures good salt retention. In the case of $\text{Li}_4(\text{OH})_3\text{Br}/\text{MgO-BM64h}$ composite, the structural stability is also ensured by the mechanism (1) described above. Additionally, although the small pore volume of MgO-BM64h 3 times lower than PMgOs) and its large pore size distribution (ranging from 2-28 nm). The specific surface area of the MgO-BM64h sample results from the small porosity of the sample, the rough surface of MgO-BM64h aggregates, and most importantly, the nanocrystalline nature of the sample. In fact, the nanocrystalline structure owns a high density of grain boundaries increasing the specific surface area of the material; hence the interfacial energy is increased, leading to good structural stability. For $\text{Li}_4(\text{OH})_3\text{Br}/\text{PMgO}$, the structural stability is ensured by both mechanisms described above. This sample has a surface area ($40.1 \text{ m}^2/\text{g}$) three times lower than the one of MgO-BMC with an almost similar pore volume ($0.217 \text{ cm}^3/\text{g}$). This is due to its larger pore size and wider pore size distribution (5-28 nm), and smooth surface morphology. Furthermore, as explained in section 6.3.1.3, each MgO sample owns a particular pore shape originated from its synthesis process. So far, the experimental analyses carried out are not sufficient to make conclusions about the effect of the pore geometry on the properties of the composite. Nevertheless, assumptions can be made based on the thermal properties of the composite. For instance, a change in the reaction temperature and enthalpy of the composite toward lower values can indicate a good infiltration of the salt within the pores. This can be related not only to the pore size but also to the pore geometry. In order to explicitly investigate the effect of the pore shape of the supporting material on the salt loading, samples with the same porosity and different pore shapes should be tested and analyzed.

6.3.2.2. Thermal characterization of $\text{Li}_4(\text{OH})_3\text{Br}/\text{MgO}$ composites

- 50 $\text{Li}_4(\text{OH})_3\text{Br}/50\text{MgO}$ -nm
- 70 $\text{Li}_4(\text{OH})_3\text{Br}/30\text{MgO}$ -BMC
- 70 $\text{Li}_4(\text{OH})_3\text{Br}/30\text{PMgO}$
- 70 $\text{Li}_4(\text{OH})_3\text{Br}/30\text{MgO}$ -BM64h
- $\text{Li}_4(\text{OH})_3\text{Br}$

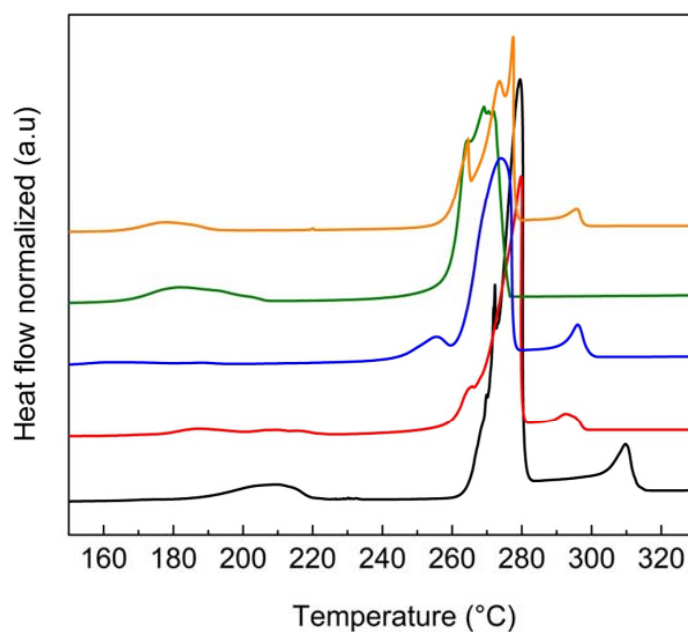
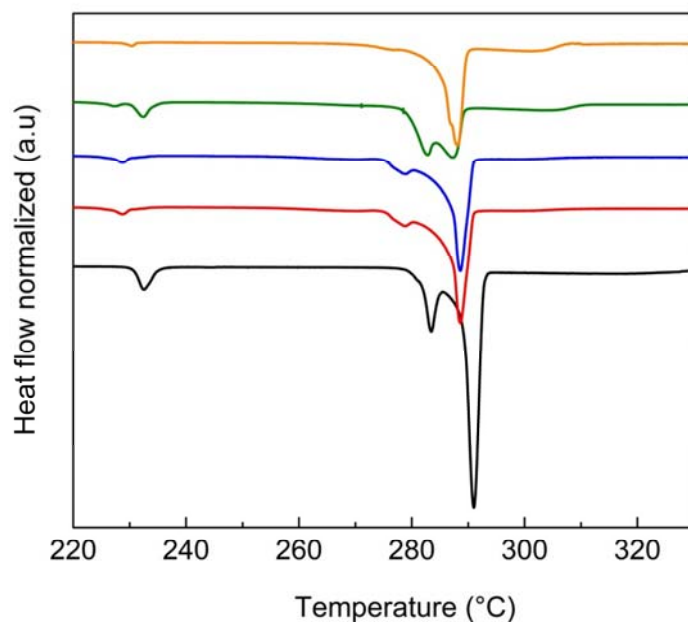


Figure 6.16. DSC curves of $\text{Li}_4(\text{OH})_3\text{Br}/\text{Porous-MgO}$ composites after thermal treatment recorded at $1^\circ\text{C}/\text{min}$: a- upon heating; b- upon cooling.

The composites $70\text{Li}_4(\text{OH})_3\text{Br}-30\text{PMgO}$, $70\text{Li}_4(\text{OH})_3\text{Br}-30\text{MgO-BMC}$, and $70\text{Li}_4(\text{OH})_3\text{Br}-30\text{MgO-BM64h}$ obtained after the heat treatment process were characterized by DSC. The objective was to study the influence of shape stabilization on the thermal properties of the salt. DSC curves of the samples obtained upon heating, and cooling steps are presented in Figure 6.16. For the sake of comparison, in the same figure are presented the DSC curves of the pure peritectic salt and the $50\text{Li}_4(\text{OH})_3\text{Br}-50\text{MgO-nm}$ obtained in the first part of this chapter. It can be seen that both heating and cooling DSC thermograms of the composites present some differences compared to the ones of the pure peritectic salt in terms of transition temperatures and enthalpies. As a reminder, the DSC thermogram (black curve) of the pure peritectic salt obtained during the heating stage presents three phase transitions (see chapter 4, section 4.3). A first and second peaks occur at $231\text{ }^\circ\text{C}$ and $279\text{ }^\circ\text{C}$, respectively, which correspond to the formation/decomposition of the intermediate compound $\text{Li}_3(\text{OH})_2\text{Br}$. Additionally, a third peak appears at $289\text{ }^\circ\text{C}$ and corresponds to the peritectic reaction ($\text{Li}_4(\text{OH})_3\text{Br} \rightarrow \text{LiOH (s)} + \text{L}$). The liquidus, estimated to be $\geq 340\text{ }^\circ\text{C}$, is hardly visible on heating whereas it is noticeable on cooling.

It is important to note that the enthalpy values reported in table 6.6 include both the enthalpy of melting of $\text{Li}_4(\text{OH})_3\text{Br}$ at $289\text{ }^\circ\text{C}$ (3rd peak in the DSC thermograms) and that of the decomposition of $\text{Li}_3(\text{OH})_2\text{Br}$ at $279\text{ }^\circ\text{C}$ (2nd peak in the DSC thermograms), whereas the reaction temperature correspond to the onset temperature of the endothermic peak related to the peritectic reaction. On heating, the DSC thermograms (Figure 6.16.a) of MgO-BM64h (red curve) and PMgO (blue curve) based composites show three transition peaks similarly to the pure peritectic salt. In addition, a slight shift in the transition temperatures related to each of the formation/decomposition of $\text{Li}_3(\text{OH})_2\text{Br}$ and the peritectic reaction toward lower temperatures is observed. As reported in table 6.6, for both samples, the peritectic reaction temperature shifted about 1 to $2\text{ }^\circ\text{C}$ toward lower temperatures. This can be explained by the confinement effect of the salt within the interparticle voids of the composites and the mesopores of the MgO samples. Moreover, the reason why the temperature shift is more important in the case of PMgO based composite is attributed to the fact that PMgO has a higher mesoporosity compared to MgO-BM64h since both materials have almost similar pore size distribution. The same observations were reported for MgO-nm based composite even though this material is not porous. The reason for that is the higher amount of MgO used (50 wt. %), which will generate a higher density of cavities and interparticle voids promoting salt confinement. Furthermore, a drop in the enthalpy of the peritectic reaction is also noticed.

Comparing the experimental enthalpy value to the theoretically calculated one, an enthalpy loss of about 11 % and 14 % was obtained for MgO-BM64h and PMgO based composites, respectively. The enthalpy loss depends highly on the density and the size of the pores of MgO and interparticle voids present in the composite. In fact, depending on the pore size, the solidification of the infiltrated salt can be partially or totally suppressed, which will decrease the enthalpy of the composite. The higher is the porosity, and the smaller is the pore size, the higher is the enthalpy loss. For this reason, higher enthalpy loss is observed for PMgO based composite compared to MgO-BM64h composite.

In the case of MgO-BMC based composites, the thermogram shows two endothermic peaks instead of one peak for each phase transition. Two endothermic peaks at 225 °C and 230 °C related to the formation of $\text{Li}_3(\text{OH})_2\text{Br}$ instead of one peak at 231 °C. Besides to two endothermic peaks at 279 °C and 280 °C related to the peritectic reaction instead of one peak at 289 °C. The same events are reproducible on cooling (figure 6.16.b) except that the two peaks overlap (higher cooling rate of 10 °C/min). Considering that MgO-BMC is a highly porous material with a small pore size and narrow pore size distribution range (2-7 nm), this phenomenon can be explained as follow, the peaks occurring at lower temperatures (225 °C and 279 °C) correspond to the phase transitions undergone by the confined and infiltrated salt. Meanwhile, the peaks appearing at higher temperatures (230 °C and 280 °C) are related to the phase transitions of the non-confined salt present within the structure of the pellet. Regarding the thermal energy, the enthalpy related to the peritectic reaction of MgO-BMC composite decreased by 33 %. The important drop in the enthalpy can be due to the fact that the solidification of the infiltrated salt is most likely to be suppressed due to the small pore size of this sample (2-7 nm)

Table 6.6. Temperatures and enthalpies corresponding to the peritectic reaction of different $\text{Li}_4(\text{OH})_3\text{Br}/\text{MgO}$ composites after thermal treatment

Composition	$T_{\text{Peritectic}}$ (°C)	$\Delta H_{\text{Experimental}}^*$ (J/g)	$\Delta H_{\text{Calculated}}^*$ (J/g)	Enthalpy loss (%)
Pure $\text{Li}_4(\text{OH})_3\text{Br}$	289	247	247	-
50 $\text{Li}_4(\text{OH})_3\text{Br}/50\text{MgO-nm}$ (see section 6.2.1.3)	285	114	124	8
70 $\text{Li}_4(\text{OH})_3\text{Br}/30\text{PMgO}$	287	149	173	14
70 $\text{Li}_4(\text{OH})_3\text{Br}-30\text{MgO-BMC}$	285	115	173	33
70 $\text{Li}_4(\text{OH})_3\text{Br}-30\text{MgO-BM64h}$	287	154	173	11

* These values correspond to the addition of the enthalpy of the decomposition of $\text{Li}_3(\text{OH})_2\text{Br}$ at 279 °C and that of $\text{Li}_4(\text{OH})_3\text{Br}$ at 289 °C.

6.3.2.3. Cycling stability of $\text{Li}_4(\text{OH})_3\text{Br}$ /Porous-MgO composites




Supporting material	PMgO	MgO-BMC	MgO-BM64h
			
Leakage assessment	No	Minor	Serious

Figure 6.17. $70\text{Li}_4(\text{OH})_3\text{Br}/30\text{Porous-MgO}$ composites with different MgO samples after 50 melting/solidification cycles

The three composite materials were submitted to thermal cycling tests applying the protocol described in section 6.2.1. The objective was to test their thermal stability and antileakage efficiency over cycling. The results of the leakage tests after 50 heating/cooling cycles are reported in Figure 6.17. MgO-BM64h based composite presents a serious salt leakage. The composite pellet completely lost its shape, and the salt leaked and filled the bottom of the crucible. MgO-BMC based composite shows a minor salt leakage after cycling. Meanwhile, the results are very promising for composites using PMgO. The pellet shape is conserved after cycling with no salt leakage.

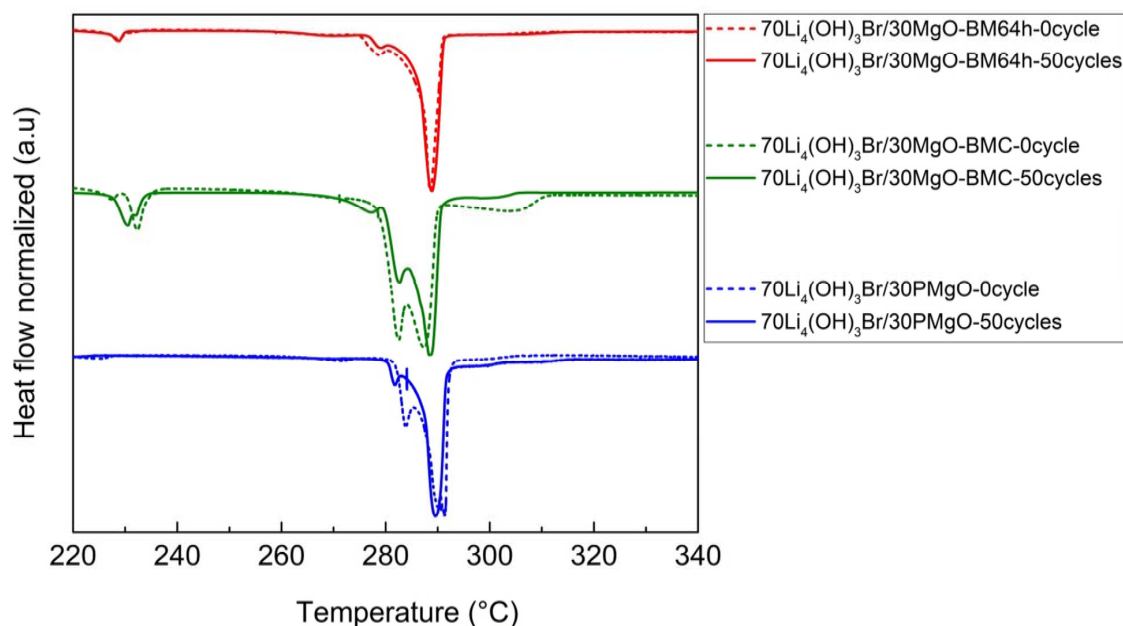


Figure 6.18. DSC thermograms (Normalized) on heating, heating rate = $1\text{ }^{\circ}\text{C}/\text{min}$ of different $\text{Li}_4(\text{OH})_3\text{Br}$ /Porous-MgO composites before and after thermal cycling

Table 6.7. Temperatures and enthalpies corresponding to the peritectic reaction of different $\text{Li}_4(\text{OH})_3\text{Br}$ /Porous-MgO composites after thermal cycling. The reference enthalpy $\Delta H_{\text{Reference}} = \Delta H_{\text{Per}} \cdot f$, where f represents the mass fraction of salt within the composite.

Composition	$T_{\text{Peritectic}}$ (°C)	$T_{\text{reference}}$ (°C)	ΔH_{per}^* (J/g)	$\Delta H_{\text{Reference}}^*$ (J/g)	Enthalpy Loss (%)
70 $\text{Li}_4(\text{OH})_3\text{Br}$ /30MgO-BM64h-50Cycles	287	289	54	173	69
70 $\text{Li}_4(\text{OH})_3\text{Br}$ /30MgO-BMC-50Cycles	284		38		78
70 $\text{Li}_4(\text{OH})_3\text{Br}$ /30PMgO-30Cycles	287		154		11
70 $\text{Li}_4(\text{OH})_3\text{Br}$ /30PMgO-50Cycles	288		156		10

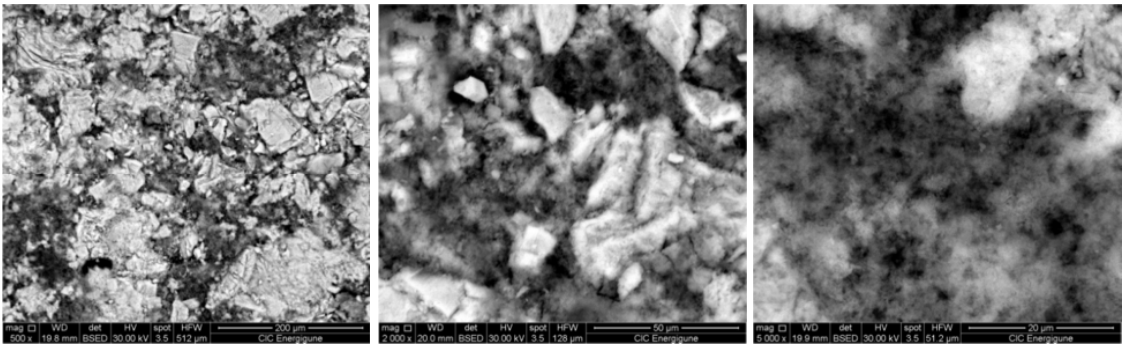
* These values correspond to the addition of the enthalpy of the decomposition of $\text{Li}_3(\text{OH})_2\text{Br}$ at 279 °C and that of $\text{Li}_4(\text{OH})_3\text{Br}$ at 289 °C

The results of the DSC analyses of different $\text{Li}_4(\text{OH})_3\text{Br}$ /Porous-MgO composites after thermal cycling are reported in table 6.7 and figure 6.18. it should be noted that the enthalpy values reported in table 6.7 include both the enthalpy of melting of $\text{Li}_4(\text{OH})_3\text{Br}$ at 289 °C (3rd peak in the DSC thermograms) and that of the decomposition of $\text{Li}_3(\text{OH})_2\text{Br}$ at 279 °C (2nd peak in the DSC thermograms), whereas the transition temperature correspond to the onset temperature of the endothermic peak related to the peritectic reaction. The peritectic temperature of MgO-BM64h and MgO-BMC based composites remains unchanged after thermal cycling. On the other hand, drastic decrease of the peritectic reaction enthalpy by 69% and 78% for MgO-BM64h and MgO-BMC based composites, respectively. The enthalpy loss is mainly due to the fact that these samples have undergone an important salt leakage over cycling. The salt leakage induces inhomogeneity of the composite structure. Consequently, the analyzed samples contain less amount of peritectic salt, thereby a less enthalpy values are obtained. Due to the structural and thermal instability of these two composites, MgO-BMC and MgO-BM64h were excluded for possible use as supporting material for shape stabilization of the peritectic salt $\text{Li}_4(\text{OH})_3\text{Br}$.

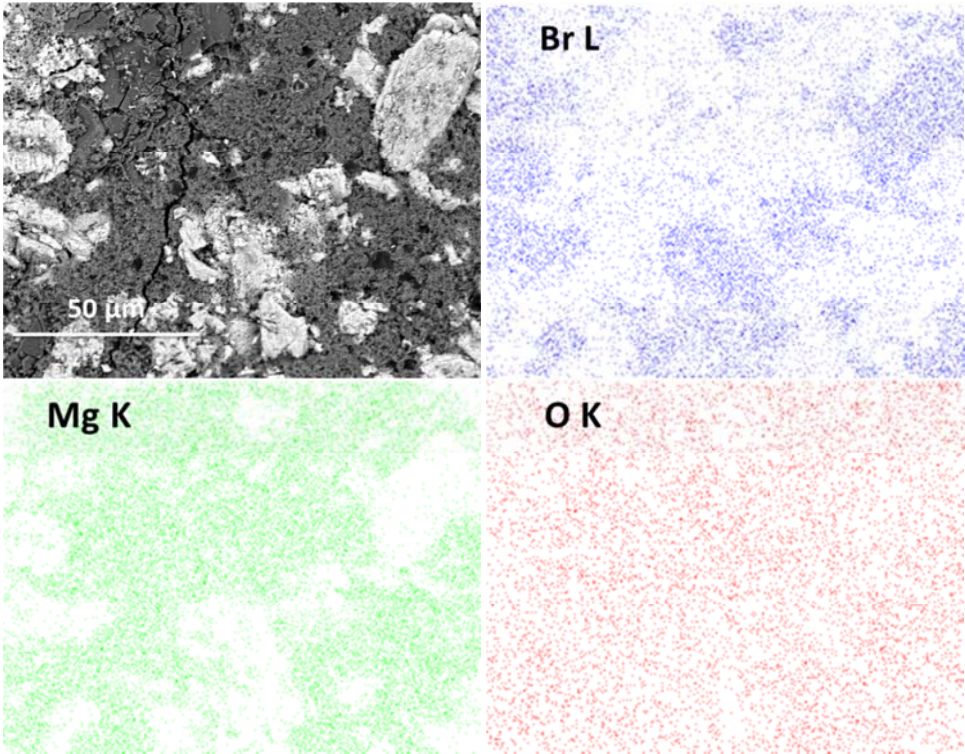
PMgO based composite shows as well a drop in the enthalpy of about 10 % after 50 cycles. Nevertheless, the enthalpy slightly improved over cycling, reporting an enhancement of about 4% after 50 cycles. This enthalpy improvement can be due to the homogeneity of the composite structure over cycling.

6.3.2.4 Microstructural analysis and thermal conductivity of PMgO based composite

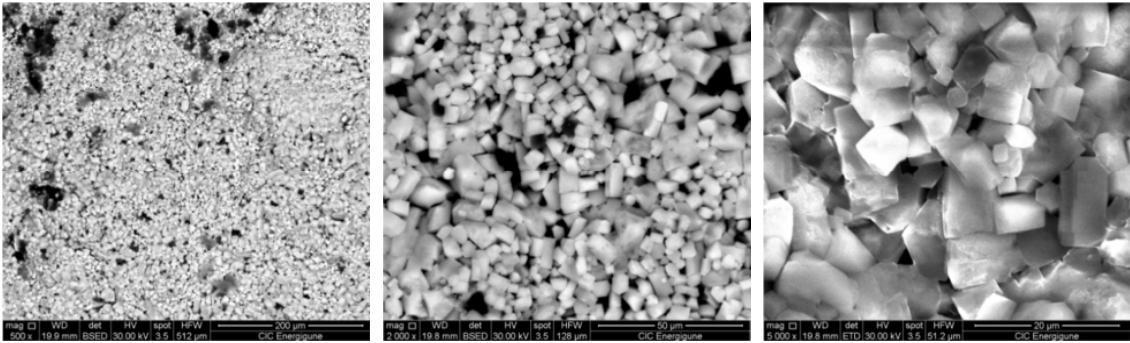
(a)



(b)



(c)



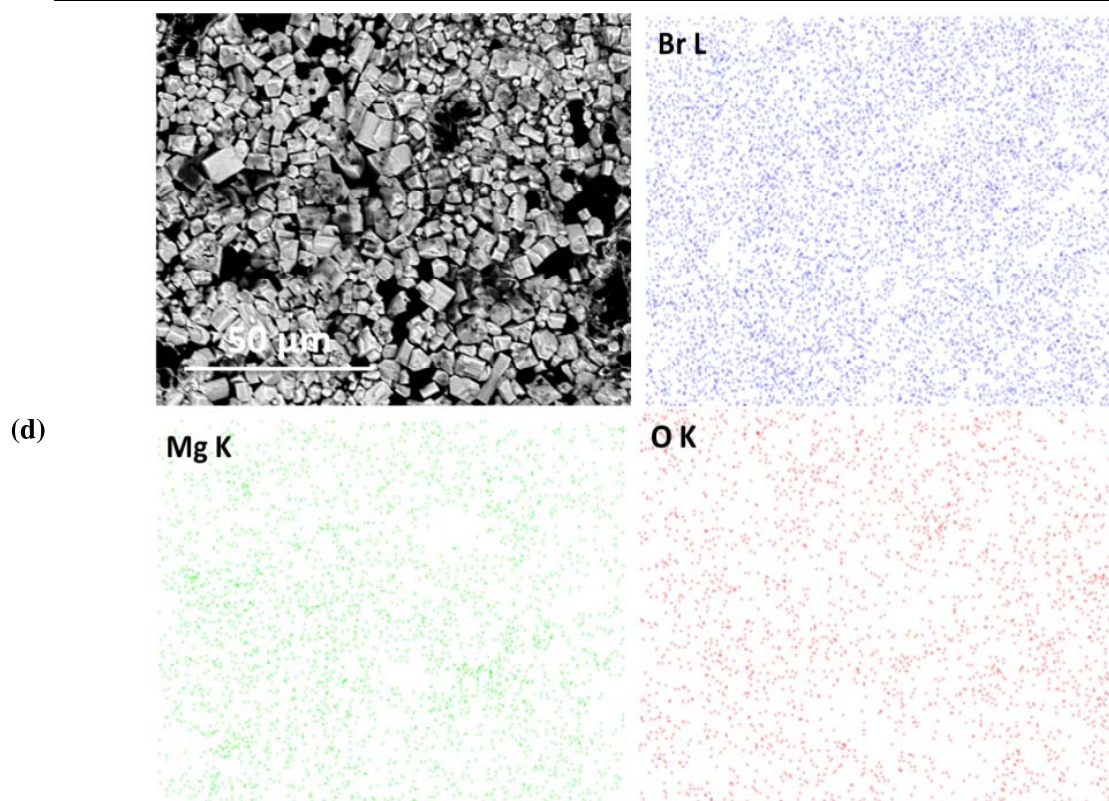


Figure 6.19. Microstructural of 70 $\text{Li}_4(\text{OH})_3\text{Br}$ /30PMgO composite (a) SEM micrographs prior thermal treatment; (b) EDS element mapping images prior thermal treatment; (c) SEM micrographs after thermal treatment; (d) EDS element mapping images after thermal treatment

The microstructural evolution of 70 $\text{Li}_4(\text{OH})_3\text{Br}$ /30PMgO composite before thermal treatment and after thermal cycling was investigated by SEM in order to study the effect of thermal cycling on the homogeneity of the composite structure. Figure 6.19.a&b present the SEM-EDS mapping images of the composite after cold compression and before thermal treatment. The micrographs show two different regions distinguished by light and dark colours. The light colours region corresponds to the peritectic salt. The morphology of the salt shows a lamellar microstructure with a slight granular aspect caused by the synthesis process. The dark colour region corresponds to PMgO particles. The latter is tightly compacted and encapsulates the salt. The overall aspect of the pellet seems inhomogeneous, which is typical considering the synthesis method of these materials. In fact, ensuring a good homogeneity of the mixture salt/oxide during the synthesis stage remains a challenge since the applied synthesis protocol relies on a physical mixing of the powders. Moreover, the microstructure shows microcracks as well as an open porosity. Figure 6.19.c&d present the SEM EDS mapping images of the composite after 50 melting/solidification cycles. The morphology of the samples changed over 50 cycles. The SEM micrographs depict cubic-like particles with asymmetric surface.

The EDS mapping show a homogeneous distribution of both PMgO and $\text{Li}_4(\text{OH})_3\text{Br}$ salt. The homogeneity of the structure was likely ensured by the redistribution of both components due to molten salt motion. Indeed, during the repeated melting/solidification processes, the salt migrates within the structure of the composite thanks to the surface tension and the volume change it undergoes. Liquid salt migration induces the rearrangement of the oxide particles through the pressure difference generated by the volume change of the salt. Migration and redistribution of both components combined with salt infiltration within the oxide pores lead to a more homogeneous structure of the composite, thus a more uniform heat transfer properties. The overall aspect of the pellet shows an open micrometric porosity (interparticle voids) with no cracks.

PMgO was used initially as a shape stabilizer in $\text{Li}_4(\text{OH})_3\text{Br}/\text{PMgO}$. However, since this ceramic has high thermal conductivity, it can potentially enhance the overall thermal conductivity of the composite. In literature, the use of MgO as a supporting material for shape stabilization was always combined with the use of a high thermal conductivity material to enhance the thermal conductivity of the composite [34], [42-43], [65-66].

In order to estimate the thermal conductivity enhancement, measurements have been carried out applying the protocol described in chapter 2, section 2.2.2.2. The measurements were repeated several times to check the reproducibility and the quality of the results. The sample was moved after each test, and different measuring times (5–10 s) and time frames were applied for parameters estimation. The thermal conductivity values are reported in Table 6.8, showing good repeatability of the results. The thermal conductivity of $70\text{Li}_4(\text{OH})_3\text{Br}/30\text{PMgO}$ composite after thermal treatment at room temperature is found to be 0.6266 ± 0.0026 W/m/K, which is higher than that of pure peritectic salt (0.471 ± 0.002 W/m/K), giving an enhancement of 33% over the pure peritectic salt. This enhancement is likely to be increased over cycling due to the amelioration of the homogeneity of the composite structure upon cycling.

Table 6.8. Thermal conductivity values of $70\text{Li}_4(\text{OH})_3\text{Br}/30\text{PMgO}$

Test	k (W/m/K)	Average (W/m/K)	Standard deviation (W/m/K)
1	0.6262	0.6266	0.0026
2	0.6268		
3	0.6256		
4	0.6232		

6.4. Conclusion

The screening methodology followed allowed to perform the selection of the most promising oxide based supporting materials, with the best shape stabilized performances, for the peritectic compound $\text{Li}_4(\text{OH})_3\text{Br}$. The combination between thermal treatment, structural analysis, thermodynamic characterization, and cycling tests allowed us to have a clear overview about:

- i) The compatibility of the different materials tested and the possible by-products formed in case of reacting behaviour upon heating;
- ii) The influence of the ceramic materials added on the energy of the peritectic reaction;
- iii) The shape stabilization capability as a function of the concentration of inert oxide;
- iv) The effect of the cycling tests (up to 50 cycles) on both the reaction energy and the leakage occurrence.

The results allowed selecting the MgO as the most promising oxide showing good behaviour for the two parameters considered. All the other oxides studied showed some type of reaction (more or less pronounced upon heating and cycling), leading to their discard as a possible candidate supporting materials. Even though the performance of MgO is good, the high amount used (50 wt. %) in the composite causes a considerable loss of energy density (only half of the reaction energy is available). For this reason, decreasing the MgO amount required for the structural stability of the composite is necessary for consideration in TES applications. To this end, $\text{Li}_4(\text{OH})_3\text{Br}/\text{MgO}$ shape stabilized composites were developed using porous MgO samples with different structural, textural, and morphological properties. The porous structure with a pore dominantly in the mesoporous range (2-50 nm) characteristic of the tested MgO samples showed to afford additional sites for salt confinement, increasing thus the antileakage performances of the composite material. This configuration helped to considerably decrease the amount of supporting material required for the structural stability of the composite by 40 %. Among the three tested porous MgO samples, PMgO is the only one to afford good structural stability at reasonable loading (30 wt. %), good thermal stability, and good cycling stability. this sample is characterized by the combination of high specific surface area and an appreciable pore volume with wide mesopores size distribution.

Although the use of PMgO as a shape stabilizer induced a drop of enthalpy of 14 %, which was then improved by 4% over cycling, this supporting material is still worth to be considered

for use as it helped to decrease the necessary oxide amount for structural stability. The SEM-EDS analyses showed an improvement of the homogeneity of the composite structure over 50 melting/solidification cycles. Moreover, the overall thermal conductivity of the composite was enhanced by 33% over pure salt.

6.5. References

- [1] Y. E. Milián, A. Gutiérrez, M. Grágeda, and S. Ushak, "A review on encapsulation techniques for inorganic phase change materials and the influence on their thermophysical properties," *Renewable and Sustainable Energy Reviews*, vol. 73. Elsevier Ltd, pp. 983–999, Jun. 01, 2017, doi: 10.1016/j.rser.2017.01.159.
- [2] C. Cárdenas-Ramírez, F. Jaramillo, and M. Gómez, "Systematic review of encapsulation and shape-stabilization of phase change materials," *Journal of Energy Storage*, vol. 30. Elsevier Ltd, p. 101495, Aug. 01, 2020, doi: 10.1016/j.est.2020.101495.
- [3] G. Leng *et al.*, "Micro encapsulated & form-stable phase change materials for high temperature thermal energy storage," *Applied Energy*, vol. 217, pp. 212–220, May 2018, doi: 10.1016/j.apenergy.2018.02.064.
- [4] R. Jacob and F. Bruno, "Review on shell materials used in the encapsulation of phase change materials for high temperature thermal energy storage," *Renewable and Sustainable Energy Reviews*, vol. 48. Elsevier Ltd, pp. 79–87, Aug. 01, 2015, doi: 10.1016/j.rser.2015.03.038.
- [5] Z. Ge, F. Ye, and Y. Ding, "Composite materials for thermal energy storage: Enhancing performance through microstructures," *ChemSusChem*, vol. 7, no. 5, pp. 1318–1325, 2014, doi: 10.1002/cssc.201300878.
- [6] F. Jiang *et al.*, "Skeleton materials for shape-stabilization of high temperature salts based phase change materials: A critical review," *Renewable and Sustainable Energy Reviews*, vol. 119. Elsevier Ltd, p. 109539, Mar. 01, 2020, doi: 10.1016/j.rser.2019.109539.
- [7] S. Liu and H. Yang, "Porous ceramic stabilized phase change materials for thermal energy storage," *RSC Advances*, vol. 6, no. 53, pp. 48033–48042, May 2016, doi: 10.1039/c6ra06503a.
- [8] J. Liu, Q. Wang, Z. Ling, X. Fang, and Z. Zhang, "A novel process for preparing molten salt/expanded graphite composite phase change blocks with good uniformity and small volume expansion," *Solar Energy Materials and Solar Cells*, vol. 169, pp. 280–286, Sep. 2017, doi: 10.1016/j.solmat.2017.05.046.
- [9] Z. Acem, J. Lopez, and E. Palomo Del Barrio, "KNO₃/NaNO₃-Graphite materials for thermal energy storage at high temperature: Part I.-Elaboration methods and thermal properties," *Applied Thermal Engineering*, vol. 30, no. 13, pp. 1580–1585, Sep. 2010, doi: 10.1016/j.applthermaleng.2010.03.013.

- [10] M. Lachheb, A. Adili, F. Albouchi, F. Mzali, and S. Ben Nasrallah, "Thermal properties improvement of Lithium nitrate/Graphite composite phase change materials," *Applied Thermal Engineering*, vol. 102, pp. 922–931, Jun. 2016, doi: 10.1016/j.applthermaleng.2016.03.167.
- [11] Y. Ren, C. Xu, M. Yuan, F. Ye, X. Ju, and X. Du, "Ca(NO₃)₂-NaNO₃/expanded graphite composite as a novel shape-stable phase change material for mid- to high-temperature thermal energy storage," *Energy Conversion and Management*, vol. 163, pp. 50–58, May 2018, doi: 10.1016/j.enconman.2018.02.057.
- [12] H. Tian, W. Wang, J. Ding, X. Wei, and C. Huang, "Preparation of binary eutectic chloride/expanded graphite as high-temperature thermal energy storage materials," *Solar Energy Materials and Solar Cells*, vol. 149, pp. 187–194, May 2016, doi: 10.1016/j.solmat.2015.12.038.
- [13] H. Tian, W. Wang, J. Ding, X. Wei, M. Song, and J. Yang, "Thermal conductivities and characteristics of ternary eutectic chloride/expanded graphite thermal energy storage composites," *Applied Energy*, vol. 148, pp. 87–92, Jun. 2015, doi: 10.1016/j.apenergy.2015.03.020.
- [14] J. Liu, M. Xie, Z. Ling, X. Fang, and Z. Zhang, "Novel MgCl₂-KCl/expanded graphite/graphite paper composite phase change blocks with high thermal conductivity and large latent heat," *Solar Energy*, vol. 159, pp. 226–233, Jan. 2018, doi: 10.1016/j.solener.2017.10.083.
- [15] J. Lopez, Z. Acem, and E. Palomo Del Barrio, "KNO₃/NaNO₃ - Graphite materials for thermal energy storage at high temperature: Part II. - Phase transition properties," *Applied Thermal Engineering*, vol. 30, no. 13, pp. 1586–1593, Sep. 2010, doi: 10.1016/j.applthermaleng.2010.03.014.
- [16] T. Kim, D. Singh, W. Zhao, W. Yua, and D. M. France, "An investigation on the effects of phase change material on material components used for high temperature thermal energy storage system," in *AIP Conference Proceedings*, May 2016, vol. 1734, doi: 10.1063/1.4949121.
- [17] D. Singh, T. Kim, W. Zhao, W. Yu, and D. M. France, "Development of Graphite Foam Infiltrated with MgCl₂ for a Latent Heat Based Thermal Energy Storage (LHTES) System 2 3 Development of Graphite Foam Infiltrated with MgCl₂ for a Latent Heat Based Thermal Energy Storage (LHTES) System 40 41." Accessed: Mar. 25, 2021. [Online]. Available: <http://www.elsevier.com/open-access/userlicense/1.0/>.
- [18] W. Zhao, D. M. France, W. Yu, T. Kim, and D. Singh, "Phase change material with graphite foam for applications in high-temperature latent heat storage systems of concentrated solar power plants," *Renewable Energy*, vol. 69, pp. 134–146, Sep. 2014, doi: 10.1016/j.renene.2014.03.031.
- [19] D. Singh, W. Zhao, W. Yu, D. M. France, and T. Kim, "Analysis of a Graphite Foam-NaCl Latent Heat Storage System for Supercritical CO₂ Power Cycles for Concentrated Solar Power," 2015.
- [20] Y. J. Zhao, R. Z. Wang, L. W. Wang, and N. Yu, "Development of highly conductive KNO₃/NaNO₃ composite for TES (thermal energy storage)," *Energy*, vol. 70, pp. 272–

- 277, Jun. 2014, doi: 10.1016/j.energy.2014.03.127.
- [21] C. Yao, X. Kong, Y. Li, Y. Du, and C. Qi, "Numerical and experimental research of cold storage for a novel expanded perlite-based shape-stabilized phase change material wallboard used in building," *Energy Conversion and Management*, vol. 155, pp. 20–31, Jan. 2018, doi: 10.1016/j.enconman.2017.10.052.
- [22] X. Xiao, P. Zhang, and M. Li, "Thermal characterization of nitrates and nitrates/expanded graphite mixture phase change materials for solar energy storage," *Energy Conversion and Management*, vol. 73, pp. 86–94, Sep. 2013, doi: 10.1016/j.enconman.2013.04.007.
- [23] G. Xu *et al.*, "Sodium nitrate – Diatomite composite materials for thermal energy storage," *Solar Energy*, vol. 146, pp. 494–502, Apr. 2017, doi: 10.1016/j.solener.2017.03.003.
- [24] Y. Deng, J. Li, T. Qian, W. Guan, and X. Wang, "Preparation and Characterization of KNO_3 /Diatomite Shape-Stabilized Composite Phase Change Material for High Temperature Thermal Energy Storage," *Journal of Materials Science and Technology*, vol. 33, no. 2, pp. 198–203, Feb. 2017, doi: 10.1016/j.jmst.2016.02.011.
- [25] T. Qian, J. Li, X. Min, Y. Deng, W. Guan, and L. Ning, "Diatomite: A promising natural candidate as carrier material for low, middle and high temperature phase change material," *Energy Conversion and Management*, vol. 98, pp. 34–45, Jul. 2015, doi: 10.1016/j.enconman.2015.03.071.
- [26] Y. Qin *et al.*, "Sodium sulfate-diatomite composite materials for high temperature thermal energy storage," *Powder Technology*, vol. 282, pp. 37–42, Dec. 2015, doi: 10.1016/j.powtec.2014.08.075.
- [27] Y. Qin, X. Yu, G. H. Leng, L. Zhang, and Y. L. Ding, "Effect of diatomite content on diatomite matrix based composite phase change thermal storage material," in *Materials Research Innovations*, May 2014, vol. 18, pp. S2453–S2456, doi: 10.1179/1432891714Z.0000000000449.
- [28] Y. Deng, J. Li, and H. Nian, "Expanded Vermiculite: A Promising Natural Encapsulation Material of LiNO_3 , NaNO_3 , and KNO_3 Phase Change Materials for Medium-Temperature Thermal Energy Storage," *Advanced Engineering Materials*, vol. 20, no. 8, Aug. 2018, doi: 10.1002/adem.201800135.
- [29] R. Li, J. Zhu, W. Zhou, X. Cheng, and Y. Li, "Thermal compatibility of Sodium Nitrate/Expanded Perlite composite phase change materials," *Applied Thermal Engineering*, vol. 103, pp. 452–458, Jun. 2016, doi: 10.1016/j.applthermaleng.2016.03.108.
- [30] R. Li, J. Zhu, W. Zhou, X. Cheng, and Y. Li, "Thermal properties of sodium nitrate-expanded vermiculite form-stable composite phase change materials," *Materials and Design*, vol. 104, pp. 190–196, Aug. 2016, doi: 10.1016/j.matdes.2016.05.039.
- [31] A. Stoporev *et al.*, "Ionic clathrate hydrates loaded into a cryogel – halloysite clay composite for cold storage," *Applied Clay Science*, vol. 191, p. 105618, Jun. 2020, doi: 10.1016/j.clay.2020.105618.

- [32] L. Peng, Y. Sun, X. Gu, P. Liu, L. Bian, and B. Wei, "Thermal conductivity enhancement utilizing the synergistic effect of carbon nanocoating and graphene addition in palmitic acid/halloysite FSPCM," *Applied Clay Science*, vol. 206, p. 106068, Jun. 2021, doi: 10.1016/j.clay.2021.106068.
- [33] Z. Ge, F. Ye, and Y. Ding, "Composite Materials for Thermal Energy Storage: Enhancing Performance through Microstructures," *ChemSusChem*, vol. 7, no. 5, pp. 1318–1325, May 2014, doi: 10.1002/cssc.201300878.
- [34] C. Li *et al.*, "MgO based composite phase change materials for thermal energy storage: The effects of MgO particle density and size on microstructural characteristics as well as thermophysical and mechanical properties," *Applied Energy*, vol. 250, pp. 81–91, Sep. 2019, doi: 10.1016/j.apenergy.2019.04.094.
- [35] Y. R. Guo, Y. Liu, G. Q. Zhang, Z. F. Deng, G. Z. Xu, and B. R. Li, "Effect of SiO_2 on the thermal stability of carbonate/MgO composite for thermal energy storage," in *IOP Conference Series: Materials Science and Engineering*, Apr. 2019, vol. 504, no. 1, doi: 10.1088/1757-899X/504/1/012011.
- [36] Q. Li *et al.*, "Effects of MgO particle size and density on microstructure development of MgO based composite phase change materials," in *Energy Procedia*, Feb. 2019, vol. 158, pp. 4517–4522, doi: 10.1016/j.egypro.2019.01.759.
- [37] Y. Lu *et al.*, "Fabrication and characterization of the novel shape-stabilized composite PCMs of $\text{Na}_2\text{CO}_3\text{-K}_2\text{CO}_3/\text{MgO/glass}$," *Solar Energy*, vol. 189, pp. 228–234, Sep. 2019, doi: 10.1016/j.solener.2019.07.064.
- [38] C. Li *et al.*, "Heat transfer of composite phase change material modules containing a eutectic carbonate salt for medium and high temperature thermal energy storage applications," *Applied Energy*, vol. 238, pp. 1074–1083, Mar. 2019, doi: 10.1016/j.apenergy.2019.01.184.
- [39] Z. Jiang *et al.*, "A Form Stable Composite Phase Change Material for Thermal Energy Storage Applications over 700 °C," *Applied Sciences*, vol. 9, no. 5, p. 814, Feb. 2019, doi: 10.3390/app9050814.
- [40] B. Suleiman, Q. Yu, Y. Ding, and Y. Li, "Fabrication of form stable $\text{NaCl-Al}_2\text{O}_3$ composite for thermal energy storage by cold sintering process," *Frontiers of Chemical Science and Engineering*, vol. 13, no. 4, pp. 727–735, Dec. 2019, doi: 10.1007/s11705-019-1823-2.
- [41] Q. Yu *et al.*, "A novel low-temperature fabrication approach of composite phase change materials for high temperature thermal energy storage," *Applied Energy*, vol. 237, pp. 367–377, Mar. 2019, doi: 10.1016/j.apenergy.2018.12.072.
- [42] Z. Ge, F. Ye, H. Cao, G. Leng, Y. Qin, and Y. Ding, "Carbonate-salt-based composite materials for medium- and high-temperature thermal energy storage," *Particuology*, vol. 15, pp. 77–81, Aug. 2014, doi: 10.1016/j.partic.2013.09.002.
- [43] F. Ye, Z. Ge, Y. Ding, and J. Yang, "Multi-walled carbon nanotubes added to $\text{Na}_2\text{CO}_3/\text{MgO}$ composites for thermal energy storage," *Particuology*, vol. 15, pp. 56–60, Aug. 2014, doi: 10.1016/j.partic.2013.05.001.

- [44] Q. Guo and T. Wang, "Preparation and characterization of sodium sulfate/silica composite as a shape-stabilized phase change material by sol-gel method," *Chinese Journal of Chemical Engineering*, vol. 22, no. 3, pp. 360–364, Mar. 2014, doi: 10.1016/S1004-9541(14)60047-1.
- [45] J. Zhu, R. Li, W. Zhou, H. Zhang, and X. Cheng, "Fabrication of Al_2O_3 -NaCl composite heat storage materials by one-step synthesis method," *Journal Wuhan University of Technology, Materials Science Edition*, vol. 31, no. 5, pp. 950–954, Oct. 2016, doi: 10.1007/s11595-016-1473-x.
- [46] Y. Li *et al.*, "Eutectic compound ($\text{KNO}_3/\text{NaNO}_3$: PCM) quasi-encapsulated into SiC-honeycomb for suppressing natural convection of melted PCM," *International Journal of Energy Research*, vol. 39, no. 6, pp. 789–804, May 2015, doi: 10.1002/er.3293.
- [47] Y. Li, B. Guo, G. Huang, S. Kubo, and P. Shu, "Characterization and thermal performance of nitrate mixture/SiC ceramic honeycomb composite phase change materials for thermal energy storage," *Applied Thermal Engineering*, vol. 81, pp. 193–197, Apr. 2015, doi: 10.1016/j.applthermaleng.2015.02.008.
- [48] Y. Jiang, Y. Sun, R. D. Jacob, F. Bruno, and S. Li, "Novel Na_2SO_4 -NaCl-ceramic composites as high temperature phase change materials for solar thermal power plants (Part I)," *Solar Energy Materials and Solar Cells*, vol. 178, pp. 74–83, May 2018, doi: 10.1016/j.solmat.2017.12.034.
- [49] Q. Guo and T. Wang, "Study on preparation and thermal properties of sodium nitrate/silica composite as shape-stabilized phase change material," *Thermochimica Acta*, vol. 613, pp. 66–70, Jun. 2015, doi: 10.1016/j.tca.2015.05.023.
- [50] L. Sang, F. Li, and Y. Xu, "Form-stable ternary carbonates/MgO composite material for high temperature thermal energy storage," *Solar Energy*, vol. 180, pp. 1–7, Mar. 2019, doi: 10.1016/j.solener.2019.01.002.
- [51] C. Li *et al.*, "Carbonate salt based composite phase change materials for medium and high temperature thermal energy storage: A microstructural study," *Solar Energy Materials and Solar Cells*, vol. 196, pp. 25–35, Jul. 2019, doi: 10.1016/j.solmat.2019.03.035.
- [52] C. Li, Q. Li, and Y. Ding, "Investigation on the thermal performance of a high temperature packed bed thermal energy storage system containing carbonate salt based composite phase change materials," *Applied Energy*, vol. 247, pp. 374–388, Aug. 2019, doi: 10.1016/j.apenergy.2019.04.031.
- [53] C. Li, Q. Li, and Y. Ding, "Carbonate salt based composite phase change materials for medium and high temperature thermal energy storage: From component to device level performance through modelling," *Renewable Energy*, vol. 140, pp. 140–151, Sep. 2019, doi: 10.1016/j.renene.2019.03.005.
- [54] Y. Jannot and Z. Acem, "A quadrupolar complete model of the hot disc," *Measurement Science and Technology*, vol. 18, no. 5, pp. 1229–1234, May 2007, doi: 10.1088/0957-0233/18/5/009.
- [55] N. Ukrainczyk, S. Kurajica, and J. Šipušia, "Thermophysical Comparison of Five

- Commercial Paraffin Waxes as Latent Heat Storage Materials,” Hrvatsko društvo kemijskih inženjera i tehnologa, Jul. 2010.
- [56] K. V. Kumar *et al.*, “Characterization of the adsorption site energies and heterogeneous surfaces of porous materials,” *Journal of Materials Chemistry A*, vol. 7, no. 17, pp. 10104–10137, Apr. 2019, doi: 10.1039/C9TA00287A.
- [57] M. Thommes *et al.*, “Physisorption of gases, with special reference to the evaluation of surface area and pore size distribution (IUPAC Technical Report),” *Pure and Applied Chemistry*, vol. 87, no. 9–10, pp. 1051–1069, Oct. 2015, doi: 10.1515/pac-2014-1117.
- [58] P. A. Ward, J. A. † Teprovich, Y. Lu, J. He, R. Zidan, and † Savannah, “High Temperature Thermal Energy Storage in the CaAl_2 System,” 2017, Accessed: Jul. 23, 2021. [Online]. Available: <http://www.elsevier.com/open-access/userlicense/1.0/>.
- [59] X. Chen *et al.*, “Highly graphitized 3D network carbon for shape-stabilized composite PCMs with superior thermal energy harvesting,” *Nano Energy*, vol. 49, pp. 86–94, Jul. 2018, doi: 10.1016/J.NANOEN.2018.03.075.
- [60] H. Gao *et al.*, “Nanoconfinement effects on thermal properties of nanoporous shape-stabilized composite PCMs: A review,” *Nano Energy*, vol. 53, pp. 769–797, Nov. 2018, doi: 10.1016/J.NANOEN.2018.09.007.
- [61] J. Tang *et al.*, “Imine-linked micron-network polymers with high polyethylene glycol uptake for shaped-stabilized phase change materials,” *RSC Advances*, vol. 6, no. 50, pp. 44807–44813, May 2016, doi: 10.1039/C6RA05283E.
- [62] S. Liu, G. Ma, S. Xie, Y. Jia, J. Sun, and Y. Jing, “Diverting the phase transition behaviour of adipic acid via mesoporous silica confinement,” *RSC Advances*, vol. 6, no. 113, pp. 111787–111796, 2016, doi: 10.1039/C6RA23498D.
- [63] R. Mitran, D. Berger, C. Munteanu, and C. Matei, “Evaluation of Different Mesoporous Silica Supports for Energy Storage in Shape-Stabilized Phase Change Materials with Dual Thermal Responses,” *Journal of Physical Chemistry C*, vol. 119, no. 27, pp. 15177–15184, Jul. 2015, doi: 10.1021/ACS.JPCC.5B02608.
- [64] T. Nomura, C. Zhu, N. Sheng, K. Tabuchi, A. Sagara, and T. Akiyama, “Shape-stabilized phase change composite by impregnation of octadecane into mesoporous SiO_2 ,” *Solar Energy Materials and Solar Cells*, vol. 143, pp. 424–429, Dec. 2015, doi: 10.1016/J.SOLMAT.2015.07.028.
- [65] N. Gokon, D. Nakano, S. Inuta, and T. Kodama, “High-temperature carbonate/MgO composite materials as thermal storage media for double-walled solar reformer tubes,” *Solar Energy*, vol. 82, no. 12, pp. 1145–1153, Dec. 2008, doi: 10.1016/J.SOLENER.2008.05.011.
- [66] C. Li, Q. Li, and Y. Ding, “Investigation on the effective thermal conductivity of carbonate salt based composite phase change materials for medium and high temperature thermal energy storage,” *Energy*, vol. 176, pp. 728–741, Jun. 2019, doi: 10.1016/j.energy.2019.04.029.

General conclusions

In this thesis, the stoichiometric peritectic compound $\text{Li}_4(\text{OH})_3\text{Br}$ was proposed and studied as a novel phase change material for compact thermal energy storage (TES) applications at high temperature ($\sim 300^\circ\text{C}$). The thermal storage performances of this material demonstrated to be convenient for application in high-pressure (c.a. 100 bar) Direct Steam Generation (DSG) solar thermal power plants affording higher performances over the currently considered and employed materials in this application. $\text{Li}_4(\text{OH})_3\text{Br}$ presents some limitations. Most importantly, a low thermal conductivity, which requires oversizing the storage tanks and heat exchangers, besides, the corrosivity to the potential container materials which necessitates the use of expensive corrosion-resistant materials for the construction of the latter. These limitations considerably impact the investment cost and can be limiting factors regarding the usability of the material for TES applications. In order to overcome these limitations, and to improve the thermophysical properties of the studied peritectic salt, various $\text{Li}_4(\text{OH})_3\text{Br}$ based composites were developed and studied in this thesis work.

Overall, the main aspects to fully develop a cost-effective high performant PCM for compact TES were addressed according to the thesis objectives reported in the introduction part. The following conclusions were derived from each objective achieved.

- 1- LiOH-LiBr binary salt system was thoroughly investigated by means of Differential Scanning Calorimetry (DSC) and X-ray analyses. The objective was to support the potential consideration of the stoichiometric peritectic compound $\text{Li}_4(\text{OH})_3\text{Br}$ as a compact TES material and to elucidate the significant discrepancies reported in the literature regarding the temperature values of phase equilibria, the peritectic reaction enthalpies (theoretical and experimental values), as well as the stoichiometric compounds present in the system. A specific DSC analysis protocol was followed giving reliable results and allowing to solve the issue reported in the literature regarding the PCM leakage during the DSC analysis. The obtained results allowed proposing a new phase diagram of the binary system in accordance with the experimental data. The study also provided reliable information about phase transition temperatures and enthalpies and the phase transitions taking place. Additionally, regardless to the phase transition/reaction taking place, the experimental enthalpy values obtained in this work found to be much

lower than the ones calculated by FactSage 7.3. Thus, considering the completed peritectoid and peritectic reactions obtained in this work (confirmed by XRD), this result must be attributed to the proven shortcomings of Sansgter's phase diagram based on which the theoretical phase diagram was established. Moreover, although lower than the theoretical value, the achieved latent heat value of $\text{Li}_4(\text{OH})_3\text{Br}$ is higher than competing material considered for high pressure (100 bar) DSG power plants applications. Finally, $\text{Li}_4(\text{OH})_3\text{Br}$ was approved as an attractive material for compact TES applications at temperatures close to 300 °C, being a potential alternative to NaNO_3 .

- 2- The thermal storage performance of stoichiometric peritectic compound $\text{Li}_4(\text{OH})_3\text{Br}$ for has been thoroughly investigated. Including, energy density, reaction temperature, specific heat capacity, thermal conductivity, thermal cycling stability. The results showed moderate subcooling when testing small samples at high cooling rates (10–50 °C/min). Therefore it is not expected to be a problem while used under actual conditions with large quantities of product and much lower cooling rates. Additionally, the synthesis of $\text{Li}_4(\text{OH})_3\text{Br}$ was successful under air atmosphere (instead of using a protective atmosphere) and applying high cooling rates during the final step of the thermal treatment, which would result in significantly reduced production cost. Thermal cycling stability tests of $\text{Li}_4(\text{OH})_3\text{Br}$ between 200 °C and 350 °C showed excellent stability over large cycle number (600 cycles). No changes in the storage properties (reaction temperatures and enthalpies) have been observed. Moreover, the mechanisms of formation of $\text{Li}_4(\text{OH})_3\text{Br}$ was found to differ from commonly observed for peritectic structures, namely peritectic reaction and peritectic transformation. It was shown that $\text{Li}_4(\text{OH})_3\text{Br}$ nucleates and grows directly from the melt so as 100% conversion rate is achieved, contrary to many other peritectic structures in which the properitectic phase is not completely consumed with, therefore, a detrimental effect on the storage capacity. Furthermore, doping $\text{Li}_4(\text{OH})_3\text{Br}$ with a low amount (1 wt %) of carbon nanoparticles, mainly fullerenes C60 and MWCNTs, showed a positive although moderate effect on the thermal storage capacity due to interfacial effects between the salt and the surface of the carbon nanoparticles. Increasing the content of nanoparticles (10 wt %) had a detrimental effect on the storage capacity, likely because of Li intercalation and salt infiltration within the nanoparticle structure. Finally, $\text{Li}_4(\text{OH})_3\text{Br}$ presents several advantages, over the reference material NaNO_3 , as storage material for high-pressure DSG solar power plants. The most important ones are higher volumetric latent heat storage capacity (+54%) and lower

volume changes during phase transitions (3% vs 11%), which would translate into smaller storage tanks (– 33%), lower size heat exchangers and longer lifetime.

- 3- The first ever corrosion study of the stoichiometric peritectic compound $\text{Li}_4(\text{OH})_3\text{Br}$ was carried out to shed light on the corrosion behaviour of potential container materials with $\text{Li}_4(\text{OH})_3\text{Br}$. CS516.Gr70 and SS316 were tested in this study. Cycling corrosion tests were carried out under argon and air atmosphere at 350 °C applying various cycling durations. Carbon steel shows to react with the salt, forming a lithium iron oxide phase (LiFeO_2). The reaction is less intense under air atmosphere. Thus the resulting corrosion rate is lower. Due to the poor adherence of the LiFeO_2 phase to metals, peeling of the CS surface was observed. The reaction enthalpy was found to gradually decrease over cycling for the carbon steel due to the reaction between the salt and the steel sample. A larger enthalpy loss was recorded after 600 cycles for the sample tested under Argon in respect to air atmosphere, particularly for the salt in direct contact with the CS. Based on these results, although the obtained corrosion rate showed the ability of this steel for long-term service, longer exposure time should be applied in order to study the long-term effect of the corrosion on the stability of the salt and to be able to evaluate whether this steel is adequate for long-term exposition with $\text{Li}_4(\text{OH})_3\text{Br}$. Stainless steel316 performed better corrosion resistance than CS A516.Gr70 with $\text{Li}_4(\text{OH})_3\text{Br}$ at 350 °C. This material seems to be a very attractive option to be used as a container material for $\text{Li}_4(\text{OH})_3\text{Br}$ salt. The preliminary corrosion results showed the ability of this steel for long term service. Further corrosion studies should be carried out for the SS316 applying longer exposure time in order to define corrosion rate of this material and eventual long-term corrosion products.
- 4- Aiming at mitigating the corrosiveness of $\text{Li}_4(\text{OH})_3\text{Br}$ under harsh working conditions on the one hand. And to improve the heat transfers performances of the material, on the other hand. $\text{Li}_4(\text{OH})_3\text{Br}$ based shape stabilized composites were developed. First, a screening methodology was established and applied for the selection of the most suitable shape stabilizer for the peritectic $\text{Li}_4(\text{OH})_3\text{Br}$ among several oxides supporting materials. The selection criteria were based on i) The thermochemical compatibility with the peritectic salt. ii) The antileakage capability as a function of the concentration of the supporting material. And iii) The thermal and structural cycling stability. The ceramic MgO (solid nanoparticles) was selected as the most promising shape stabilizer. Porous MgO structures with various structural, textural, and morphological properties were synthesized,

characterized and tested as supporting materials with the aim of reducing the amount of MgO required for structural stability, thus increasing the overall storage capacity of the composite material. The porous structure of the solid MgO particles would afford additional sites for salt confinement and higher capillary forces, increasing thus the antileakage performances of the composite material at lower oxide loading. The results showed a 40% decrease of the required MgO loading providing similar performances in terms of antileakage efficiency while using the porous MgO (PMgO) structures combining an appreciable specific surface area, and a high pore volume with parallel plate-shaped pores in the range of (5-28 nm). The obtained shape stabilized composite presented good structural stability and homogeneity over cycling, besides an overall enhancement of the thermal conductivity of the composite by 33%. Finally, despite the small decrease of the reaction enthalpy of the composite due to the salt confinement effect, PMgO shape stabilizer is still worth to be considered for use as it helped to considerably enhance the overall storage capacity of the composite by decreasing the required supporting material loading. Further research should be carried out in order to improve the efficiency of $\text{Li}_4(\text{OH})_3\text{Br}/\text{MgO}$ composites following two points. 1) Study of the effect of the pore dimensions and geometry on the composite's thermal properties to be able to customize the former to limit the confinement effect as much as possible. 2) The addition of thermal conductivity enhancement materials to improve the overall heat transfer performances of the shape stabilized composite.

Annex

List of contributions

❖ Publications in international journals

- 1- F. Achchaq, E. Risueño, **I. Mahroug**, P. Legros, E. Lebraud, B. Karakashov, E. P. del Barrio, A. Celzard, V. Fierro, J. Toutain, “Development of a Carbon Felt/Salt-Based Hybrid Material for Thermal Energy Storage Applications,” *Journal of Energy and Power Engineering*, vol. 12, no. 7, Jul. 2018.
- 2- C. Mailhé, M. Duquesne, **I. Mahroug**, and E. P. del Barrio, “Improved infrared thermography method for fast estimation of complex phase diagrams,” *Thermochimica Acta*, vol. 675, pp. 84–91, May 2019.
- 3- **I. Mahroug**, S. Doppiu, J. L. Dauvergne, A. Serrano, and E. P. Del Barrio, “Li₄(OH)₃Br-based shape stabilized composites for high-temperature tes applications: Selection of the most convenient supporting material,” *Nanomaterials*, vol. 11, no. 5, May 2021.
- 4- **I. Mahroug**, S. Doppiu, J.-L. Dauvergne, M. Echeverria, J. Toutain, and E. Palomo del Barrio, “Study of peritectic compound Li₄(OH)₃Br for high temperature thermal energy storage in solar power applications,” *Solar Energy Materials and Solar Cells*, vol. 230, p. 111259, Sep. 2021.

❖ Articles in progress for publication in scientific journals

- 1- **I. Mahroug**, S. Doppiu, J.-L. Dauvergne, J. Toutain, and E. Palomo del Barrio, “Extended investigation of LiOH-LiBr binary system for high temperature thermal energy storage applications,” Under review in *Journal of Thermal Analysis and Calorimetry* (Submitted 22th July 2021).
- 2- **I. Mahroug**, S. Doppiu, J.-L. Dauvergne, and E. Palomo del Barrio, “Li₄(OH)₃Br/MgO shape stabilized composite as novel high temperature thermal energy storage material” (In preparation”).

❖ Contributions to conferences

- 1- **I. Mahroug**, E. Risueño, B. Karakashov, F. Achchaq, P. Legros, E. Palomo del Barrio, A. Faïk, J. Toutain, A. Godin, M. Duquesne, A. Celzard, “Infiltration of a carbon felt with a non-eutectic mixture for thermal energy storage,” ICOM 2018 conference (Poster + short oral Presentation).
- 2- **I. Mahroug**, S. Doppiu, J.-L. Dauvergne, and E. Palomo del Barrio, “Li₄ (OH)₃Br-Based Shape Stabilized Composites for High-Temperature TES Applications,” 15th international virtual conference on energy storage ENERSTOCK2021 (Poster+ oral Presentation)